Faculté des bioingénieurs
Institute of Condensed Matter and Nanosciences
Louvain Drug Research Institute

Macroporous scaffolds for tissue engineering:
3D printing
&
modification of the surface mechanical properties

Thèse soutenue en vue de l'obtention du grade de
docteur en sciences agronomiques et ingénierie biologique par

Loïc Germain

Composition du Jury
Pr. Anne des Rieux (UCLouvain/LDRI) – *Co-promotrice*
Pr. Christine Dupont-Gillain (UCLouvain/IMCN) – *Co-promotrice*
Pr. Eric Gaigneaux (UCLouvain/IMCN) – *Président*
Pr. Sophie Demoustier (UCLouvain/IMCN)
Pr. Sylvain Gabriele (UMons)
Pr. Julian Leprince (UCLouvain/LDRI)
Pr. Elżbieta Pamuła (AGH University of Science and Technology, Poland)
Pr. Benoît Raucent (UCLouvain/IMMC)

Louvain-la-Neuve
Octobre 2019

Je tiens à adresser des remerciements à un grand nombre de personnes sans qui cette thèse n'aurait sans doute pu aboutir.

Premièrement, je tiens à remercier mes promotrices, les Professeures Anne des Rieux et Christine Dupont. Je leur suis reconnaissant de m'avoir toujours fait confiance, aussi bien lors de la proposition de mon projet que lors de l'orientation que celui-ci prenait. Leurs précieux conseils m'ont permis d'avancer, d'apprendre et m'ont aidé à résoudre les problèmes auxquels je faisais face.

Ensuite, je tiens à remercier le Prof. Eric Gaigneaux d'accepter la présidence de mon Jury. I would also like to thank the members of my jury, Prof. Sophie Demoustier, Prof. Elżbieta Pamuła, Prof. Benoît Raucent, Prof. Julian Leprince and Prof. Sylvain Gabriele for the evaluation of this work.

Un travail ne peut être correctement accompli sans une bonne ambiance ! Faisant partie de deux laboratoires différents pendant 6 ans, j'ai pu rencontrer de nombreuses personnes qui ont toutes contribué à une excellente atmosphère. Tout d'abord à tous les collègues, anciens et nouveaux : Aiswarya, Kiran, Pauline, John, Dario, Audrey, Yasmine L., Ariane, Viridiane, Niki, Valéry, Eléana, Mathilde, Elia, Xiao, Nikos, Thibaut F., Jean-François, Sara, Aurélien, Anna, Eva, Cédric, Thibaut H., Vincent ainsi que tous les collègues de la cafétéria du Lavoisier. Je tiens vraiment à vous remercier pour les parties de rigolade, les taquineries (à double sens), ainsi que pour l'écoute et la compréhension dont vous avez tous fait preuve. Vous êtes bien plus que des collègues à mes yeux, vous êtes de vrais amis.

Pour qu'un équipement puisse être utilisé ou pour qu'une expérience puisse être réalisée, toute une logistique est nécessaire. Logisticiens de recherche, gestionnaires logistiques et comptables, secrétaires et techniciens coordonnent, réparent, entretiennent, réalisent des commandes et nous aident dans toutes nos tâches ! A Bernard, Kévin, Nathalie, Murielle, Pierre E., Claude, Yasmine A., Sylvie, Delphine, Pascale, Cécile, Colette, Rose-Anne et Françoise B., Françoise S., je tiens à dire MERCI. Merci pour votre gentillesse, vos enseignements, votre patience, vos conseils, votre oreille attentive, … Sans vous les laboratoires ne pourraient pas tourner.

J'ai eu la chance de pouvoir encadrer trois super mémorants. Mirasbek, Robin et Nicola, je souhaite encore vous féliciter pour votre mémoire et vous remercier pour tout l'aide que vous m'avez apportée dans ce projet ainsi que

pour la patience dont vous avez fait preuve lors de mes nombreuses tâches d'assistanat.

Je remercie Tamara, ma binôme de laboratoire didactique pendant 6 ans, avec qui j'ai partagé le plaisir de l'encadrement des étudiants et l'enfer des corrections. Merci pour ton soutien dans les moments délicats et ta bonne humeur continue. Merci également à Marie-France pour les « TPs du vendredi » que j'attendais toujours avec impatience. Maude, Kelly, Lucie, Amandine, Jean-Paul, Yves et Adrien, grâce à vous les TPs se sont toujours organisés sans problème, sans stress et toujours dans la bonne humeur. Ricky, Joséphine, Pierre D., Perrin, Romain et Perrine, collègues assistants, merci pour ces chouettes journées de TPs que l'on a partagées. Je pense que l'assistanat que j'ai pu réaliser avec vous tous va vraiment me manquer…

A mes amis de longue date (20 ans !) et de moins longue dates (8 ans, tout est relatif…), Mathias, Florent, Jérôme, Damien et à mon groupe d'amis de Charleroi, je tiens à dire merci pour votre soutien, pour tous les fous rires et pour toutes les sorties qui m'ont permis de déconnecter du boulot.

Merci enfin à ma famille, Maman, Papa et Lucas, merci d'avoir toujours été là pour moi. De m'avoir toujours soutenu, encouragé et de m'avoir aidé tout au long de cette thèse aussi bien dans le domaine privé que professionnel. Caroline, merci pour ton soutien, tes conseils scientifiques et pour tes relectures. Mamy, tes petits plats et tes mousses au chocolat m'auront bien servi de combustible pour rédiger ce manuscrit.

Foreword

This thesis is related to tissue engineering, a branch of biomedicine that aims at reconstructing damaged tissues using the unique potential of cells and biomolecules. The work can be described along the two main following axes.

The first axis is related to **applied research** and aims at producing personalized scaffolds for bone reconstruction. The obtained results could moreover be extended to other fields of application, *e.g.* by selecting other materials for scaffold production. The **challenge** of this part of the thesis is to build a scaffold with a complex geometry and pore size on the millimeter scale using an easy-to-transfer 3D printing technique, presenting a limit of resolution around 0.1 – 0.4 mm. The **originality** of the approach mainly resides in the complex geometry of the printed scaffolds, in rupture with more conventional geometries reported in the literature.

The second axis is more **fundamental** and aims at better understanding the influence of the surface mechanical properties of the scaffold on stem cell behavior. Surface modifications allow to selectively modify the microscopic mechanical properties at cell contact, while maintaining intact the scaffold macroscopic mechanical properties required to resist to the forces applied by the body itself. The **challenge** lies in developing such coating strategy on three-dimensional macroporous structures as most of the techniques used to produce thick coatings are rather adapted to two-dimensional substrates. The **originality** is brought by the proposed coating method and by the study of the effect of mechanical properties in macroporous scaffolds on stem cell behavior.

As a whole, this thesis should be considered as delivering tools that can be further developed into different applications related to tissue engineering as well as to other fields in which tailored macroporous structures are needed.

Abstract

Additive manufacturing techniques are promising technologies to produce patient-specific and effective scaffolds for tissue engineering. Chemical and physical surface modifications are often performed on scaffolds to control cell behavior and foster tissue regeneration. On the other hand, surface mechanical properties are known to influence stem cell proliferation and to direct their differentiation.

The aim of this work was to produce degradable poly(lactic acid) (PLA) and poly(ε-caprolactone) scaffolds using a so-called gyroid geometry, which features an isotropic and spring-shaped design. This was achieved by adapting the parameters to get closer to the resolution limit of fused deposition modeling, an easy-to-use and low-cost 3D printing technology. A semi-interpenetrating polymer network made with poly(dimethylsiloxane) crosslinked at different densities was then designed to modify the surface mechanical properties of PLA gyroid scaffolds. Finally, the effect of the coating mechanical properties on the proliferation and osteogenic differentiation of stem cells from the apical papilla was evaluated.

The production of complex scaffolds was successfully achieved using 3D printing. The coating technology that was further developed paves the way towards the modification of the surface mechanical properties of macroporous scaffolds with a complex shape, with a view to control stem cell behavior.

Contributions and participations

The author contributed to the following papers:

- Germain, L.; De Berdt, P.; Vanacker, J.; Leprince, J.; Diogenes, A.; Jacobs, D.; Vandermeulen, G.; Bouzin, C.; Préat, V.; Dupont-Gillain, C.; Des Rieux, A., Fibrin hydrogels to deliver dental stem cells of the apical papilla for regenerative medicine. *Regen. Med.* **2015,** *10* (2), 153-167.
- Viswanath, A.; Vanacker, J.; Germain, L.; Leprince, J. G.; Diogenes, A.; Shakesheff, K. M.; White, L. J.; des Rieux, A., Extracellular matrix-derived hydrogels for dental stem cell delivery. *J. Biomed. Mater. Res. Part A* **2017,** *105* (1), 319-328.
- Vander Straeten, A.; Bratek-Skicki, A.; Germain, L.; D'Haese, C.; Eloy, P.; Fustin, C. A.; Dupont-Gillain, C., Protein-polyelectrolyte complexes to improve the biological activity of proteins in layer-by-layer assemblies. *Nanoscale* **2017,** *9* (44), 17186-17192.
- Germain, L.; Fuentes, C. A.; van Vuure, A. W.; des Rieux, A.; Dupont-Gillain, C., 3D-printed biodegradable gyroid scaffolds for tissue engineering applications. *Mater. Des.* **2018,** *151*, 113-122.

The author participated to the following international scientific events:

- Oral presentation at the Scandinavian Society for Biomaterials (ScSB) conference, Sigulda, Latvia, May 2015.
- Presentation of a poster at the Advanced Materials for Biomedical Applications (AMBA) conference, Ghent, Belgium, September 2017.
- Presentation of a poster at the workshop on nanocomposite polymers for 3D printing of high-tech structures, Namur, Belgium, May 2018.
- Oral presentation at the 3rd Annual 3D printing and bio-printing in healthcare conference. Sheraton Brussels Airport Hotel, Belgium, October 2018.
- Oral presentation at the Belgian Symposium on Tissue Engineering (BSTE) conference, Ghent, Belgium, November 2018.

List of abbreviations

α-A	α-actinin
ΔCp	change in specific heat capacity
µCT	micro-computed tomography
µSLA	micro-stereolithography
AFM	atomic force microscopy
Al_2O_3	alumina
ALP	alkaline phosphatase
AM	additive manufacturing
AMSC	adipose-derived mesenchymal stem cells
B_2O_3	borate
BCC	body centered cubic
BDNF	brain-derived neurotrophic factor
BMSC	bone marrow mesenchymal stem cells
CAD	computer-aided design
CAM	computer-aided manufacturing
CaP	calcium phosphates
Co-Cr	cobalt-chromium
CT	computerized tomography
Đ	dispersity
DFSC	dental follicle stem cells
DLP	digital Light Processing/Printing
DMD	digital mirror device
DMLS	direct metal laser sintering
DPSC	dental pulp stem cells
EBM	electron beam melting
ECM	extracellular matrix
EDX	energy-dispersive X-ray spectroscopy
EMA	European Medicines Agency
ESC	embryonic stem cells
FAK	focal adhesion kinase
FDA	Food and Drug Administration
FDC	fused deposition of ceramics
FDM	fused deposition modelling
Fe	iron
FFF	fused filament fabrication
Fn	fibronectin
FWHM	full width at half maximum

GMSC	gingival-derived mesenchymal stem cells
GPCR	G-protein coupled receptor
HA	hydroxyapatite
HIPS	high impact polystyrene
HSC	hematopoietic stem cells
iPS	induced pluripotent stem cells
IUPAC	International Union of Pure and Applied Chemistry
LbL	layer-by-layer
LC	lateral compressions
LDM	low-temperature deposition manufacturing
MHDS	multi-head deposition system
M-LDM	multi-nozzel low-temperature deposition manufacturing
Mg	magnesium
Mn	number-average molar mass
MRI	magnetic resonance imaging
mRNA	messenger RNA mRNA
MSC	mesenchymal stems
Ni	nickel
OMS	oral mucosa stem cells
OCN	osteocalcin
P(DLLA-co-CL)	poly(D,L-lactic acid-co-ε-caprolactone)
P_2O_5	phosphate
PA	polyamide
PAA	polyacrylamide
PAM	pressure-assisted microsyringe
PAM2	piston-assisted microsyringe
Pax	paxilin
PBS	phosphate buffered saline
PCL	Poly(ε-caprolactone)
PDLLA	poly(D,L-lactic acid)
PDLSC	periodontal ligament stem cells
PDMS	poly(dimethylsiloxane)
PE	polyethylene
PED	precision extruding deposition
PGA	poly(glycolic acid)
PLA	poly(lactic acid)
PLGA	poly(lactic-co-glycolic acid)
PLLA	poly(L-lactic acid)
PMMA	poly(methyl methacrylate)
PP	polypropylene
PPF	poly(propylene fumarate)
PS	polystyrene

PVA	poly(vinyl alcohol)
qRT-PCR	quantitative reverse-transcriptase polymerase chain reaction
RGD	arginine-glycine-aspartic acid
ROCK	Rho-associated kinase
RPL13	60S ribosomal protein L13
RUNX2	runt-related transcription factor 2
RP	rapid prototyping
RTKs	receptor tyrosine kinases
SAC	stretch activated channel
SCAP	stem cells from the apical papilla
SEM	scanning electron microscope
SFF	solid-freeform fabrication
SGSC	salivary gland-derived stem cells
SHED	stem cells from human exfoliated deciduous teeth
SiO_2	silicate
SIPN	semi-interpenetrating polymer network
SLA	stereolithography
SLM	selective laser melting
SLS	selective laser sintering
SSLS	surface selective laser sintering
T	talin
TCP	tricalcium phosphates
TCPS	tissue culture-treated polystyrene
Ten	tensin
Tg	glass transition temperature
TGF-β_1	transforming growth factor-β_1
TGPC	tooth germ progenitor cells
Ti	titanium
Ti-Ni SMA	titanium-nickel shape memory alloys
TIPS	thermally induced phase separation
TOF-SIMS	time-of-flight – secondary ion mass spectrometry
TPMS	triply periodic minimal surfaces
TPP *or* 2PP	two-photon polymerization
UV	ultraviolet
V	vinculin
VC	vertical compressions
VEGF	vascular endothelial growth factor
XPS	X-ray photoelectron spectroscopy
ZrO_2	Zirconia

Table of contents

Part I : Context of research 1
1 Tissue engineering 4
2 Cells 5
2.1 Stem cells 6
2.1.1 Classification based on the differentiation potential 6
2.1.2 Classification based on origin 7
2.1.3 Stem cells from the oral cavity 9
2.2 Receptors and mechanotransduction 12
2.2.1 Cell membrane receptors 12
2.2.2 Adhesion receptors 13
2.2.2.1 Cell adhesion 14
2.2.2.2 Cell sensing 15
3 Scaffolds 17
3.1 Desired scaffold properties for tissue engineering 17
3.2 Conventional fabrication techniques 18
3.3 Additive Manufacturing techniques 24
3.3.1 Light-based systems 27
3.3.1.1 Basic principle: Stereolithography (SLA) 27
3.3.1.2 Advanced technology 27
3.3.2 Sintering-based methods 28
3.3.2.1 Basic principle: Selective laser sintering (SLS) 28
3.3.2.2 Advanced technology 29
3.3.3 Ink/binder jetting-based methods 30
3.3.3.1 Basic principle: Ink-jet printing or 3D printing (3DP) . 30
3.3.3.2 Advanced technology 30
3.3.4 Extrusion-based processes 31
3.3.4.1 Basic principle 31

3.3.4.2 Advanced technology 33
3.4 Available biocompatible materials for printing 34
3.4.1 Metals 34
3.4.2 Ceramics 35
3.4.3 Polymers 37
3.4.4 Composites 42
3.5 Scaffold and mesh geometry 43
3.5.1 Scaffold porosity 43
3.5.2 Mesh geometry and struts orientation 47
3.5.2.1 The two main kinds of geometries 47
3.5.2.2 Geometric-related parameters to consider for tissue engineering 76
4 Cell signaling 78
4.1 Signaling biomolecules 78
4.2 Surface modifications 79
4.2.1 Chemical properties 79
4.2.2 Topography 81
4.2.3 Mechanical properties 82
5 References 85
Part II : Aims of the thesis 99
Part III : Strategy 103
1 Fused deposition modeling 105
2 Mesh designs proposed for the scaffold 110
3 Poly(lactic acid) (PLA) 112
4 Poly(dimethylsiloxane) (PDMS) 114
5 Coating method 115
6 Stem cells from the apical papilla (SCAP) 117
7 References 119
Part IV : Outline 123

Part V : Results 127

Chapter 1: 3D-printed biodegradable gyroid scaffolds for tissue engineering applications 129

1 Introduction 131

2 Materials and methods 134

2.1 3D models 134

2.2 Materials and printing conditions 135

2.3 µCT scan 136

2.4 Porous fraction measurement 137

2.5 Surface topography 138

2.6 Crystallinity fraction evaluation 138

2.7 Compression tests 138

2.8 Scaffold *in vitro* degradation 139

2.9 Statistical analysis 139

3 Results and discussion 140

3.1 3D scanning of printed gyroid structures 140

3.2 Porous fraction of printed gyroids 141

3.3 Profilometry of printed gyroid scaffolds 142

3.4 Influence of the support on shape fidelity 143

3.5 Impact of annealing on printed PLA 143

3.6 Impact of geometry, printing resolution and crystallinity of the structures on mechanical resistance 144

3.7 Impact of geometry, printing resolution and crystallinity of the structures on *in vitro* degradation kinetics 147

4 Conclusions 151

5 Supporting information 152

6 References 154

Chapter 2: Optimization of poly(ε-caprolactone) 3D printing 161

1 Introduction 163

2 Materials and methods 164

2.1 PCL scaffold model and 3D printing....164
2.2 Morphological characterization....167
2.3 Porous fraction evaluation....167
2.4 Compression tests....168
3 Results and discussion....169
3.1 PCL gyroid scaffold printed with HIPS support....169
3.2 PCL gyroid scaffold printed with PVA support....172
3.3 PCL scaffold topography....174
3.4 Scaffold porosity....175
3.5 Impact of mesh geometry on mechanical resistance....176
4 Conclusion and future prospects....179
5 References....180
Chapter 3: PDMS coating optimization and preliminary studies....185
1 Introduction....187
2 Coating through the formation of a SIPN and optimizable parameters....189
3 Selection of the coating mixture....191
3.1 Materials and methods....191
3.2 Results and discussions....192
4 Coating characterization through surface chemical analysis....196
4.1 Materials and methods....196
4.2 Results and discussions....197
4.2.1 Water contact angle in dynamic conditions....197
4.2.2 XPS analysis....199
5 Influence of the coating mixture composition on coating thickness....202
5.1 Materials and methods....202
5.2 Results and discussions....203
6 Development of other coating methods....205

7 Further tentative developments to adapt the coating protocol using the formation of a SIPN to PLA macroporous scaffolds 208
8 Conclusion and future prospects 213
9 References 214
Chapter 4: Preliminary cell culture studies 217
1 Introduction 219
2 Impact of adhesion protein adsorption on AMSC adhesion 220
2.1 Materials and methods 220
2.2 Results and discussions 221
3 Impact of cell seeding method on AMSC adhesion 223
3.1 Materials and methods 223
3.2 Results and discussions 225
4 SCAP adhesion on gyroid scaffolds 227
4.1 Materials and methods 227
4.2 Results and discussions 228
5 Improvement of SCAP adhesion yield by adjustment of cell density 231
5.1 Materials and methods 231
5.2 Results and discussions 231
6 Conclusion and future prospects 234
7 References 235
Chapter 5: The crosslinking density of a PDMS coating on macroporous scaffolds influences the proliferation of stem cells from the apical papilla but not their osteogenic differentiation 241
1 Introduction 243
2 Materials and methods 245
2.1 PDMS mechanical properties 245
2.2 3D model and printing 246
2.3 PDMS coating on the PLA gyroid scaffold 246
3 Evaluation of coating morphology and thickness 247

3.1 Preparation of scaffolds for SCAP culture and seeding in 3D scaffolds 248
3.2 Evaluation of SCAP seeding and proliferation 248
3.3 Evaluation of SCAP *in vitro* osteogenic differentiation 249
3.4 Statistical analysis 250
4 Results and discussion 250
4.1 PDMS viscoelastic properties 250
4.2 Validation of PDMS coating and measurement of coating thickness on PLA gyroid scaffolds 251
4.3 SCAP seeding and proliferation on coated gyroid scaffolds 256
4.4 SCAP *in vitro* differentiation on PDMS-coated gyroid scaffolds 259
5 Conclusions 264
6 Supporting information 266
7 References 266
Part VI : Conclusions and future prospects 273
1 Main achievements 275
1.1 PLA gyroid scaffold production 275
1.2 PCL gyroid scaffold production 276
1.3 Optimization of PDMS coating protocol 276
1.4 Preliminary cell culture studies 277
1.5 Effect of macroporous scaffold surface mechanical properties on SCAP behavior and osteogenic differentiation 277
2 Future prospects 278
2.1 Production of scaffolds presenting complex geometry using fused deposition modelling 278
2.2 PDMS polymer coating 280
2.3 Cell mechanotransduction in macroporous scaffolds presenting tuned pore surface stiffness. 283

2.4 General long-term future prospects 285
3 References 287
Annex : Detailed protocols of PDMS coating methods 291

Part I : Context of research

Nowadays thanks to progresses in medicine, people live better and longer. However, organ or tissue failures still may occur because of diseases or trauma. This can in some cases be solved by a transplantation from a donor. Still, donors are limited and the offer does not meet the demand. Most of the patients cannot get a transplant. Besides, rejection of the graft may always occur. Surgeon have been using biomaterials for decades, to help the body to recover or to substitute a failing or missing part of the body.

Biomaterial was first defined as "*a nonviable material used in a medical device, intended to interact with biological systems*."[1, 2] Later, owing to the evolution of material science and health technology, a new definition was proposed. ''*A biomaterial is a substance that has been engineered to take a form which, alone or as part of a complex system, is used to direct, by control of interactions with components of living systems, the course of any therapeutic or diagnostic procedure, in human or veterinary medicine*.''[2] Hence, biomaterials gather a broad category of materials that can be bioinert or trigger a specific response of cells at their contact. They are notably used to produce implantable devices such as heart valves, prostheses, sutures and drug delivery systems. While devices based on biomaterials are suitable in many situations, they are not able to follow the dynamics of the body, to grow with it or to self-repair as they are not "living entities". For example, an artificial heart-valve implanted in a child is not able to grow with the heart while the child is growing. Similar issues can arise for adults if the body changes with aging.

Tissue engineering appeared in the 1980's[3] but was defined clearly by Langer and Vacanti[4] later in 1992. "*A new field, tissue engineering, applies the principles of biology and engineering to the development of functional substitutes for damaged tissue.*" The goal of this field is to produce artificial tissues and organs using cell transplantation and transformation into functional tissues and organs that are equivalent to their natural counterparts. In order to achieve this goal, it is important to give to cells a suitable environment for colonization and multiplication (*i.e.* proliferation) as well as the suitable signals for their differentiation to regenerate the desired tissue or organ.[5] Thanks to the progress in chemistry, biology and material science and engineering, tissue engineering is rapidly evolving.[6, 7]

In the field of tissue engineering, Additive Manufacturing (AM) techniques, commonly known as 3D printing, have emerged and are attracting more and

more interest for the possibility to build three-dimensional environments (scaffolds) for cells to expand. These techniques are low cost and allow personalization to meet patient-to-patient variability. The Holy Grail, in a distant future, would be the ability to print organs directly using patient's cells.

This thesis aims at producing scaffolds using an AM technique and focuses on cell-material interactions for tissue engineering applications.

1 Tissue engineering

In tissue engineering, three main components are used: cells, biomaterials and bioactive factors.[8] Briefly, cells should be healthy, viable, accessible, non-immunogenic and show plasticity. The biomaterial, commonly termed as "scaffold", is used as a carrier and a delivery vehicle. The bioactive factor gives signals to cells for their development, proliferation and differentiation. These factors are commonly soluble molecules or proteins that reach or enter the cells to direct their behavior. However, this could be extended to any morphological, chemical or mechanical modification made on the scaffold that gives signals to the cells.

Several combinations of these three components can be made. At least three approaches were pointed as tissue engineering strategies.[8] The first approach is the most widely used and is presented in Figure 1.[8, 9] Cells seeded in a three-dimensional biodegradable scaffold are transplanted to replace the function of the altered tissues. Briefly, cells, usually stem cells, can be harvested from the patient (a), they are expanded using conventional cell culture methods (b). Once reaching a sufficient number of cells, they can be seeded on/in a scaffold. Bioactive compounds can be added at the same time or be already present in the scaffold (c). Cells are further cultured and differentiated (d) to form a construct that is implanted in the patient (e). The second rely on the use of a combination between a scaffold and bioactive factors to induce migration, proliferation and differentiation of the cells from surrounding tissues.[8] The third is the transplantation of encapsulated cells in a semi-permeable membrane to have at least a partial restoration of tissue functions.[8, 10] This semi-permeable membrane allows metabolites, proteins and oxygen to pass but is hermetic to cells.

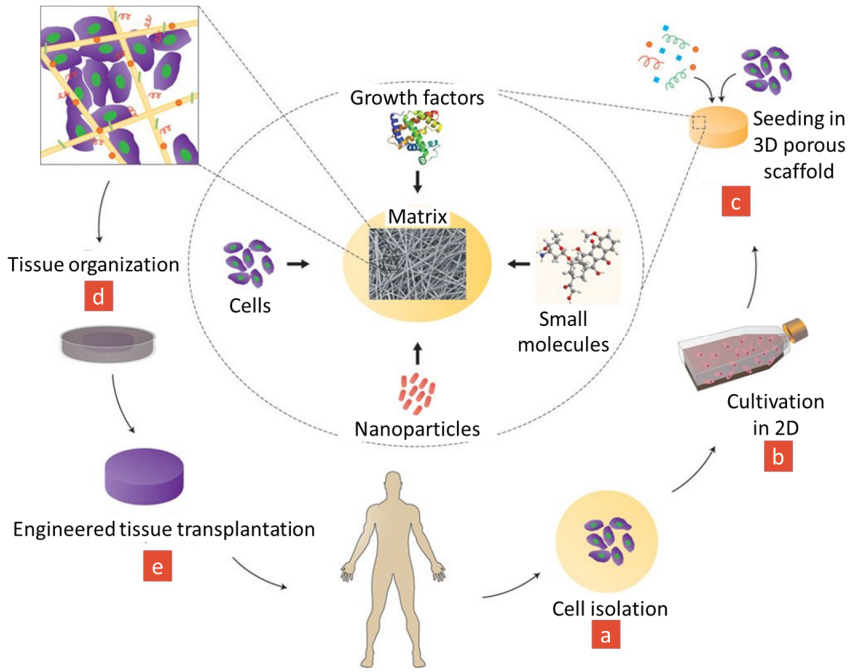


Figure 1: Tissue engineering process based on autologous cells isolation and reimplantation. (a) Stem cells are harvested from the patient, (b) their number is increased using conventional cell culture methods. (c) Once reaching a sufficient number, cells are seeded on/in a scaffold. Bioactive compounds can be added at the same time or be already present in the scaffold. (e) Cells are further cultured and differentiated (d) before being implanted in the patient. Adapted from [9]

2 Cells

Our body is estimated to be made of more than 10^{13} individual cells.[11] They belong to more than 200 different cell types and, together with extracellular matrices, are forming tissues. The organization of many cell types in tissues is well defined and related to their function.[12] Tissues can assemble to form organs. A first distinction can be made between somatic cells and stem cells. Somatic cells are specialized cells that ensure a specific function in a tissue. They adopt well-defined expression patterns, morphologies, positions and orientations closely related to the type and the function of the tissue. Stem cells are undifferentiated cells that are able to divide with a high proliferative rate and have the ability to differentiate into a specific type of somatic cell.[13] Stem cell niches can be found in every organ or tissue and are a reservoir of regenerative cells that contribute to the maintenance of the body.

2.1 Stem cells

Stem cells are capable of self-renewal and differentiation in a range of specialized cell types.[14] Tissue-specific stem cells are present in most organs and tissues of the body.[15] They are present everywhere but also at any stage of the development of a living organism, from the embryo to the adult stage.[14] At the time of their discovery, stem cells were considered as an "elixir of life".[15] Even if they are promising, several decades after their discovery, scientists still have difficulties to control their fate and to organize them in functional three-dimensional tissues. Two distinct classifications of stem cells exist. The first classification focuses on their differentiation potential. Not all stem cells have the same possibilities regarding the ability to give rise to the wide range of specialized cells of the body. The second classification is based on the origin of stem cells: this includes the development stage of the living organism and the cell location.

2.1.1 Classification based on the differentiation potential

Stem cells can be categorized in five groups depending on their differentiation potential (Figure 2).[14-16]

Totipotent cells (or **omnipotent cells**) are able to differentiate into any existing body cell type as well as into placenta cells.[14-16] They are present at the first stages of embryonic development, just after oocyte fertilization.

Pluripotent cells cannot give rise to the placenta and its supporting tissue but are able to self-renew and to differentiate into any cells of the three germ layers (ectoderm, mesoderm and endoderm).[14-16] The only known natural pluripotent cells are embryonic stem cells (ESC). They come from the inner cell mass of the embryo at the blastocyst stage. Artificial stem cells named induced pluripotent stem cells (iPS) also belong to this category. These iPS will be presented later.

Multipotent cells are able to self-renew but differentiate only in a few cell types related to their location.[14-16] Multipotent cells can be isolated from niches present in many adult tissues and organs. The most studied are mesenchymal (MSC) and hematopoietic stem cells (HSC). MSC are used by the body to replace lost or damaged cells in organs and tissues.

Some authors also identify **oligopotent cells** as a distinct category.[14] They are also able to self-renew but only differentiate into closely related cell types.

Finally, **unipotent cells** are the least potent as they have a limited proliferative potential and are able to differentiate only in one cell type.[14-16] As a consequence, unipotent cells are not always considered as stem cells but more as *committed progenitors*.

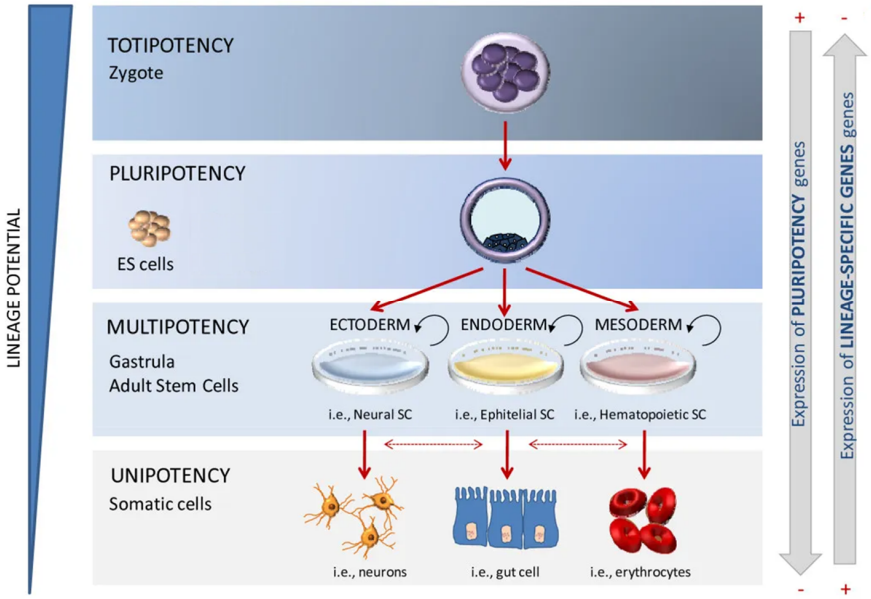


Figure 2: Classification of stem cells based on their differentiation potential. Adapted from [13]

2.1.2 Classification based on origin

Stem cells can also be organized in 5 categories depending on their origin.[14]

Embryonic stem cells (ESC) come from the embryo five or six days after oocyte fertilization at the blastocyst stage.[14] The blastocyst is composed of a surrounding layer of cells, named trophoblast, which forms the placenta and its supporting tissues and an inner cell mass, which forms the embryo. This inner cell mass constitutes these ESC and is separated from the trophoblast. If plated in culture dishes and cultured in very specific conditions, they can proliferate infinitely and remain in an undifferentiated state. Even if this source seems promising, their isolation and their use rise obvious ethical problems.

Fetal stem cells are isolated from embryos obtained after abortion.[14] They are less potent compared to ESC and cannot divide indefinitely. Their

isolation and their use are subject to strict regulations, which vary from a country to another.

Perinatal stem cells can be separated into three subgroups following their origins: stem cells from amniotic fluid, placenta and umbilical cord.[14] Stem cells from the umbilical cord are the most talked about as parents are more and more asking for conservation of this umbilical cord in case of serious disease of their child. Stem cells banking has become a lucrative business even though the low number of isolated stem cells and their low proliferation severely limit their use.

Adult stem cells (also named resident stem cells or tissue-restricted stem cells) reside in niches in tissues and organs all over the body.[14] They allow reparations and a continuous self-renewal of tissues. For example, human epidermis is fully renewed every three to four weeks and gastrointestinal epithelium every few days. This repair process is allowed by the proliferation and the differentiation of these adult stem cells. These cells are hence subjected to a great interest and many researchers try to understand how to stimulate their proliferation and their mobilization to heal parts of the body. Their isolation from each location is not always possible (*e.g.* cardiac and pancreatic stem cells) and some of them are easier to access (*e.g.* adipose and dental stem cells). There is much less ethical concern using adult stem cells compared to the previous categories.[17]

A subcategory of adult stem cells is the mesenchymal stem cell (MSC) family, which is defined by the International Society for Cellular Therapy.[18] Briefly, mesenchymal stem cells should (i) adhere to tissue culture-treated polystyrene (TCPS), (ii) express some surface antigens (*e.g.* CD105, CD90,…) and not others (*e.g.* CD45, CD34,…) and (iii) have a multipotent differentiation potential (osteo-, adipo-, chondrolineages). Bone marrow mesenchymal stem cells (BMSC) were the first discovered mesenchymal stem cells and were considered for long as the gold standard.[19] Owing to the complexity of the procedure and surgical trauma caused by bone marrow isolation, alternative sources of mesenchymal stem cells were evaluated.[17] The most popular easy-to-access stem cells are adipose-derived mesenchymal stem cells (AMSC), which are easily accessible from liposuction and are present in large numbers.[20] Considering their availability and their potential for tissue engineering strategies, AMSC are becoming the new gold standard.[21]

Induced pluripotent stem cells (iPS) are artificially created stem cells.[14] Somatic cells (like mesenchymal cells) are reprogrammed introducing a cocktail of transcription factors (Oct4, Sox2, c-Myc and Klf4) in their genome.[22, 23] These reprogramming factors silence somatic genes and reactivate proliferation- and pluripotency-inducing genetic programs to bring the cell back to a pluripotent state very similar to ESC. iPS can be patient-specific (which circumvents immunological issues), proliferate indefinitely and can be differentiated into any mature cell type of the body. Moreover, iPS do not raise ethical concerns. However, their current use for clinical application is still limited by the gene delivery technique used to produce them. Indeed, these techniques carry enormous risks of permanent genetic modifications and could be tumorigenic.

2.1.3 Stem cells from the oral cavity

Stem cells from the oral cavity, including dental stem cells, are among the last adult stem cells that were discovered and identified as MSC.[24] Six different types of dental stem cells and two types in the surrounding tissues are distinguished mostly according to their location (Figure 3). Depending on their origin, they can differentiate into slightly different cells and tissues (Table 1).

Tooth germs are formed from the neural crest during embryogenesis.[17] During the development, these progenitor cells differentiate into the dental organ, dental papilla and dental follicle. A reservoir of undifferentiated cells resides into dental tissues even at adult stage.

The first identified dental stem cells were **dental pulp stem cells** (DPSC), isolated from permanent third molar dental pulp and responsible of the repair of the dentin.[25-28] Ikeda and coworkers identified **tooth germ progenitor cells** (TGPC) present in third molar in an earlier stage of development (late-bell stage).[29] They were showing high proliferation activity. **Stem cells from human exfoliated deciduous teeth** (SHED) are harvested from the pulp of deciduous teeth.[25-28] SHED showed also a higher proliferation rate compared to DPSC and different potential regarding differentiation but were unable to regenerate the dentin-pulp complex.

Between teeth roots and alveolar bone in the jaw lies a complex connective tissue, the periodontal ligament.[26, 30] **Periodontal ligament stem cells** (PDLSC) can be isolated from the periodontal ligament that attaches the

teeth to the jaw and protect de roots against forces generated during mastication.

Dental follicle stem cells (DFSC) and **stem cells from the apical papilla** (SCAP) can be isolated from developing tissues, the dental follicle and the apical papilla, respectively.[25-27] The dental follicle is the connective tissue surrounding the developing tooth, which differentiates into the periodontal ligament. The apical papilla is a tissue attached at the apex of permanent teeth roots in formation. SCAP are mostly isolated from immature wisdom teeth. They have a higher proliferation rate than DPSC and BMSC.[25-27, 31, 32] This work will use SCAP, and more precisely a clone, named RP89, that was selected for its sustained expression in culture of required MSC markers as well as for its high differentiation capacity.[33]

The oral mucosa, composed of the epithelium and underlying connective tissues, is another tissue present in the oral cavity and also contains stem cells.[25]To date, two different types of adult stem cells were isolated form the oral mucosa: **Gingival-derived mesenchymal stem cells** (GMSC) and **Oral mucosa stem cells** (OMSC).

Dental stem cells concentrate several advantages. They are easily accessible[34], present no ethical issues[24], are low-cost to isolate and expand. They have a high proliferation rate and can differentiate into osteo-, neuro-, adipo-, chondro- and ondontolineages.[25, 27]

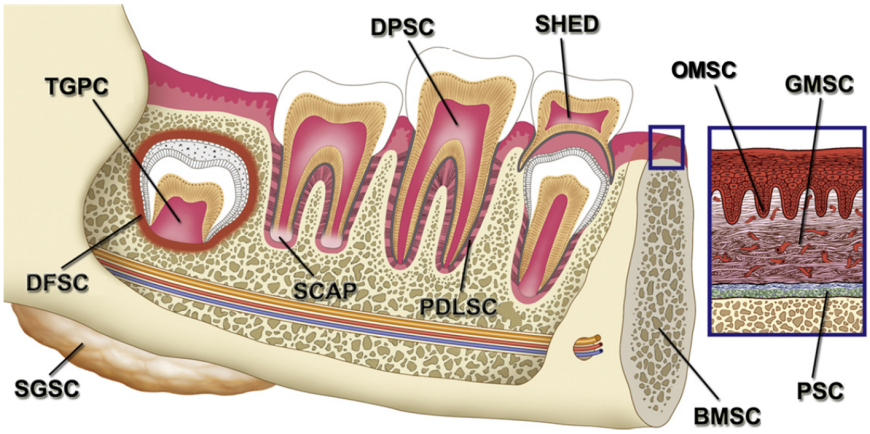


Figure 3: Sources of oral adult stem cells. DFSC: dental follicle stem cells; TGPC: tooth germ progenitor cells; SCAP: stem cells from the apical papilla; DPSC: dental pulp stem cells; PDLSC: periodontal ligament stem cells; SHED: stem cells from human exfoliated deciduous teeth; OMSC: oral mucosa stem cells; GMSC: gingival-derived mesenchymal stem cells; SGSC: salivary gland-derived stem cells; BMSC: bone marrow-derived mesenchymal stem cells from orofacial bone. Adapted from [25]

Table 1: Characteristics of human stem cells from the oral cavity. Adapted from [25] and [27].

Stem cells	**Location**	**Proliferation rate**	***In vitro* differentiation capacity**	***In vivo* tissue formation capacity**
DPSC	Permanent tooth pulp	Moderate	Odontoblast, osteoblast, adipocyte, chondrocyte, myocyte, neurocyte, corneal epithelial cell, melanoma cell, iPS	Bone, neural tissue, adipose tissue, muscle, dentin, pulp
SHED	Exfoliated deciduous tooth pulp	High	Odontoblast, osteoblast, adipocyte, chondrocyte, myocyte, endothelial cell, neurocyte, iPS	Bone, microvessel, neural tissue, dentin
PDLSC	Periodontal ligament	High	Odontoblast, osteoblast, adipocyte, chondrocyte, cementoblast, neurocyte	Bone, teeth root, periodontal ligament, cementum
DFSC	Dental follicle of developing tooth	High	Odontoblast, osteoblast, adipocyte, chondrocyte, cementoblast, neurocyte	Bone, periodontal ligament, cementum
TGPC	Tooth germ	High	Osteoblast, adipocyte, endodermal lineage, neurocyte, hepatocyte	Bone
SCAP	Apical papilla of developing root	High	Odontoblast, osteoblast, adipocyte, neurocyte, adipocyte, iPS	Bone, neural tissue, dentin, pulp, teeth root
GMSC and OMSC	Oral mucosa	/	osteoblast, adipocyte, chondrocyte, neurocyte, glial cell, endoderm cell	Bone, cartilage, adipose tissue, muscle, epithelia, neural tissue

2.2 Receptors and mechanotransduction

2.2.1 Cell membrane receptors

For cells to assemble, form tissue and ensure a function, communication is critical. Cells are able to communicate with the environment through membrane receptors, which are proteins or group of proteins that play the role of sensors and detect extracellular signals (*e.g.* growth hormones, neurotransmitters, peptides, odorant, light and extracellular matrix cues).[35] The receptors reside in a complex and heterogeneous hydrophobic membrane environment containing lipids and protein domains. Other membrane proteins, lipids and even the cytoskeleton regulate receptors activity. The detection of extracellular signals triggers intracellular signal transduction pathways that control key physiological functions and cellular behavior (Figure 4). The study and the understanding of the mechanisms linked to cell communication are very challenging. Owing to the complexity of the plasma membrane and the number of possible interactions/regulation, all mechanisms are not yet fully understood.

The three major classes of receptors are receptor tyrosine kinases (RTKs), G-protein coupled receptors (GPCRs), and adhesion receptors.[35] RTKs control cell growth, differentiation and motility. GPCRs comprise the largest and most diverse group of membrane receptor. Their regulation extends to a wide variety of physiological processes as various as vision, smell, immune response and mood regulation. The third class, adhesion receptors, allows the attachment of cells to each other and to the extracellular matrix. They also play a role in development, motility, wound healing and other contact dependent signaling. This last group of receptors will be further discussed, as they constitute a central part in this work.

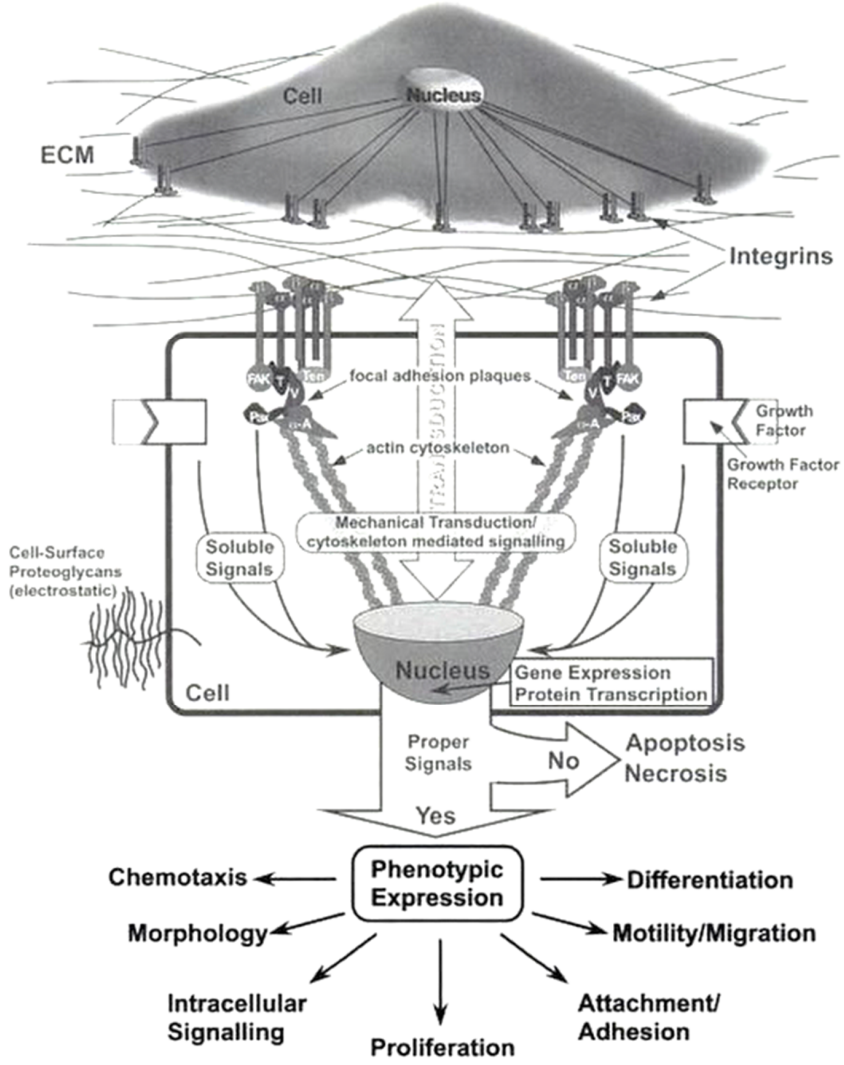


Figure 4: Interaction of a cell with its environment. Global signaling pathways form the detection of a signal by membrane receptors to changes in cell behavior. FAK: focal adhesion kinase; T: talin; V: vinculin; Ten, tensin; Pax: paxilin; α-A: α-actinin.[36]

2.2.2 Adhesion receptors

Whether cultured in two-dimensional or in three-dimensional systems, most of mammalian cell types needs to adhere to a substrate in order to survive.[37] It involves the recognition of specific sequences present in extracellular matrix, such as arginine-glycine-aspartic acid (RGD) that can be found in

collagen, fibronectin or vitronectin.[38, 39] These cell-binding sequences are recognized by transmembrane proteins called integrins. This part focuses on recognition mechanisms and adhesion and on how cells are able to sense surrounding elasticity and transduce a mechanical signal into biochemical signaling events.

2.2.2.1 Cell adhesion

At least 24 varieties of integrins exist in human being but they all are organized in a same way.[40] Integrins are transmembrane glycoproteins (Figure 5) and are composed of two subunits (α and β). Both subunits have a short intracellular C-terminated tail and a long extracellular N-terminated domain. Allosteric regulation rules the conformation of these receptors and thus their activity. This can be done in a bidirectional manner. The extracellular parts of inactive integrin are folded and they expand when they bind to a ligand. This change in active conformation separates intracellular α and β subunits and exposes a binding site for talin, which is present on the intracellular part of subunit β. The binding of talin triggers a signal transduction pathway inside the cell. This process is known as “outside-in activation”. For the reverse operation, talin is activated by intracellular regulatory molecules and competes with α subunit for the binding site on subunit β. Once activated, talin binds to β subunit, α and β subunits are separated and unfold to active conformation. This reverse process is named “inside-out activation”.

After binding with extracellular matrix (ECM) proteins, integrins move laterally in plasma membrane to gather and form clusters.[41] Intra-cellular proteins such as vinculin, paxillin, tensin and talin are recruited by the clustered integrins and promote the assembly of actin filaments.[42] These aggregates are named focal adhesions and their formation activates several signaling pathways through the activation of kinases such as the focal adhesion kinase and the mitogen-activated protein kinase. These enzymes allow the assembly of actin filaments as well as their structuration and the regulation of gene expression in the nucleus, respectively.[36, 41]

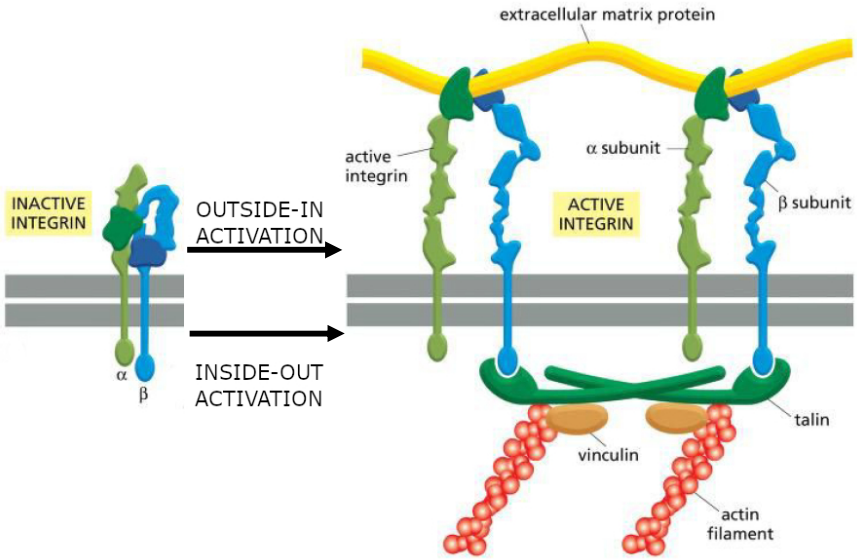


Figure 5: Integrins in active and inactive conformations. Adapted from [40]

2.2.2.2 Cell sensing

Through these focal adhesions, cells are able to sense mechanical properties from their extracellular environment and to convert these properties into biochemical signals.[43-45] This ability is known as mechanotransduction and two kinds of sensing can be depicted.[43] On the one hand, shear stress, extension or compression can be applied on the cells ("outside-in" or "passive" sensing). On the other hand, cells are able to exert forces and pull against the extracellular environment to analyze features such as stiffness, topography and ligand density ("inside-out" or "active" sensing). The changes in extracellular substrate rigidity significantly influence cell spreading, proliferation, and migration of somatic cells in addition to direct stem cell differentiation.[45] Knowledge about mechanical signaling is still limited compared to hormones or growth factor signaling but three mains mechanisms have been proposed for the inside-out sensing: the **Rho/ROCK signaling pathway**, the use of **stretch activated channels** (SACs) and the force induced **protein unfolding**.[43, 44]

Once integrins bind to the ECM, the amount of contractile force is translated into **Rho-associated kinase (ROCK)** phosphorylation via the phosphorylating enzyme "RhoA".[43] Activated ROCK affects several cellular processes such as actin organization and cell contractility. RhoA, through other pathway, is also

responsible of the formation of new actin stress fibers. Altogether, these pathways upregulate and stabilize the number of stress fibers in response to an increase in “inside-out” forces.

Some ion channels present in the membrane are mechanosensitive: the **stretch activated channels**.[43, 44] These transmembrane proteins open and become permeable to some soluble ions, such as calcium, when the membrane is tensed. Higher amplitude of oscillation in cytoplasmic calcium ion concentration was observed for cells cultured on stiff versus soft substrates.[46] Changes in calcium ion concentration in cytoplasm can affect numerous pathways inside the cell.[43]

Force induced **protein unfolding** is a third proposed mechanism able to gauge molecular strain.[43, 44] Proteins from the focal adhesion are able to unfold under stretching forces and to expose several binding domains for other proteins and signaling molecules. Talin is an example of these proteins and has many inaccessible vinculin-binding sites trapped in the middle of 5 α-helices. Tensions unfold talin and can expose up to 11 binding domains for vinculin recruitment, which in turn mediates downstream events.

All these three mechanisms interact and lead to a synergistic mechanosensing system.[43] For example, the Rho/ROCK pathway is used to strengthen actin filament and to increase contractile force which likely activates stretch activated channels and unfolds proteins. However, stretch activated channels also reinforce the Rho/ROCK cascade.

It is noteworthy that these mechanisms are presented as “on-off” static switches. However, most of the interactions exposed here are dynamic and last from ten seconds to few minutes.[44] Even focal adhesions have a rapid internal dynamic, and constantly exchange proteins. The frequency of all these events (competitions, association-dissociation, conformal changes, duration of applied forces, bond breakage,…) thus also plays a role in mechanosensing.

Besides mechanical properties, two other surface characteristics influence (stem) cell behavior and differentiation: surface chemistry and topography.[12] This will be further discussed in section 4.2 (Surface modifications) of this Part.

3 Scaffolds

3.1 Desired scaffold properties for tissue engineering

The second main component of tissue engineering strategy is the scaffold. It is a temporary framework which is used for cell anchorage and implantation.[47, 48] The scaffold has to be as close as possible to the ECM regarding cell adhesion, proliferation and differentiation *in vitro* as well as *in vivo*.[48] It should be designed not only to allow tissue formation but also to stimulate and guide the process.[49] Several key characteristics should be considered when producing a scaffold:

- **Mechanical properties** should be adapted and similar to the ones of the tissue where the scaffold will be implanted.[47, 48] In the body, soft tissue elastic moduli range from 0.1 kPa (neural tissues) to 10 kPa (muscles).[50] The elastic moduli of trabecular and cortical bones are significantly higher with values of 0.01-1.57 GPa and 5-23 GPa, respectively.[51] Mechanical properties should be considered both at the macroscopic and the microscopic levels. The macroscopic mechanical properties of the scaffold should be sufficient to resist to dynamic loading conditions and constraints routinely applied from the body.[47, 51] Microscopic mechanical properties found on cell scale influence cell behavior and differentiation through mechano-transduction mechanisms (section 2.2.2 of this Part).[47]
- **Architectural properties** (including scaffold shape, mesh and porosity) are linked to mechanical properties and should be well thought. Indeed, for all porous structures, strength decreases drastically with an increase in porous fraction.[52] However, tissue engineering requires a high porous fraction to ensure efficient transport of oxygen, nutrients and waste products as well as a sufficient pore size and interconnectivity for cell migration and vascularization.[37, 47, 48, 51, 52] An equilibrium has to be found between mechanical and architectural properties taking into account the implantation site and the tissue.
- **High affinity for cells** and **biocompatibility** are needed to promote interactions and allow cell adhesion while being immunologically compatible to avoid excessive inflammation or rejection.[47]
- **Biodegradability** should be tuned to respect the rate of new tissue formation with a view to avoid mechanical collapse.[47, 51] Indeed,

scaffolds are not meant to stay permanently and should degrade to leave the place when the new tissue arises.[47] Biodegradation rate and mechanism depend on the class of material used (metal, polymer or ceramic) and on its exact nature and composition.[52] Regarding polymers, functional groups, crystallinity and molecular weight also affect the degradation rate.[37, 52-54] Enzymatic degradation and hydrolysis, two biodegradation mechanisms, are influenced by architectural properties such as porous fraction and pore size.[47, 55] Besides properties from the scaffold, environmental conditions such as pH, temperature and fluid exchange also affect its degradation rate.[53, 54]

- **Bioactivity**, potential bioactive compounds incorporation and potential **chemical modification** are key parameters to improve cell adhesion and proliferation and to control cell behavior as well as cell differentiation.[37, 48, 51]
- **Manufacturing** has to be considered regarding ease of process and should be cost effective to maximize the chances of translation to clinics.[47, 48, 52] Size and shape should be easily customizable to fit patient-specific defect and sterilization has to be possible.[37, 47, 51]

The chosen parameters for each characteristic depend on the desired tissue and the implant location in the body. For example, though most of the tissues need a good oxygenation, hypoxic conditions are preferred to allow cartilage differentiation.[56]

Scaffold fabrication techniques can be separated into two main categories: conventional fabrication techniques and Additive Manufacturing (AM) techniques.

3.2 Conventional fabrication techniques

Several techniques and their variations are available but seven methods are most commonly used for conventional scaffold fabrication.

- **Solvent casting** involves the dissolution of a polymer.[57] The mixture is then cast in a mold, the solvent evaporates and leaves a bulk material without pores. Because of the absence of pores, this technique can be used to create sheets or tubes or has to be combined with other techniques to obtain porous scaffolds.

- **Particulate leaching** is often combined with solvent casting (Figure 6 A).[37, 57-59] Porogen particles such as crystal salt or sugar can be added to the solubilized polymer. After solvent evaporation, the particles are leached out using the adequate solvent. The resulting scaffold has a porous fraction and a pore size corresponding to the number and the size of the particles, respectively.
- **Gas foaming** uses gas, usually CO_2 as porogen (Figure 6 B).[37, 57, 59] The polymer is placed in a chamber and is saturated with high pressure liquid CO_2. The pressure is then released which initializes gas nucleation and gas expansion forming pores in the polymer bulk. Similar results can be obtained by mixing with the polymer a foaming or blowing agent, such as sodium bicarbonate, which releases gas through reaction or chemical decomposition.[58]
- **Freeze-drying** and **Thermally induced phase separation (TIPS)** also uses a mixture of organic solvent (or water) and polymer but do not require porogen particles (Figure 6 C and 6 D).[37, 57-59] The solubilized polymer is frozen in liquid nitrogen (which induces phase separation) and the solvent is freeze-dried or evaporated via sublimation to leave a highly interconnected porous scaffold. For TIPS techniques, a curing step can be added before freeze-drying.[58]
- **Electrospinning**, a fiber production method, can also be used (Figure 6 E).[37, 58, 59] A high voltage is applied between a syringe containing a polymer solution and a collector. The high charge density present in a droplet at the tip of the syringe deforms the droplet and stretches it to draw a fiber from the liquid. Solvent evaporates and fibers solidify while reaching the collector.
- **Powder-forming processes** were developed to produce ceramic or glass scaffolds.[57] Suspension of ceramic particles, binding agents, fillers (such as sucrose, gelatin or poly(methyl methacrylate) (PMMA) microbeads) and wetting agents are poured in a mold or used as a coating and dried. Fillers and wetting agents burn during the sintering step and, hence, create pores.
- **Sol-gel techniques** involve the formation of a colloidal solution through the use of a surfactant followed by condensation and gelation reactions.[57]

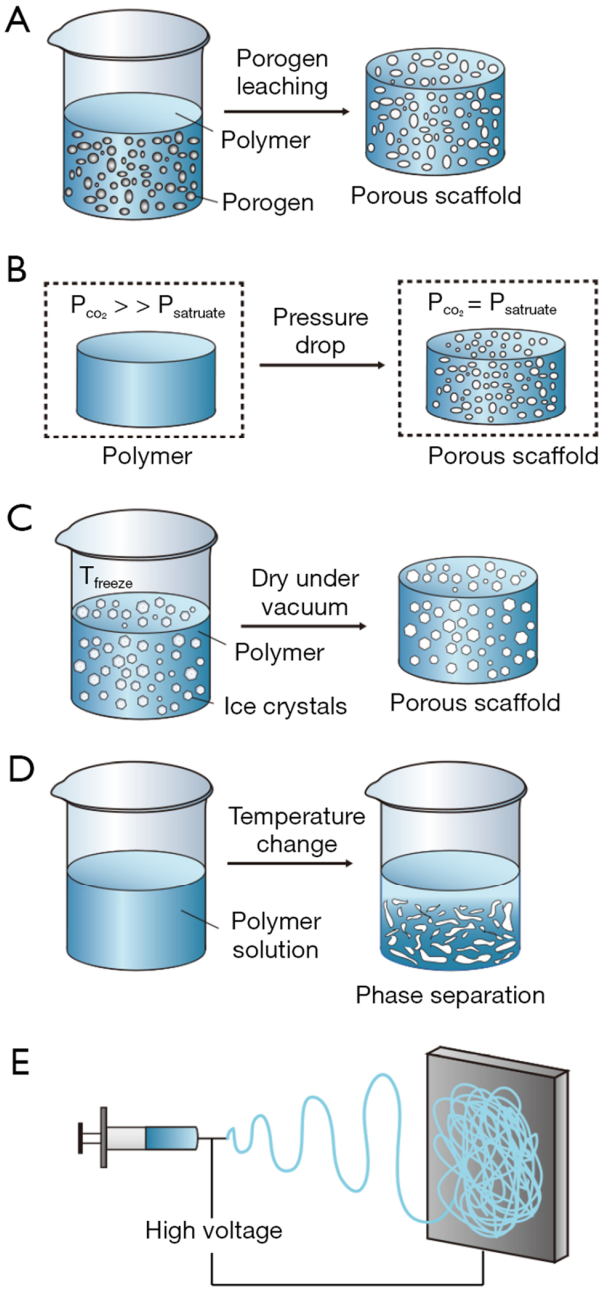


Figure 6: Conventional scaffolding techniques. (A) Solvent casting and particulate leaching; (B) gas foaming; (C) freeze drying; (D) thermally induced phase separation; (E) electrospinning. Adapted from [59]

Table 2 summarizes the properties of the scaffolds obtained with the different techniques as well as their advantages and disadvantages. Typical pore morphologies are presented in Figure 7. The majority of these techniques shares common drawbacks.[57] They are not able to have fully interconnected pores and pore size as well as distribution are not uniform throughout the structure. Some parameters can be adjusted to control pore size, morphology and distribution but not precisely. As some of these techniques are manual based, this reduces the reproducibility. Most of the porogens and solvents are toxic but sometimes required. Residue possibly present in the scaffold could trigger severe inflammatory responses.

Table 2: Advantages and disadvantages of conventional scaffolding techniques. Adapted from [57]

Technique	Pore size (µm)	Porous fraction (%)	Architecture	Advantages	Disadvantages
Solvent casting/ particulate leaching	30–300	20–50	Spherical pores	Simple method; controlled porous fraction and pore size	Possibility of residual solvent and salt particles; structures generally isotropic; insufficient mechanical integrity for use in load-bearing application
Freeze-drying	15–35	>90	High volume of interconnected micropores	Pore structure with high interconnectivity; good porous fraction	Insufficient mechanical integrity for use in load-bearing application; small pore sizes
Thermally induced phase separation	5–600	<90	High volume of interconnected micropores	Simple method; high porous fractions; pore structure with high interconnectivity; controllable structure and pore size by varying preparation conditions	Long time to sublime solvent; possibility of residual solvent; shrinkage issues; small scale production

Gas foaming/ supercritical fluid processing	30–700	>85	High volume of non-interconnected micropores	Free of toxic solvents; control of porosity	Insufficient mechanical integrity for use in load-bearing application; inadequate pore interconnectivity; possibility of closed pore structure; formation of an outer skin
Textile technology (electrospinning)	<1–10	90		Simple method; high interconnected porous fraction; high surface area to volume ratio	Insufficient mechanical integrity for use in load-bearing application; possibility of residual solvent; limitation of thickness
Powder-forming processes (bioglass produced by replication technique)	300–700	>80	High volume of interconnected micropores	Simple method; porous structure similar to sponge bone; highly porous and with open pores; free of toxic chemicals	Insufficient mechanical integrity for use in load-bearing application
Sol–gel techniques (bioactive glasses)	>600	>70		High surface area; microstructure similar to that of dry human trabecular bone	Insufficient mechanical integrity for use in load-bearing application; possibility of residual solvent

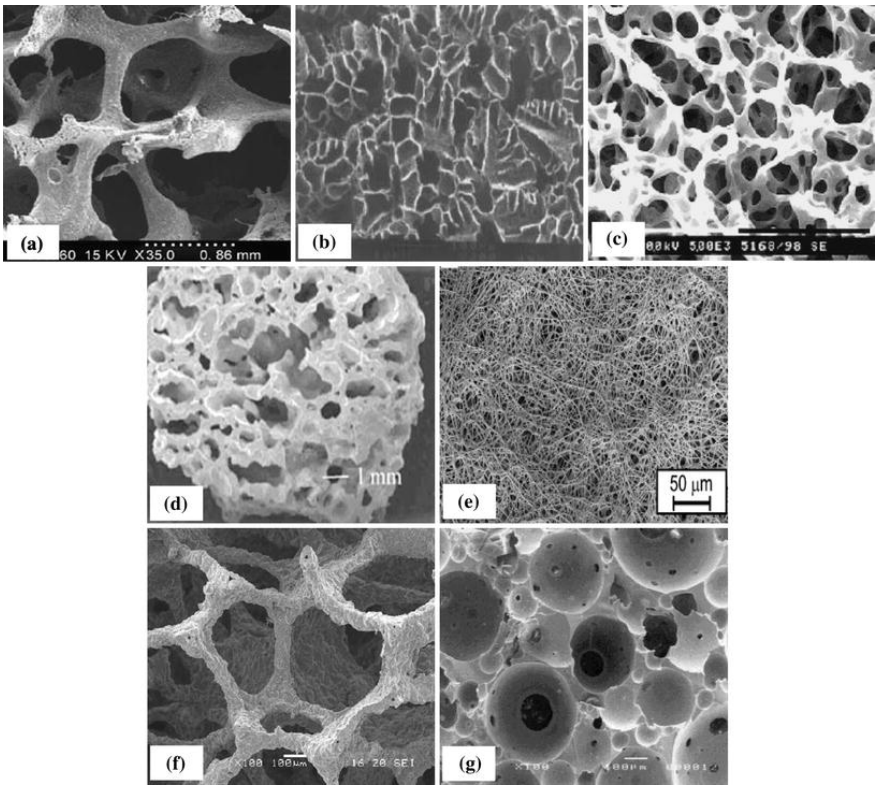


Figure 7: Typical pores morphologies for scaffolds produced by some conventional techniques. (a) Solvent casting/particulate leaching; (b) freeze-drying; (c) thermally induced phase separation; (d) gas foaming; (e) electrospinning; (f) replication technique; (g) sol-gel technique.[57]

Besides the seven conventional techniques producing scaffolds, a specific category is the use of injectable hydrogels. Hydrogels are crosslinked polymers containing a high amount of hydrophilic functions. This high hydrophilicity allows the polymer to entrap a high amount of water.[58, 59] The polymer is able to swell but crosslinks avoid complete dissolution. These crosslinks can be non-covalent (physical entanglement or ionic bonds) or covalent through the use of crosslinkers (*e.g.* genipin, glutaraldehyde) or enzymes. Hydrogels are advantageous regarding mass transfer efficiency and the ease of cell and bioactive agent encapsulation.[37, 58, 59] Moreover, hydrogel can be injected before gelation, which seriously reduces the invasiveness, and flows to take the shape of the lesion. One inconvenience of hydrogel is their poor mechanical properties.

Additive Manufacturing techniques represent a promising alternative or complement to the abovementioned techniques.

3.3 Additive Manufacturing techniques

AM, also known as rapid prototyping (RP), solid-freeform fabrication (SFF), or more commonly as 3D printing are bottom up techniques used to build objects.[60, 61] They were first proposed by Charles Hull in 1986 and were later used for medical applications in the early 2000s (dental implants and prosthetics).

AM encompasses a large number of techniques working with different principles but all based on a layer-by-layer building. Solid sheets, powders or (semi-)liquids are processed to form two-dimensional solid layers (X,Y) which are stacked along Z axis.[57, 62] The whole process can be divided in three main steps.[60-62] First, a model of the object has to be designed using a computer-aided design (CAD) software. Then, still using computers, the designed model is sliced in a sequence of two-dimensional layers. The program, called "slicer", also defines how these layers will be built (pathway, layer height, infill, …). These fully defined cross-sections are finally sent to the printer and are reproduced one at a time from the base to the top.

In contrast to conventional fabrication techniques, the fully automated bottom up process of AM allows high levels of consistency and reproducibility.[37, 57-60, 62] Precise control of the architecture is possible and enables fine-tuning to reach the balance between mechanical properties and biological performances. Though conventional techniques are cost-effective at industrial scales, most of them are unable to provide patient-specific customization, which could lead to complications and implant failure. AM techniques can be combined with three-dimensional imaging techniques such as computerized tomography (CT) or magnetic resonance imaging (MRI) to produce perfectly fitted scaffolds (Figure 8). Altogether, patient specific scaffold with a high complexity and fully interconnected well-defined pores can be achieved. Structure and porosity can be precisely tailored throughout the structure to fulfill mechanical requirements, improve matter transfer and cell migration.

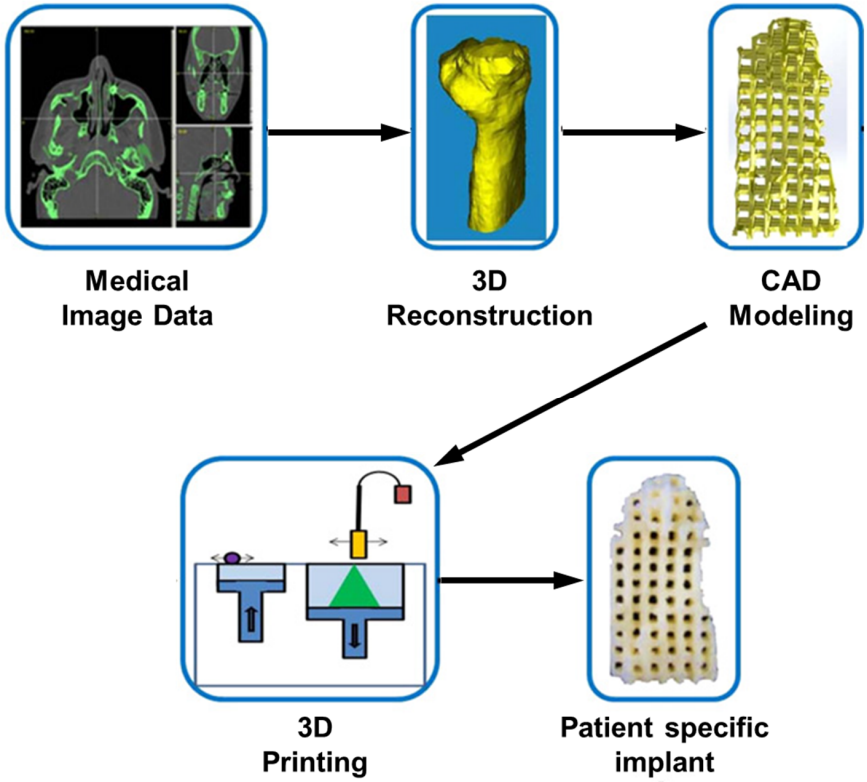


Figure 8: Production process of a patient specific implant. Adapted from [63]

Classification of AM techniques is quite challenging considering the number of different techniques and similarities of some denominations. In this description, most of existing AM techniques applied to biomaterial implants or tissue engineering were classified according to four basic principles (Figure 9). For each, the basic techniques are explained and advances giving rise to other techniques are presented.

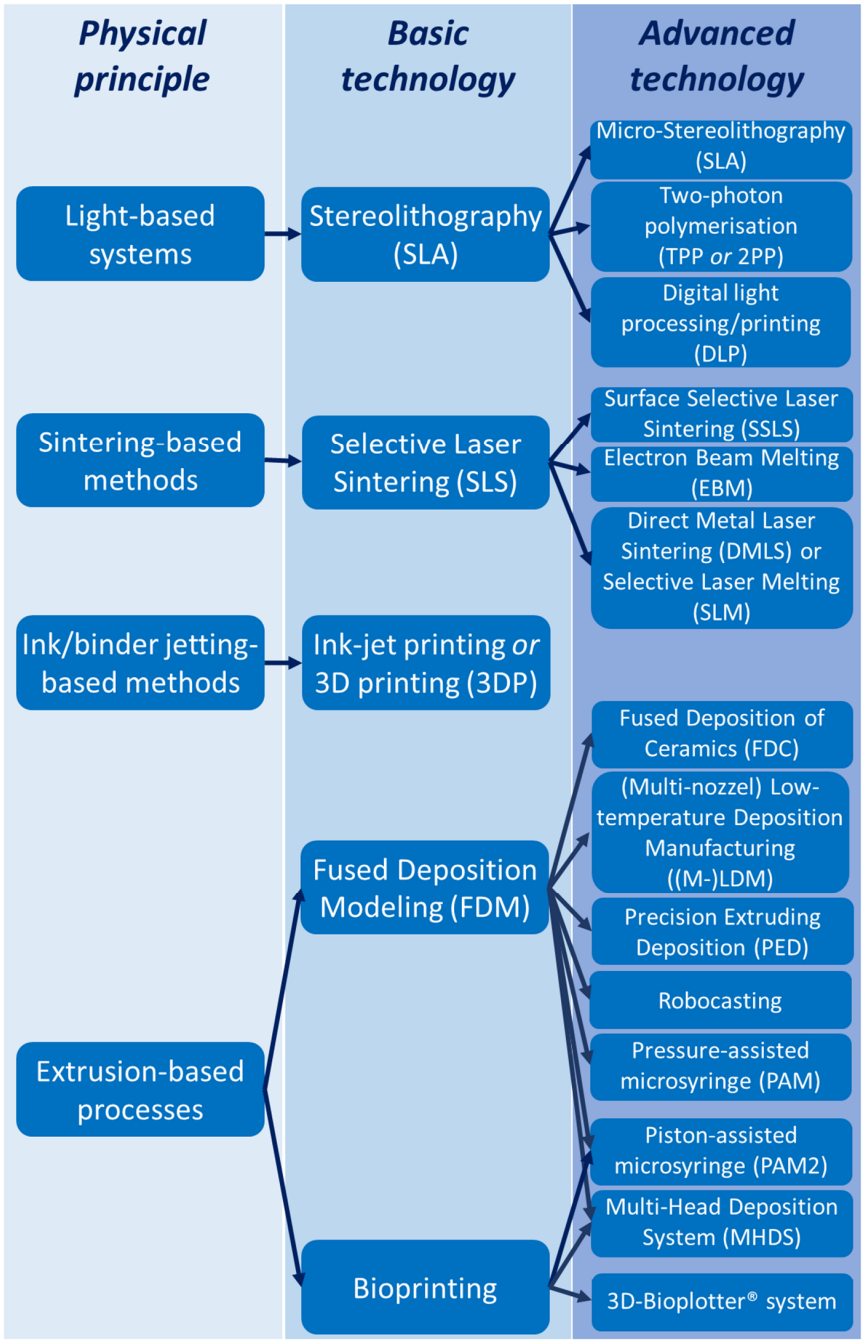


Figure 9: Additive manufacturing techniques classification depending on the basic technology and the physic principle.

3.3.1 Light-based systems

Light-based systems gather all techniques that use light to cure a photo-crosslinkable polymer.

3.3.1.1 Basic principle: Stereolithography (SLA)

SLA (Figure 10) is composed of (1) a bath containing a photocrosslinkable polymer, (2) a platform capable to move up and down in the bath, (3) a ultraviolet (UV) laser and (4) a scanner system or a dynamic mirror system.[57, 64] The laser is used to crosslink the resin in desired places to get the solid object. The platform is immersed and placed close to the surface. The first layer is drawn by the scanner or the dynamic mirror, which reflects the UV laser and solidifies the resin by irradiation. Once the first layer is finished, the platform is vertically lowered by a layer thickness within the bath. A new layer of liquid polymer flows over the first layer still attached to the platform. The second layer is drawn by the mirror and the process is repeated until all the layers are built. The object is detached and uncured resin is washed off. Finally, a UV post-treatment is needed to fully cure the polymer.

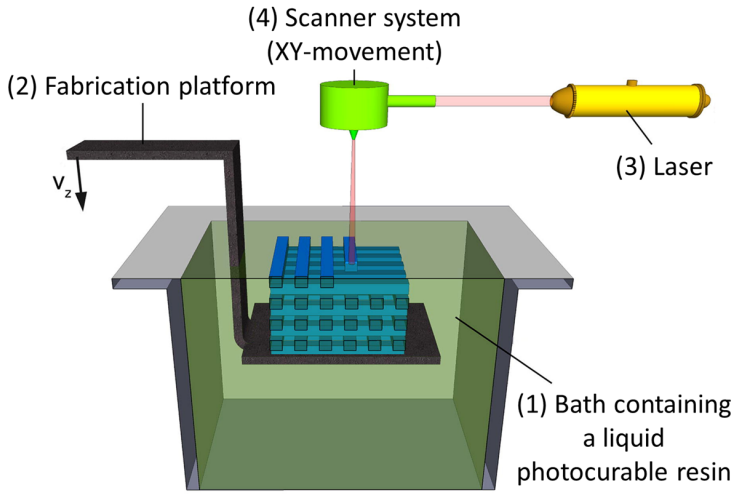


Figure 10: SLA process. Adapted from [64]

3.3.1.2 Advanced technology

New generations have emerged reducing the power of the laser and improving lateral and vertical resolution as well as printing speed.

- **Micro-stereolithography (µSLA)** uses a single photon beam, which can be more precisely focused to have a smaller exciting spot.[57]
- **Two-photon polymerization (TPP *or* 2PP)** employs an ultra-short laser pulse in the near-infrared.[65] It allows the polymerization in an extremely localized focal volume, smaller than the diffraction limit of the incident laser beam. Resolution can reach nanolevels and depth as well as speed are increased. Even lower resolution were reached using radical quenching mechanisms.[57]
- **Digital Light Processing/Printing (DLP)** improved print speed of SLA by the use of a dynamic mask.[60] This mask is a digital mirror device (DMD) and allows the curing of the full layer at once. This technology uses a visible blue light and does not need a laser which limits its cost. In addition, the lateral resolution is slightly improved compared to SLA (40 µm instead of 50 µm).[57]

3.3.2 Sintering-based methods

Sintering-based methods gather all printers that use an energy source to heat and sinter a ceramic powder, a polymer powder or a metallic powder.

3.3.2.1 Basic principle: Selective laser sintering (SLS)

In SLS process (Figure 11), a long wavelength laser or high-energy light source is used to melt or sinter material (polymers, metal and ceramics) powder.[57, 60, 62] As for SLA, SLS is composed of a laser, mirrors and a platform. Instead of liquid polymer, SLS uses flowable particles, which are dispensed by a roller. The roller pushes the powder from the stock to form a thin and flat layer onto the platform. The laser oriented by mirrors selectively sinters (or melts) the first layer according to the first layer of the sliced model. Once the first layer is printed, the platform lowers down by the equivalent of one layer and the roller lays down the next powder layer. The second layer is sintered and the process is repeated until the full object is printed. The object is retrieved and not-sintered powder is removed from the structure. During printing, this solid powder acts as structural support preventing the printed object to collapse.

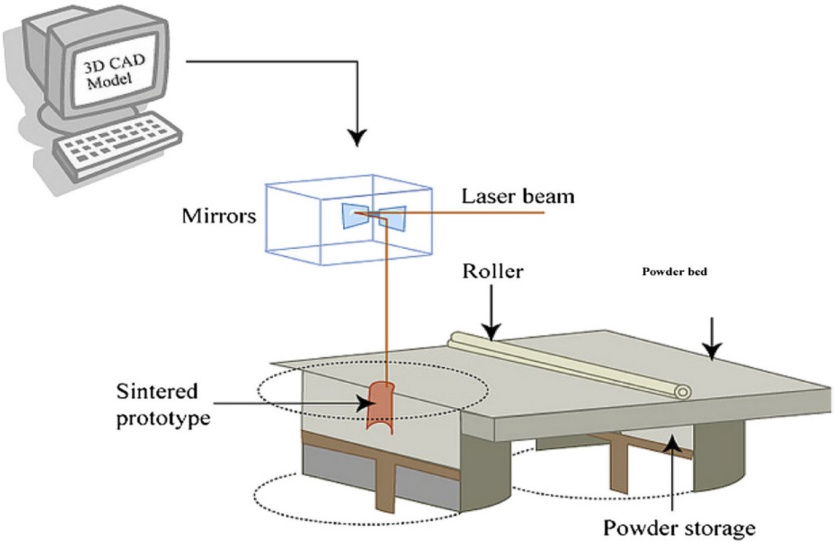


Figure 11: SLS process[57]

3.3.2.2 Advanced technology

Similar to this technology, more advanced techniques are based on the same principle of melting/ sintering:

- **Surface selective laser sintering (SSLS)** employs a different laser to limit the fusion to the surface of polymer particles.[57] Indeed, in SLS, the particles are completely melted and fused to each other to form a bulk shape. That leads to severe volume shrinkage and deformation of the object. SSLS uses a near-infrared laser, which is not absorbed by the particles but only by a carbon coating applied on the surface of the particles. As the melting is limited to the surface, sintering can occur but the object is less subjected to shrinkage. Furthermore, the bulk of the particle is not overheated during scaffold fabrication and can encapsulate thermolabile biomolecules.
- **Electron beam melting (EBM)** uses a high-energy electron beam instead of a laser to fuse metal powders.[62]
- **Direct metal laser sintering (DMLS)** or **Selective laser melting (SLM)** are two other denominations of SLS but using higher energy beams and a controlled atmosphere in printing chamber for the specific application of metal printing.[66-68]

3.3.3 Ink/binder jetting-based methods

Ink jetting-based methods (Figure 12) use a binder (usually a polymer) and a polymeric or ceramic powder material.

3.3.3.1 Basic principle: Ink-jet printing or 3D printing (3DP)

Ink-jet printing, as SLS, is a powder-based technique. Instead of sintering material powder, ink-jet printers spray a liquid binder to merge the particles.[57, 60, 62] Like for SLS, the powder is dispensed from the supply tank to the platform by a roller. The ink-jet printer head sprays droplets of binders in desired area to solidify the powder. Once the first layer is printed, the platform lowers down and a new powder layer is applied by the roller. The process is repeated until the object is completely printed. The object is retrieved and unbound powder is removed. Hydrogel can be used as binder, which allows the direct printing of cells or biological compounds. Ceramic-based materials can be printed but a heat treatment after printing is necessary to achieve a higher density and better mechanical properties.

Theoretically, only ink-jet should be called “3D printing” as this particular process was patented under this name. Thereafter, the public progressively replaced the “additive manufacturing” term by “3D printing”.

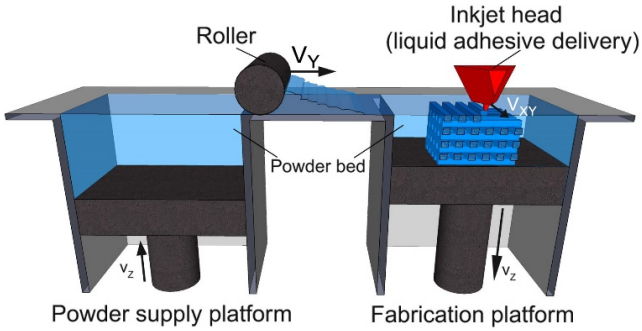


Figure 12: Ink-jet printing process[64]

3.3.3.2 Advanced technology

Even though a lot of variation of inks, powders and post-processings have been proposed for ink-jet printing, no advanced techniques were inspired from this basic principle.[57]

3.3.4 Extrusion-based processes

Extrusion-based processes rely on the deposition of a semi-liquid compound extruded through a nozzle. The basic principle can be split in two categories depending on the possibility to print living cells.

3.3.4.1 Basic principle

- **Fused deposition modelling (FDM), also known as fused filament fabrication (FFF),** (Figure 13) builds 3D objects by depositing molten struts of thermoplastic polymers.[57, 60, 62] Polymer filament is driven by rollers inside a heated head where the polymer is melted. Struts of molten polymer are extruded through a nozzle on a platform. The head, moving along x and y axes, places struts side by side to form the first layer according to the first layer of the sliced model. The polymer cools shortly after extrusion and solidifies. The platform moves down and a second layer of molten struts of polymer is placed on top of the previous layer and binds to it. The process is repeated until the object is completely printed. During printing, the object is not surrounded by liquid or powder like for SLA or SLS. If overhangs are part of the design of the object, supporting structures have to be printed at the same time. Indeed, the deposition can be done only on a preexisting layer. Otherwise, the molten polymer drops due to gravity. A second nozzle can be present on the printer and allows to print a second polymer at the same time to bring additional features to the scaffold or to add a sacrificial polymer used as temporary supporting material during printing.

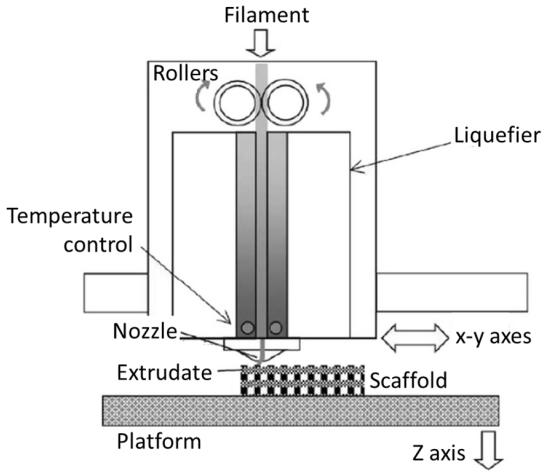


Figure 13: FDM process. Adapted from [57]

- **Bioprinting**, (Figure 14) also called as bioplotting, is the second extruding process. It does not require high temperature and, hence, allows direct printing of cells or bioactive molecules.[57, 62, 64] The printing process is the same as FDM except that printed materials are mainly hydrogels and that syringes are used to push the hydrogel through the nozzle. Once extruded, hydrogel struts solidify by curing. Several syringes containing different cell types or hydrogels can be placed in parallel. This allows to organize the deposition of different cells or material in the same scaffold to produce more elaborated systems.

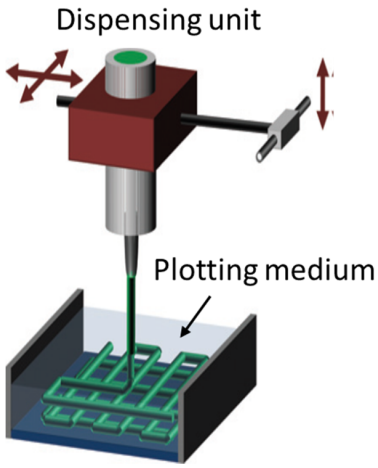


Figure 14: 3D-Bioplotter® Adapted from [57, 69]

3.3.4.2 Advanced technology

Several new processes were proposed to overcome limitations or improve FDM and bioprinting.

- **Fused deposition of ceramics (FDC)** uses composite filaments of polymer, ceramic powder and binder.[57] Once printed, the binders are removed and the object is sintered using a thermal treatment to improve mechanical properties.
- **Low-temperature deposition manufacturing (LDM)** was developed to resolve the problem of the high temperature needed in FDM.[57] LDM is a combination of nozzle extrusion and thermally induced phase separation (TIPS). The fabrication of the scaffold is operated in a low-temperature environment (under 0°C) to solidify the material solution when deposited on the platform. **Multi-nozzle low-temperature deposition manufacturing (M-LDM)** are further proposed to print scaffolds composed of heterogeneous materials.
- **Precision extruding deposition (PED)** includes a heating chamber that allows the direct use of raw material in the form of pellets.[57] The preparation of filament is not needed anymore.
- **Robocasting**, also named "robotic deposition" or "direct-write assembly" uses highly concentrated pseudoplastic-like colloidal suspensions.[57] This water-based ink is extruded from a small nozzle inside an oil bath. Once water evaporates, the soft pseudoplastic paste becomes rigid.
- **Pressure-assisted microsyringe (PAM)** improves resolution using narrow capillary needles (10-20 µm) and pasty polymer solutions.[57] A constant air pressure is applied to extrude the pasty solution. Paste solidifies after solvent evaporation.
- **Piston-assisted microsyringe (PAM2)** also uses capillary needles but the driving force for extrusion is ensured by a mechanical piston.[57] This technique was developed aiming at the microfabrication of cell-incorporated hydrogels.
- **Multi-head deposition system (MHDS)** is a more general denomination for the use of more than one head on the same technique. Depending on the authors, this refers to FDM techniques[57] or to bioprinting techniques[61].

3.4 Available biocompatible materials for printing

Owing to the advances in AM techniques and their versatility, almost all materials that have been or are developed for tissue engineering can be used. Three main categories of biomaterials are generally used: metals, polymers and ceramics. As each of these materials alone could not satisfy all requirements for a given application[70], combination of materials, called composites, are often used.

3.4.1 Metals

Metals and alloys are classically used for the fixation and replacement of load-bearing bones in the body.[70] They possess favorable properties such as high strength, ductility and fracture toughness (Table 3). Still their biomechanical compatibility is low owing to their higher elastic modulus compared to bones, which leads to stress-shielding. Stress is not adequately transferred from the metal implant to the bone.[71] The consequence of the lack of adequate stress stimulation on the bone is osteocytes death. Therefore, bone density is reduced and the bone becomes more fragile. Most of these implantable metals are not biodegradable and should be considered as implantable devices instead of scaffolds.[70] In addition, stainless steel, cobalt-chromium (Co-Cr) alloys and titanium-nickel shape memory alloys (Ti-Ni SMA) contain nickel (Ni) whose ions can be leached out and cause deleterious effect on the surrounding tissues. Some coatings of apatite can slow down the migration of the ions at short term for bulk part but are inefficient on a porous part owing to the higher surface-to-volume ratio.[52] In this precise case, *in situ* recolonization of a porous part to form a hybrid bone-metal tissue cannot thus be considered.

Titanium (Ti) and Ti alloys (*e.g.* Ti-6Al-4V), even if not degradable, have markedly emerged as implantable biomaterials.[52] Ti has a relatively low density with respect to other metals and has a good mechanical strength, which is much higher than the one of biomedical polymers. Ti elastic modulus (~110 GPa) is closer to bone elastic modulus (cortical bone: ~7 to 30 GPa) as compared to other metals (190 GPa and 210 GPa for stainless steel and Co-Cr alloys, respectively). Furthermore, owing to the high resistance of the titanium oxide surface layer to corrosion, Ti does not release heavy metal ions and has good properties for osteointegration.[72, 73]

Some metals are biodegradable and degrade in metal ions naturally present in our body.[52] Their use as material for scaffold production raised interest. At first, **magnesium (Mg)** was underestimated in the context of general engineering application mainly because of its sensitivity to corrosion. As the human body is a highly corrosive environment, this issue turns into an advantage for tissue engineering, which requires degradable materials. Mg is the fourth most important cation in cellular organisms and degradation products are easily resorbed. Besides, Mg mimics certain properties that are found in human bones and aids in the growth of osteoblasts within the scaffold. The main drawback of Mg is its too fast degradation rate as compared to healing rate. This issue can be solved by using Mg alloys, by coating the surface or by modifying porosity.[51]

Iron (Fe) is also naturally present in the body and plays important roles such as oxygen storage and transport in the blood.[51] Fe and alloys were investigated as bone replacement owing to their interesting properties and biocompatibility.

Table 3: Mechanical properties of magnesium compared to other related biomaterials and to natural bones.[51]

	Pure Mg annealed	Pure iron	Cortical bone	Ti alloy	316L stainless steel	Cancellous bone	Synthetic hydroxy-apatite
Tensile Strength (MPa)	160	180-210	35-283	760	586	1.5-38	-
Yield Strength (MPa)	90	120-150	104.9-114.3	485	331	-	-
Modulus of Elasticity (GPa)	45	211.4	5-23	110	190	10-1570 (MPa)	77-117
Density	1.74	7.87	1.8-2.0	4.5	7.9	1.0-1.4	3.1

3.4.2 Ceramics

Ceramics represents a large group of inorganic materials produced by sintering or melting the raw materials to produce an amorphous or a crystalline solid part.[37] The major components of these ceramics are calcium, silicon, phosphorus, magnesium, potassium and sodium. Ceramics were used for long in orthopedics. Owing to a structure similar to that of natural bone,

they show excellent bone bonding properties as well as excellent biocompatibility.[47, 70] Moreover, they have demonstrated to stimulate vascularization and to promote cell adhesion, proliferation and differentiation to osteoblasts. If degradable, ceramics degrade through solubilization. However, low compressive strength and fracture toughness make ceramics difficult to use for load bearing applications (Table 4).[47]

Calcium phosphates (CaP), such as hydroxyapatite (HA) and tricalcium phosphates (TCP), have a composition and a structure similar to the mineral phase of human bones and teeth and, consequently, have an excellent biocompatibility.[57, 74] They are bioactive and osteoconductive (*i.e.* support osteoblastic cell attachment, proliferation and differentiation). Osteoprogenitor cells are able to process and resorb CaP materials. Solubilized calcium and phosphate ions trigger highly effective intracellular signaling, which leads to a rapid bone formation at the surface and a direct binding to the surrounding bone tissue. HA presents two major limitations. First, its degradation rate is too slow, lasting for 6 or 7 years after implantation, which limits their use for bone-regeneration applications. In contrast, TCP has a good bioresorbability (10 to 20 times faster than HA)[37, 52, 70]. Then, it shows unsatisfactory mechanical properties.[57, 70, 74] HA and most of CaP have much higher compressive strength values compared to bone and are too brittle (tensile strength and fracture toughness failure). Their use is therefore limited to non-load-bearing sites.

Bioglasses are polycrystalline ceramics[37] and many compositions have been developed using bioactive silicate (SiO_2), phosphate (P_2O_5) and borate (B_2O_3) glasses[57]. Bioglasses of different compositions dissolve at different rates after implantation.[52] Resulting ions induce extra- and intracellular responses, stimulating new bone formation. Same limitation as CaP can be drawn regarding mechanical properties.[57, 74]

Inert bioceramics gather non-resorbable ceramics such as alumina (Al_2O_3), zirconia (ZrO_2), silicon nitride and carbon.[37] They are biocompatible and very stable in the human body environment.[52]

Table 4: Mechanical properties of ceramics compared to human bone.[57]

Ceramics	Compressive strength (MPa)	Tensile strength (MPa)	Elastic modulus	Fracture toughness (MPa$\sqrt{m}$)
Calcium phosphates	20-90	30-200	30-103	<1.0
HA	>400	~40	~100	~1.0
45S5 Bioglass®	~500	42	35	0.5-1
Cortical bone	130-180	50-151	12-18	6-8

3.4.3 Polymers

Polymers are used for many applications in the medical field as well as for tissue engineering.[37, 52, 57, 70, 74] Their characteristics such as degradation rate and mechanical properties are highly tunable. Their chemical composition can be tailored, polymer blends or copolymers from polymers presenting different advantages can be done and chemical reactions on side chains can be performed. Polymers used in tissue engineering can be classified in three categories depending on their source and degradability: natural polymers, synthetic degradable polymers and synthetic non-degradable polymers.

Natural polymers are present in or derived from the nature.[51] They belong to two main classes: proteins or polysaccharides.[56] They mimic the structure, chemical composition and biochemical properties of the extra-cellular matrix. Natural polymers exhibit low immunogenicity, are able to stimulate an appropriate cellular response and can be remodeled by cells.[74] Besides, they are relatively abundant, commercially available and easy to process.[37] Main examples of commonly used natural polymers are briefly presented hereunder.

- **Fibrin** is a protein network that plays a major role in wound healing as it provides a physical barrier to prevent bleeding and allows recolonization by fibroblasts.[37] An enzyme, the thrombin, converts fibrinogen, a precursor protein in fibrin monomers. Gelation occurs through self-assembly of fibrin monomers. Mechanical properties of fibrin hydrogel can be tuned using different concentrations in fibrinogen and thrombin.[75] Fibrin gels degrade through hydrolytic and enzymatic reactions.[37]

- **Collagen** (and gelatin, its denatured form) is de most abundant protein present in ECM of mammalian tissues.[47, 74, 76] Hence, this material has been widely explored as biomaterial. At least 22 types of collagens are present in human body but collagen types I, II and III are the most abundant.[37] Collagen consists of a triple helix of amino acid chains and helices combine to form microfibrils. This protein allows excellent cellular attachment and induces chemotaxis.[47, 57] Some drawbacks should be mentioned as too fast or uncontrollable degradation, poor mechanical properties and risks of disease transmission.[47, 57, 74]
- **Decellularized ECM** are protein hydrogels made from the decellularization of mammalian tissues.[77] Hydrogels derived from ECM do not retain the three-dimensional ultrastructure. However, they retain the functional complexity of the tissue they are derived from. These hydrogels maintain differentiation stimuli, signaling molecules and growth factors required to support and deliver cells.
- **Silk**, made of proteins, is widely used in clinic as suture material.[37] It is composed of a core usually in fibroin and a gluelike coating in sericin protein. In nature, silk is produced by silkworms and some spiders. Fibroin was increasingly studied and tested as biomaterial for tissue engineering. It shows good biocompatibility, slow degradation and remarkable mechanical properties compared to other natural polymers. Processability of this material allows to achieve scaffolds with a variety of shapes[37], which present good *in vitro* and *in vivo* results[37, 74]. Consequently, fibroin is a good candidate for the regeneration of a range of different tissue such as bone, ligament, cartilage, skin and nerve.[37] Even though fibroin shows better mechanical properties compared to other natural polymers, its compressive strength is still very low, which limits the application to non-load-bearing sites.[74]
- **Alginate**, a polysaccharide produced by seeweeds, is a block copolymer composed of two repeating monosaccharides: L-guluronic acid and D-mannuronic acid.[37] These linear polymer chains are water-soluble and gelation can occur through the formation of ionic bonds. Bivalent cations such as Ca^{2+} are able to interact with carboxylates from blocks of guluronic acid to link polymer chains. However, alginate being not native to the human body can trigger immune response and is not fully degradable.

- **Hyaluronic acid** is a glycosaminoglycan abundantly present in cartilage ECM.[37] Unmodified, this polymer is not a suitable biomaterial because of its high water solubility and fast resorption. However, chemical reaction such as esterification can help to tailor degradation rates and improve biocompatibility.
- **Chitosan** is a polysaccharide produced by a deacetylation of chitin, which is a main component of arthropod exoskeleton.[37, 47] Chitosan is composed of a simple glucosamine monomer and has physicochemical properties close to many glycosaminoglycans. Owing to its abundance, chitin is relatively cheap. In addition, chitosan is reasonably biocompatible, bioactive and biodegradable, it does not trigger a strong immune response and shows good reactivity towards chemical modification processes. At body pH, chitosan possesses a positive charge that allows interactions with negatively charged compounds such as cell membranes, proteins, glycosaminoglycans and proteoglycans.[74]
- **Agarose** is another example of polysaccharide and is extracted from some algae.[37] Agarose forms a thermoreversible hydrogel that jellifies around 40°C.

Despite their remarkable bioactive advantages, natural polymers suffer from several drawbacks. As they are produced by or extracted from living organisms, these materials are subjected to batch-to-batch variability and are difficult to produce consistently.[37, 47] The risk of cross-contamination from unknown viruses or other pathogens cannot be completely avoided. Concerning polysaccharides, even though they are biocompatible, they do not foster cell attachment.[56] Furthermore, natural polymers lack the required mechanical properties for load-bearing applications.[37, 47]

Synthetic degradable polymers can be produced under controlled methods to adjust mechanical and physical properties as well as degradation rate.[47, 56, 57] Molecular structure and molecular weight can be adjusted during synthesis process.[37] Batch-to-batch reproducibility and control over scaffold properties are also improved compared to natural polymers.[56, 57] An important number of different synthetic degradable polymers exists. Only the most important are described.

- Aliphatic polyesters, such as **poly(lactic acid)** (PLA), **poly(glycolic acid)** (PGA), **poly(lactic-co-glycolic acid)** (PLGA) and **poly(ε-caprolactone)** (PCL) are commonly used polymers owing to their

good biocompatibility, mechanical stability, controllable degradation rate and good processability.[37, 57, 74] They are approved by Food and Drug Administration (FDA) and European Medicines Agency (EMA) for clinical applications.[37, 57, 74, 78] Besides, achievable mechanical properties are wider compared to natural polymers.[74] Degradation occurs through hydrolysis of ester bonds[51] and products are endogenous to the human metabolism and are remove by natural pathways.[47, 57, 74] Degradation of these polyesters is influenced, among others, by their hydrophobicity, crystallinity and average molecular weight.[47, 52] PGA owing to its relative hydrophilicity degrades fast in aqueous conditions and is completely resorbed within four to six months.[51, 57] PLA is much more hydrophobic and, hence, has a slower degradation rate for over one year.[37] It exhibits high mechanical strength but is brittle.[70] Intermediate degradation rate and mechanical strength can be finely tuned using PLGA copolymers with different ratios of PGA and PLA.[51, 70, 74] PCL, more hydrophobic than both PGA and PLA, has the slowest degradation rate.[51, 79] Another reason of its slow degradability is its high crystallinity.[57] PCL is preferred for its flexibility and has already been used as long-term implant for bone tissue engineering.[57, 74] Even though endogenous, the degradation products of such polymers are quite acidic and can cause undesirable local changes in pH, which in turn provoke inflammation and limit tissue development.[37, 57, 74] In addition, their hydrophobic properties are not favorable for cell attachment.

As PLA is a central material in this work, it is presented in more details. The PLA monomer is a 2-hydroxypropanoic acid molecule, which is commonly named lactic acid (Figure 15 A). As the lactic acid monomer is chiral, it possesses two stereoisomers: L-lactic acid and D-lactic acid (S and R, respectively).[80] Combinations of these monomers give PLA presenting different stereochemistries (Figure 15 B): poly-(L-lactic acid) (PLLA), poly-(D-lactic acid) (PDLA) and poly-(D,L-lactic acid) (PDLLA). The latter may even possibly show different tacticities (*i.e.* relative stereochemistry of adjacent chiral centers). In the biomedical field, only PLLA and PDLLA were shown to be promising and were extensively studied.[81]

The glass transition temperature of PLA typically lies between 50 and 60°C. PLA molar mass and the stereochemistry of its backbone

dramatically influence its mechanical properties and crystallization behavior.[82] If the monomers are purely of the L or D form, PLLA and PDLA are semi-crystalline and have a melting point around 180°C. A decrease in purity of L- or D-lactic acid will provoke reduced crystallinity and melting point.[80] PDLLA is completely amorphous due to the random position of the two stereoisomers and has a lower mechanical strength.[81] The stereo-regularity of D- and L-monomers can be finely controlled to tune mechanical and physical properties such as degradation rate, crystallinity and melting temperature.[80]

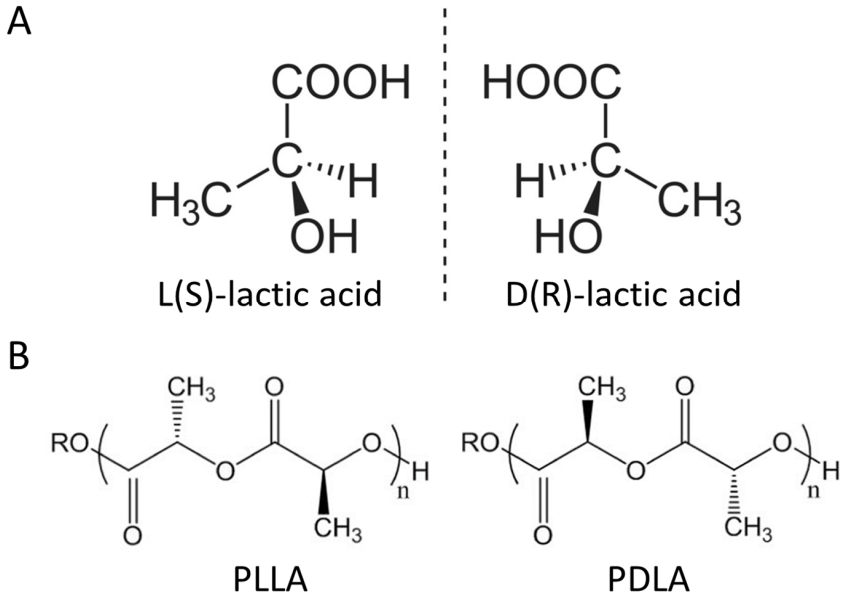


Figure 15: (A) Stereoisomers of lactic acid. (B) Lactic acid-based polymers: PLLA (L monomers only) and PDLA (D monomers only). Adapted from [80]

- **Poly(propylene fumarate)** (PPF) is an unsaturated linear polyester that is also presenting good biocompatibility and degradation parameters.[47] Like aliphatic polyesters cited above, it degrades trough ester hydrolysis.[37, 51] Owing to the double bond found in each monomer, the crosslinking between chains is possible.[47, 83] That feature presents a major advantage as it allows its use as an injectable polymer that can be crosslinked *in situ* or as resin for light-based AM techniques. Mechanical properties and degradation rate can also be further controlled by the extend of crosslinks.[37, 47]

- **Poly(vinyl alcohol)** (PVA) is not strictly speaking degradable as it does not contain hydrolysable bonds in its backbone.[37] However, PVA is soluble in water and, consequently, resorbs in the body. For its application in tissue engineering, attention should be paid to use low-molecular weight PVA (around 15,000 g/mole) to allow its elimination by kidneys. PVA is relatively biocompatible and is easily molded into desired shape. It can swell and hold a large amount of water to form a hydrogel. Alcohol functions present along its backbone allow easy chemical modifications such as crosslinking or incorporation of other molecules to influence polymer properties.

Synthetic polymers also have their limitations. The risk of rejection once implanted cannot be neglected and by-products from the degradation process may negatively influence surrounding tissues (*e.g.* burst release of lactic acid).[56] Synthetic polymers may also be unable to integrate with host tissue.[57]

Synthetic non-degradable polymers should be avoided for regenerative medicine as they could provoke chronic foreign-body reactions[37] or tissue compression, harmful especially for nerve regeneration[48]. Some important examples of synthetic non-degradable polymers among others are silicones, polyethylene and polypropylene (PE and PP), polyamides (PA) and poly(methyl methacrylate) (PMMA). There main advantages are the ease of process into desired shapes and their low cost. Other polymers such as polypyrrole and polyaniline are conductive, which can be useful for nerve regeneration.[48]

3.4.4 Composites

Composites are combinations of two or more materials to bring together advantages of each of these materials and to alleviate drawbacks of single-phase biomaterials.[47, 56] In general, these combinations aim at proposing a composite material having good mechanical properties, suitable biodegradability and improved bioactivity.[47] Almost all kinds of combinations using material categories proposed above were already studied. Natural polymers were combined with synthetic polymers to allow the creation of more complex geometries and improve properties and bioactivity.[56] Combination between ceramics such as HA and synthetic polymers such as PLA decreases inflammatory response caused by degradation products.[47] Moreover, HA-PLA composites also represent a solution to stress-shielding

posed by metallic implants.[70] HA coating on PLGA improves its mechanical properties and bioactivity[57, 70] and HA in combination with collagen, a natural polymer, induces bone formation and resorption similar to autologous bone implants. [47] The supplementation of Mg^{2+} into bioceramics improves integration of the implant to local tissues.[52] AM techniques are particularly suitable for the use of composites. Extrusion-based processes are able to print different materials using different heads (*e.g.* PCL and cell-loaded alginate[84]) or using an already modified raw material. Besides, ink-jet systems are able to use polymeric binders (natural or synthetic) jetted on a ceramic powder.

3.5 Scaffold and mesh geometry

Conventional scaffolding techniques are characterized by a lack of control of scaffold shape and internal geometry. Internal geometries are dependent on the technique used (*e.g.* fibers for electrospinning and spherical pores for gas foaming). AM techniques brought new degrees of freedom owing to the layer-by-layer fabrication. This allows a fine tuning of the material(s) deposited and the geometry obtained. Hence, it brings more controlled and reproducible physical and chemical properties such as strength and degradation rate. In addition to intrinsic parameters related to the cell itself, stem cell fate depends on the microenvironmental properties. The reproducibility of AM allows to decrease these extrinsic variability for a better control of cells fate.[85] In this part, the importance of porosity and mesh geometry are presented and discussed.

3.5.1 Scaffold porosity

Porosity in a scaffold is crucial for nutrient and oxygen supply for cells and waste disposal.[85, 86] If **pore size** is sufficient or if the material is degradable or malleable by the cells, porosity allows cell migration. Porosity is a wide concept that encompasses several other notions. **Porous fraction** refers to the ratio of the volume of void present in a scaffold to the apparent volume of the scaffold (including void). A **pore** (Figure 17 A) is a subunit of the porosity and is defined as a small void space within the scaffold. Porous fraction should always be referred to pore size as same porous fractions presenting different pore sizes could influence cells differently.

When designing a scaffold, pores can be classified* in three categories depending on their dimensions relative to cell size:[85, 86]

- **Macropores** are bigger than cell size (*i.e.* above ~50 µm).[85, 86] Nutrient distribution as well as waste disposal are improved and tissue ingrowth is promoted. Cells tend to attach on pore walls or on fibers and spread as they would do it on two-dimensional substrates (Figure 16 A). Typically, most AM techniques produce scaffolds with macropores.
- **Micropores** present a size close to cell size (*i.e.* below ~50 µm).[85, 86] At this scale, cells are completely surrounded by the material. This situation is closer to the one encountered by cells in the body and it has an effect on their activity (Figure 16 B). However, in contrast with macropores, nutrient and waste diffusions are decreased and tissue ingrowth can be slowed down. Cells encapsulated in hydrogels are in contact with a microporous environment.
- **Nanopores** present a size much lower than cell size (between 1 nm and 1 µm) and are not accessible for cell penetration (Figure 16 C).[85, 86] Cells recognize them as a surface texture.

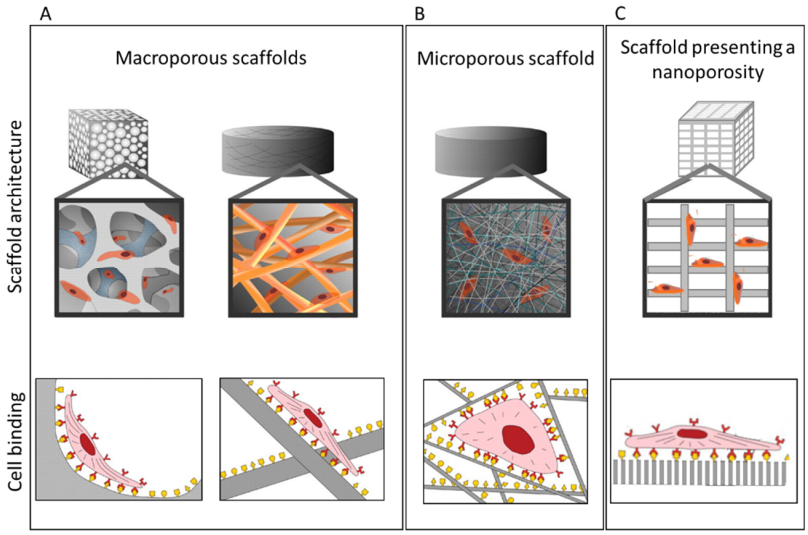


Figure 16: Classification of pores depending on their size relative to cell size. (A) Macroporous scaffolds, (B) Microporous scaffold and (C) Macroporous scaffold presenting a nanoporosity. Adapted from [87]

* Note that this classification does not refer to pore nomenclature according to IUPAC but presents the common classification used in tissue engineering.

Even though a high porous fraction (ideally around 90%) does not always fit biological needs, it is often preferred as it provides more space for cell invasion and production of their own ECM.[85, 86] However, a higher porous fraction consequently results in decreased mechanical properties in accordance to a power-law relationship. In compression tests, compressive stiffness (E) and yield strength (σ) are related to porosity as follows: [86, 88, 89]

$$E = C_1(100 - P)^m$$

$$\sigma = C_2(100 - P)^n$$

Where, C_1 and C_2 are constants, $(100 - P)$ represents the relative density and m and n are constants that depend on pore architecture. E and σ are both expressed in Pa. AM techniques are able to independently modulate porosity and mechanical properties through the design of pore shape.[85] This will be discussed in the next section.

Porosity was also shown to influence *in vitro* cell seeding.[49] If porous fraction and pore size increase, fluid velocity increases and less time is given for the cells to adhere on the material. Hydrogel loading inside a rigid scaffold is also affected by pore size and porous fraction.[90] PCL printed scaffold with an infill density of 40% (*i.e.* 60% of porous fraction) and pore size about 800 µm was found to be optimal for uniform cell seeding of fibrin-loaded cell-aggregates.

Large pore sizes and high porous fractions are often preferred for reasons already cited above. However, they do not always fulfill biological needs. For example, hypoxic conditions promote chondrogenesis of MSC and would be ensured by small pore sizes and a limited porous fraction.[56, 91] Therefore, the ideal pore size for tissue engineering is debated in literature and depends on the tissue as well as on the kind of study (*in vitro* or *in vivo*).[49, 84] The optimal pore size for vascularization was reported to be 5 µm[84] or 250 µm[92]. Bone regeneration is promoted by pores with a size between 100 µm and 400 µm.[84, 93] Lower pore sizes were reported to promote cell aggregation *in vitro* while larger pores promoted bone regeneration *in vivo*.[49] Adult mammalian skin regeneration is favored by 20 µm to 125 µm pores while hepatocytes prefer 20 µm pores.[84]

It has to be noted that tissue regeneration is a transient phase and the scaffold is used to help to the reconstruction. The scaffold is not designed to mimic the final tissue but rather built with features that will allow body cells to produce the final tissue. Then, scaffold porous fraction and pore size may be completely different from the ones found in body tissues. For cartilage

reconstruction, higher pore size (70-120 µm compared to smaller than 10 µm) promoted chondrocyte proliferation and matrix production while the natural pore size of cartilage is estimated to be 2.5 to 6.5 nm.[94] The value of the porous fraction of body tissues cannot be generalized and depends on the localization and the function in the body of each particular tissue. For example, trabecular and cortical bone tissues present a natural porous fraction of 50-90% and 3-12%, respectively. The pores of trabecular bone are fully interconnected and their size is in the millimeter range, while cortical bone tissue is crossed by channels of less than 150 µm in diameter.[95]

Interconnectivity (Figure 17 B, C and D) is also an important parameter for scaffolding as it affects regeneration processes and is overlooked in scaffold design.[49, 86] Pores need to be connected to each other by void links to serve their purpose.[85, 86] Completely isolated pores are useless and merely decrease mechanical properties. A 100% interconnecting pore volume is highly preferred as it maximizes cell infiltration and diffusion of nutrient and oxygen throughout the scaffold as well as waste disposal. Besides, the **accessible pore volume** is defined as "the total volume of pores that can be infiltrated from all peripheral borders to the interior of the scaffold".[86] It is not always equal to the interconnectivity as a pore can be connected with the borders through other pores but not to other direct surrounding pores (Figure 17 C). Fluid perfusion or mercury intrusion porosimetry can be used to evaluate accessible pore volume. However, these techniques are not suitable for large and 100% connected pores. In contrast, micro-computed tomography (µCT) combined with image analysis can give accessible and not accessible porosity as well as average pore diameter of scaffold with varying architecture (for pore sizes between 6 µm and 1500 µm).[86]

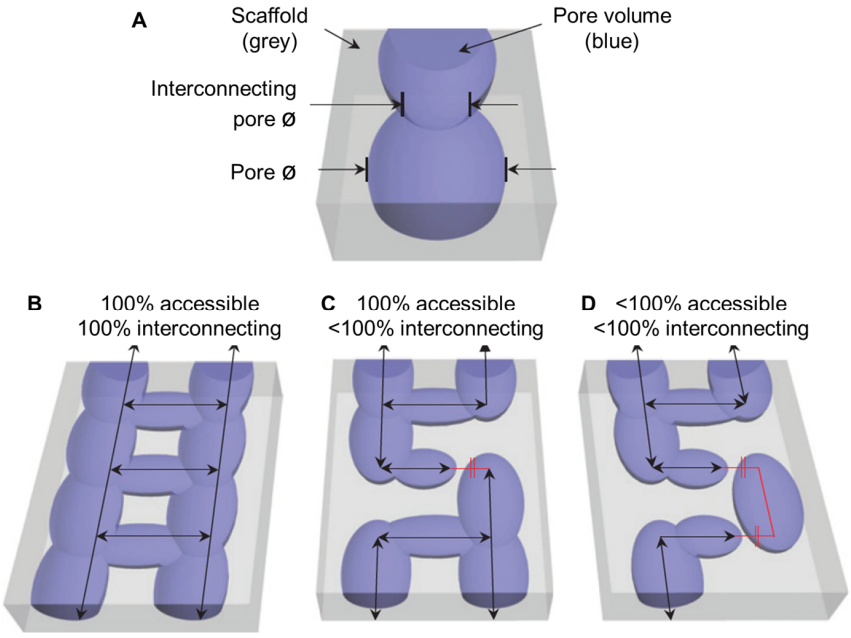


Figure 17: Schematic representation of (A) a pore as well as (B,C,D) interconnectivity and accessible pore volume. Adapted from [86]

3.5.2 Mesh geometry and struts orientation

Mesh geometry has an influence on many parameters such as degradation[85], mechanical properties[85], fluid dynamic in bioreactors[96] and cell behavior[49]. However, compared to the number of studies carried out using AM for tissue engineering, the impact of scaffold geometries has not been much studied.

3.5.2.1 The two main kinds of geometries

Two kinds of geometries can be identified: struts-based structures and complex structures. Nowadays, most studies in tissue engineering using extrusion-based AM techniques are presenting **strut-based structures**. It consists in placing simple struts side-by-side with an interspace and stacking them layer-by-layer to obtain the final 3D object (Figure 18 A). The mesh is extended in two dimensions (X and Y) and is repeated layer-by-layer. In **complex structures** the mesh is developed and continuous in the three dimensions (X, Y and Z). That brings much more complexity in printing but allows a higher degree of freedom regarding the design (Figure 18 B). These kind of meshes were especially studied using metal printing techniques or light-based AM techniques.

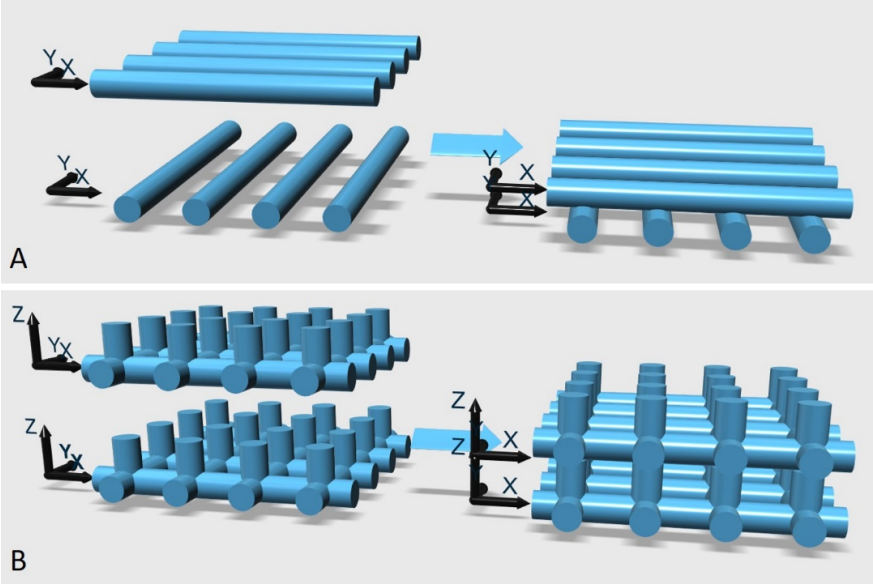


Figure 18: Distinctions between (A) strut-based structure and (B) complex structure. (A) Strut-based structures consist in placing simple struts side-by-side with an interspace and stacking them layer-by-layer to reach the final 3D object. The mesh is extended in two dimensions (X and Y) and is repeated layer-by-layer. (B) In complex structures, the mesh is developed and continuous in the three dimensions (X, Y and Z).

An overview of the studies focusing on the impact of scaffold geometry on their mechanical properties for **struts-based structures** is summarized in Table 5 and in Figure 19. The main conclusion of these studies is that pore shape influences mechanical properties, even though most of the studies do not evaluate the effect of geometry on mechanical properties in a systematic way. Mechanical properties may be influenced by many different geometrical parameters (*e.g.* pore sizes, pore geometries, strut sizes, strut orientations, porous fraction,…). However, more than one parameter often change simultaneously making it difficult to understand the effect of each parameter individually. Furthermore, porous fraction is not always taken into account while it has an influence on mechanical properties. Park and coworkers compared the mechanical properties of salt leached scaffold with three different printed scaffolds (Figure 19 F).[97] This comparison is interesting as it compares a conventional scaffold fabrication technique with an AM technique, even though porosities are completely different and general conclusions are difficult to draw. Among the three printed scaffolds, strut sizes, strut interspaces and porous fractions are different. The effect of each parameter on mechanical properties cannot be isolated. Some inconsistencies can be raised among the other studies. Displaced struts

(Figure 19 B, 19 D and 19 E) significantly decrease mechanical properties owing to the bending effect of horizontal struts.[98-100] However, Korpela and coworkers showed no significant differences between displaced and not displaced strut geometries (Figure 19 H).[101] Finally, some studies focus on compression test along only one axis (*i.e.* force applied perpendicular to printed layers). *In vivo*, pressure comes from all directions, while in the case of large size scaffold printing for specific patients, orientation of the object (and thus strut orientation) in the printer is not always adjustable. Hence, a more complete characterization of mechanical properties in each scaffold direction is needed.

Table 5: Impact of scaffold geometry on their mechanical properties for strut-based scaffolds.

Reference and printing technique	**Model (Fig.19)**	**Material**	**Aim of the study**	**Scaffold variation tested**	**Compression/Traction axis(es)**	**Porous fraction evaluation**	**Observations regarding mechanical properties**
Trachtenberg et al., 2014[89] Home-made extrusion-based technique	A	PCL	• Optimization of printing parameters with an open-source system • Effect of fiber spacing and porous fraction on mechanical properties	• Fiber spacing: 1.2mm; 1.5mm; 2.0mm; 2.5mm (uniform and gradient) • Porous fraction: from 10% to 40%	Compression along Z orientation (force applied perpendicular to printed layers).	Yes: from 10% to 40%	• No effect of pore size on mechanical properties (compressive yield strength and compressive modulus) • Porous fraction has an effect on mechanical properties according to a power-law relationship
Serra et al., 2013[100] Nozzel-deposition system	B	• PLA/PEG • PLA/PEG/G5 (CaP glass)	• Fabrication • Characterization: processing effect, architecture, mechanical properties, surface properties, biological response	• 0°/90° layer configuration (ORTH) • 0°/90° displaced double-layer design (DISPL)	Compression along Z orientation (force applied perpendicular to printed layers).	For ORTH: yes For DISPL: Not clearly stated	Significant decrease of the compressive modulus from ORTH to DISPL structure: • ORTH: more dense (closer layers and smaller pore size in the transversal direction). • DISPL: synergistic effect of higher separation between layers and displacement of the struts that leads to the bending effect of horizontal struts during compression.

Rajzer et al., 2018[102] Fused deposition modelling (FDM)	C	Poly(L-lactic acid) (PLLA)	• Combination of macroporous PLLA scaffold with electrospun-gelatin fibers coating • Scaffold development and characterization • *In vitro* biological study	Scaffold presenting different pore geometries and struts arrangements	Traction (orientation not clearly stated. Force likely applied parallel to printed layers.)	No	Layer arrangement has an effect on tensile strength
Buyuksungur et al., 2017[99] FDM	E	• PCL • PCL + Hydroxyapatite (HAp) coating • PCL + HAp/PPF coating	• Coating of PCL 3D printed scaffold with HAp or HAp/PPF • Evaluation of physical and chemical properties of the scaffolds • *In vitro* and *in vivo* evaluations	Scaffold with struts presenting different displacements (0, 0.10,0.15,0.20, 0.25, 0.50 mm for a strut interspace of 1 mm)	Compression along Z orientation (force applied perpendicular to printed layers).	No	0.15 mm struts displacement for a fiber diameter of 0.55 mm and fiber interspace of 1 mm decrease by two the compressive modulus
Park et al., 2009[97] Bioplotter® System	F	PCL	• Investigation of pore geometry and scaffold architecture • Characterisation of morphology and mechanical properties • *In vitro* biological study	Comparison of four scaffolds (struts size/ struts interspace): • 200/300 • 250/500 • 330/700 • Salt leaching	Compression along Z orientation (force applied perpendicular to printed layers) Measured under an ambient temperature of 30°C.	• 45-75% (printed scaffold) • 82.4% (salt leaching)	• Printed scaffold have higher compressive modulus than salt leached scaffolds • Mechanical properties can be modified by adjusting the scaffold geometry
Ribeiro et al., 2017[98] Bioplotter® System	D	PCL	Proof of concept of an affordable device combining mechanical compression tests and micro computerized tomography imaging.	Scaffolds with different struts alignment: • 0°/90° layer configuration	Compression along Z orientation (force applied perpendicular to printed layers)	Yes: close to 50%	• Compressive modulus: 0°/90° (highest) > 0°/45° > 0°/90° with displacement (lowest)

				• 0°/45° layer configuration • 0°/90° layer configuration with struts displacement			• Playing with scaffold structure allows to considerably adjust scaffold mechanical behavior under compression
Zein et al., 2002[88] FDM	G	PCL	• Investigation of the anisotropy of scaffold presenting different internal architecture • Effect of different porous fractions and channel size on scaffold mechanical properties	Scaffolds with different struts alignment and struts size: • 0°/90° layer configuration • 0°/60°/120° layer configuration • 0.508 mm strut size • 0.610 mm strut size • 0.711 mm strut size	Compression along three axes: X, Y and Z (force applied perpendicular and parallel to printed layers)	Yes: from 45% to 80%	• Compression stiffness (same porous fraction): -0°/90° > 0°/60°/120° -0°/90°: depend on loading direction -0°/60°/120°: no significant differences among orientations • Yield strength (same porous fraction): -0°/90°: depend on loading direction -0°/60°/120°: no significant differences among orientations • Yield strain (same porous fraction): -0°/90° < 0°/60°/120° -0°/90°: no significant differences among orientations -0°/60°/120°: depend on loading direction • Mechanical properties generally depend on scaffold porous fraction, regardless of

							the lay-down pattern and channel size • Bounding strength between layers influences mechanical properties (weak bonds provoke layer detachment and lower mechanical properties)
Korpela et al., 2013[101] FDM	H	• PCL (Mechanical properties studied) • PCL/Bioactive glass (Mechanical properties studied) • PLA (Mechanical properties not studied) • PLC (L-lactide/ε-caprolactone 75/25 mol % copolymer) (Mechanical properties not studied)	• FDM printability of a PCL/ Bioactive glass composite and a PLC copolymer • Comparison with PCL and PLA • Compressive testing on scaffold with different geometries • *In vitro* biological study	Scaffolds with different struts alignment (pore size): • 0°/90° layer configuration (550x550x400 µm³) • 0°/90° layer configuration (400x400x400 µm³) • 0°/90° layer configuration (400x400x400 µm³) with struts displacement • 0°/60°/120° layer configuration (350x350x400 µm³ (diagonal layers) and 700x700x400 µm³ (horizontal layers))	Compression along two or three axes: X, Y and Z (force applied perpendicular and parallel to printed layers)	No	• Scaffolds with the highest porous fraction had significantly lower compressive moduli • No significant differences in compressive moduli between 0°/90° layer configuration (400x400x400 µm³) with and without struts displacement • 0°/60°/120° present similar Z- and X-axis compressive moduli compared to 0°/90° (400x400x400 µm³ with and without struts displacement) but 0°/60°/120° Y-axis compressive moduli is higher than all Z- and X-axis compressive moduli

							• All samples had a significantly higher X-axis compressive moduli compared to Z-axis compressive moduli

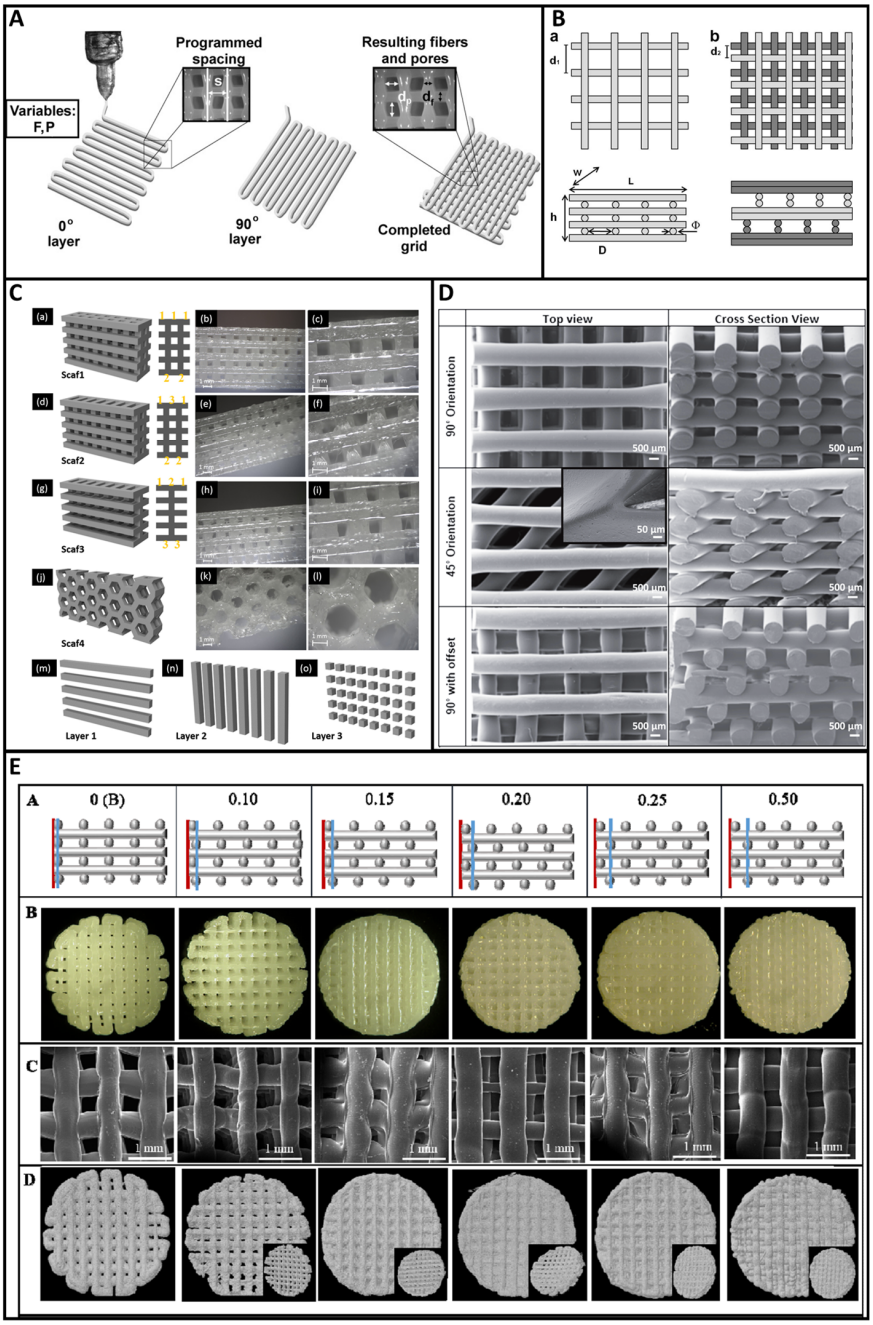


Figure 19 A, B, C, D and E: Model of strut-based scaffolds presented in Table 5. Adapted from [89, 98-100, 102]

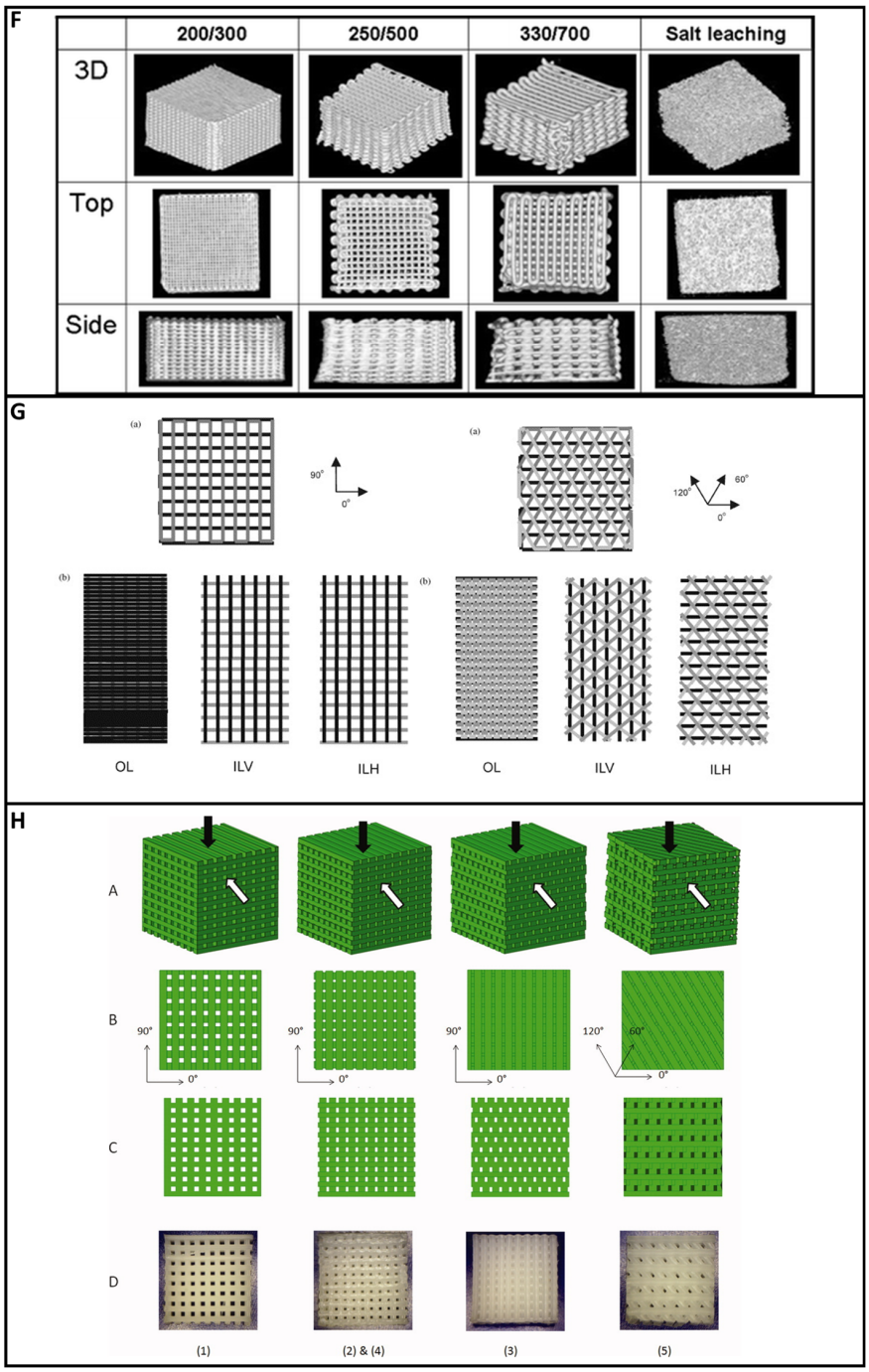


Figure 19 F, G and H: Model of strut-based scaffolds presented in Table 5. Adapted from [88, 97, 101]

Complex structures are much more interesting as they bring more freedom in design and more tunable properties. The latest studies on the impact of the geometry of complex structures on their mechanical properties are summarized in Table 6. Complex structures, like crystal organization, are made of "unit cells" that share the same design and are periodically repeated in X, Y and Z directions to reach the complete lattice structure. These unit cells can be simple cubes or polyhedra put side-by-side. Alternatively, they can be more complex and modeled by mathematical equations. An example that drew attention is the so-called family of "minimal surfaces" and more precisely the "triply periodic minimal surfaces" (TPMS).[49, 103] They are defined as structures locally minimizing surface energy and having a mean curvature of zero at each point of the surface. It means that two curvatures are present in the same point of the surface of a three-dimensional plane and these two curvatures have the same value with an opposite sign (Figure 20). A familiar object showing that kind of mean curvature is a horse saddle. The first curvature fits the horse in the transverse plane, the second fits the rider in the sagittal plane. The trabecular bone also presents an average mean curvature close to zero.[49] Hence, TPMS are good biomimetic designs for trabecular bones. Mathematical equations that give TPMS-based structures only provide the surface of a structure (infinitesimal thickness). To have a printable object, a volume should be added. Either the surfaces are thickened to create a sheet-based lattice structure, or the enclosed volume is filled to create a skeletal-based lattice structure.[103] One of the most studied TPMS is the Schoen's gyroid. TPMS, and especially Schoen's gyroid, were shown to be suitable for biomedical applications owing to their high specific stiffness to weight ratio while maintaining isotropy.[104-106] Even though most of the soft tissues as well as bone tissues are oriented and anisotropic[107, 108], the isotropy of a model allows to print the scaffold and implant it vertically or horizontally with only minor changes in its mechanical properties. Another advantage regarding mechanical properties of these types of structures is their high fatigue life owing to the continuous curvature throughout the structure.[106] This continuous curvature eliminate the effect of stress concentrators at nodal points.

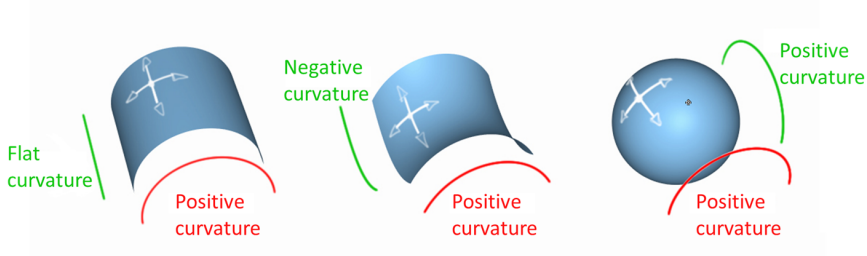


Figure 20: Surfaces presenting different combinations of null, positive and negative curvatures at a same point in perpendicular directions. The surface presenting at a same point a negative and a positive curvature (middle) is called "minimal surface". Adapted from [109]

Gradients of geometries could be beneficial as geometrical requirements (porosity, curvature,…) could be different depending on the stage of tissue regeneration.[49] Not many studies have looked into this kind of design while these geometries could be easily produced using AM. A drawback reproached to periodic lattice structures is the lack of irregularities in the structures as found in the human body.[71] However, uncontrollable irregularities lead to poor repeatability of morphology and mechanical properties. To closely mimic body irregularities while keeping control on "controllability", Wang and coworkers proposed a design method based on the Voronoi-Tessellation method to produce porous scaffolds (Figure 21 J).[71] They proposed to create probability spheres around each node of a regular lattice structure. The nodes are then moved inside this probability spheres to reach a new position and to produce a new structure. This new structure, with nodes stochastically placed inside probability spheres, is irregular. The irregularity of the structure is controlled through the design of those probability spheres.

Compared to strut-based structures, the studies presented for complex structures are more systematic and porous fraction is always taken into account (Table 6). Nevertheless, these complex geometries have been studied mainly for metal structures or for some photo-curable resins. Besides, most of the time compressions studies are uniaxial, even though some studies take into account unit cells orientation. Torsion, bending and tensile testing are less reported probably owing to the difficulty to prepare and adequately attach the samples for such tests. It was raised by the authors that some of their results are artefact of the printing technique they use.[110] Therefore, the printing technique also has an influence on mechanical properties and should raise as much concern as geometry. AM techniques are the perfect tool to propose a theory regarding the understanding of the

impact of geometry on mechanical properties. To reach that goal, a study systematically and deeply comparing mechanical properties (compression in every directions, torsion, bending, tensile testing, *etc*.) of printed samples with different unit cell design (strut-based, diamond, TPMS,…) and dimensions, in different materials (polymers, metal,…) using different AM techniques and post-treatment (annealing, surface smoothing,…) would be necessary.

Table 6: Impact of scaffold geometry on their mechanical properties for complex scaffolds.

Reference and printing technique	**Model (Fig.21)**	**Material**	**Aim of the study**	**Scaffold variation tested**	**Mechanical testing and axi(e)s studied**	**Porous fraction/solid fraction evaluation**	**Observations regarding mechanical properties**
Al-Ketan et al., 2018[103] Selective Laser Sintering (SLS)	A	Maraging steel (Composition: Fe, Ni, Co, Mo, Ti,, Al, Cr, C, Mn, Si, P, S)	• Evaluation of triply periodic minimal surfaces (TPMS) as lattice structures. • Numerical simulation of mechanical properties exhibited by the architecture of investigated structures. • Printing, characterization and compressive mechanical study.	• Body Centered Cubic (BCC) strut-based • Primary, secondary and sheet-based Schoen's I-WP	Compression along Z orientation (force applied perpendicular to printed layers)	Solid fraction: • BCC: from 10% to 22% • Primary IWP: from 9% to 21% • Secondary IWP: from 17% to 26% • Sheet-based IWP: from 15% to 24%	• Deformation mechanism is independent of the relative density. • BCC strut-based and Primary IWP: layers start to fail diagonally • Secondary IWP: buckling of the structure. • Sheet-based IWP: structure deforms collectively, every layer deforms in the same way. • Sheet-based IWP stiffness and strength values are two times higher than strut-based and skeletal-based lattice structures.
Yan et al., 2012[110] Selective Laser Melting (SLM)	B	316L stainless steel	• Manufacturability of Schoen gyroid structure by SLM. • Effect of unit cell size on manufacturability, strut density and	Gyroid lattice structure with various unit cell size: 2, 3.5, 4.5, 5.5, 6.5 and 8 mm	Uniaxial compression (orientation not mentioned)	Use of the same volume fraction (15%)	• No visible signs of local brittle failure during compression • Yield strength and compression modulus decrease as unit cell size increases. Result of a

			compression properties.				decrease in strut density observed for increased unit cell size. (Phenomenon linked to SLM. May not be transposable to other AM techniques.)
Weiβmann et al., 2016[111] SLM	C	Ti6Al4V titanium	Investigation of the effect of unit cell orientation in the sample on mechanical properties.	• Design of the unit cell: crossing struts • Tested unit cell sizes: ○ 3.00x2.12x2.12 mm³; strut diameter: 0.9 mm (T1) ○ 4.00x2.83x2.83 mm³; strut diameter: 1.1 mm (T2) • Tested orientations: ○ 0° (for T1 and T2) ○ 45° - y-axis (for T2) ○ 45° - y-axis; 45° - x-axis (for T2) ○ 90° - y-axis (for T1 and T2) ○ 90° - y-axis; 45° - x-axis (for T1 and T2)	Compression along Z orientation (force applied perpendicular to printed layers)	Yes (from 54 to 55 % for T1 and from 56 to 60% for T2)	• Demonstrated the influence of cell size and orientation on the mechanical properties. Phenomenon attributed to: ○ Geometric conditions of the unit cell, and especially length ratio ($\lambda = cell\ size/sample\ size$) ○ Position of struts compared to applied force ○ Position of struts in the building process • Magnitude of change in mechanical properties is function of geometrical dimensions of unit size • Elastic modulus and compressive strength/strain are correlated for the geometric design studied (for both unit size and all orientations) • A power law equation was found between the elastic

							modulus and porous fraction/elastic modulus. This relationship was verified for other studies. • Influence of unit cell orientation on mechanical properties reveals the anisotropy of the designed scaffold and that orientation should be taken into account for bone scaffold development.
Wieding et al., 2012[112] SLM	D	Ti6Al4V titanium	• Mechanical testing of three different designs of open-porous structures with controlled pore geometry • *In vitro* evaluation of cell infiltration and collagen I production	• Scaffold with rectangular struts aligned in the vertical direction. Pore size: 800 x 800 µm²; strut section size: 400 x 800 µm²; distance between two layers: 1.3 mm • Scaffold with rectangular struts aligned in the vertical direction. For each level, strut alignment is shifted by half of pore size (*i.e.* 400 µm). Pore size: 800	Uniaxial compression (orientation not clearly stated. Force likely applied perpendicular to printed layers.)	Yes: approximately 70% for all samples	• Ultimate compressive strengths were similar for all scaffold geometries • Significant differences were observed regarding compression moduli: ○ Highest compressive modulus for diagonally-oriented circular struts scaffold ○ Lowest modulus for shifted rectangular strut scaffold • Those results show that mechanical properties are not only affected by porous fraction

				x 800 µm²; strut section size: 400 x 800 µm²; distance between two layers: 1.3 mm • Scaffold with diagonally-oriented circular struts. Pore size: 550 x 550 µm²; strut diameter: 300 µm; distance between two layers: 1.2 mm			
Challis et al., 2014[104] SLM	E	Ti6Al4V titanium	• Comparison of two scaffold architectures • Verification of the high strength of a specifically designed architecture • Comparison with values found in literature	• Gyroid with 3.33 mm unit cell size • "Optimized" scaffold with 3.33 mm and 5 mm unit cell sizes	• Uniaxial compression (orientation not clearly stated. Force likely applied perpendicular to printed layers.) • Finite element calculation method	Yes, samples printed to reach a defined solid fraction. • Gyroid: 5%, 10% and 15% solid fraction • "Optimized" scaffold: solid fractions between 7% and 20%	• "Optimized" scaffold shows high and isotropic strength and stiffness to weight ratios. • More deformation within the gyroid structure which implies lower compression moduli while "optimized" scaffold ensures a better distribution of the load throughout the structure • Finite element calculations accurately predict the stiffness of geometries. Could help to develop a

							theory of the strength of porous , open cell materials
Speirs et al., 2017[106] SLM	F	Nitinol (NiTi; near equiatomic nickel-titanium alloy)	• Investigation of fatigue behavior of three structures presenting different unit cell designs • Printing, morphological evaluation and mechanical testing	• Octahedron ○ Strut thickness: 260 µm ○ Pore size: 1000 µm ○ Unit cell size: 1.75 mm • Cellular gyroid ○ Strut thickness: 320 µm ○ Pore size: 850 µm ○ Unit cell size: 1.65 mm • Sheet gyroid ○ Strut thickness: 195 µm ○ Pore size: 900 µm ○ Unit cell size: 1.4 mm	Uniaxial compression (orientation not clearly stated. Force likely applied perpendicular to printed layers.)	Yes, solid fraction about 25% for all geometry	• Yield stress is the lowest for the octahedron geometry and the highest for the sheet gyroid geometry • Both gyroid geometries show a superior fatigue life compared to octahedron with the sheet gyroid showing the most superior fatigue life • Results are explained by: ○ the presence of continuous rate of curvature without clear notch points in gyroid geometries (those point acting as stress concentrators) ○ less residual particles attachment (stress concentrators) and the minimized staircase effect owing to gyroid design
Heinl et al., 2008[113] Electron beam melting (EBM)	G	Ti6Al4V titanium	• EBM fabrication of structures with controlled and interconnected pores	• Diamond lattice structure • Strut-based structure	Compression along two axes: Z and X (force applied perpendicular and parallel to	Yes: • Diamond: 80% • Strut-based: 60%	• The lower porous fraction of strut-based scaffold enhances mechanical properties • Loading direction has a strong influence on

			• Study of mechanical properties and comparison to human bones • Surface chemical treatment in HCl and NaOH to improve bioactivity • *In vitro* evaluation		printed layers, respectively)		measured mechanical properties for both structures. Higher stiffness and strength values are obtained if load is applied parallel to building direction (perpendicular to printed layer) • Mechanical properties of the proposed structures are close to human bones, which should minimize stress-shielding effects.
Wang et al., 2016[114] SLM	H	Cu-bearing stainless steel (316L stainless steel + 4.5 wt% Cu)	• Production of anti-microbial scaffold with satisfied biocompatibility • Comparison of scaffold mechanical properties with and without Cu • *In vitro* antibacterial performance study	• Gyroid structure • Body Centered Cubic (BCC) structure	Uniaxial compression (orientation not mentioned)	Yes, solid fraction of 25% and 40% for both gyroid and BCC structures	• The Increase in solid fraction increases both compression modulus and yield strength (for the same structure) • Addition of Cu has a minor impact on mechanical properties (slightly increase strength and stiffness) • Gyroid structure has a higher compressive modulus and a lower yield strength compared to BCC structure • Stiffness of the structures is much lower than bulk stainless steel, which leads to less stress shielding when implanted

Yánez et al., 2016[105] EBM	I	Ti6Al4V titanium	• Study of mechanical behavior of gyroid structure regarding struts orientation and comparison with previously developed designs • Evaluation of the use of EBM to produce Ti6Al4V gyroid scaffolds	• Gyroid structure: different eccentricities of the pore tested. Eccentricity expressed as angle between the struts and the axial direction (Figure 21 I). Angles tested: 19°, 21.5°, 26°, 35°, 45°, 55°, 64°, 68.5° • Diamond lattice structure: different porosities tested ○ Strut radius (R): 0.3 mm – cell size (S): 2.5 mm ○ R: 0.35 mm – S: 4 mm ○ R: 0.5 mm – S: 4 mm • Rhombic dodecahedron (data taken from the literature)	Uniaxial compression (orientation not clearly stated. Force likely applied perpendicular to printed layers.)	Yes (data not shown)	• High correlation between compression modulus and pore eccentricity • Compression modulus and compressive strength increase when pores are elongated following the compression axis. • Gyroid structures, compared to other structures, show better strength to weight ratios for certain pore eccentricities • Elastic modulus of gyroid Ti6Al4V structures produced by EBM similar to elastic modulus of cancellous human bone
Wang et al., 2018[71] SLM	J	Ti6Al4V ELI titanium	• Production of irregular but controllable porous scaffold	• Production of irregular scaffold designed with a method based on	Uniaxial compression	Yes, from 63% to 92%	• Compressive properties are affected by both porous fraction and irregularity (and

			• Morphological evaluation and study of mechanical properties	probability spheres (Figure 21 J) • Variation of porous fraction • Variation of irregularity • Porous scaffold with gradient distribution of porosity	(orientation not mentioned)		could be adjusted to the level of cortical bone) • Establishment of a power relationship between compressive strength and porous fraction as well as a linear relationship between compressive modulus and porous fraction • The compressive modulus decreases as the irregularities increase. • For low irregularities, compressive strength tends to decrease as the irregularities increase. When irregularities exceed a certain value, a new balance is found and the compressive strength tends to be steady as irregularities increase. • Greater loads are required to destruct samples with larger porosity gradient
Melchels et al., 2010[115] Stereolithography	K	• Poly(D,L-lactic acid) (PDLLA) dimethacrylate • Poly(D,L-lactic acid-co-ε-	• Design of biodegradable structures with refined architecture	• Cube architecture unit cell: ○ Pore size: 530x530 µm² ○ Strut thickness: 150 µm	• Uniaxial compression (orientation not clearly stated. Force likely applied	Yes: • Cubes: 64% • Diamond: 68% • Gyroid: 69%	• Cube architecture presents a high stiffness as a result of alignment of the vertical struts with the compressive struts

		caprolactone) (P(DLLA-co-CL)) dimethacrylate	• Printing in high resolution using stereolithography • Shows in which ways mechanical properties of the scaffolds can be tailored	• Gyroid structure • Diamond structure (not studied for mechanical properties) • Salt leached structure (not studied for mechanical properties)	perpendicular to printed layers.) • Finite element analysis	• Salt-leached: 77%	• Gyroid structure shows a less rigid behavior owing to its curved surfaces • In gyroid structure, stress and strain are homogeneously dispersed throughout the structure. Seeded cells would be exposed to more equal mechanical stimuli throughout the structure. • Excellent agreement between experimental data and model prediction • The use of P(DLLA-co-CL) copolymer considerably decreases compressive modulus (1000 times lower). Intermediate mechanical properties are achievable adjusting copolymer composition.
Walker et al., 2017[116] Stereolithography	L	Poly(propylene fumarate) (PPF) Two different molecular masses: 1500 Da and 2450 Da	• Fabrication of scaffold using stereolithography • Evaluation of the effect of molecular mass and pore architecture on mechanical	Gyroid structures: • Fine architecture: ○ Strut size: 200 µm ○ Pore size: 700 µm • Coarse architecture: ○ Strut size: 400 µm	Uniaxial compression (orientation not mentioned)	Yes, samples designed to reach a defined porous fraction of 88.2% for both fine and coarse	• No significant differences in yield stress between the two architectures (1500 Da). Both yield stresses are significantly higher than yield stress of fine with 2450 Da chain length. • Fine architecture with 1500 Da chain length has a

			integrity and degradation rate	○ Pore size: 1400 µm		gyroid structure	significantly higher stiffness compared to coarse architecture (1500 Da) and to fine architecture with 2450 Da chain length. Stiffnesses of 1500 Da coarse architecture and 2450 Da fine architecture are not significantly different.
Jung et al., 2014[117] Mold construct by stereolithography	M	PCL	• Design and fabrication (molding) of scaffold with octahedron pore architecture • Proof of high flexibility of this pore architecture • *In vitro* evaluation • Comparison with conventional types of pores	• Octahedron pore architecture • Cube pore architecture • Strut-based architecture • For all architectures: ○ Unit cell size: 1 mm ○ Strut size: 500 µm	• Uniaxial compression (orientation not mentioned) • Three-point bending test	Yes, samples designed to reach a defined porous fraction of 50% for each architecture	• Compressive moduli are significantly different among the structure: Octahedron (lowest) < cube < strut-based (highest) • Flexibility are significantly different among the structure: Octahedron (highest) > cube > strut-based (lowest)

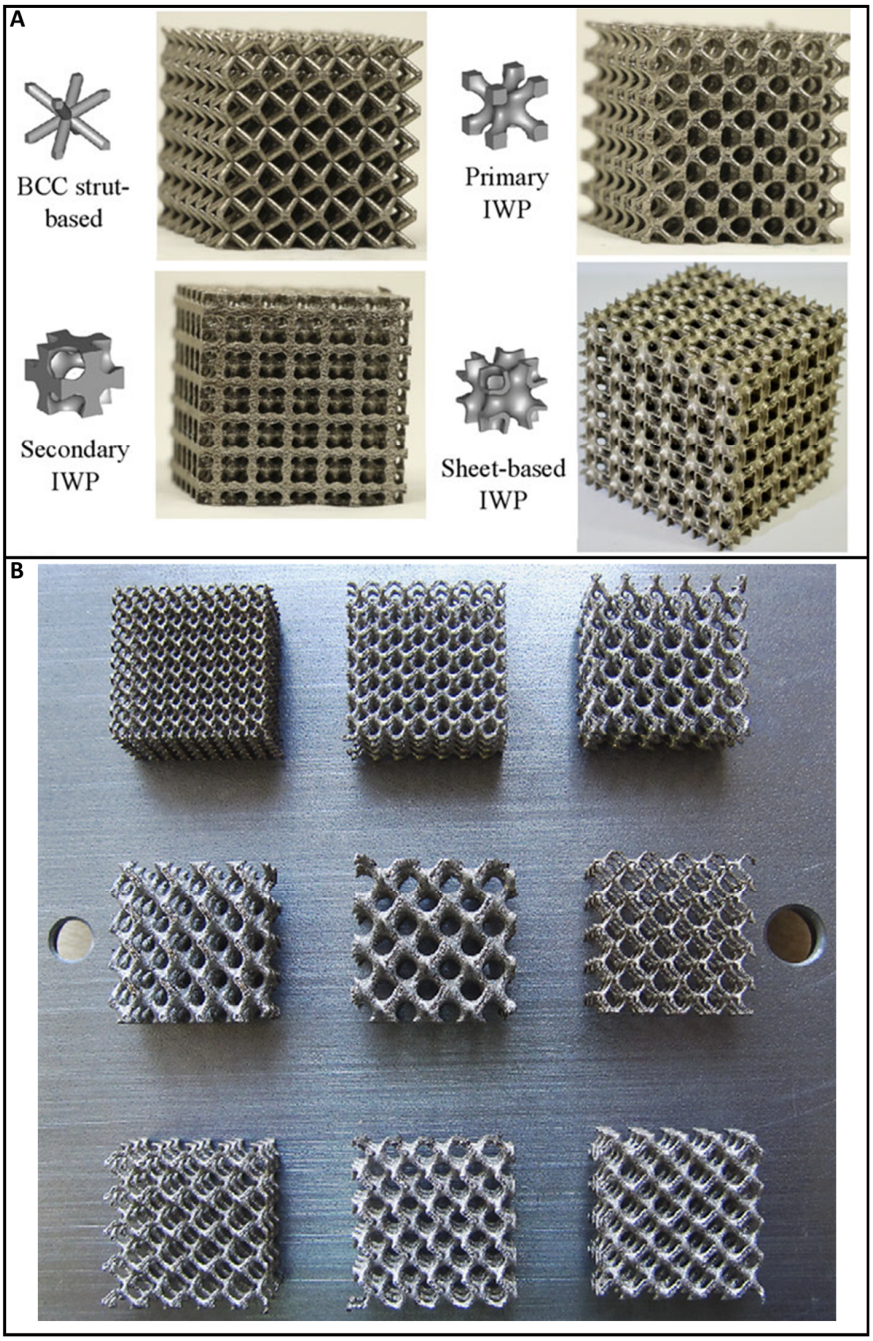
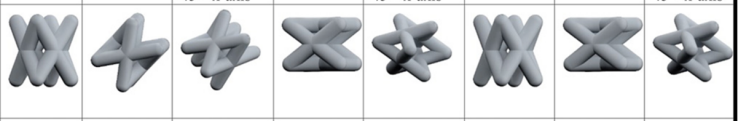
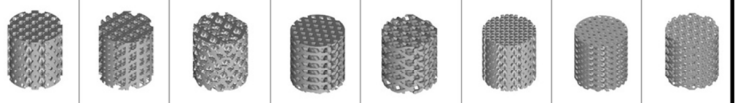
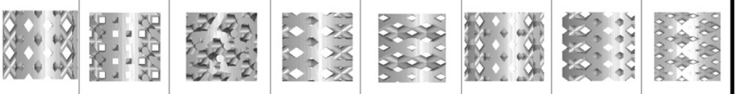
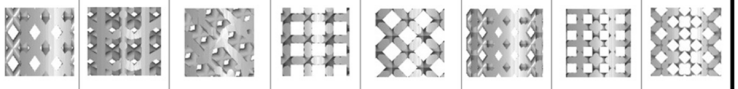
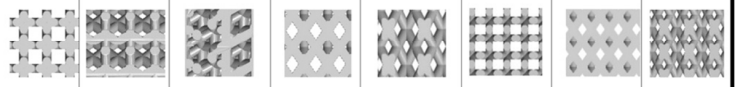


Figure 21 A and B: Model of strut-based scaffolds presented in Table 6. Adapted from [103, 110]

C

Orientation type	T 2 - I	T 2 - II	T 2 - III	T 2 - IV	T 2 - V	T 1 - I	T 1 - IV	T 1 - V
Orientation	0°	45°– y-axis	45°– y-axis 45°- x-axis	90°-y-axis	90°- y-axis 45°- x-axis	0°	90°– y-axis	90°- y-axis 45°- x-axis
Unit cell								
Scaffold								
Scaffold								
Scaffold								
Scaffold								
Number of unit cells in a scaffold	64	64	72	60	60	192	182	210

D

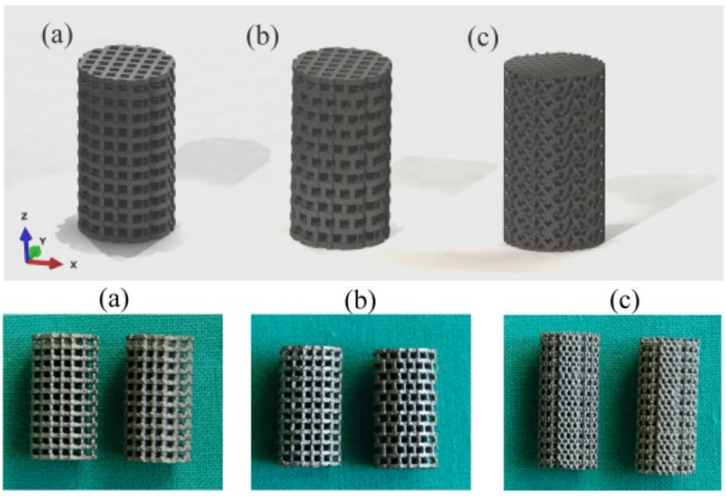


Figure 21 C and D: Model of strut-based scaffolds presented in Table 6. Adapted from [111, 112]

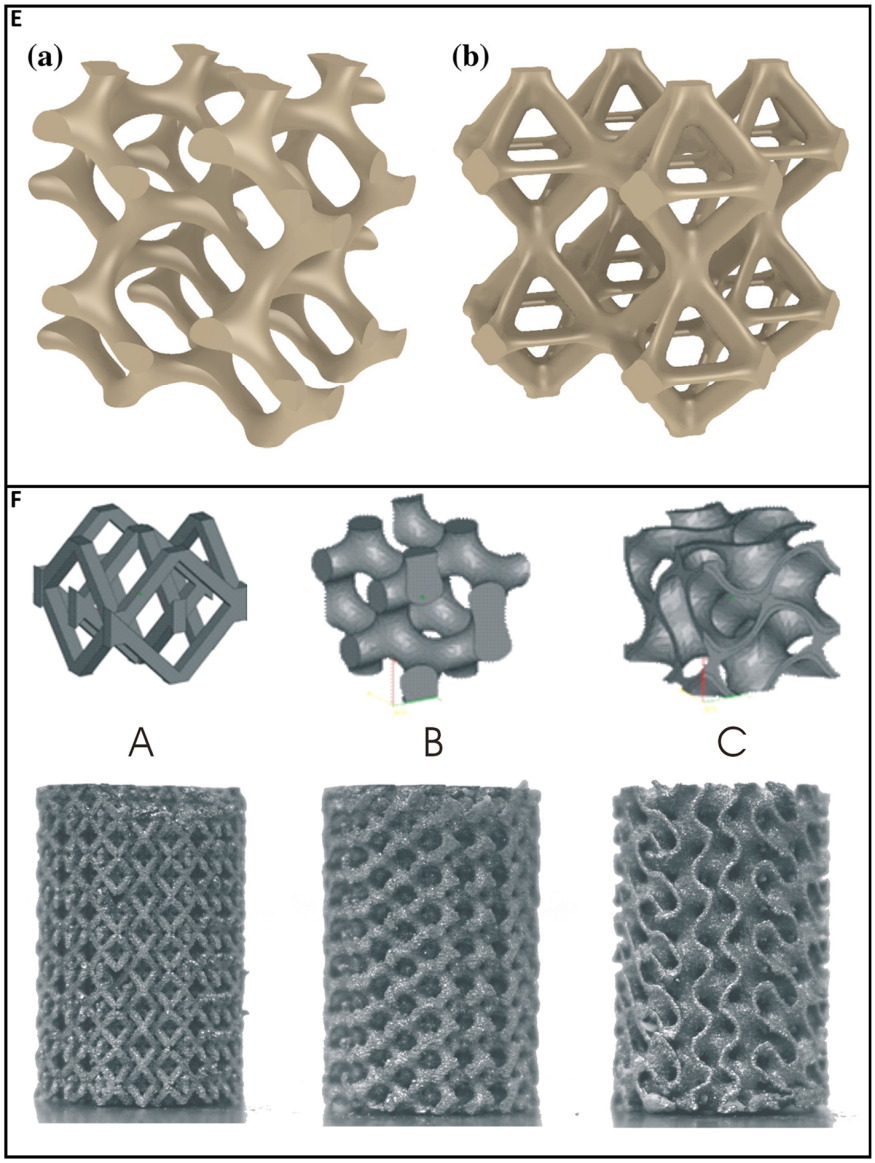


Figure 21 E and F: Model of strut-based scaffolds presented in Table 6. Adapted from [104, 106]

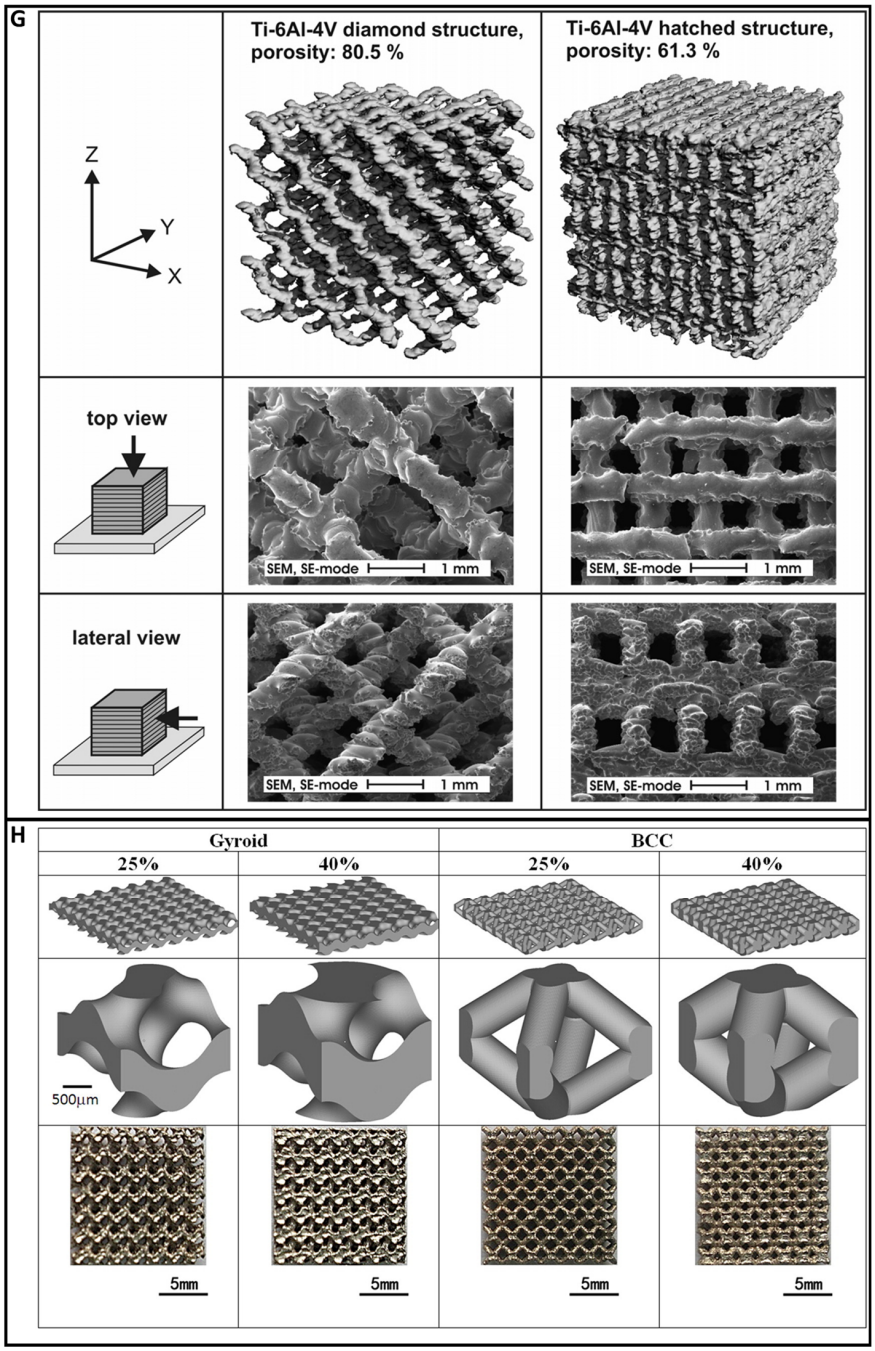


Figure 21 G and H: Model of strut-based scaffolds presented in Table 6. Adapted from [113, 114]

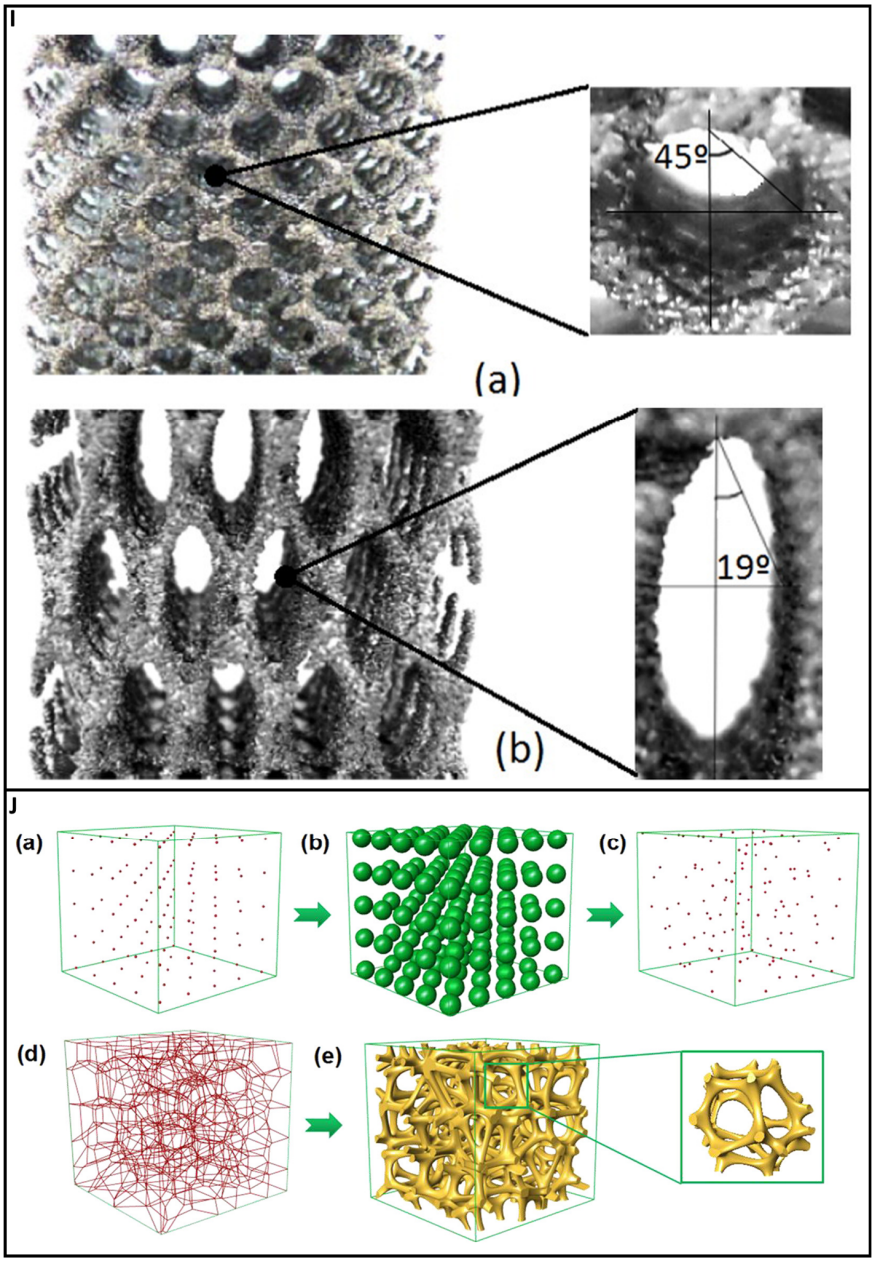


Figure 21 I and J: Model of strut-based scaffolds presented in Table 6. Adapted from [71, 105]

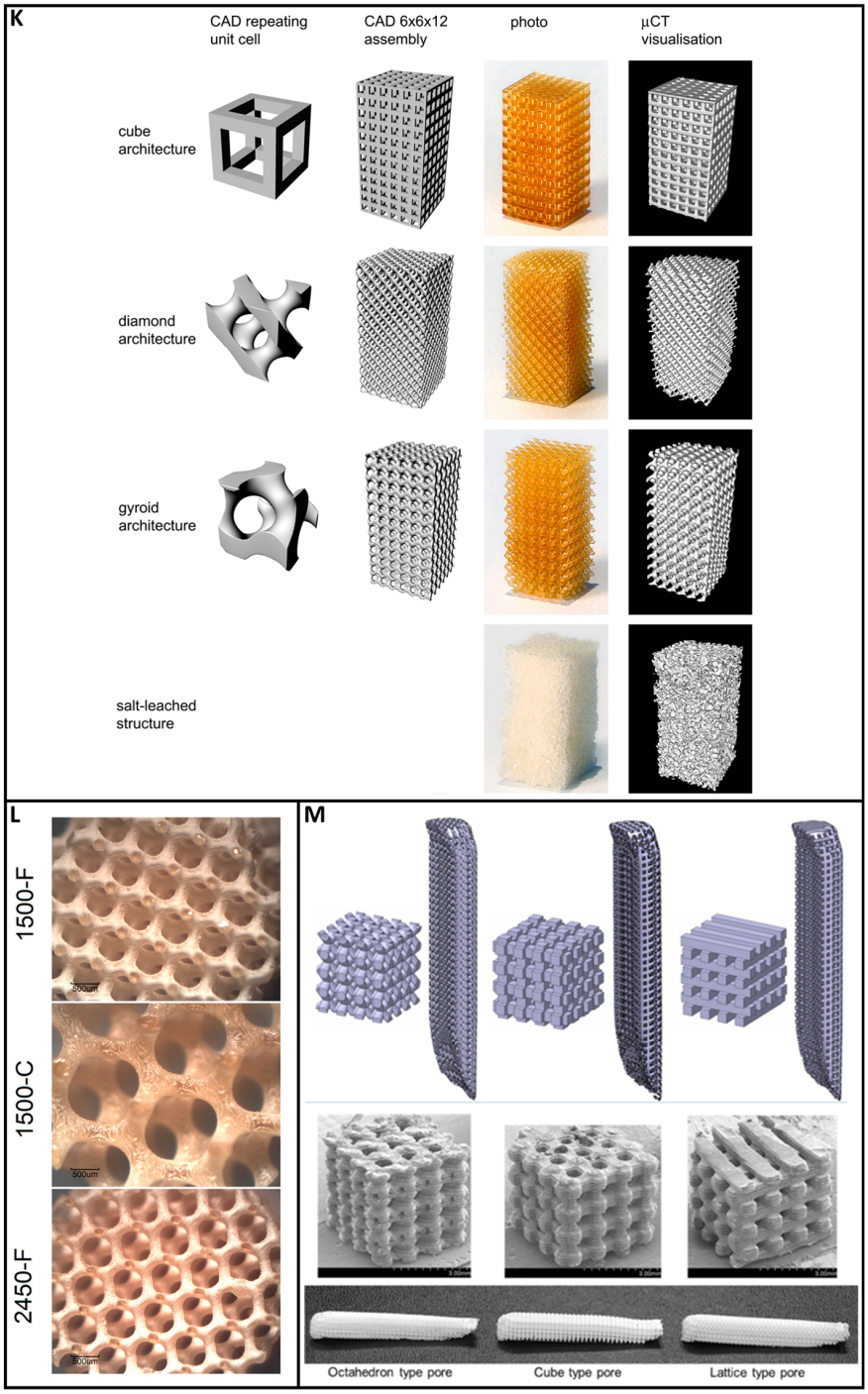


Figure 21 K, L and M: Model of strut-based scaffolds presented in Table 6. Adapted from [115-117]

3.5.2.2 Geometric-related parameters to consider for tissue engineering

The **curvature**, one of the main parameters of pore architecture, has an influence on tissue regeneration.[49] Several studies demonstrated that curvatures with radii largely above cell size interact with cells and influence their behavior. *In vitro*, the curvature influences cell attachment rate, cell migration speed, cell cytokine secretions, cell differentiation, and cell morphology such as cell spreading area.[49, 118] However, knowledge related to the mechanisms of such phenomena is still limited. The best choice regarding curvature for tissue regeneration is unclear and seems to be cell type-dependent. Concave surfaces are preferred by some cell types compared to convex or flat surfaces.[49] By contrast, epithelial cell spreading and migration speed are increased on convex surfaces.[119] The impact of the curvature on tissue regeneration or tissue migration is also a function of the amplitude of the curvature .[49, 119] The mechanism of curvature sensing was highlighted using MSC.[118] Such sensing is ensured by a dynamic interaction between the nucleus and the cytoskeleton. Indeed, focal adhesions close to concave curvatures present an increased mechanical tension as well as a higher longevity inside the cell, which contributes to the positioning of the cell in concave regions. In addition, the nucleus presents a more spherical and relaxed shape when placed above a concave curvature. The actin-myosin network as well as the proteins involved in nucleo-cytoskeletal coupling link the focal adhesions to the nucleus. They are responsible for intracellular tensions and nucleus compression, which also play a central role in curvature sensing. In turn, gene expression is affected by the nucleus relaxation state.

Besides curvature, different pore shapes such as squares, triangles and parallelograms were also compared *in vitro*. The highest alkaline phosphatase (ALP) activity was measured for scaffold with parallelogram pores. Another parameter affecting cells is the applied load on the samples, as bone regeneration, for example, is positively affected by an applied load.[49] The design of the structure defines how the stress is dispersed throughout the structure.[112, 115] There may be other geometrical features that can influence cell behavior but not yet evidenced.[49]

When a **large scaffold** is needed for tissue regeneration, static culture conditions are not sufficient.[96] Static conditions rely on diffusion for mass transfer, which can be limited to hundreds of micrometers depending on pore size. To overcome the issue, a dynamic fluid movement can be applied in the culture chamber. The medium is pumped and perfuses the whole

structure from one side to another. A more homogeneous distribution of the cultured cells and the ECM is observed with perfusion bioreactors. In addition, the direction and the rate of the flow orients cultured cells and ECM. However, high fluid velocities are detrimental for the cells and can result in detachment and cell wash-out from the structure. Small flow-associated shear stresses also have a positive effect on tissue growth while higher shear stresses resulted in reduced or inhomogeneous tissue growth.[120] Cell proliferation, factor release, and differentiation are regulated by hydrodynamic shear.[96] Scaffold mesh geometry has an impact on flow direction and local shear stresses. These parameters are important to consider throughout mesh design process. Fluid flow has to be uniform and variations of local shear stresses should be minimized.

Scaffold **degradation** is also influenced by its geometry, even though the effect may be different depending on the degradation mechanisms of the material. Two 3D-printed structures in PPF presenting the same porous fraction and different surface areas were degraded in accelerated conditions (0.1M NaOH).[116] This study showed that the scaffold with approximatively twice the surface area degraded twice as fast. PLLA 3D-printed grids presenting different meshes (rectilinear, Archimedean chords and honeycomb) were degraded in PBS for 6 months.[121] The honeycomb mesh had a lower surface area and the weight loss observed was constantly lower throughout the 6 months. This was expected considering the hydrolysis degradation mechanism of those synthetic polymers. The higher surface area in contact with water, the higher its diffusion inside the polymer and the more hydrolytic degradation.[121] In another study, calcium phosphate scaffolds were implanted in dogs.[122] Foam scaffold degradation rate was higher than robocasting-printed scaffold's, while both scaffolds had identical chemistry as well as similar nanostructure and surface area. Furthermore, a higher number of osteoclast-like cells was present in concave macropores of foam scaffolds. It was then suggested that the concave microenvironment enhanced cell-mediated degradation. Those examples show that the degradation rate of a scaffold should be studied on the scaffold itself in an environment as close as possible to the body environment. Degradation study on simplified samples such as bulk material, powder, sheets or fibers as done in many studies should be avoided.

Even if this research fields are moving toward a better understanding of the properties and the interest of tuned geometrical structures, a lot is still unknown and cohesion is missing. However, AM techniques are the perfect

tools for those kind of studies as they allow a perfect tuning of each structural parameters. Some more systematic studies are still needed. Besides, complex geometries have impressive advantages but are still under-used regarding polymer printing for scaffolding applications.

4 Cell signaling

In addition to the material and the geometry used for the scaffold, other features can be added to control cell behavior. The addition of bioactive molecules to the scaffold and the surface modification of macroporous scaffolds are two main strategies that are employed to that effect. In the case of hydrogel scaffolds, surface modification is meaningless, though signaling molecules can be loaded and bulk mechanical properties and chemistry can be tuned.

4.1 Signaling biomolecules

Bioactivity of a scaffold can be improved using biologically active compounds. These bioactive compounds can influence cell viability, proliferation, differentiation, migration and gene expression to promote tissue regeneration.[37, 47] **Growth factors** are signaling proteins that interact with cell membrane proteins. Transforming growth factor-β_1 (TGF-β_1) or brain-derived neurotrophic factor (BDNF) are used notably to induce osteogenesis and chondrogenesis, or stimulate spinal cord regeneration, respectively.[37] Vascular endothelial growth factor (VEGF) plays an important role in tissue engineering as it stimulates proliferation, vascularization and ossification during bone formation.[74] Some **small molecules** can also control stem cell differentiation. A novel indene compound (KR-34893) promotes osteoblast differentiation while inhibiting osteoclast differentiation.[123] Many **metal ions**, such as calcium, play roles in physiological pathways and are effective in the regulation of tissue growth.[80] Another considered approach is **gene delivery**. Growth factor genes are delivered to cells at the lesion site.[37, 74] This would overcome the limited bioactivity of growth factors due to their high clearance rate, owing to a constant and localized growth factor synthesis by the cells.

All these bioactive molecules or ions can be added to the scaffold in different ways. Bioactive molecules can be integrated in the bulk of the scaffold (chemical or physical entrapment) or can be immobilized at the surface.

Different options are available to immobilize compounds at the surface such as adsorption, encapsulation in a hydrogel that covers the surface, covalent bounding using a spacer, *etc*. These immobilizations have to be studied and tailored to allow a sustained release for the desired amount of time. Depending on the option selected for immobilization, release rate can be optimized using "passive" mechanisms such as diffusion, flow, erosion/degradation, surface charge, charge density, swelling, wettability, dissolution or using "responsive" mechanisms using pH, temperature, enzymes, light, electric/magnetic field, and ultrasound.[37, 74] In our laboratory, vander Straeten and coworkers developed a method to immobilize proteins at the surface of a macroporous reactor using protein complexes and the layer-by-layer coating technique.[124, 125] This process was used to create multilayers of lysozyme but could be theoretically used for any protein or growth factor. A release study should be still performed to see if the proteins are released in physiological conditions and if the release is tunable.

4.2 Surface modifications

Cell-material interactions are a determinant factor of graft success and are thus important to characterize and study. The main factors influencing cell behavior are the chemical, the mechanical and the topographical properties of the biomaterial. Many studies were carried out modifying the surface of two-dimensional samples and investigating what was their effect on the cells. Theoretically, most of those modifications could be performed at the surface of three-dimensional macroporous samples. This part focuses mainly on two-dimensional modifications.

4.2.1 Chemical properties

When a biomaterial is exposed to a biological solution or is implanted in the body, the first step of surface colonization is the adsorption of proteins. Cells, via their integrins, recognize adhesion peptide sequences carried by some proteins (*e.g.* RGD sequence). This recognition by the cells allows their attachment to the surface. Surface chemistry does not directly interact with cells and orient their behavior but influences protein adsorption. Surface chemistry defines protein conformation, which modulates protein bioactivity.[126] In turn, adsorbed proteins influence cell behavior. Slightly hydrophilic surfaces are better for cell adhesion (Figure 22).[36] Indeed, hydrophobic surface (water contact angle higher than 80°C) favors

adsorption of non-adhesive proteins or provokes denaturation of adhesive proteins. In both cases, no attachment sequences are available for cells to allow their attachment. In contrast, if the surface is too hydrophilic (water contact angle lower than 45°C), adhesion depends on other surface properties such as material stiffness.

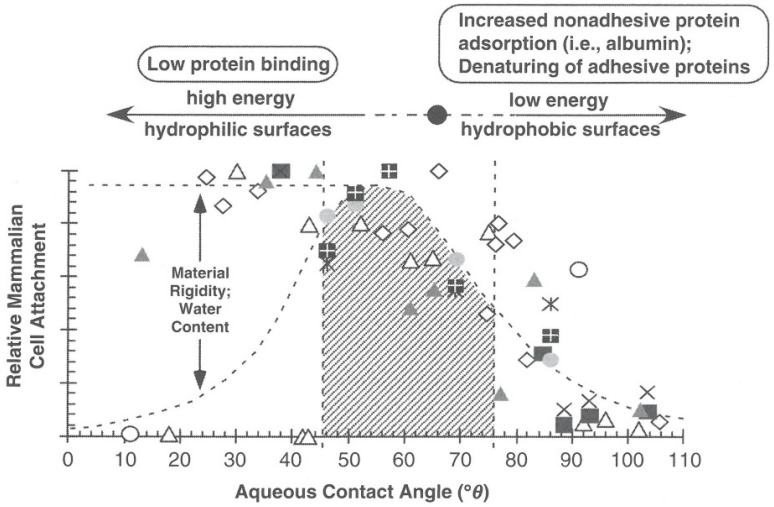


Figure 22: Cell adhesion depending on surface hydrophilicity.[36]

In a study carried out in our laboratory, Zuyderhoff and coworkers showed that the material on which collagen was adsorbed influenced the conformation of this protein.[127] Collagen was more fibrillar on hydrophobic polystyrene (PS) substrates than on hydrophilic poly(methylmethacrylate) (PMMA) substrates. Different collagen organizations were obtained using lateral heterogeneities of these two polymers. In addition, MC3T3 preosteoblast cells presented different morphologies when cultured on these different surface chemistries.[128] More elongated cells were observed when PS fraction was higher (*i.e.* more hydrophobic surface), while round shaped cells were obtained when PS fraction was lower (*i.e.* more hydrophilic surface).

Lin and coworkers proposed surfaces modified using self-assembled monolayers with terminal -OH, $-CH_3$, and $-NH_2$.[129] Adsorption forces of fibronectin, another adhesive protein, were much lower on -OH surfaces than on $-NH_2$ surfaces, while cell binding domains of fibronectin were more exposed when the protein was adsorbed on -OH surfaces. Cell adhesion on these modified surfaces with adsorbed fibronectin were compared. It was shown that, after 2 hours, cell adhesion was better on -OH surfaces, while

after 12 hours, adhesion was better on -NH_2 surfaces. These results showed that early adhesion is governed by accessibility of binding domains. In contrast, late adhesion requires proteins sufficiently bound to the surface to endure cell traction.

Spatial patterns of modified chemistry with modified surface areas, shapes or spacings were also shown to greatly affect cell behavior.[130, 131] Moreover, coating with adhesion proteins as well as grafting of anchorage peptide ligands can help cell adhesion on surface presenting inappropriate chemistry.[48]

4.2.2 Topography

The effect of curvature with radius higher than cell size was already discussed. Modification of surface topography at cellular or sub-cellular level can also affect cell behavior. Photolithography, electron-beam lithography, colloidal lithography or polymer demixing are techniques that allow to obtain organized patterns of structures such as grooves, pillars and pits.[132] Less organized roughness is obtained by acid etching, grit blasting or anodization.[133, 134] Both organized or less organized topography have an important impact on cell behavior.[87, 132] The most known example is the better osteointegration of dental and bone implants.[133, 135] For example, a rough surface microtopography increases secretion of factors improving osteoblast differentiation and decreasing osteoclast formation and activity.[134] Despite this established effect of roughness on osteointegration, other effects of topography on cell (attachment, proliferation, differentiation, …) are difficult to generalize and are debated in the literature. However, it is agreed that, for a defined pattern, the size of the pattern has an influence on the effect on cells.[132] Both microscale (close-to-cell size) and nanoscale (sub-cellular size) patterns influence cells but do not always have the same influence. Therefore, mechanisms for each scale and pattern are supposed to be different.

Each AM technique relies on layer-by-layer construction of material that results in a groovy surface on the structure. Hence, the study of groove is of particular interest. Charest and coworkers obtained grooved surfaces with groove widths ranging from 5 to 75 µm.[136] Myoblasts aligned parallel to the grooves and better alignments were obtained for grooves between 5 and 25 µm with a maximum for 10 µm. However, myogenic differentiation was not influenced by grooves for 96 h culture time. Fibroblasts cultured on 12.5 µm-

wide grooves also aligned parallel to the grooves.[137] Nuclei followed the same alignment and gene expression was shown to be affected. Elongation along a ridge/grooved pattern (350 nm wide and 500 nm high) was again obtained for human embryonic stem cells.[138] In addition, neural differentiation was induced without the addition of biochemical cues. It was hypothesized that a tensional force, due to change in cell morphology, is transferred to nuclei and influences gene expression and signal transduction.

4.2.3 Mechanical properties

Owing to mechanotransduction mechanisms already presented in section 2.2.2.2 of this Part, cells are sensitive to the mechanical properties of their environment. Each body tissue has its own stiffness (Figure 23) and this mechanical property is instructive for cells and directs their differentiation.[50] Engler and coworkers cultured mesenchymal stem cells on substrates presenting different elastic moduli.[139] Substrates from 0.1 to 1 kPa, from 8 to 17 kPa and, from 25 to 40 kPa supported neurogenic, myogenic and osteogenic differentiation, respectively. Hard microenvironment favors cell differentiation into hard tissue cell types, while soft microenvironment favors cell differentiation into soft tissue cell types. Therefore, the control of bulk or surface mechanical properties of the scaffold is important to direct cells to the expected cell type and ensures the success of tissue regeneration.

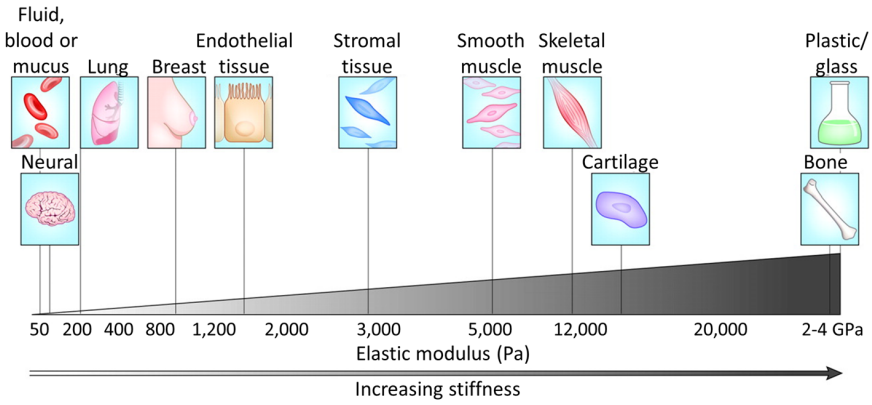


Figure 23: Stiffness of body tissues expressed in Pa. Stiffness of the tissues depends on tissue function or on the mechanical load they have to handle. Adapted from [50]

Substrates presenting surface heterogeneous mechanical properties were achieved and cell culture studies improved our understanding. Almodóvar and coworkers produced surfaces with a stiffness gradient from 600 kPa to

200 kPa.[140] MC3T3 pre-osteoblast cells cultures attached on these gradients and spread better on regions of high stiffness. In our laboratory, Degand and coworkers developed surfaces presenting mechanical heterogeneities and studied the behavior of three different cell types cultured on these surfaces.[141] The surfaces were designed using colloidal lithography of silica particles covered with an elastomer layer. Surface chemistry was homogeneous but regions above colloids were stiffer. The adhesion and the proliferation rate of MC3T3 osteoblasts and C2C12 myoblasts were higher on mechanically heterogeneous substrates compared to homogeneous ones (*i.e.* same layer of elastomer without colloidal lithography). Furthermore, gingival fibroblasts adhesion and proliferation rate were not significantly different between mechanically heterogeneous and homogeneous samples. It was hypothesized that cells are able to make use of the areas with the most favorable stiffness.

Most of the studies have focused on the rigidity of the samples and have neglected the relative contribution of storage (elastic) and loss (viscous) moduli. To understand the contribution of the loss modulus on cell behavior, Cameron and coworkers developed polyacrylamide gels with a constant compressive modulus and varied loss moduli.[45] Culture of human bone marrow derived mesenchymal stem cells on these surfaces showed a higher cell spreading area and a higher proliferation for higher loss moduli, while the increase in loss moduli decreased the size and maturity of focal adhesions. Besides, cell differentiation ability was enhanced on substrates presenting a high loss modulus. The proposed mechanism is linked to the mechanotransduction as presented in Part I section 2.2.2.2. The distinction by the cell between the elastic modulus and the loss modulus seems to be related to the loss of tension inside the cell through the dissipation of the energy by dynamic creep inside the substrate.[45, 142] The sensing process involves both passive and active tensional forces including isometric tensions (*i.e.* actomyosin-based contractile mechanisms) and isotonic tensions (*i.e.* distension of a cell as it increases its spreading area).[45] In addition, the nature of the involved adhesion proteins (*e.g.* collagen or fibronectin) seems to play an important role in sensing.[142] It is assumed that (i) the distinct biochemical signals from different classes of triggered integrins determine the threshold sensitivity to the loss modulus and/or that (ii) the respective association/dissociation constants of integrins with their ligands, as well as the kinetic of their coupling to actomyosin system, could influence the

frequency of mechanosensing. Indeed, the perceived loss modulus is a function of the frequency of applied tensions.

Examples of studies described above and many other examples in literature prove that material mechanical properties affect cell behavior. However, a less discussed information is that, like chemical properties, anchorage proteins play a crucial role as intermediate in mechanosensing.[143] Cells pull on the anchorage protein and wait for a mechanical feed-back. If these proteins are loosely bound, they cannot give the mechanical feed-back required for cell fate decision.

In a remarkable recent study, Darnell and coworkers employed a 3D culture system allowing the independent control of material stiffness, stress relaxation, and adhesion ligand density.[144] They explored systematically the effect of each biophysical parameter on cell transcriptional program using RNA sequencing (transcriptomic) coupled with bioinformatics. Mouse mesenchymal stem cells and human cortical neuron progenitors behavior were studied. They showed that each parameter had an influence on cell response and that there were interactions among parameters. The response to the value of a parameter is dependent on the value of another parameter. In addition, the relative contribution of each parameter to changes in gene expression varies with cell type.

This introduction gave a broad overview about scaffolding from separated cells, materials and biological cues to the final "bioengineered" construct. Many parameters and features from the nano to the macro level affect the construct and influence the success of a graft. Figure 24 presents a simple but complete summary of such a complex field.

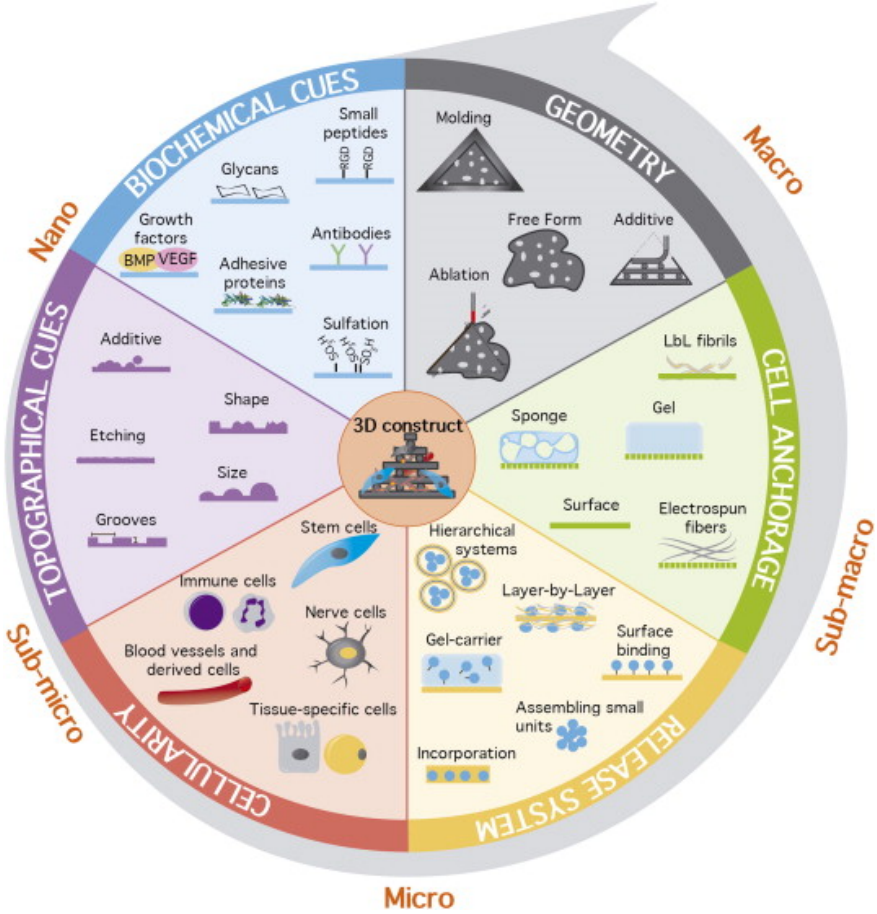


Figure 24: Scaffolds parameters (classed anti-clockwise depending on their size) influencing the success of a graft.[145]

5 References

1. Ratner, B. D., Biomaterials Science: An Interdisciplinary Endeavor. In *Biomaterials Science: An Introduction to Materials in Medicine*, Ratner, B. D.; Hoffman, A. S.; Schoen, F. J.; Lemons, J. E., Eds. Academic Press: San Diego, 1996; pp 1-8.

2. Williams, D. F., On the nature of biomaterials. *Biomaterials* **2009,** *30* (30), 5897-5909.

3. Perez-Basterrechea, M.; Esteban, M. M.; Vega, J. A.; Obaya, A. J., Tissue-engineering approaches in pancreatic islet transplantation. *Biotechnol. Bioeng.* **2018,** *115* (12), 3009-3029.

4. Langer, R.; Vacanti, J. P., Tissue engineering. *Science* **1993,** *260* (5110), 920-926.
5. Tabata, Y., Tissue regeneration based on tissue engineering technology. *Congenit. Anom.* **2004,** *44* (3), 111-124.
6. VanKoevering, K. K.; Zopf, D. A.; Hollister, S. J., Tissue Engineering and 3-Dimensional Modeling for Facial Reconstruction. *Facial Plast. Surg. Clin. North Am.* **2019,** *27* (1), 151-161.
7. Ghosal, K.; Agatemor, C.; Špitálsky, Z.; Thomas, S.; Kny, E., Electrospinning tissue engineering and wound dressing scaffolds from polymer-titanium dioxide nanocomposites. *Chem. Eng. J.* **2019,** *358*, 1262-1278.
8. Ahmed, T. A. E.; Dare, E. V.; Hincke, M., Fibrin: A versatile scaffold for tissue engineering applications. *Tissue Eng. Part B Rev.* **2008,** *14* (2), 199-215.
9. Dvir, T.; Timko, B. P.; Kohane, D. S.; Langer, R., Nanotechnological strategies for engineering complex tissues. *Nat. Nanotechnol.* **2011,** *6* (1), 13-22.
10. Desai, T. A.; Tang, Q., Islet encapsulation therapy — racing towards the finish line? *Nat. Rev. Endocrinol.* **2018,** *14* (11), 630-632.
11. Bianconi, E.; Piovesan, A.; Facchin, F.; Beraudi, A.; Casadei, R.; Frabetti, F.; Vitale, L.; Pelleri, M. C.; Tassani, S.; Piva, F.; Perez-Amodio, S.; Strippoli, P.; Canaider, S., An estimation of the number of cells in the human body. *Ann. Hum. Biol.* **2013,** *40* (6), 463-471.
12. Schwarz, U. S.; Bischofs, I. B., Physical determinants of cell organization in soft media. *Med. Eng. Phys.* **2005,** *27* (9), 763-772.
13. Berdasco, M.; Esteller, M., DNA methylation in stem cell renewal and multipotency. *Stem Cell Res. Ther.* **2011,** *2* (5), 42.
14. Ilic, D.; Polak, J. M., Stem cells in regenerative medicine: Introduction. *Br. Med. Bull.* **2011,** *98* (1), 117-126.
15. Alison, M. R.; Poulsom, R.; Forbes, S.; Wright, N. A., An introduction to stem cells. *J. Pathol.* **2002,** *197* (4), 419-423.
16. Appasani, K.; Appasani, R. K., Introduction to Stem Cells and Regenerative Medicine. In *Stem Cells & Regenerative Medicine: From Molecular Embryology to Tissue Engineering*, Appasani, K.; Appasani, R. K., Eds. Humana Press: Totowa, NJ, 2011; pp 3-18.
17. Yalvac, M. E.; Ramazanoglu, M.; Rizvanov, A. A.; Sahin, F.; Bayrak, O. F.; Salli, U.; Palotás, A.; Kose, G. T., Isolation and characterization of stem cells derived from human third molar tooth germs of young adults: Implications in neo-vascularization, osteo-, adipo-and neurogenesis. *Pharmacogenomics J.* **2010,** *10* (2), 105-113.
18. Dominici, M.; Le Blanc, K.; Mueller, I.; Slaper-Cortenbach, I.; Marini, F. C.; Krause, D. S.; Deans, R. J.; Keating, A.; Prockop, D. J.; Horwitz, E. M.,

Minimal criteria for defining multipotent mesenchymal stromal cells. The International Society for Cellular Therapy position statement. *Cytotherapy* **2006,** *8* (4), 315-317.
19. Izquierdo-Barba, I.; Santos-Ruiz, L.; Becerra, J.; Feito, M. J.; Fernández-Villa, D.; Serrano, M. C.; Díaz-Güemes, I.; Fernández-Tomé, B.; Enciso, S.; Sánchez-Margallo, F. M.; Monopoli, D.; Afonso, H.; Portolés, M. T.; Arcos, D.; Vallet-Regí, M., Synergistic effect of Si-hydroxyapatite coating and VEGF adsorption on Ti6Al4V-ELI scaffolds for bone regeneration in an osteoporotic bone environment. *Acta Biomater.* **2019,** *83*, 456-466.
20. Dai, R.; Wang, Z.; Samanipour, R.; Koo, K. I.; Kim, K., Adipose-Derived Stem Cells for Tissue Engineering and Regenerative Medicine Applications. *Stem Cells Intl.* **2016,** *2016*, 6737345.
21. O'Halloran, N.; Courtney, D.; Kerin, M. J.; Lowery, A. J., Adipose-Derived Stem Cells in Novel Approaches to Breast Reconstruction: Their Suitability for Tissue Engineering and Oncological Safety. *Breast Cancer Basic Clin. Res.* **2017,** *11*, 1178223417726777.
22. Okano, H.; Nakamura, M.; Yoshida, K.; Okada, Y.; Tsuji, O.; Nori, S.; Ikeda, E.; Yamanaka, S.; Miura, K., Steps toward safe cell therapy using induced pluripotent stem cells. *Circ. Res.* **2013,** *112* (3), 523-533.
23. Haridhasapavalan, K. K.; Borgohain, M. P.; Dey, C.; Saha, B.; Narayan, G.; Kumar, S.; Thummer, R. P., An insight into non-integrative gene delivery approaches to generate transgene-free induced pluripotent stem cells. *Gene* **2019,** *686*, 146-159.
24. Bianco, J.; De Berdt, P.; Deumens, R.; Des Rieux, A., Taking a bite out of spinal cord injury: Do dental stem cells have the teeth for it? *Cell. Mol. Life Sci.* **2016,** *73* (7), 1413-1437.
25. Egusa, H.; Sonoyama, W.; Nishimura, M.; Atsuta, I.; Akiyama, K., Stem cells in dentistry - Part I: Stem cell sources. *J. Prosthodontic Res.* **2012,** *56* (3), 151-165.
26. Lymperi, S.; Ligoudistianou, C.; Taraslia, V.; Kontakiotis, E.; Anastasiadou, E., Dental stem cells and their applications in dental tissue engineering. *Open Dent. J.* **2013,** *7* (1), 76-81.
27. Estrela, C.; de Alencar, A. H. G.; Kitten, G. T.; Vencio, E. F.; Gava, E., Mesenchymal stem cells in the dental tissues: Perspectives for tissue regeneration. *Braz. Dent. J.* **2011,** *22* (2), 91-98.
28. Wang, X.; Sha, X. J.; Li, G. H.; Yang, F. S.; Ji, K.; Wen, L. Y.; Liu, S. Y.; Chen, L.; Ding, Y.; Xuan, K., Comparative characterization of stem cells from human exfoliated deciduous teeth and dental pulp stem cells. *Arch. Oral Biol.* **2012,** *57* (9), 1231-1240.
29. Ikeda, E.; Yagi, K.; Kojima, M.; Yagyuu, T.; Ohshima, A.; Sobajima, S.; Tadokoro, M.; Katsube, Y.; Isoda, K.; Kondoh, M.; Kawase, M.; Go, M. J.; Adachi, H.; Yokota, Y.; Kirita, T.; Ohgushi, H., Multipotent cells from the

human third molar: Feasibility of cell-based therapy for liver disease. *Differentiation* **2008,** *76* (5), 495-505.
30. Sharpe, P. T., Dental mesenchymal stem cells. *Development* **2016,** *143* (13), 2273-2280.
31. Sonoyama, W.; Liu, Y.; Yamaza, T.; Tuan, R. S.; Wang, S.; Shi, S.; Huang, G. T. J., Characterization of the Apical Papilla and Its Residing Stem Cells from Human Immature Permanent Teeth: A Pilot Study. *J. Endod.* **2008,** *34* (2), 166-171.
32. Yu, S.; Zhao, Y.; Ma, Y.; Ge, L., Profiling the Secretome of Human Stem Cells from Dental Apical Papilla. *Stem Cells Dev.* **2016,** *25* (6), 499-508.
33. Ruparel, N. B.; de Almeida, J. F.; Henry, M. A.; Diogenes, A., Characterization of a stem cell of apical papilla cell line: effect of passage on cellular phenotype. *J. Endod.* **2013,** *39* (3), 357-363.
34. Sunil, P. M.; Manikandan, R.; Muthumurugan; Yoithapprabhunath, T. R.; Sivakumar, M., Harvesting dental stem cells - Overview. *J. Pharm. Bioallied Sci.* **2015,** *7* (Suppl 2), S384-S386.
35. Hristova, K., Interactions between membrane receptors in cellular membranes. *Biochim. Biophys. Acta Biomembr.* **2017,** *1859* (9), 1397.
36. Harbers, G. M.; Grainger, D. W., Cell-Material Interactions: Fundamental Design Issues for Tissue Engineering and Clinical Considerations. In *An Introduction to Biomaterials*, Guelcher, S. A.; Hollinger, J. O., Eds. CRC Press: Boca Raton, 2006; pp 15-45.
37. Khang, G., Biomaterials and manufacturing methods for scaffold in regenerative medicine. In *Handbook of Intelligent Scaffolds for Tissue Engineering and Regenerative Medicine*, Pan Stanford Publishing Pte. Ltd.: 2012; pp 3-47.
38. Grzesik, W. J.; Robey, P. G., Bone matrix RGD glycoproteins: Immunolocalization and interaction with human primary osteoblastic bone cells *in vitro*. *J. Bone Miner. Res.* **1994,** *9* (4), 487-496.
39. Onak, G.; Yurtseven, B.; Gökmen, O.; Karaman, O. In *Comparison the Effect of RGD Peptide Conjugation on Titanium Discs with Different Methods on Cell Adhesion and Proliferation*, 2018 Medical Technologies National Congress (TIPTEKNO), 8-10 Nov. 2018; 2018; pp 1-3.
40. Alberts, B.; Johnson, A.; Lewis, J.; Raff, M.; Roberts, K.; Walter, P.; Wilson, J.; Hunt, T., *Molecular Biology of The Cell. Fifth edition*. Garland Science: New York, 2008.
41. Giliberti, D. C.; White, K. K.; Dee, K. C., Control of Cell-Biomaterial Interactions. In *Polymeric Biomaterials, Revised and Expanded*, Dumitriu, S., Ed. Marcel Dekker, Inc.: New York, Basel, 2002; pp 361-375.
42. Giancotti, F. G.; Ruoslahti, E., Integrin signaling. *Science* **1999,** *285* (5430), 1028-1032.

43. Holle, A. W.; Engler, A. J., More than a feeling: Discovering, understanding, and influencing mechanosensing pathways. *Curr. Opin. Biotechnol.* **2011,** *22* (5), 648-654.
44. Hoffman, B. D.; Grashoff, C.; Schwartz, M. A., Dynamic molecular processes mediate cellular mechanotransduction. *Nature* **2011,** *475* (7356), 316-323.
45. Cameron, A. R.; Frith, J. E.; Cooper-White, J. J., The influence of substrate creep on mesenchymal stem cell behaviour and phenotype. *Biomaterials* **2011,** *32* (26), 5979-5993.
46. Kobayashi, T.; Sokabe, M., Sensing substrate rigidity by mechanosensitive ion channels with stress fibers and focal adhesions. *Curr. Opin. Cell Biol.* **2010,** *22* (5), 669-676.
47. Wheelton, A.; Mace, J.; Khan, W. S.; Anand, S., Biomaterials and fabrication to optimise scaffold properties for musculoskeletal tissue engineering. *Curr. Stem Cell Res. Ther.* **2016,** *11* (7), 578-584.
48. Subramanian, A.; Krishnan, U. M.; Sethuraman, S., Development of biomaterial scaffold for nerve tissue engineering: Biomaterial mediated neural regeneration. *J. Biomed. Sci.* **2009,** *16*, 108.
49. Zadpoor, A. A., Bone tissue regeneration: The role of scaffold geometry. *Biomater. Sci.* **2015,** *3* (2), 231-245.
50. Cox, T. R.; Erler, J. T., Remodeling and homeostasis of the extracellular matrix: Implications for fibrotic diseases and cancer. *DNM Dis. Models Mech.* **2011,** *4* (2), 165-178.
51. Malladi, L.; Mahapatro, A.; Gomes, A. S., Fabrication of magnesium-based metallic scaffolds for bone tissue engineering. *Mater. Technol.* **2018,** *33* (2), 173-182.
52. Wang, M., Materials selection and scaffold fabrication for tissue engineering in orthopaedics. In *Advanced Bioimaging Technologies in Assessment of the Quality of Bone and Scaffold Materials: Techniques and Applications*, Springer Berlin Heidelberg: 2007; pp 259-288.
53. Zhang, H.; Zhou, L.; Zhang, W., Control of scaffold degradation in tissue engineering: A review. *Tissue Eng. Part B Rev.* **2014,** *20* (5), 492-502.
54. Samami, H., Computer modeling of the degradation behavior of polyester-based tissue engineering scaffolds. In *Characterisation and Design of Tissue Scaffolds*, Elsevier Inc.: 2015; pp 45-74.
55. Wu, L.; Ding, J., Effects of porosity and pore size on *in vitro* degradation of three-dimensional porous poly(D,L-lactide-co-glycolide) scaffolds for tissue engineering. *J. Biomed. Mater. Res. A* **2005,** *75A* (4), 767-777.
56. Gaut, C.; Sugaya, K., Critical review on the physical and mechanical factors involved in tissue engineering of cartilage. *Regen. Med.* **2015,** *10* (5), 665-679.

57. Thavornyutikarn, B.; Chantarapanich, N.; Sitthiseripratip, K.; Thouas, G. A.; Chen, Q., Bone tissue engineering scaffolding: computer-aided scaffolding techniques. *Prog. Biomater.* **2014,** *3* (2), 61-102.
58. Levengood, S. K. L.; Zhang, M., Chitosan-based scaffolds for bone tissue engineering. *J. Mater. Chem. B* **2014,** *2* (21), 3161-3184.
59. Shi, C.; Yuan, Z.; Han, F.; Zhu, C.; Li, B., Polymeric biomaterials for bone regeneration. *Ann. Joint* **2016,** *1* (9), 27.
60. Gross, B. C.; Erkal, J. L.; Lockwood, S. Y.; Chen, C.; Spence, D. M., Evaluation of 3D printing and its potential impact on biotechnology and the chemical sciences. *Anal. Chem.* **2014,** *86* (7), 3240-3253.
61. Miar, S.; Shafiee, A.; Guda, T.; Narayan, R., Additive Manufacturing for Tissue Engineering. In *3D Printing and Biofabrication*, Ovsianikov, A.; Yoo, J.; Mironov, V., Eds. Springer International Publishing: Cham, 2018; pp 3-54.
62. O'Brien, C. M.; Holmes, B.; Faucett, S.; Zhang, L. G., Three-dimensional printing of nanomaterial scaffolds for complex tissue regeneration. *Tissue Eng. Part B Rev.* **2015,** *21* (1), 103-114.
63. Lee, J. Y.; Choi, B.; Wu, B.; Lee, M., Customized biomimetic scaffolds created by indirect three-dimensional printing for tissue engineering. *Biofabrication* **2013,** *5* (4), 045003.
64. Billiet, T.; Vandenhaute, M.; Schelfhout, J.; Van Vlierberghe, S.; Dubruel, P., A review of trends and limitations in hydrogel-rapid prototyping for tissue engineering. *Biomaterials* **2012,** *33* (26), 6020-6041.
65. Obata, K.; El-Tamer, A.; Koch, L.; Hinze, U.; Chichkov, B. N., High-aspect 3D two-photon polymerization structuring with widened objective working range (WOW-2PP). *Light: Sci. Appl.* **2013,** *2*, e116.
66. Singh, R.; Singh, S.; Hashmi, M. S. J., Implant Materials and Their Processing Technologies. In *Reference Module in Materials Science and Materials Engineering*, Elsevier: 2016.
67. Zhu, C.; Liu, T.; Qian, F.; Chen, W.; Chandrasekaran, S.; Yao, B.; Song, Y.; Duoss, E. B.; Kuntz, J. D.; Spadaccini, C. M.; Worsley, M. A.; Li, Y., 3D printed functional nanomaterials for electrochemical energy storage. *Nano Today* **2017,** *15*, 107-120.
68. Moritz, T.; Maleksaeedi, S., 4 - Additive manufacturing of ceramic components. In *Additive Manufacturing*, Zhang, J.; Jung, Y.-G., Eds. Butterworth-Heinemann: 2018; pp 105-161.
69. Gurr, M.; Mülhaupt, R., Rapid Prototyping. In *Polymer Science: A Comprehensive Reference, 10 Volume Set*, Elsevier: 2012; Vol. 8, pp 77-99.
70. Alizadeh-Osgouei, M.; Li, Y.; Wen, C., A comprehensive review of biodegradable synthetic polymer-ceramic composites and their manufacture for biomedical applications. *Bioact. Mater.* **2019,** *4* (1), 22-36.
71. Wang, G.; Shen, L.; Zhao, J.; Liang, H.; Xie, D.; Tian, Z.; Wang, C., Design and Compressive Behavior of Controllable Irregular Porous Scaffolds:

Based on Voronoi-Tessellation and for Additive Manufacturing. *ACS Biomater. Sci. Eng.* **2018,** *4* (2), 719-727.
72. Asri, R. I. M.; Harun, W. S. W.; Samykano, M.; Lah, N. A. C.; Ghani, S. A. C.; Tarlochan, F.; Raza, M. R., Corrosion and surface modification on biocompatible metals: A review. *Mater. Sci. Eng. C Mater. Biol. Appl.* **2017,** *77*, 1261-1274.
73. de Viteri, V. S.; Fuentes, E., Titanium and Titanium Alloys as Biomaterials. In *Tribology*, Gegner, J., Ed. IntechOpen: Rijeka, 2013; pp 155-181.
74. Thrivikraman, G.; Athirasala, A.; Twohig, C.; Boda, S. K.; Bertassoni, L. E., Biomaterials for Craniofacial Bone Regeneration. *Dent. Clin. N. Am.* **2017,** *61* (4), 835-856.
75. Germain, L.; De Berdt, P.; Vanacker, J.; Leprince, J.; Diogenes, A.; Jacobs, D.; Vandermeulen, G.; Bouzin, C.; Préat, V.; Dupont-Gillain, C.; Des Rieux, A., Fibrin hydrogels to deliver dental stem cells of the apical papilla for regenerative medicine. *Regen. Med.* **2015,** *10* (2), 153-167.
76. Mauquoy, S.; Dupont-Gillain, C., Combination of collagen and fibronectin to design biomimetic interfaces: Do these proteins form layer-by-layer assemblies? *Colloids Surf. B Biointerfaces* **2016,** *147*, 54-64.
77. Viswanath, A.; Vanacker, J.; Germain, L.; Leprince, J. G.; Diogenes, A.; Shakesheff, K. M.; White, L. J.; des Rieux, A., Extracellular matrix-derived hydrogels for dental stem cell delivery. *J. Biomed. Mater. Res. Part A* **2017,** *105* (1), 319-328.
78. Silva, J. M.; Videira, M.; Gaspar, R.; Préat, V.; Florindo, H. F., Immune system targeting by biodegradable nanoparticles for cancer vaccines. *J. Control. Release* **2013,** *168* (2), 179-199.
79. Zhang, X.; Peng, X.; Zhang, S. W., 7 - Synthetic biodegradable medical polymers: Polymer blends. In *Science and Principles of Biodegradable and Bioresorbable Medical Polymers*, Zhang, X., Ed. Woodhead Publishing: 2017; pp 217-254.
80. Gritsch, L.; Conoscenti, G.; La Carrubba, V.; Nooeaid, P.; Boccaccini, A. R., Polylactide-based materials science strategies to improve tissue-material interface without the use of growth factors or other biological molecules. *Mater. Sci. Eng. C Mater. Biol. Appl.* **2019,** *94*, 1083-1101.
81. Ulery, B. D.; Nair, L. S.; Laurencin, C. T., Biomedical applications of biodegradable polymers. *J. Polym. Sci. B Polym. Phys.* **2011,** *49* (12), 832-864.
82. Ghalia, M. A.; Dahman, Y., Biodegradable poly(lactic acid)-based scaffolds: synthesis and biomedical applications. *J. Polym. Res.* **2017,** *24* (5), 74.
83. Luo, Y.; Dolder, C. K.; Walker, J. M.; Mishra, R.; Dean, D.; Becker, M. L., Synthesis and Biological Evaluation of Well-Defined Poly(propylene

fumarate) Oligomers and Their Use in 3D Printed Scaffolds. *Biomacromolecules* **2016,** *17* (2), 690-697.
84. Lee, H.; Ahn, S.; Bonassar, L. J.; Kim, G., Cell(MC3T3-E1)-printed poly(ε-caprolactone)/alginate hybrid scaffolds for tissue regeneration. *Macromol. Rapid. Comm.* **2013,** *34* (2), 142-149.
85. Criscenti, G.; De Maria, C.; Vozzi, G.; Moroni, L., Characterization of Additive Manufactured Scaffolds. In *3D Printing and Biofabrication*, Ovsianikov, A.; Yoo, J.; Mironov, V., Eds. Springer International Publishing: Cham, 2018; pp 55-78.
86. Hutmacher, D.; Woodfield, T.; Dalton, P.; Lewis, J., Chapter 14 - Scaffold design and fabrication. In *Tissue Engineering*, Blitterswijk, C. v.; Thomsen, P.; Lindahl, A.; Hubbell, J.; Williams, D. F.; Cancedda, R.; Bruijn, J. D. d.; Sohier, J., Eds. Academic Press: Burlington, 2008; pp 403-454.
87. Stevens, M. M.; George, J. H., Exploring and engineering the cell surface interface. *Science* **2005,** *310* (5751), 1135-1138.
88. Zein, I.; Hutmacher, D. W.; Tan, K. C.; Teoh, S. H., Fused deposition modeling of novel scaffold architectures for tissue engineering applications. *Biomaterials* **2002,** *23* (4), 1169-1185.
89. Trachtenberg, J. E.; Mountziaris, P. M.; Miller, J. S.; Wettergreen, M.; Kasper, F. K.; Mikos, A. G., Open-source three-dimensional printing of biodegradable polymer scaffolds for tissue engineering. *J. Biomed. Mater. Res. A* **2014,** *102* (12), 4326-4335.
90. Temple, J. P.; Hutton, D. L.; Hung, B. P.; Huri, P. Y.; Cook, C. A.; Kondragunta, R.; Jia, X.; Grayson, W. L., Engineering anatomically shaped vascularized bone grafts with hASCs and 3D-printed PCL scaffolds. *J. Biomed. Mater. Res. A* **2014,** *102* (12), 4317-4325.
91. Dong, L.; Wang, S.-J.; Zhao, X.-R.; Zhu, Y.-F.; Yu, J.-K., 3D-Printed Poly(ε-caprolactone) Scaffold Integrated with Cell-laden Chitosan Hydrogels for Bone Tissue Engineering. *Sci. Rep.* **2017,** *7* (1), 13412.
92. Melissinaki, V.; Gill, A. A.; Ortega, I.; Vamvakaki, M.; Ranella, A.; Haycock, J. W.; Fotakis, C.; Farsari, M.; Claeyssens, F., Direct laser writing of 3D scaffolds for neural tissue engineering applications. *Biofabrication* **2011,** *3* (4), 045005.
93. Seyednejad, H.; Gawlitta, D.; Kuiper, R. V.; de Bruin, A.; van Nostrum, C. F.; Vermonden, T.; Dhert, W. J. A.; Hennink, W. E., *In vivo* biocompatibility and biodegradation of 3D-printed porous scaffolds based on a hydroxyl-functionalized poly(ε-caprolactone). *Biomaterials* **2012,** *33* (17), 4309-4318.
94. Griffon, D. J.; Sedighi, M. R.; Schaeffer, D. V.; Eurell, J. A.; Johnson, A. L., Chitosan scaffolds: Interconnective pore size and cartilage engineering. *Acta Biomater.* **2006,** *2* (3), 313-320.

95. Karageorgiou, V.; Kaplan, D., Porosity of 3D biomaterial scaffolds and osteogenesis. *Biomaterials* **2005,** *26* (27), 5474-5491.
96. Forrestal, D. P.; Klein, T. J.; Woodruff, M. A., Challenges in engineering large customized bone constructs. *Biotechnol. Bioeng.* **2017,** *114* (6), 1129-1139.
97. Park, S.; Kim, G.; Jeon, Y. C.; Koh, Y.; Kim, W., 3D polycaprolactone scaffolds with controlled pore structure using a rapid prototyping system. *J. Mater. Sci. Mater. Med.* **2009,** *20* (1), 229-234.
98. Ribeiro, J. F. M.; Oliveira, S. M.; Alves, J. L.; Pedro, A. J.; Reis, R. L.; Fernandes, E. M.; Mano, J. F., Structural monitoring and modeling of the mechanical deformation of three-dimensional printed poly(ϵ-caprolactone) scaffolds. *Biofabrication* **2017,** *9* (2), 025015.
99. Buyuksungur, S.; Endogan Tanir, T.; Buyuksungur, A.; Bektas, E. I.; Torun Kose, G.; Yucel, D.; Beyzadeoglu, T.; Cetinkaya, E.; Yenigun, C.; Tonuk, E.; Hasirci, V.; Hasirci, N., 3D printed poly(ε-caprolactone) scaffolds modified with hydroxyapatite and poly(propylene fumarate) and their effects on the healing of rabbit femur defects. *Biomater. Sci.* **2017,** *5* (10), 2144-2158.
100. Serra, T.; Planell, J. A.; Navarro, M., High-resolution PLA-based composite scaffolds via 3-D printing technology. *Acta Biomater.* **2013,** *9* (3), 5521-5530.
101. Korpela, J.; Kokkari, A.; Korhonen, H.; Malin, M.; Narhi, T.; Seppala, J., Biodegradable and bioactive porous scaffold structures prepared using fused deposition modeling. *J. Biomed. Mater. Res. B Appl. Biomater.* **2013,** *101* (4), 610-619.
102. Rajzer, I.; Kurowska, A.; Jabłoński, A.; Jatteau, S.; Śliwka, M.; Ziąbka, M.; Menaszek, E., Layered gelatin/PLLA scaffolds fabricated by electrospinning and 3D printing- for nasal cartilages and subchondral bone reconstruction. *Mater. Des.* **2018,** *155*, 297-306.
103. Al-Ketan, O.; Abu Al-Rub, R. K.; Rowshan, R., The effect of architecture on the mechanical properties of cellular structures based on the IWP minimal surface. *J. Mater. Res.* **2018,** *33* (3), 343-359.
104. Challis, V. J.; Xu, X.; Zhang, L. C.; Roberts, A. P.; Grotowski, J. F.; Sercombe, T. B., High specific strength and stiffness structures produced using selective laser melting. *Mater. Des.* **2014,** *63*, 783-788.
105. Yánez, A.; Herrera, A.; Martel, O.; Monopoli, D.; Afonso, H., Compressive behaviour of gyroid lattice structures for human cancellous bone implant applications. *Mater. Sci. Eng. C Mater. Biol. Appl.* **2016,** *68*, 445-448.
106. Speirs, M.; Van Hooreweder, B.; Van Humbeeck, J.; Kruth, J. P., Fatigue behaviour of NiTi shape memory alloy scaffolds produced by SLM, a unit cell design comparison. *J. Mech. Behav. Biomed. Mater.* **2017,** *70*, 53-59.

107. Chanda, A.; Callaway, C., Tissue anisotropy modeling using soft composite materials. *Appl. Bionics Biomech.* **2018,** *2018*, 4838157.
108. Cullinane, D. M.; Salisbury, K. T., Biomechanics. In *Bone Tissue Engineering*, CRC Press: 2004; pp 245-274.
109. Autodesk Evaluation 3: Surface Curvature. https://knowledge.autodesk.com/support/alias-products/getting-started/caas/CloudHelp/cloudhelp/2019/ENU/Alias-Tutorials/files/GUID-E44AB3A3-18DF-42F4-B4D4-870EFB42534A-htm.html (accessed March 3, 2019).
110. Yan, C.; Hao, L.; Hussein, A.; Raymont, D., Evaluations of cellular lattice structures manufactured using selective laser melting. *Int. J. Mach. Tool. Manu.* **2012,** *62*, 32-38.
111. Weißmann, V.; Bader, R.; Hansmann, H.; Laufer, N., Influence of the structural orientation on the mechanical properties of selective laser melted Ti6Al4V open-porous scaffolds. *Mater. Des.* **2016,** *95*, 188-197.
112. Wieding, J.; Jonitz, A.; Bader, R., The effect of structural design on mechanical properties and cellular response of additive manufactured titanium scaffolds. *Materials* **2012,** *5* (8), 1336-1347.
113. Heinl, P.; Müller, L.; Körner, C.; Singer, R. F.; Müller, F. A., Cellular Ti-6Al-4V structures with interconnected macro porosity for bone implants fabricated by selective electron beam melting. *Acta Biomater.* **2008,** *4* (5), 1536-1544.
114. Wang, Q.; Ren, L.; Li, X.; Zhang, S.; Sercombe, T. B.; Yang, K., Antimicrobial Cu-bearing stainless steel scaffolds. *Mater. Sci. Eng. C Mater. Biol. Appl.* **2016,** *68*, 519-522.
115. Melchels, F. P. W.; Bertoldi, K.; Gabbrielli, R.; Velders, A. H.; Feijen, J.; Grijpma, D. W., Mathematically defined tissue engineering scaffold architectures prepared by stereolithography. *Biomaterials* **2010,** *31* (27), 6909-6916.
116. Walker, J. M.; Bodamer, E.; Krebs, O.; Luo, Y.; Kleinfehn, A.; Becker, M. L.; Dean, D., Effect of Chemical and Physical Properties on the *In Vitro* Degradation of 3D Printed High Resolution Poly(propylene fumarate) Scaffolds. *Biomacromolecules* **2017,** *18* (4), 1419-1425.
117. Jung, J. W.; Park, J. H.; Hong, J. M.; Kang, H.-W.; Cho, D.-W., Octahedron pore architecture to enhance flexibility of nasal implant-shaped scaffold for rhinoplasty. *Int. J. Precis. Eng. Man.* **2014,** *15* (12), 2611-2616.
118. Pieuchot, L.; Marteau, J.; Guignandon, A.; Dos Santos, T.; Brigaud, I.; Chauvy, P. F.; Cloatre, T.; Ponche, A.; Petithory, T.; Rougerie, P.; Vassaux, M.; Milan, J. L.; Tusamda Wakhloo, N.; Spangenberg, A.; Bigerelle, M.; Anselme, K., Curvotaxis directs cell migration through cell-scale curvature landscapes. *Nat. Commun.* **2018,** *9* (1), 3995.

119. Xi, W.; Saw, T. B.; Delacour, D.; Lim, C. T.; Ladoux, B., Material approaches to active tissue mechanics. *Nat. Rev. Mater.* **2019,** *4* (1), 23-44.
120. Guyot, Y.; Papantoniou, I.; Luyten, F. P.; Geris, L., Coupling curvature-dependent and shear stress-stimulated neotissue growth in dynamic bioreactor cultures: a 3D computational model of a complete scaffold. *Biomech. Model. Mechan.* **2016,** *15* (1), 169-180.
121. Ravi, P.; Shiakolas, P. S.; Welch, T. R., Poly-l-lactic acid: Pellets to fiber to fused filament fabricated scaffolds, and scaffold weight loss study. *Addit. Manuf.* **2017,** *16*, 167-176.
122. Barba, A.; Diez-Escudero, A.; Maazouz, Y.; Rappe, K.; Espanol, M.; Montufar, E. B.; Bonany, M.; Sadowska, J. M.; Guillem-Marti, J.; Öhman-Mägi, C.; Persson, C.; Manzanares, M.-C.; Franch, J.; Ginebra, M.-P., Osteoinduction by Foamed and 3D-Printed Calcium Phosphate Scaffolds: Effect of Nanostructure and Pore Architecture. *ACS Appl. Mater. Inter.* **2017,** *9* (48), 41722-41736.
123. Kim, J. A.; Yun, H.-s.; Choi, Y.-A.; Kim, J.-E.; Choi, S.-Y.; Kwon, T.-G.; Kim, Y. K.; Kwon, T.-Y.; Bae, M. A.; Kim, N. J.; Bae, Y. C.; Shin, H.-I.; Park, E. K., Magnesium phosphate ceramics incorporating a novel indene compound promote osteoblast differentiation *in vitro* and bone regeneration *in vivo*. *Biomaterials* **2018,** *157*, 51-61.
124. Vander Straeten, A.; Bratek-Skicki, A.; Germain, L.; D'Haese, C.; Eloy, P.; Fustin, C. A.; Dupont-Gillain, C., Protein-polyelectrolyte complexes to improve the biological activity of proteins in layer-by-layer assemblies. *Nanoscale* **2017,** *9* (44), 17186-17192.
125. Vander Straeten, A.; Bratek-Skicki, A.; Jonas, A. M.; Fustin, C. A.; Dupont-Gillain, C., Integrating proteins in layer-by-layer assemblies independently of their electrical charge. *ACS Nano* **2018,** *12* (8), 8372-8381.
126. Lee, J.; Cuddihy, M. J.; Kotov, N. A., Three-dimensional cell culture matrices: State of the art. *Tissue Eng. Part B Rev.* **2008,** *14* (1), 61-86.
127. Zuyderhoff, E. M.; Dupont-Gillain, C. C., Nano-organized collagen layers obtained by adsorption on phase-separated polymer thin films. *Langmuir* **2012,** *28* (4), 2007-2014.
128. Zuyderhoff, E. Heterogeneous surfaces with organized collagen layers for the control of cell behavior. PhD thesis, UCLouvain, Louvain-la-Neuve, Belgium, 2012.
129. Lin, M.; Wang, H.; Ruan, C.; Xing, J.; Wang, J.; Li, Y.; Wang, Y.; Luo, Y., Adsorption Force of Fibronectin on Various Surface Chemistries and Its Vital Role in Osteoblast Adhesion. *Biomacromolecules* **2015,** *16* (3), 973-984.
130. Spatz, J. P., Cell–Nanostructure Interactions. In *Nanobiotechnology*, Niemeyer, C. M.; Mirkin, C. A., Eds. 2005; pp 53-65.

131. Chen, C. S.; Mrksich, M.; Huang, S.; Whitesides, G. M.; Ingber, D. E., Geometric control of cell life and death. *Science* **1997,** *276* (5317), 1425-1428.
132. Kearns, V. R.; McMurray, R. J.; Dalby, M. J., 7 - Biomaterial surface topography to control cellular response: technologies, cell behaviour and biomedical applications. In *Surface Modification of Biomaterials*, Williams, R., Ed. Woodhead Publishing: 2011; pp 169-201.
133. Sammons, R. L., 15 - Modifying biomaterial surfaces to optimise interactions with bone. In *Surface Modification of Biomaterials*, Williams, R., Ed. Woodhead Publishing: 2011; pp 365-400.
134. Lossdörfer, S.; Schwartz, Z.; Wang, L.; Lohmann, C. H.; Turner, J. D.; Wieland, M.; Cochran, D. L.; Boyan, B. D., Microrough implant surface topographies increase osteogenesis by reducing osteoclast formation and activity. *J. Biomed. Mater. Res. Part A* **2004,** *70* (3), 361-369.
135. Lin, L.; Wang, H.; Ni, M.; Rui, Y.; Cheng, T.-Y.; Cheng, C.-K.; Pan, X.; Li, G.; Lin, C., Enhanced osteointegration of medical titanium implant with surface modifications in micro/nanoscale structures. *J. Orthop. Transl.* **2014,** *2* (1), 35-42.
136. Charest, J. L.; García, A. J.; King, W. P., Myoblast alignment and differentiation on cell culture substrates with microscale topography and model chemistries. *Biomaterials* **2007,** *28* (13), 2202-2210.
137. Dalby, M. J.; Riehle, M. O.; Yarwood, S. J.; Wilkinson, C. D. W.; Curtis, A. S. G., Nucleus alignment and cell signaling in fibroblasts: response to a micro-grooved topography. *Exp. Cell. Res.* **2003,** *284* (2), 274-282.
138. Lee, M. R.; Kwon, K. W.; Jung, H.; Kim, H. N.; Suh, K. Y.; Kim, K.; Kim, K. S., Direct differentiation of human embryonic stem cells into selective neurons on nanoscale ridge/groove pattern arrays. *Biomaterials* **2010,** *31* (15), 4360-4366.
139. Engler, A. J.; Sen, S.; Sweeney, H. L.; Discher, D. E., Matrix Elasticity Directs Stem Cell Lineage Specification. *Cell* **2006,** *126* (4), 677-689.
140. Almodóvar, J.; Crouzier, T.; Selimović, S.; Boudou, T.; Khademhosseini, A.; Picart, C., Gradients of physical and biochemical cues on polyelectrolyte multilayer films generated via microfluidics. *Lab Chip Miniaturisation Chem. Biol.* **2013,** *13* (8), 1562-1570.
141. Degand, S. Design of surfaces with mechanical nanoheterogeneities for a better control of cell-material interactions. PhD thesis, UCLouvain, Louvain-la-Neuve, Belgium, 2013.
142. Charrier, E. E.; Pogoda, K.; Wells, R. G.; Janmey, P. A., Control of cell morphology and differentiation by substrates with independently tunable elasticity and viscous dissipation. *Nat. Commun.* **2018,** *9* (1), 449.
143. Trappmann, B.; Gautrot, J. E.; Connelly, J. T.; Strange, D. G.; Li, Y.; Oyen, M. L.; Cohen Stuart, M. A.; Boehm, H.; Li, B.; Vogel, V.; Spatz, J. P.;

Watt, F. M.; Huck, W. T., Extracellular-matrix tethering regulates stem-cell fate. *Nat. Mater.* **2012,** *11* (7), 642-649.
144. Darnell, M.; O'Neil, A.; Mao, A.; Gu, L.; Rubin, L. L.; Mooney, D. J., Material microenvironmental properties couple to induce distinct transcriptional programs in mammalian stem cells. *P. Natl. Acad. Sci. USA* **2018,** *115* (36), E8368-E8377.
145. Oliveira, S. M.; Reis, R. L.; Mano, J. F., Towards the design of 3D multiscale instructive tissue engineering constructs: Current approaches and trends. *Biotechnol. Adv.* **2015,** *33* (6), 842-855.

Part II : Aims of the thesis

Tissue engineering focuses on the production of patient-specific combinations of cells, scaffolds and signaling cues to allow tissue/organ replacement or healing. Recently, AM techniques were identified as suitable tools for patient-specific scaffold production. In this context, the present work has two distinct aims.

Depending on the implantation site, the requirements regarding scaffold mechanical properties may vary. Apart from the material used, the scaffold structure can also be adjusted to modify its mechanical properties. AM techniques have a high potential regarding the production of structures with a high degree of design freedom. However, the number of proposed scaffold designs as well as the diversity of mechanical properties arising from these designs are still relatively poor. **The first aim of this thesis is to produce degradable scaffolds displaying a defined geometry with added value for tissue engineering**. The gyroid, a complex geometry well-known by mathematicians, is printed with a porous fraction comparable to the one of strut-based scaffolds usually found in the literature. Due to its geometry, the printed gyroid scaffold is expected to present isotropic mechanical properties. This first part of the work will ultimately highlight the importance of geometry on the scaffold mechanical properties.

Cell-material interactions are determinant for the success of tissue repair, as they define how cells behave and, hence, determine cell fate. **The second aim of this thesis is to modify the surface mechanical properties of the macropores on which cells adhere in the scaffold, with a view to better control cell behavior**. The surface modification is performed by the deposition of a coating whose stiffness is controlled by the crosslinking degree. Indeed, cells are sensitive to the stiffness of their environment. Stiffness will influence cell behaviors such as proliferation, migration and differentiation. In this thesis, cell proliferation and osteogenic differentiation are studied. This second part of the work is more fundamental and explores a domain at the crossroad between traditional two-dimensional (2D) cell culture and three-dimensional (3D) cell culture inside hydrogels. For both kind of systems, the effect of mechanical properties on cell behavior was already investigated. Cell response as a function of mechanical properties varies depending on the 2D or 3D configuration of the system. Cell culture inside 3D macroporous structures could be considered as a third intermediate configuration. In macroporous structures, cells are anchored on a substrate as in traditional 2D culture systems but are evolving inside a 3D environment. The system developed in this thesis, *i.e.* a macroporous

scaffold with a range of different surface mechanical properties, will be used to unravel cell behavior and understand whether cells behave as on a traditional 2D culture substrate, as in 3D culture conditions, or in a completely different way. This scaffold is proposed for fundamental research and needs further modifications prior to considering its implantation.

Coating deposition on the scaffolds allows the effects of macroscopic and microscopic mechanical properties to be decoupled. Macroscopic mechanical properties are important for the resistance of the scaffold in the body, while microscopic ones give signals to cells and control their behavior. The same scaffold then ensures two different functions. Through the thesis, the complexity of surface modification of complex three-dimensional objects is moreover emphasized.

Part III : Strategy

Scaffolds were printed in poly(lactic acid) (PLA) using fused deposition modeling. PLA is a biocompatible and bioresorbable polymer already widely used in medicine . Once printed, a coating was applied at the surface of these complex structures. This coating allows a change in mechanical properties localized at the surface of the scaffold while keeping the mechanical properties constant at the scaffold level. A crosslinkable poly(dimethylsiloxane) (PDMS) was used for this coating. Variation of the ratio between the polymer itself and its curing agent allows a change in crosslinking density and, hence, a change in mechanical properties. Chemistry was shown to affect cell behavior. A change in crosslinking density ensures a same surface chemistry for different mechanical properties. Therefore, coating effects on cells are not attributed to a change in chemistry but only to a change in mechanical properties. Stem cells from the apical papilla (SCAP) were seeded in the prepared macroporous scaffolds. SCAP proliferation and osteodifferentiation were evaluated in scaffolds with surfaces presenting different mechanical properties. Figure 1 illustrates the different steps of the strategy of this work.

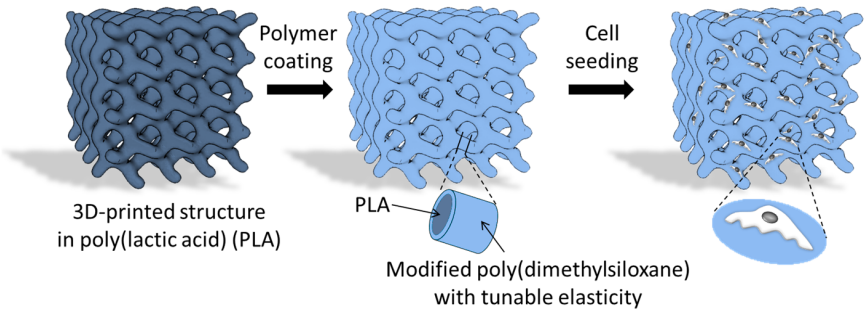


Figure 1: Strategy of the thesis represented in three steps. Printing of the scaffold in poly(lactic acid) using fused deposition modeling (left). Coating of scaffold surface using a crosslinkable poly(dimethylsiloxane) (middle). Cell seeding inside macropores of the structure (right).

1 Fused deposition modeling

Fused deposition modeling (FDM) is one of the most known AM techniques. The principle of FDM is based on the deposition of melted thermoplastic polymers to form the final object layer by layer. A filament of thermoplastic polymer is inserted into a printing head also named extruder. This printing head is made of (i) two rollers (or drive gears), (ii) a heated chamber (liquefier) and (iii) a nozzle. The rollers insert the thermoplastic filament inside the heated chamber. In the chamber, the polymer melts and is extruded through the nozzle. The extrusion is allowed by the insertion of the

unmolten polymer filament acting like a piston on molten polymer. The filament is moved back and forward by the rollers to control polymer deposition. Extruded polymer struts are deposited on a platform side-by-side according to a predefined pathway. The deposition of the molten polymer at the right place on the platform is allowed by the movement of the printing head in X and Y directions. Once the layer is completely printed, the platform moves down and a new layer is printed on top of the previous one. The layer-by-layer deposition process continues until the full 3D object is printed. Printing heads can be placed in parallel on the same printer to allow the deposition of more than one thermoplastic polymer.

3D models from many sources can be printed. 3D models can be designed using computer-aided design (CAD) softwares or obtained using various 3D scanning techniques. Therefore, computed tomography scans or magnetic resonance imaging scans routinely used for medical imaging can be used, which makes AM techniques particularly suitable for medical purposes. The 3D model is sliced by a slicing program (or "slicer") and converted into a pile of layers with given thicknesses. For each layer, the printing head pathway will be decided and saved. Decisions are made by the slicer depending on the user parameters. In addition to pathways, other instructions such as printing temperature, head speed and deposition flow rate are saved in the same file.

This technique was used in this work for its numerous advantages. As other AM techniques, FDM is particularly suited for the production of personalized and complex objects. Besides, medical grade polymers used in healthcare are often expensive owing to the high purity and controlled specifications required. AM techniques, and especially FDM techniques, add to the object only the needed material, which reduces wasted material compared to subtractive techniques. Specific advantages of FDM, compared to the other AM techniques, are its relative ease of use and the low cost linked to the machine as well as its use. Such advantages could be in favor of the incorporation of 3D printers in hospitals. Printers could be directly used by surgeons to drastically reduce the time and cost of production of an implant or a surgical tool. This low-cost technique would also be available to improve healthcare in developing countries. The large and growing panel of printable polymers as well as composite materials is also worth to mention.

In addition to the need of thermoplastic polymers with suitable viscoelasticities[1], the drawbacks of FDM mainly reside in its limited resolution. The horizontal resolution (X and Y axes) is mainly defined by the

nozzle diameter of the printer and the precision of the extruder movement in X and Y orientations. The most standard nozzle diameter for FDM printers is 0.4 mm. It implies that the deposited struts are 0.4 mm wide and this dimension will correspond to the smallest achievable feature. Layer height resolution (Z axis) is fixed by the distance between the nozzle and the platform (or the previous layer). The quantity of deposited polymer is adapted to fill the gap. Conventional layer height lies between 100 µm and 300 µm. Some printers claim better resolution up to 20 µm, though this resolution seems not achievable for any kind of polymer.

The printer used in this work was a Makerbot Replicator 2X. This printer possesses two extruders with 0.4 mm nozzles, which allows to print objects using two different polymers. The platform can be heated up to 130°C to increase polymer attachment on the platform and heads can be heated up to 280°C. During the course of the research (see Part V, chapter 5), the printer was upgraded to improve polymer cooling once deposited. A cooling fan as well as a fan duct (orienting the airflow on the deposited polymer) were fixed on the printer head.

For the sake of clarity of the next chapters, some printing features or parameters are presented in Figure 2 and are explained hereunder:

- As stated earlier, FDM relies on the deposition of layers one on top of the other. The extruded filament has to be deposited on a previously deposited layer since, otherwise, the fused filament would collapse after deposition. However, in 3D objects, some overhangs or bridges may be suspended in the void. **The support** is a polymer, printed at the same time as the structure, that will fill the void to ensure that each layer is deposited on a previous layer. The support can be printed in the same polymer as the object or in another polymer. After printing, the support can be mechanically removed or selectively dissolved if the support is printed using a soluble material. The slicer can automatically design the supporting structure according to various user parameters such as support density *i.e.* the density of struts deposited as support. The higher the density, the stronger the support will be. However, a stronger support is difficult to remove mechanically.
- **The raft** is a layer of polymer printed under the object and will ensure a suitable adhesion of the structure on the platform. The raft is used for object with a small footprint, which could detach during the

printing process, or for structures possessing too large contact surface with the platform, which could be difficult to detach after printing. Furthermore, the raft is useful for polymers susceptible to warping. Warping occurs when a polymer significantly shrinks during cooling, resulting in corner deformations and detachments. The raft ensures a better attachment to the platform and thereby helps maintaining the shape of the object.

- **Purge walls** are wall-shaped structures built around the object, especially when two extruders are used in parallel. Purge walls have a dual purpose. As they are built at the same time as the object, the first purpose is to scrape off the polymer leaking out of the nozzle that is not in use. It avoids unwanted deposition of this leaking material on the printed object. Besides, walls are used for polymer purge. Only one extruder can work at a time for printing. Then, for each layer, each extruder in turn has to wait for the other extruder to finish printing. Hence, the polymer stays in the liquefier and may start to burn. Before starting the deposition of a layer, each extruder content will be purged on the purge wall.
- The first features printed at the beginning of layer deposition are the boundaries of the object, called **shells**. Inside shell boundaries, **the infill** corresponds to the polymer printed inside the object as a filler. The thickness of the boundaries can be adjusted in terms of number of shells (*i.e.* number of struts used as boundaries of the layer). Infill density is adjusted in percentage (0% to 100%), from an empty object to a fully filled object. Different layer patterns can be used to fill the object.

Printing duration varies depending on the **volume of deposited polymer**, the **extrusion head speed** and the **extrusion head travel length** to fulfill the printing. Several parameters presented above will influence the volume of deposited polymer: the number of shells, the infill, the amount of support used (if any), the use of rafts and purge walls. The extrusion speed typically ranges between 1 and 100 mm/s and the total travel length to complete the printing strongly depends on the layer resolution. Indeed, a higher resolution means that more layers are required. For example, assuming a head speed of 90 mm/s, the printing time required for the “UCLouvain” model (14x2x0.8 cm^3) with the proposed parameters (Figure 2) will vary from 40 min to 2 h for a layer resolution of 0.3 mm to 0.1 mm (support, raft and purge walls

included), respectively. If we decrease the head speed to 10 mm/s, the 0.3mm-resolution printing will last around 5 h.

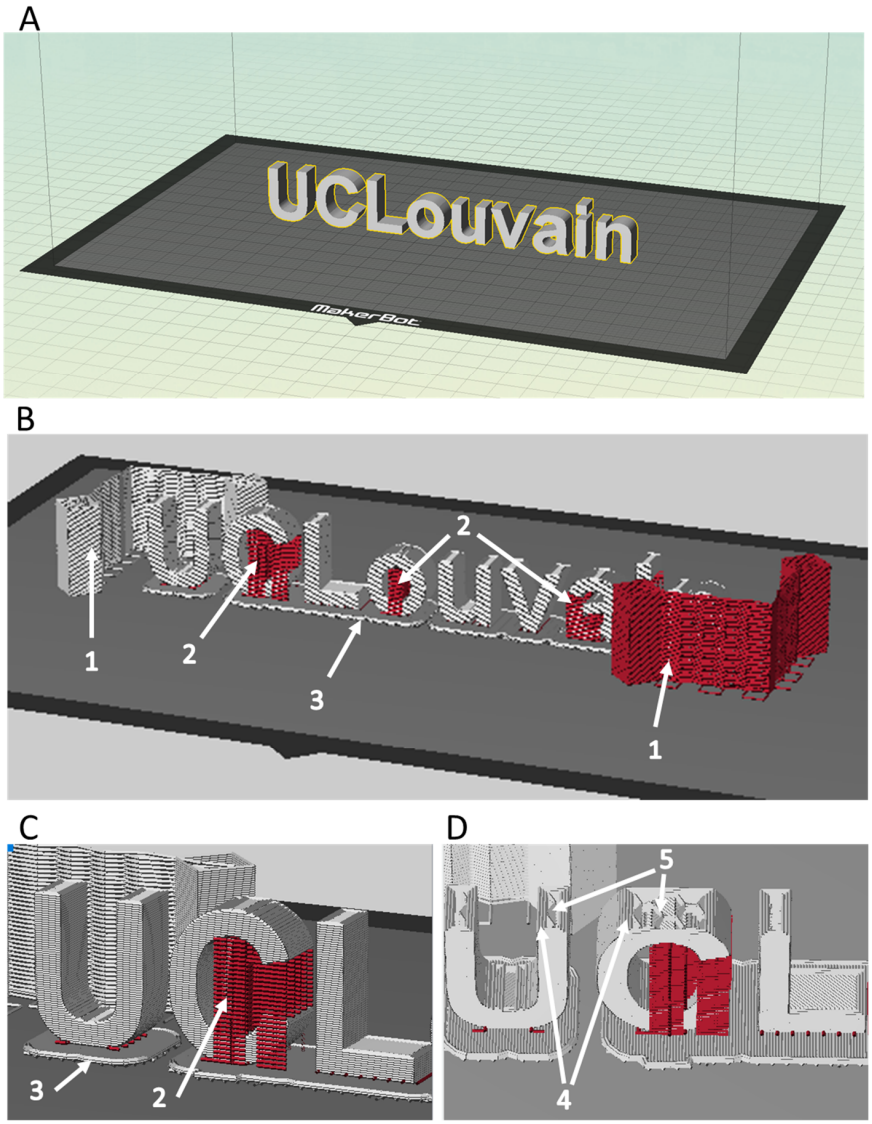


Figure 2: (A) CAD design of the word "UCLouvain" before slicing and (B, C and D) slicing previews of the object. White and red colors correspond to the polymer deposited by the first and the second extruder, respectively. 1. Purge walls are placed around the object to purge the extruders and scrape off the nozzles. 2. Supports are designed by the slicer to prevent the extruded polymer to collapse while deposited. 3. The raft is placed below the object to improve adhesion. 4. Shells are the boundaries of the object and are the first features printed at the beginning of layer deposition. 5. The infill fills the object, here with a chosen honeycomb design and an infill density of 25%.

2 Mesh designs proposed for the scaffold

FDM, as other AM techniques, offers much freedom for the design of a scaffold. However, in the literature, this advantage seems to be underexploited. Most researchers using FDM are printing scaffolds based on struts placed side by side, with a defined interspace, and then successively adding layers of similar struts oriented perpendicularly to the first layer of struts (Figure 3C).

In this work, the use of a more complex design, called gyroid (Figure 3B), is proposed. Its comparison with conventional strut-based scaffolds is carried out regarding mechanical properties and degradation. The gyroid model was shown with metals to have interesting mechanical properties (higher fatigue resistance and high specific stiffness-to-weight ratio while keeping an isotropic behavior).[2-4] Besides, concave curvatures were shown to have beneficial impacts on *in vitro* and *in vivo* cell development.[5] Furthermore, the gyroid design could be used to mimic trabecular bone (Figure 3A) owing to the strong similarity of their networks.[6]

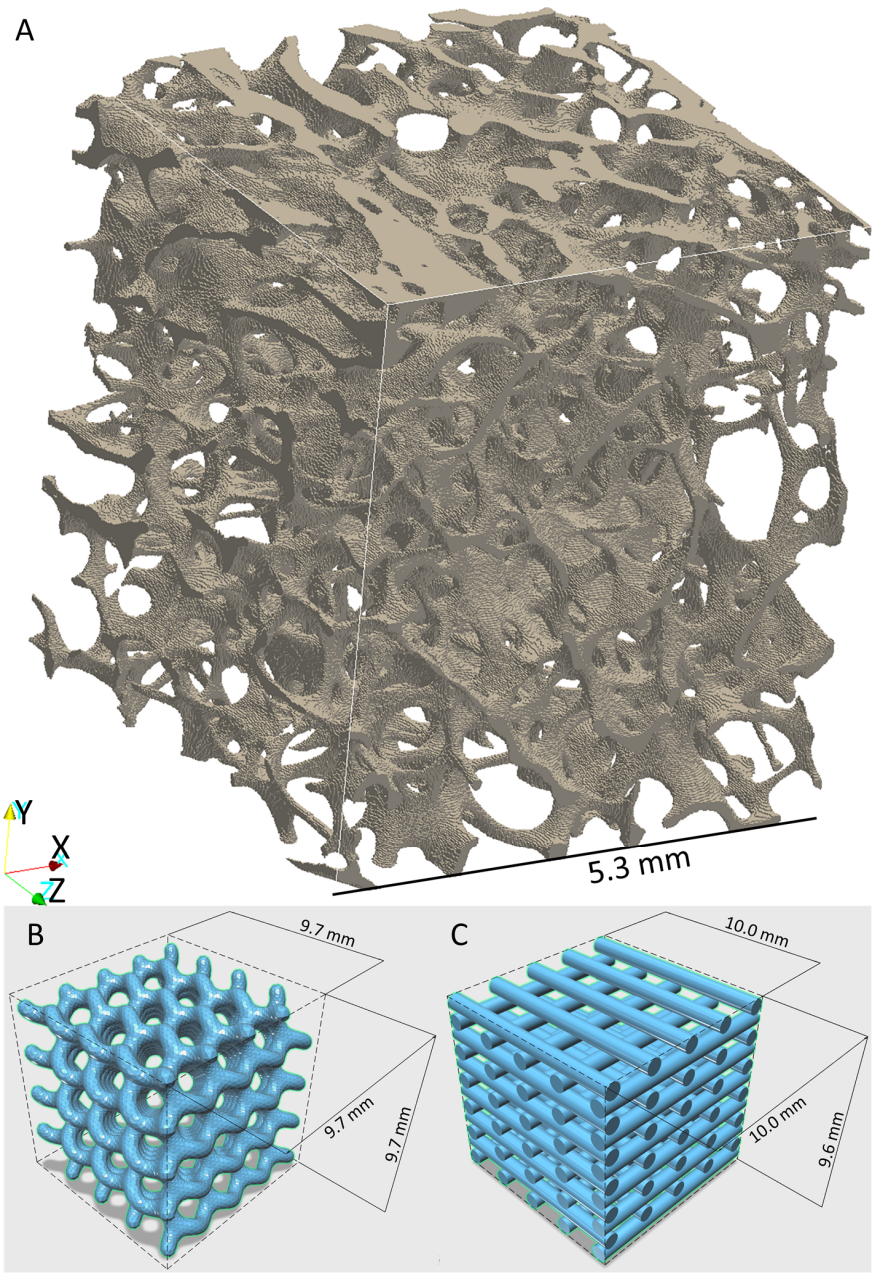


Figure 3: (A) Model based on the segmented µCT data of the trabecular bone from a human wrist[7], (B) gyroid 3D model (pore projection diameter of 0.85 mm) and (C) control structure (strut-based scaffold; pore size: 1.5 x 1.5 mm² (top view) and 0.8 x 1.5 mm² (side view)).

3 Poly(lactic acid) (PLA)

Poly(lactic acid) is a thermoplastic aliphatic polyester. It has attracted considerable attention as biomaterial owing to its biocompatibility, biodegradability and versatility. It has numerous advantages[8]:

- Several products made of PLA have since long been approved by the Food and Drug Administration for direct contact with biological fluids;
- PLA can be obtained from renewable sources at relatively low cost;
- PLA is easy to process by casting, foaming, extrusion and fiber spinning;
- Its production requires only a low energy consumption;
- PLA as well as its degradation products are non toxic.

Some drawbacks of PLA should also be mentioned:

- Its degradation rate is too slow for many applications,
- PLA is brittle,
- The hydrophobicity of this material makes the interactions with cells difficult, which potentially elicits an inflammatory response when implanted. Additionally, the acidic by-products of degradation may trigger an inflammation process.

Nevertheless, many strategies were developed to overcome these issues. Modification of the polymer or combination with other polymers increasing PLA hydrophilicity or acting as plasticizers allowed to tune the degradation rate and mechanical properties, respectively. Besides, bioactivity can be provided by other components using diverse strategies such as blending, fabrication or inclusion of (nano-)composites, surface bio-functionalization, and plasma treatment. Such strategies must be tailored depending on the targeted tissue and application.[8, 9] The polymer used in this work was a PLLA commercialized by NatureWorks LLC (USA) under the name of Ingeo 4043D.[10]

PLA degrades in the body by hydrolysis of ester linkages, and its product of degradation (lactic acid) is a physiological metabolite. Still, some concerns are raised regarding the acidic character of these degradation products, which limit the permitted implantable amount.[11] Even though PLA is relatively hydrophobic, water is able to enter into the bulk of this polymer. Once an ester linkage is cleaved, a carboxylic acid function is formed, which releases a proton and decreases the pH inside the polymer bulk. The

reduction of pH will further catalyze the cleavage of other ester bonds. The process is autocatalytic and a "bulk degradation" mechanism is observed (Figure 4). "Bulk degradation" has to be distinguished from "surface erosion", which occurs for more hydrophobic polymers such as polycaprolactone. In the latter case, water is not able to penetrate inside the polymer bulk and hydrolysis proceeds starting from the surface of the polymer.[12, 13] Mainly non-enzymatic degradations occur[11], though enzymes seem to participate to the degradation. It is still unclear if enzymes directly react with the polymer and increase its degradation rate or if they enhance the removal of degradation products.[8] Parameters influencing PLA degradation rate are, among others, molar mass, crystallinity, morphology of the sample, chain stereo-configuration, polymer purity and temperature.[8, 9, 11, 13] High molar mass, high crystallinity, high purity and stereochemically pure polymers will have a lower degradation rate.

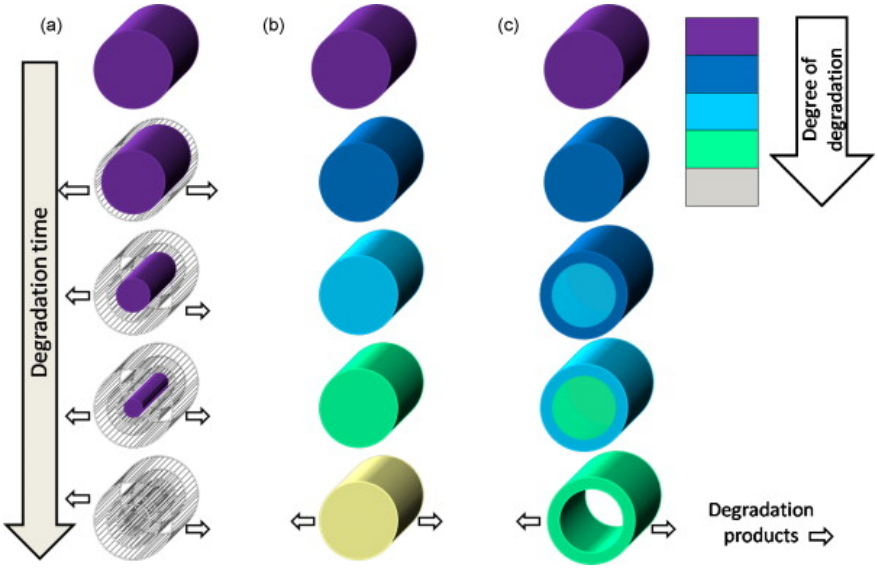


Figure 4: Degradation mechanisms of degradable polymers. (a) ***Surface erosion****: water is not able to diffuse inside the polymer. Degradation of the polymer starts from the surface. (b)* ***Bulk degradation****: water is able to diffuse inside the polymer and the degradation occurs uniformly throughout the polymer bulk. (c)* ***Bulk degradation with autocatalysis****: If degradation products catalyze the degradation, and if an equilibrium is not reached between bulk degradation and product diffusion outside the bulk, a higher degradation rate can be observed inside the bulk compared to the surface.[12]*

4 Poly(dimethylsiloxane) (PDMS)

In this work, a polymer coating is deposited to locally modify the mechanical properties at the surface of a complex 3D object while keeping the macroscopic mechanical properties of the object constant. As stem cells are sensitive to the mechanical properties of their environment, such changes in the surface mechanical properties are hypothesized to affect stem cell behavior as well as their fate.

For this coating, a crosslinkable PDMS was used in reason of the ease of tuning its stiffness by changing the density of crosslinks. Furthermore, PDMS is non-toxic[14], has already been used in our laboratory for similar purpose[15, 16] and is one of the gold standard for mechanotransduction studies[17-23]. PDMS is considered as a highly inert elastomer and is currently used for many medical devices or implant such as catheters, plastic surgery implants or intraocular lenses.[11]

Strictly speaking, PDMS is a polymer possessing a backbone of alternated silicon and oxygen atoms as well as methyl side-chains attached on the silicon atom (Figure 5). The word siloxane is derived from its different components: **sil**icon, **ox**ygen and alk**ane**.

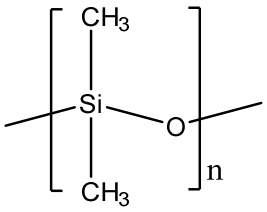


Figure 5: Chemical formula of poly(dimethylsiloxane) (PDMS).

The modified PDMS used in this study is commercialized by Dow under the name of Sylgard 184. The resulting crosslinked PDMS is obtained by mixing two components of a kit, the base and the curing agent (Figure 6 A and B), and curing the obtained mixture using heat to obtain a PDMS network (Figure 6 C). To allow this process, PDMS has been modified both in the base and the curing agent. In the base, PDMS chains are ended by vinyl functions while, in the curing agent, some methyl groups are replaced by hydrogen atoms. Once both components are mixed, the vinyl groups react with silicon-hydride bonds owing to a platinum-based catalyst to form the three-dimensional network. This process is known as hydrosilation of the double bond.[24] Controlling the amount of curing agent offers an easy way to control the

stiffness of the polymer. If less curing agent is present, less crosslinks are made throughout the network, which results in a softer polymer.

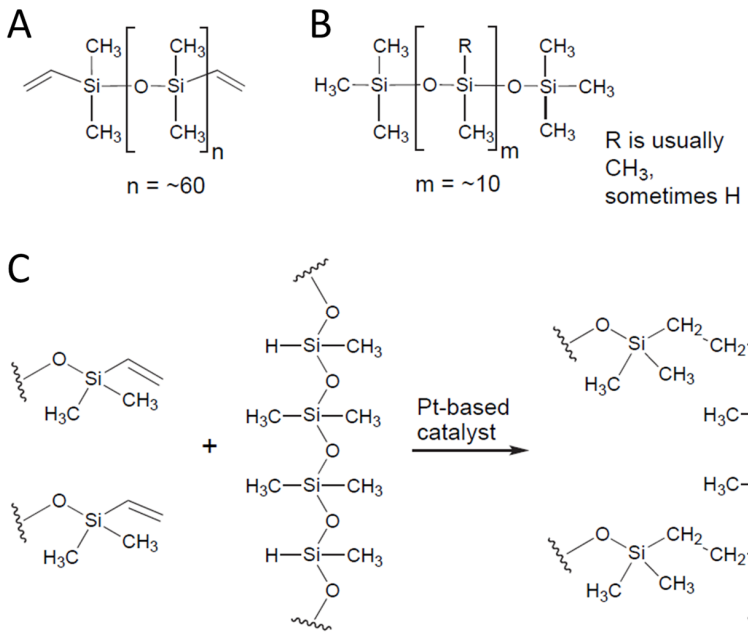


Figure 6: Sylgard 184 kit compounds. (A) Base and (B) curing agent. (C) Hydrosilation reaction allowed by platinum-based catalyst and leading to the formation of a crosslinked PDMS network.[24]

5 Coating method

The deposition of a material onto a surface to form a coating is widely used for many applications in material science. The nanoscale deposition of materials can be performed by chemical vapor deposition, atomic layer deposition, solution deposition and layer-by-layer deposition. Higher coating thicknesses can be obtained by spin, dip or spray coatings.[25] However, these techniques may not all apply to reach micrometer to millimeter-thickness coatings on complex 3D surfaces such as the one developed by the gyroid structure proposed in section 2 of this part. In this work, a coating protocol reported by Nguyen and coworkers, based on the formation of a semi-interpenetrating polymer network (SIPN), was used.[25] The SIPN was defined by the International Union of Pure and Applied Chemistry (IUPAC) as "*a polymer comprising one or more networks and one or more linear or branched polymer(s) characterized by the penetration on a molecular scale of at least one of the networks by at least some of the linear or branched*

macromolecules".[26] As it is the case in our work, their study was centered on a PLA structure coated with a PDMS layer.

Figure 7 presents the different steps of the process. A coating solution is prepared containing a mixture of a solvent (dioxane) and a non-solvent (hexane) of the polymer structure (PLA). The mixture also contains the polymer to be deposited as a coating (PDMS) in a solubilized state as well as the curing agent. The structure is immersed in the coating solution and the mixture of solvent and non-solvent allows the surface of the PLA to swell without being completely dissolved. The PDMS base and the curing agent diffuse inside the swollen layer. The structure is then rinsed in its non-solvent, which provokes a deswelling of the surface and the entrapment of the PDMS. The PDMS is finally cured to form the SIPN and to obtain a coating on the surface of the 3D structure. Several parameters influence the coating formation such as coating solution composition and temperature, structure residence time in the mixture, and the characteristic size scale of the sample. In addition to the optimization of these parameters, the process can be repeated to increase coating thickness (the solvent mixture has to be adapted to swell the already deposited PDMS layer).[25]

The formation of a SIPN between the PLA structure and the PDMS coating allows a good adhesion owing to the crosslinking of the PDMS around the PLA chains on a molecular scale. This method is quite versatile as it does not require particular chemistries or modifications.[25] Small modifications of the procedure can be done to accommodate a variety of polymer materials.

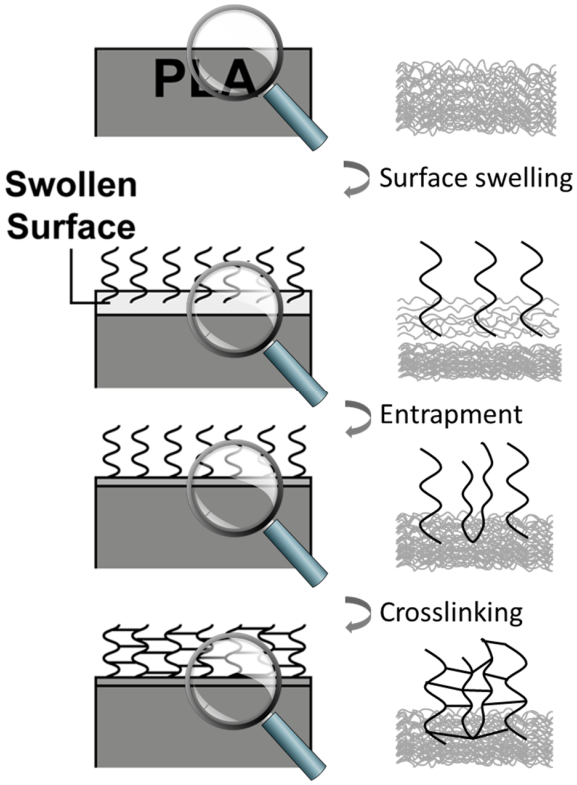


Figure 7: Coating process through the formation of a SIPN. The PLA (grey) structure is immersed in a mixture of solvent and non-solvent containing the PDMS (black) base and the curing agent. The surface of the structure swells and the PDMS chains interpenetrate with PLA chains. The structure is rinsed surface deswells and entraps PDMS chains. The entrapped PDMS chains are cured to form the SIPN and to obtain a PDMS coating at the surface of the structure. Adapted from [25]

6 Stem cells from the apical papilla (SCAP)

Mesenchymal stem cells (MSC) are extensively studied and are one of the most explored strategy (or part of) for tissue repair stimulation. They are present in niches all over the body. Cells are considered as MSC if they express some molecular markers such as CD73, CD90 and CD105 but are negative for others such as CD43.[27] The stem cell molecular profile was shown to be very dynamic owing to their ability to express a tremendous number of genes depending on their differentiation state, activation or passage (*i.e.* action of detaching cells from their growing support and cell reseeding in a lower density on a new growing support). Therefore, stem cells used for research or clinical application need to be fully characterized. In the present study, a fully characterize clone of SCAP, named RP89, was used.

These cells were kindly provided, in the frozen state, by Prof. Anibal Diogenes (UT Health San Antonio).

SCAP (described in Part I, section 2.1.3) have a high proliferation rate compared to bone marrow mesenchymal stem cells and to dental pulp stem cells.[27, 28] They already showed promising results in regenerative endodontics. *In vitro*, SCAP can differentiate into osteo-, odonto-, chondro-, adipo- and neurolineages.[29-32] Furthermore, those cells are easily accessible and do not raise ethical concerns. Ruparel and coworkers (UT Health San Antonio) selected and characterized the RP89 that preferably expressed and maintained MSC markers through passages.[27] The RP89 were isolated form the mandibular third molar apical papilla (Figure 8) of a 17-year-old female patient. The expression of genes specific to MSCs, the co-expression of CD73, CD90 and CD105 as well as the absence of CD45 were monitored up to 20 passages. The RP89 cell line steadily maintained the expression of these MSC markers (both at gene and protein levels).[27] This ensures an undifferentiated phenotype for RP89 cells up to at least 20 passages if not in contact with differentiation signals.

In tissue engineering, a critical concern is the oxygen supply to the cells. Each parameter of the scaffold is optimized to increase oxygen transport. Still, depending on the size of the scaffold and implantation site, oxygen supply can be relatively low. Implanted cells will have to survive until a blood capillary network is formed by angiogenesis. SCAP can resist to hypoxia and even present an increased differentiation potential when grown in hypoxia (1% of oxygen) compared to normoxia (21% of oxygen).[32]

Considering that (i) RP89 have been fully characterized, (ii) their undifferentiated phenotype remains steady for at least 20 passages, (iii) they are able to differentiate into at least three different lineages, and (iv) proliferation as well as differentiation are not inhibited by hypoxic conditions, RP89 SCAP are ideal candidates for the present work.

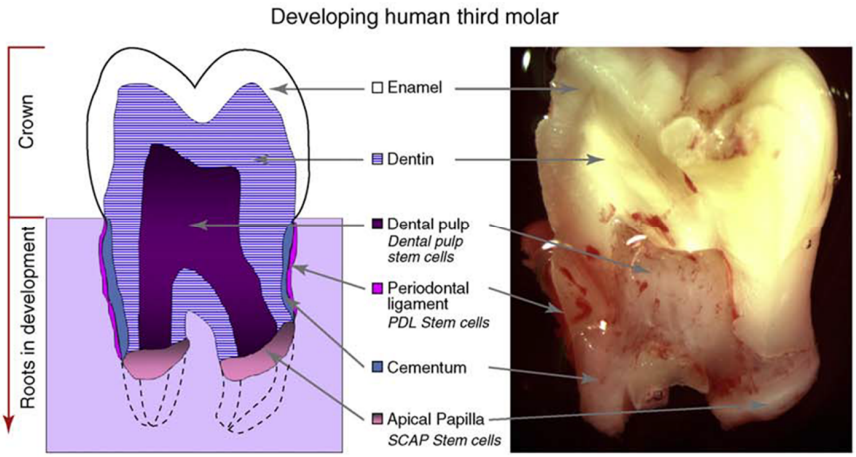


Figure 8: Photograph after the extraction of human third molar tooth in development (right) and diagram (left). The different parts of the tooth are presented as well as stem cell niches. Stem cells from the apical papilla used in this work are present in the apex of teeth roots in formation.[33]

7 References

1. Moreno Madrid, A. P.; Vrech, S. M.; Sanchez, M. A.; Rodriguez, A. P., Advances in additive manufacturing for bone tissue engineering scaffolds. *Mater. Sci. Eng. C Mater. Biol. Appl.* **2019,** *100*, 631-644.

2. Challis, V. J.; Xu, X.; Zhang, L. C.; Roberts, A. P.; Grotowski, J. F.; Sercombe, T. B., High specific strength and stiffness structures produced using selective laser melting. *Mater. Des.* **2014,** *63*, 783-788.

3. Yánez, A.; Herrera, A.; Martel, O.; Monopoli, D.; Afonso, H., Compressive behaviour of gyroid lattice structures for human cancellous bone implant applications. *Mater. Sci. Eng. C Mater. Biol. Appl.* **2016,** *68*, 445-448.

4. Speirs, M.; Van Hooreweder, B.; Van Humbeeck, J.; Kruth, J. P., Fatigue behaviour of NiTi shape memory alloy scaffolds produced by SLM, a unit cell design comparison. *J. Mech. Behav. Biomed. Mater.* **2017,** *70*, 53-59.

5. Zadpoor, A. A., Bone tissue regeneration: The role of scaffold geometry. *Biomater. Sci.* **2015,** *3* (2), 231-245.

6. Rammohan, A. V.; Tan, V. B. C., Morphological models of trabecular bone suitable for high-porosity regions and vertebrae. *Comput. Methods Biomech. Biomed. Eng.* **2016,** *19* (13), 1418-1422.

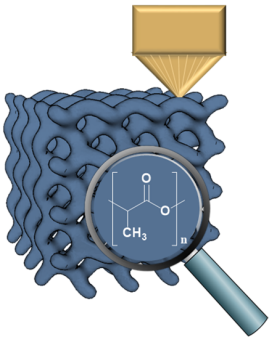
7. Klintström, E.; Klintström, B.; Moreno, R.; Brismar, T. B.; Pahr, D. H.; Smedby, Ö., Predicting Trabecular Bone Stiffness from Clinical Cone-Beam

CT and HR-pQCT Data; an *In Vitro* Study Using Finite Element Analysis. *PLOS ONE* **2016,** *11* (8), e0161101.
8. Gritsch, L.; Conoscenti, G.; La Carrubba, V.; Nooeaid, P.; Boccaccini, A. R., Polylactide-based materials science strategies to improve tissue-material interface without the use of growth factors or other biological molecules. *Mater. Sci. Eng. C Mater. Biol. Appl.* **2019,** *94*, 1083-1101.
9. Ghalia, M. A.; Dahman, Y., Biodegradable poly(lactic acid)-based scaffolds: synthesis and biomedical applications. *J. Polym. Res.* **2017,** *24* (5), 74.
10. Domingues, R. C. C.; Pereira, C. C.; Borges, C. P., Effect of stereoisomerism of poly(lactic acid) during neural guide conduit membrane synthesis. *J. Appl. Polym. Sci.* **2018,** *135* (18), 46190.
11. Maitz, M. F., Applications of synthetic polymers in clinical medicine. *Biosurf. Biotribol.* **2015,** *1* (3), 161-176.
12. Woodruff, M. A.; Hutmacher, D. W., The return of a forgotten polymer - Polycaprolactone in the 21st century. *Prog. Polym. Sci.* **2010,** *35* (10), 1217-1256.
13. Henton, D. E.; Gruber, P.; Lunt, J.; Randall, J., Polylactic Acid Technology. In *Natural Fibers, Biopolymers, and Biocomposites*, Group, T. F., Ed. CRC Press Boca Raton, 2005; pp 527-577.
14. Colas, A.; Curtis, J., B - Silicones. In *Biomaterials Science (Third Edition)*, Ratner, B. D.; Hoffman, A. S.; Schoen, F. J.; Lemons, J. E., Eds. Academic Press: 2013; pp 82-91.
15. Degand, S. Design of surfaces with mechanical nanoheterogeneities for a better control of cell-material interactions. PhD thesis, UCLouvain, Louvain-la-Neuve, Belgium, 2013.
16. Degand, S.; Knoops, B.; Dupont-Gillain, C. C., Design and characterization of surfaces presenting mechanical nanoheterogeneities for a better control of cell-material interactions. *Colloids Surf. A Physicochem. Eng. Asp.* **2013,** *442*, 164-172.
17. Brown, X. Q.; Ookawa, K.; Wong, J. Y., Evaluation of polydimethylsiloxane scaffolds with physiologically-relevant elastic moduli: Interplay of substrate mechanics and surface chemistry effects on vascular smooth muscle cell response. *Biomaterials* **2005,** *26* (16), 3123-3129.
18. Cheng, C. M.; Steward Jr, R. L.; LeDuc, P. R., Probing cell structure by controlling the mechanical environment with cell-substrate interactions. *J. Biomech.* **2009,** *42* (2), 187-192.
19. Feinberg, A. W.; Wilkerson, W. R.; Seegert, C. A.; Gibson, A. L.; Hoipkemeier-Wilson, L.; Brennan, A. B., Systematic variation of microtopography, surface chemistry and elastic modulus and the state dependent effect on endothelial cell alignment. *J. Biomed. Mater. Res. Part A* **2008,** *86* (2), 522-534.

20. Fuard, D.; Tzvetkova-Chevolleau, T.; Decossas, S.; Tracqui, P.; Schiavone, P., Optimization of poly-di-methyl-siloxane (PDMS) substrates for studying cellular adhesion and motility. *Microelectron. Eng.* **2008,** *85* (5-6), 1289-1293.
21. Teixeira, A. I.; Ilkhanizadeh, S.; Wigenius, J. A.; Duckworth, J. K.; Inganäs, O.; Hermanson, O., The promotion of neuronal maturation on soft substrates. *Biomaterials* **2009,** *30* (27), 4567-4572.
22. Yim, E. K. F.; Darling, E. M.; Kulangara, K.; Guilak, F.; Leong, K. W., Nanotopography-induced changes in focal adhesions, cytoskeletal organization, and mechanical properties of human mesenchymal stem cells. *Biomaterials* **2010,** *31* (6), 1299-1306.
23. Trappmann, B.; Gautrot, J. E.; Connelly, J. T.; Strange, D. G.; Li, Y.; Oyen, M. L.; Cohen Stuart, M. A.; Boehm, H.; Li, B.; Vogel, V.; Spatz, J. P.; Watt, F. M.; Huck, W. T., Extracellular-matrix tethering regulates stem-cell fate. *Nat. Mater.* **2012,** *11* (7), 642-649.
24. Lisensky, G. C.; Campbell, D. J.; Beckman, K. J.; Calderon, C. E.; Doolan, P. W.; Ottosen, R. M.; Ellis, A. B., Replication and Compression of Surface Structures with Polydimethylsiloxane Elastomer. *J. Chem. Educ.* **1999,** *76* (4), 537.
25. Nguyen du, T.; Kleiman, M.; Ryu, K. A.; Hiew, S.; Brubaker, K.; Mughnetsyan, R.; Truong, R.; Dolan, B.; Tackett, E.; Esser-Kahn, A. P., Three-dimensional conformal coatings through the entrapment of polymer membrane precursors. *ACS Appl. Mater. Inter.* **2014,** *6* (4), 2830-2835.
26. Jenkins, A. D.; Stepto, R. F. T.; Kratochvíl, P.; Suter, U. W., Glossary of basic terms in polymer science (IUPAC Recommendations 1996). *Pure Appl. Chem.* **1996,** *68* (12), 2287-2311.
27. Ruparel, N. B.; de Almeida, J. F.; Henry, M. A.; Diogenes, A., Characterization of a stem cell of apical papilla cell line: effect of passage on cellular phenotype. *J. Endod.* **2013,** *39* (3), 357-363.
28. Yu, S.; Zhao, Y.; Ma, Y.; Ge, L., Profiling the Secretome of Human Stem Cells from Dental Apical Papilla. *Stem Cells Dev.* **2016,** *25* (6), 499-508.
29. Huang, G. T. J.; Gronthos, S.; Shi, S., Critical reviews in oral biology & medicine: Mesenchymal stem cells derived from dental tissues vs. those from other sources: Their biology and role in Regenerative Medicine. *J. Dent. Res.* **2009,** *88* (9), 792-806.
30. Zhang, W.; Zhang, X.; Li, J.; Zheng, J.; Hu, X.; Xu, M.; Mao, X.; Ling, J., Foxc2 and BMP2 induce osteogenic/odontogenic differentiation and mineralization of human stem cells from apical papilla. *Stem Cells Intl.* **2018,** *2018*, 2363917.
31. Zhu, Y.; Zhang, P.; Gu, R. L.; Liu, Y. S.; Zhou, Y. S., Origin and Clinical Applications of Neural Crest-Derived Dental Stem Cells. *Chin. J. Dent. Res.* **2018,** *21* (2), 89-100.

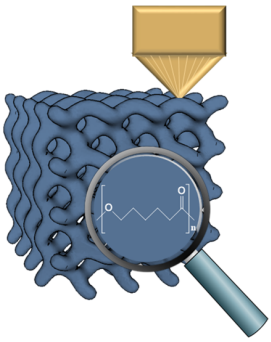
32. Vanacker, J.; Viswanath, A.; De Berdt, P.; Everard, A.; Cani, P. D.; Bouzin, C.; Feron, O.; Diogenes, A.; Leprince, J. G.; des Rieux, A., Hypoxia modulates the differentiation potential of stem cells of the apical papilla. *J. Endod.* **2014,** *40* (9), 1410-1418.
33. Volponi, A. A.; Pang, Y.; Sharpe, P. T., Stem cell-based biological tooth repair and regeneration. *Trends Cell Biol.* **2010,** *20* (12), 715-722.

Part IV : Outline



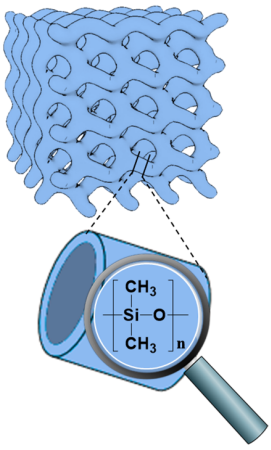
Chapter 1: 3D-printed biodegradable gyroid scaffolds for tissue engineering applications

The gyroid design is used as a mesh to produce PLA scaffolds for tissue engineering. These PLA gyroid scaffolds are prepared by fused deposition modeling and are characterized. Their mechanical properties as well as their degradation are compared to the ones of common strut-based scaffolds.



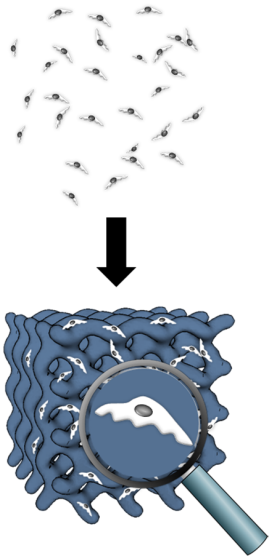
Chapter 2: Optimization of poly(ε-caprolactone) 3D printing

The parameters of 3D printing are adapted to obtain gyroid scaffolds made of PCL, which are compared to PCL strut-based scaffolds. Both the scaffold morphology after printing and the mechanical properties are evaluated and compared.



Chapter 3: PDMS coating optimization

A crosslinkable polydimethylsiloxane is used to vary the surface mechanical properties of the scaffold . A coating method is developed based on the formation of a semi-interpenetrating polymer network at the PLA surface. The coating presence is assessed and its thickness is measured.



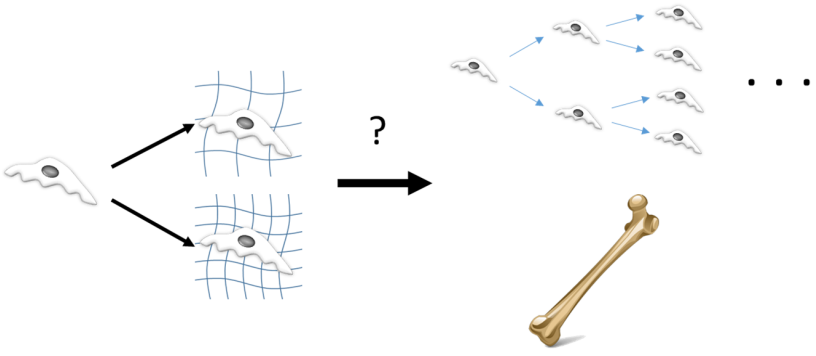
Chapter 4: Preliminary cell culture studies

Preliminary studies on the seeding of AMSC and SCAP, performed to set up further experiments, are presented.



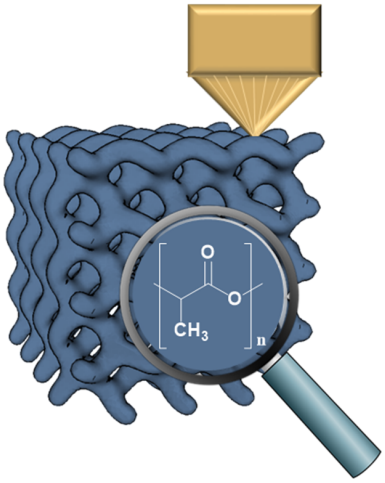
Chapter 5: The crosslinking density of a PDMS coating on macroporous scaffolds influences the proliferation of stem cells from the apical papilla but not their osteogenic differentiation

SCAP proliferation and osteogenic differentiation are monitored on PLA scaffolds presenting PDMS coatings with different crosslinking densities.



Part V : Results

Chapter 1: 3D-printed biodegradable gyroid scaffolds for tissue engineering applications



Fused deposition modeling (FDM), a low-cost and easy-to-use additive manufacturing technique, was used to produce poly(lactic acid) (PLA) gyroid scaffolds. Such morphology was selected for its spring shape, high porous fraction leading to good nutrient and waste diffusion, and favorable mechanical properties. Printing parameters were optimized and the need of a support material to improve printing was evidenced. The gyroid was compared to the common strut-based structure. Scaffold porous fraction was measured by micro-CT, and mechanical properties were determined by compression tests, taking into account the effect of geometry, printing resolution, and PLA crystallinity. The impact of scaffold geometry and crystallinity on its degradation was studied *in vitro*. Porous fraction of the gyroid structure was 71%, as expected from the printing model. The compression tests showed an isotropic behavior for the gyroid, in contrast with the strut-based scaffold. Upon aging in physiological conditions, gyroid scaffolds retained their integrity during 64 weeks, while control scaffolds lost struts starting from week 33, in a way that depended on crystallinity and printing resolution. Based on these results, the gyroid design is proposed as a suitable mesh architecture for tissue engineering scaffolds that can be elaborated using FDM techniques, to produce low-cost and personalized implants.

Based on the publication : Germain, L.; Fuentes, C. A.; van Vuure, A. W.; des Rieux, A.; Dupont-Gillain, C., 3D-printed biodegradable gyroid scaffolds for tissue engineering applications. *Mater. Des.* **2018,** *151*, 113-122.

We sincerely thank Michel Sclavons and Prof. Sophie Demoustier-Champagne for helpful discussions, the Bio- and Soft Matter division (BSMA) for access to the 3D printer, Julian

Leprince for access to the mechanical test instrument and Luc Randolph for his help in stress-strain curve analysis, Pascal Van Velthem for DSC training, Prof. Arnaud Delcorte for access to the profilometer and Claude Poleunis for the training, and Prof. Yves Dufrêne for access to the low magnification microscope. The work was supported by the Interuniversity Attraction Pole Program (P07/05) and the Belgian National Foundation for Scientific Research (FNRS).

1 Introduction

Tissue engineering is an interdisciplinary field linking engineering and biology in order to recover, maintain or improve the function of a tissue or organ.[1] It focuses on three main components: cells, biomaterials and bioactive factors, that are combined to mimic the physical and chemical structure of the body.[2] These components are implanted or injected to stimulate the regeneration of a damaged tissue. Cells, usually stem cells, proliferate, differentiate and form the new tissue or, at least, improve the recovery of the lesion, notably owing to their unique immunomodulatory properties.[3-5] The biomaterial will generally be processed as a scaffold, to which bioactive compounds can be added, with a view to carry cells and guide their behavior.[6, 7]

The physical properties of the scaffold are of upmost importance. The mechanical properties have to fit with the ones of the implantation site. For instance, a too soft scaffold could lose its primary shape due to compression by native tissues [8], as is the case for musculoskeletal implantations. For applications such as nasal implants, flexibility is however needed to avoid complications such as infection or extrusion.[9] The scaffold design can also impact cell attachment, proliferation, migration and differentiation.[10, 11] One important parameter influencing these cell behaviors is porosity. Indeed, pore size and interconnectivity determine communication among cells as well as nutrient, gas and waste diffusion.[6, 11] Too small pores and a lack of interconnectivity could lead to cell necrosis.[8]

Scaffolds meeting these requirements can be produced with a range of different techniques such as salt leaching, gas foaming, fiber bonding, solvent casting, melt molding, phase separation, freeze drying, photolithography and electrospinning.[6, 8] Besides, Solid Freeform Fabrication (SFF) methods, also known as additive manufacturing techniques, and popularized under the name of 3D printing methods, are easier to implement to reach designs with controlled dimensions, complex shapes and high porous fractions. This is ensured by the layer-by-layer construction process which relies on computer-aided design/computer-aided manufacturing (CAD/CAM) systems. SFF methods do not require the use of a mold, and models can be directly generated from computerized tomography, laser scanning or magnetic resonance imaging data, allowing the production of personalized implants.[12] Moreover, complex shapes that could not be obtained with molding can be produced based on layer-by-layer construction.

Recent research in the field of additive manufacturing for tissue engineering mainly focuses on three directions: (i) 3D bioprinting, (ii) 3D printing of polymers, and (iii) 3D printing of ceramics. The use of 3D (bio)printing concepts is sometimes confusing in the literature. 3D bioprinting refers to the production of cell-loaded scaffolds, meaning that cells are printed at the same time as the scaffold.[13] Ho and Hsu (2018) proposed a synthetic thermo-responsive waterborne polyurethane gel as bioink. Using an extrusion-based 3D printer, they demonstrated that human fibroblasts co-printed with FoxD3 plasmids in this hydrogel could be reprogrammed and differentiated into a neural-like construct.[14] Beside synthetic bioinks, natural bioinks can also be used. Di Giuseppe et al. (2018) used an alginate-gelatin mixed hydrogel. Blends were prepared by varying individual constituent concentrations and were tested for printability and printing accuracy, compressive behavior, and viability of encapsulated mesenchymal stem cells.[15] 3D printing refers to the production of inert or bioactive scaffolds. Cells can be added to such scaffolds in a second step.[13] Two main classes of materials are used for 3D printing: polymers and ceramics. The most common polymers used in additive manufacturing for tissue engineering are polylactides, poly(ε-caprolactone) (PCL), and poly(propylene fumarate), which are selected for their mechanical stability, cytocompatibility and resorbability.[13, 16] However, most of these polymers possess a limited bioactivity. Some studies aim at modifying the scaffold surface by deposition of molecules or proteins. Teixeira et al. (2018) used polydopamine to coat poly(lactic acid) (PLA) scaffolds and showed an improved immobilization of collagen I at the surface, increasing the scaffold osteoinductivity.[17] Ceramics such as calcium phosphate or magnesium phosphate are promising biomaterials for bone tissue regeneration.[13] Researchers are focusing on the effect of pore architecture on differentiation[18] and on the addition of dopants such as manganese[19] or of indene compounds[20] to promote bone and cartilage regeneration.

Hybrid scaffolds, which combine two features of the systems presented above, *i.e.* cell-loaded hydrogels, 3D printed polymers, and 3D printed ceramics, are also proposed. The addition of β-tricalciumphosphate in a copolymer hydrogel improved the physicochemical properties of the scaffold and stimulated human bone marrow stem cells proliferation and differentiation.[21] Dome-shaped tissue constructs were proposed combining PCL printing and decellularized adipose tissue matrix bioprinting. Human adipose derived mesenchymal stem cells were encapsulated and printed without any deleterious effect. Printing rather increased adipogenic genes

expression.[22] Hydroxyapatite and poly(propylene fumarate) were used as coating on a PCL scaffold printed with the fused deposition modeling technique. This coating enhanced the compressive modulus, cell adhesion, and proliferation rate.[23]

Most SFF techniques are unfortunately expensive. Fused Deposition Modeling (FDM) is however a low cost and easy-to-use SFF method.[10] This nozzle-based technique is based on the layer-by-layer deposition of thermoplastic polymers in a semi-liquid state along an extrusion path. It can be applied to a large variety of materials, and allows the production of patient-personalized scaffolds with a precise control of the geometry, with a typical resolution of $0.4 \times 0.4 \times 0.1$ mm^3.[10, 24, 25]

Polymers, owing to their versatile mechanical properties and their ease of processing, have been extensively used as biomaterials in the tissue engineering field.[10] They have to fulfill several conditions in order to be used as scaffolds for this application. Among others, a suitable degradation rate, mechanical properties close to the native tissue and absence of cytotoxicity are required.[9] PLA fulfills these requirements and has also been approved by the Food and Drug Administration (FDA) and the European Medicines Agency (EMA) as a material for several biomedical applications.[26] Even though PLA has already been employed extensively for 3D scaffolding, the use of this biodegradable polymer has been scarcely reported for nozzle-based deposition methods.[24, 25] PLA mechanical resistance and degradation rate are influenced by its crystallinity. Crystallites present in semi-crystalline PLA are zones of high polymer density that reinforce the material, because of a much slower degradation compared to amorphous regions.[27, 28] Therefore, scaffold mechanical properties and degradation rate could be tuned by controlling PLA crystallinity.

Nowadays, the production of scaffolds using nozzle-based systems usually consists in stacking struts of the selected material on top of each other to reach a final 3D object.[6, 8, 10, 29, 30] Many parameters related to these struts and the resulting mesh can be varied such as strut diameter, space between them and orientation from one layer to another. However, more complex mesh designs are of great interest, especially in the field of tissue engineering. The gyroid morphology (Figure 1 a) is a mesh composed of units made of quadruple junction points.[31] The branches have a curved shape and link other nodes throughout the structure. This kind of mesh provides interesting features for tissue scaffolding such as mechanical energy

absorption and robustness, as well as good nutrient and waste diffusion owing to the high porous fraction and the minimal surface area.[32, 33] Gyroids for bone implantation were already printed in titanium or stainless steel by Electron Beam Melting (EBM) or Selective Laser Melting (SLM), two SFF methods.[32, 34, 35] However, these materials are heavy, non-degradable, and not suitable for all applications. Moreover, these SFF techniques are expensive. Digital Light Printing, a photocrosslinking-based method, has also been used with success to produce gyroids in poly(propylene fumarate) for biomedical applications.[16, 36] Gaining approval and reaching the clinics by producing photopolymerizable resins containing nontoxic photoinitiators, solvents and other additives remain however challenging. In contrast, FDM is low cost, easy to implement and allows the use of several available medical grade thermoplastics, which could notably be biodegradable or not depending on the requirements. FDM has not been much considered for tissue engineering applications yet, probably because of its poor resolution compared to other additive manufacturing techniques. It has, to our knowledge, not yet been used for small and complex PLA model construction in the field of tissue engineering.

The aim of this work is to optimize the printing parameters of a PLA-based complex object at a scale close to the resolution limit of fused deposition modeling. The gyroid design will be used as a mesh for the 3D printing of scaffolds in reason of its remarkable properties, including large pore size, high interconnectivity, high porous fraction and isotropy. The effect of mesh design, polymer crystallinity, and printing layer resolution on mechanical properties and degradation rate will also be assessed.

2 Materials and methods

2.1 3D models

The gyroid 3D model was downloaded from the 3DVIA website[37] and modified with an open source software (Blender V2.69.0, Blender Foundation, The Netherlands). The whole structure was made four times thicker to enable its printing with a common fused deposition modeling apparatus. Control models were also designed to produce scaffolds made of struts stacked on top of each other (Figure 1 b), as often done in the literature related to 3D-printed scaffolds.[6, 8, 10, 29, 30] These models were drawn with the

123D Design software (Autodesk, V1.6) in order to have similar strut diameter and similar porous fraction as with the gyroid model.

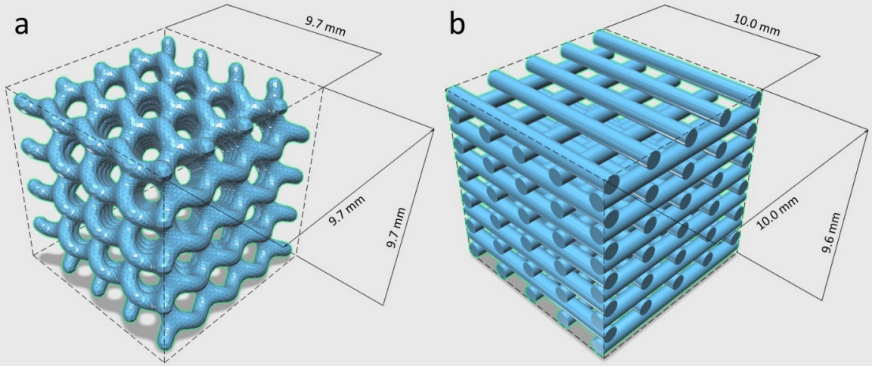


Figure 1: (a) Gyroid 3D model and (b) control structure (strut-based scaffold).

2.2 Materials and printing conditions

Polymers were printed by fused deposition modeling with a Makerbot Replicator 2X 3D printer (Makerbot, Germany) equipped with a dual extruder. Scaffolds were printed in poly(lactic acid) (PLA) (Makerbot, Germany), and High Impact polystyrene (HIPS) (Makerbot, Germany) was used as support material for printing optimization. Supports are polymer parts printed simultaneously with the structure, which carry PLA layers not supported by a layer already present underneath and would thus be deposited on void; the support material is then removed after printing. PLA blends from Makerbot are made from pellets of NatureWorks polylactide resin 4043D (NatureWorks LLC, USA). Number-average molar mass (Mn) and dispersity (Đ) values were previously determined with gel permeation chromatography using light scattering and were 57.0 kg/mol and 2.43, respectively.[38] Before printing, PLA was dried overnight at 80 °C, resulting in a change of its crystallinity (see more details in Sections 2.6 and 3.5). HIPS was removed after printing by dissolution in (R)-+-Limonene (VWR, USA). Then, the use of water-soluble poly(vinyl alcohol) (PVA) (Formfutura, the Netherlands) as a support material was evaluated to avoid the immersion of the scaffold in an organic solvent, with a view to better fit the requirements for clinical use.

Once modifications were made (see Section 2.1 of this chapter), the 3D model was imported in the MakerWare software (V. 2.4.1.24) and was

duplicated to enable the printing of nine objects in parallel. Custom parameters were applied to program these structures with a set of printer path instructions. For all samples, PLA was printed with a concentric pattern, and the infill density, representing the fraction of void filled with polymer inside the pillars, was set to 1. Gyroid samples (Figure 1 a) were printed with a Z resolution of 100 µm and with a nozzle diameter of 400 µm. Temperatures applied for the printing of PLA, HIPS and PVA were 220 °C, 250 °C and 230 °C, respectively. The support was printed 0.4 mm away from the structure, and its density, defined as the fraction of void filled with supporting polymer, was set to 0.5. Purge walls were printed at the sides of the printed structures to get rid of overheated polymer and to sweep the nozzles. Nine gyroid samples were printed in parallel and around 4 h were needed to complete the printing process. After printing, the supporting polymer (HIPS or PVA) was dissolved in limonene or water, respectively, in 3 baths of 8 h each. The need of a supporting material was further investigated. Supported and non-supported gyroid structures were compared. For samples without support, the set of printer path instructions was exactly the same as for the one with PVA support, but no filament was loaded into the second head of the printer.

Control samples (Figure 1 b) were printed without support and the flow rate through the extrusion head was optimized to get the same void fraction as for the gyroid samples. These controls were printed with two different Z resolutions: 100 µm and 400 µm (named control 100 µm and control 400 µm, respectively, hereafter), in order to analyze the effects of the printing resolution.

2.3 µCT scan

HIPS-supported PLA scaffolds, treated with limonene to remove HIPS, were 3D imaged using a Phoenix NanoTom X-ray computed tomography equipment (General Electric Company, Fairfield, USA). This allowed the complex 3D scaffold structure to be imaged without destructive effects. The applied voltage and current were 40 kV and 620 µA respectively, with a molybdenum target. The exposure time was 500 ms and a frame averaging of 3 and image skip of 1 were applied. The obtained voxel size was 6.1 μm^3. The stack of scan images was then thresholded with CTVox software (Bruker microCT, Kontich, Belgium) to differentiate the polymer from the pores. The porous fraction was determined with the ImageJ 1.47v software (Wayne

Rasband, National Institutes of Health, USA).[39] Images were imported, cropped at the edges of the sample, thresholded into a binary stack and analyzed with the Voxel Counter plugin in ImageJ. Taking into account the distance between two images from the stack, the program evaluates the presence or absence of polymer voxel by voxel and sums up the information into a volume fraction.

2.4 Porous fraction measurement

Gyroid structure porous fraction (including both accessible and possibly occluded porosity) was measured experimentally on samples printed with a PVA support that was further eliminated with water. Mass and dimensions (width, W, length, L, and height, H of the imaginary cube containing the structure) of gyroid and control structures were measured on 27 objects printed in three different batches (nine objects per batch). The porous fraction was computed from the following equation:

$$Porous\ fraction\ [\%] = \frac{V_{obj}[m^3] - V_{PLA}[m^3]}{V_{obj}[m^3]} x100 \quad (1)$$

Where:

V_{obj} represents the entire volume of the object, obtained by equation (2)

$$V_{obj}[m^3] = W[m] x\ L[m] x\ H[m] \quad (2)$$

V_{PLA} represents the volume occupied by PLA and is obtained by equation (3)

$$V_{PLA}[m^3] = \frac{m\ [kg]}{\rho_{PLA}[kg/m^3]} \quad (3)$$

Where:

m is the mass of the object;

ρ_{PLA} is the density of PLA, equal to 1250 kg/m^3.[28]

These experimental values were compared to the theoretical porous fraction measured with Netfabb Basic (V5.1) on the models used for printing. It should be noted that the porous fraction obtained using such an experimental approach may also include a potential and unwanted inner porosity (bubbles or insufficient deposited amount of polymer) even though

the model and printing parameters were designed to build structures with an infill of 100% (*i.e.* no void inside the structure).

2.5 Surface topography

PVA-supported PLA structures, treated with water to remove PVA, were analyzed with a Dektak XT (Bruker, USA) profilometer equipped with a 0.7 µm curvature radius needle and using the Vision64 acquisition software (V5.40). As the surface at the edges of the samples was analyzed, the gyroid structure was filled almost entirely with a large cube to prevent the needle of the profilometer to be stuck in a pore (Figure 3). Three different sides of each sample (n=3) were scanned with a line resolution of 0.075 µm/pt and a 12 µm distance was applied between analyzed lines. The force applied on the needle was 0.06 mg (sides) and 0.5 mg (top).

2.6 Crystallinity fraction evaluation

PVA-supported PLA gyroid structures, treated with water to remove PVA, and PLA control samples were annealed overnight at 80 °C. Crystallinity, glass transition temperature (Tg) and change in specific heat capacity (ΔCp) at the Tg of annealed and not annealed printed samples were measured by differential scanning calorimetry (Mettler Toledo DSC821, Belgium). Calibration was done with Indium. Samples were cut to obtain fragments with a mass ranging from 8 to 11 mg (n=3 per condition) and loaded into 40 µl aluminum pans. For Tg measurement and ΔCp at this Tg, a temperature ramp was applied from 20 °C to 250 °C at a rate of 10 °C/min. The samples were then cooled at a rate of 10 °C/min, and a second cycle was used as polymer state control. For crystallinity measurement, the heating ramp was increased to 100 °C/min in order to minimize sample re-crystallization inside the chamber. Percentage of crystallinity was computed based on the linear increase of enthalpy of fusion with crystallinity, and using a reference heat of enthalpy of 0 J/g and 93.1 J/g for theoretically 0% and 100% crystalline PLA, respectively.[28]

2.7 Compression tests

Compression tests were performed (LRX plus, Lloyd Instruments, max load=1 kN) on both amorphous and crystalline gyroids (n=3), control 400 µm (n=3) and control 100 µm (n=3) structures to evaluate the effect of mesh geometry,

crystallinity and printing resolution on scaffold mechanical properties. The speed used for the compression test was 1 mm/min. Each sample was placed between two parallel steel plates along two axes: perpendicular and parallel to the printed layers of the sample. The parallelism between the two plates and between each plate and the faces of the sample was respected. Force and displacement were recorded and converted into stress and strain, respectively, taking into account scaffold dimensions. The square coming from the horizontal cross section of the imaginary cube containing the scaffold was chosen as the area needed for the conversion of force into strain. Apparent compression moduli were obtained from the slope of the linear region of the sigmoid (slope at the initial linear part of stress-strain curve) and yield strengths were extracted using the offset method with a value of 1% (see Figure SI2 in Supporting Information for details).

2.8 Scaffold *in vitro* degradation

Amorphous (n=4) and annealed (n=4) gyroid, control 100 µm and control 400 µm structures were weighed. They were then disinfected in ethanol 70%, dried and placed in 5 ml of phosphate buffered saline (PBS) as recommended by the ISO 13781 standard: "Poly(L-lactide) resins and fabricated forms for surgical implants – *In vitro* degradation testing". 0.5% of NaN_3 was added to hinder the development of microorganisms. Samples were incubated at 37 °C and each week, half of the degradation medium was replaced by fresh PBS containing NaN_3. Each month, samples were dehydrated in ethanol and dried at 37 °C during 6 h and then weighed. Only the main parts of samples (pieces bigger than 1 strut) were taken into account. Again, samples were disinfected in ethanol 70%, rinsed twice in PBS and once in PBS containing 0.5% of NaN_3 before placing them back in their own degradation medium (5 ml PBS containing 0.5% of NaN_3). The study was carried out until the main body of the scaffold fell apart. At week 64, pictures of the samples were taken with a low magnification microscope, at the same magnification (12×) and with the same backlight intensity.

2.9 Statistical analysis

ANOVA and Tukey's HSD were performed using JMP®, Version 12 Pro. (SAS Institute Inc., USA) (α=0.05).

3 Results and discussion

3.1 3D scanning of printed gyroid structures

The HIPS-supported gyroid structure was scanned by µCT after HIPS dissolution. Figure 2 a and b show the model and the printed gyroid scan, respectively, both cropped at the front and the top of the structure for the sake of clarity. The three-dimensional reconstruction matches the computerized model very well, and nodes as well as gyrating junctions are well defined and clearly visible. Besides, the µCT scan shows large pores that are completely interconnected. Cross-sections can be extracted and isolated from the 3D *in silico* model and from the µCT scan. Figure 2 d presents a printed slice of the sample, which is in close agreement with the slice coming from the model (Figure 2 c). This cross-section shows that the bean-shaped units, corresponding to the pillars of the gyroid structure, are similar to the model. Objects printed in PLA, compared to the ones printed in Acrylonitrile Butadiene Styrene, are less subject to deformation and tension in the material, which could lead to warping (*i.e.* deformation and detachment of the object from the platform) upon cooling.[40, 41] In our study, no deformation of the scaffolds was observed during or after printing. Besides a good nutrient and waste diffusion, the interconnection and the large pore size (pore projections of 800 µm) should allow a good cell-cell communication and favor tissue ingrowth. As pore projections are at least 10 times larger than cells, this structure should allow cells to migrate, proliferate and differentiate within the scaffold, and vascularization could be initiated.[11] Geometrical scaffold properties such as pore size and shape and even local curvature were shown to have an impact on the control of cell proliferation and fate, both *in vitro* and *in vivo*.[42] Depending on pore size and scaffold dimensions, a dynamic culture environment (with perfusion reactors) is sometimes needed to increase mass transport of nutrient and oxygen.[43] Flow-associated shear stress linked to geometric features of the scaffold has been shown to influence neotissue growth kinetics. Small shear stress (0.015 Pa for human bone marrow MSCs) has a positive effect while higher shear stresses (0.05 Pa) decrease neotissue growth or result in inhomogeneous tissue-engineered constructs. The spring shape design of the gyroid shows a lot of curved surfaces and only rare spots of the structure would be perpendicular to the flow in the case of culture in dynamic conditions. Shear stress should therefore be reduced compared to a strut-based scaffold, and

flow patterns should be more uniform. The printed gyroid structure is thus an appropriate scaffold for tissue reconstruction.

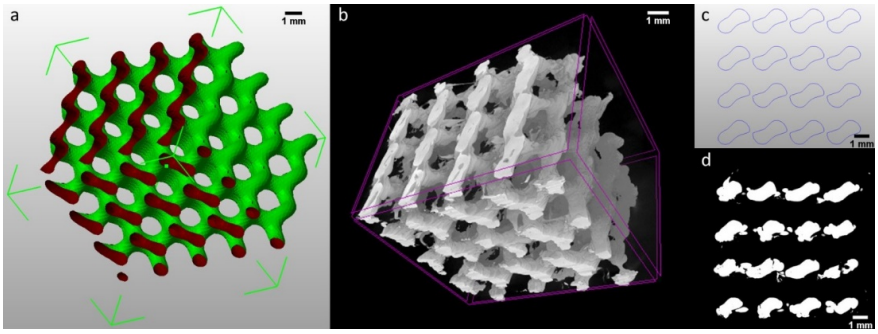


Figure 2: (a) Model and (b) printed gyroid µCT scan both cropped at the front and the top of the structure for the sake of visualization. (c) Model and (d) µCT scan of the corresponding printed cross-sections.

3.2 Porous fraction of printed gyroids

In complement to the 3D visualization of the gyroid structure, its porous fraction was determined, based on the mass and dimensions of the samples (see section 2.4 of this chapter), and on µCT stack images (Table 1). Both values were compared to the porous fraction predicted theoretically, according to the *in silico* model. In each case, porous fraction is in the range of 70–75%. The similarity of experimental and theoretical porous fraction values, as well as the small standard deviation of experimental values based on mass and dimensions emphasize the reliability of the gyroid model printing. Moreover, void fraction is important as it will affect mechanical resistance.

Table 1: Printed gyroid porous fraction computed from mass and dimensions of gyroid structure (n=27; standard deviation; middle) and from µCT images processing (n=1; bottom), as compared to the theoretical value (top).

	Porous fraction (%)
Theoretical	73.7
Experimental – From mass and dimensions	70.8 (0.5)
Experimental – From µCT scan images	74.7

3.3 Profilometry of printed gyroid scaffolds

Characterization was further conducted at the micrometer scale, which is of interest regarding cell-material interactions. Profilometry was used to analyze the surface at the edges of the sample. As represented in Figure 3, the top and two sides of printed cubes, representing different orientations of the junctions compared to the printed layer, were analyzed. Profilometry analysis shows the stacked polymer layers of around 100 µm thick. The surface of these layers is, in each case, rather smooth at the micrometer scale. Despite the presence of the layering artifact, the 3D design is respected at the 100 µm-scale, as already evidenced by the µCT scan (n=3). Micro- and nano-topography on 2D surfaces has been shown to influence cell shape, morphology and in some cases proliferation. Cells from many different origins were shown to align parallel to micro-and nano-grooves and, in some cases, this even influenced their migration.[44-46] Here, cells could align parallel to the grooves created by the stacking of the layers. This layer artifact inherent to 3D printing techniques could be exploited to guide cell growth and migration.

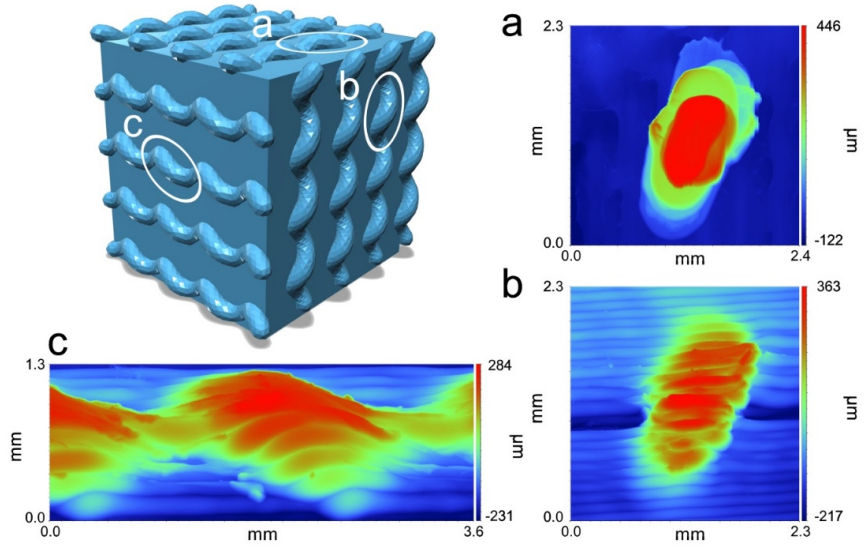


Figure 3: Simplified geometry for profilometry analysis (upper left) and topographic scans obtained by profilometry of circled areas on (a) the top and (b, c) two different sides of the sample.

3.4 Influence of the support on shape fidelity

The need of a supporting polymer to achieve good gyroid printing was investigated. Since most of the structure is self-supported, almost no overhang is present in the design, and all bridges are sufficiently small for the printer to overcome printing issues, printing without support should be possible and would constitute an interesting alternative since a dissolution step would not be required to eliminate the supporting material. Gyroids were printed with and without the addition of PVA in the second nozzle. Scaffold morphology was significantly impacted by the absence or presence of a supporting structure during printing, as it can be observed in Figure 4 where black arrows point out the presence of polymer leaking out of the nozzle, known as oozing, on the non-supported samples and their absence on the supported ones. In addition, the support improves the deposition of the layers with straight orientation instead of wavy-like structure (grey arrows) and leads to less polymer drops (white arrows). The support improves the printing quality, even though the structure can be printed without support. The absence of support results in a decrease in shape accuracy.

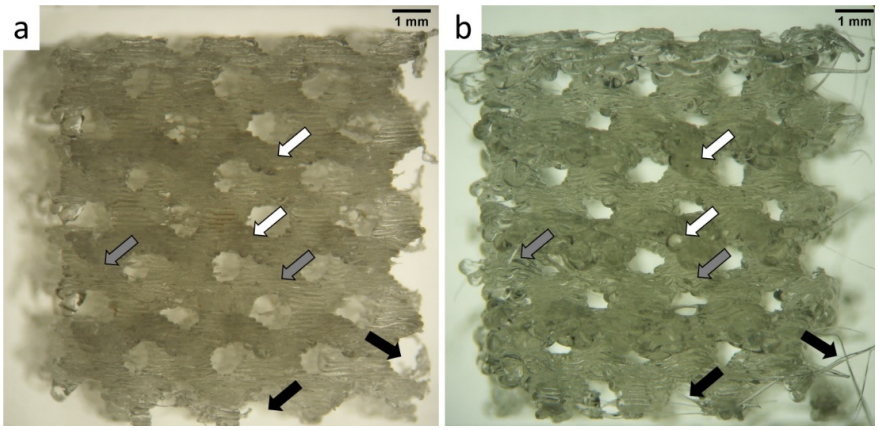


Figure 4: Pictures of gyroid structures printed (a) with and (b) without PVA support (that was later dissolved in water). Black, grey and white arrows show the presence or absence of stringing, wavy like layers and polymer drops, respectively.

3.5 Impact of annealing on printed PLA

The crystallinity of printed samples annealed overnight at 80°C was compared to the crystallinity of the as-printed polymer, using DSC (Table 2). For all samples, Tg values were close to each other and to the theoretical

value of around 58°C.[28] The structures, regardless of the design, came out of the printer in an amorphous state (crystallinity below detection level). The absence of crystallinity for not-annealed samples can be easily explained by a quick cooling of the polymer once deposited by the nozzle after being melted at 220°C (melting point around 150°C). The polymer does not have time to crystallize before reaching its Tg. Sample annealing overnight at 80°C is sufficient to reach a crystallinity of 37% for the gyroid structure, and of 40% for the control structures. Upon annealing, the polymer is kept at a temperature above the Tg during a period of time sufficient for the chains to rearrange in small crystalline zones and form spherulites. These results are consistent with the measurement of ΔCp, *i.e.* the energy required to turn the state of the amorphous part of a polymer from vitreous to viscous, which is around 0.53 $J \cdot g^{-1} \cdot K^{-1}$ for the amorphous samples compared to 0.22 $J \cdot g^{-1} \cdot K^{-1}$ for the annealed ones. This annealing process, performed after printing the structures, can be used to modify the crystallinity of the scaffold and hence, to tune its mechanical properties and its degradation rate.

Table 2: DSC measurement of glass transition temperature (T_g), change in specific heat capacity (ΔC_p) and degree of crystallinity for not-annealed and annealed gyroid and control samples. Mean (standard deviation); BDL = below detection limit (n=3).

Sample	Annealing	T_g (°C)	ΔC_p ($J.g^{-1}.K^{-1}$)	Crystallinity (%)
Gyroid	No	59.4 (0.2)	0.55 (0.02)	BDL
	Yes	58.1 (0.2)	0.23 (0.02)	36.6 (0.9)
Control 400 µm	No	58.0 (0.5)	0.51 (0.04)	BDL
	Yes	58.0 (0.7)	0.22 (0.02)	40.2 (0.2)
Control 100 µm	No	59.2 (0.4)	0.55 (0.01)	BDL
	Yes	57.3 (0.3)	0.20 (0.02)	39.6 (0.9)

3.6 Impact of geometry, printing resolution and crystallinity of the structures on mechanical resistance

The gyroid structure was chosen for its spring shape design that should provide isotropic resistance to pressure and high elasticity. Mechanical tests were performed to study the behavior of the structure depending on (i) the direction of compression with respect to the printed layers, (ii) printing

resolution, and (iii) polymer crystallinity. All these parameters are expected to influence the mechanical properties of a scaffold.[47-49] Figure 5 presents a typical stress-strain curve for each type of sample and in each direction of compression (force applied parallel or perpendicular to the printed layers). Stress-strain curves can be compared for the different conditions as the nature of the polymer and the porous fraction were kept the same. For the crystalline and amorphous gyroid structures, the curves are similar whatever the compression direction. In contrast, the compression direction significantly impacts the behavior of control scaffolds. When the compression load is applied parallel to the printed layers, peaks appear in the graphs. This phenomenon is due to buckling of the columns of the structures, one level after the other, in the process of compression. The crystallinity and the thickness of the printed layers do affect this buckling behavior. Yield strengths were determined (see Supporting Information, Figure SI3) and they are significantly higher for crystalline samples and for thicker printed layers (400 µm versus 100 µm). This means that more pressure is needed to allow the buckling of the columns for crystalline compared to amorphous samples, as well as for thicker compared to thinner printed layers. This was expected since buckling is a phenomenon of elastic instability, which happens at lower loads when the bending stiffness of a loaded column decreases. Bending stiffness is proportional to the elastic modulus, which will be higher for the crystalline phase. On the other hand, thinner printed layers create more weak boundaries within each column, which may decrease bending stiffness.

Slopes were extracted from the linear part of the stress-strain curves, to give an apparent compression modulus (see Supporting Information, Figure SI3). The results show that the gyroid structure, with an apparent compression modulus of about 50 MPa, has a more deformable behavior owing to its spring shape. Besides, layer thickness has an effect only if the load is applied parallel to the printed layers. The crystallinity, surprisingly, does not have much influence on the apparent compression modulus.

These results reveal a clear effect of the mesh geometry, the printed layer thickness and the crystallinity on the resistance to compression. The gyroid sample shows a more deformable and isotropic behavior when compressed compared to both control structures. This isotropy is of high interest in tissue engineering as it would allow the printing and the implantation of scaffolds that would support the pressure coming from any direction equally, regardless of the printing or implant orientation.

Gyroid geometry was studied in the case of Solid Freeform Fabrication of metals (titanium alloys). Even though materials are different than in the present study, comparison between structure geometries can be discussed.[50] Changing the eccentricity of pore projections in a gyroid design influenced elastic moduli and compressive strength.[34] Mechanical properties of titanium alloy gyroids were compared to octahedron models and displayed a higher yield and plateau stress.[51] A superior fatigue resistance was also evidenced and could be attributed to the continuous rate of curvature of gyroids, removing nodal points which may favor cracks initiation. The fatigue of a material is the development of structural damages after repetitive cycles of applied stresses that are lower than ultimate tensile strength or even yield strength.[52] However, all these compression studies were realized along only one axis. As shown by Heinl et al., loads applied in other directions can strongly modify the mechanical behavior of the structure.[47] They compared a diamond and a strut-based design printed in titanium alloy. Both diamond and strut-based structure showed an elastic modulus 2 and 3 times lower, respectively, for a compression parallel to printed layers if compared with a perpendicular compression. This is, however, quite inconsistent with our results, as in our case the lower moduli were observed for a compression perpendicular to printed layers. This could be due to the difference in the model used (mesh design, size of struts, space between strut, *etc*.) or to the difference in product manufacture (electron beam melting versus fused deposition modeling).

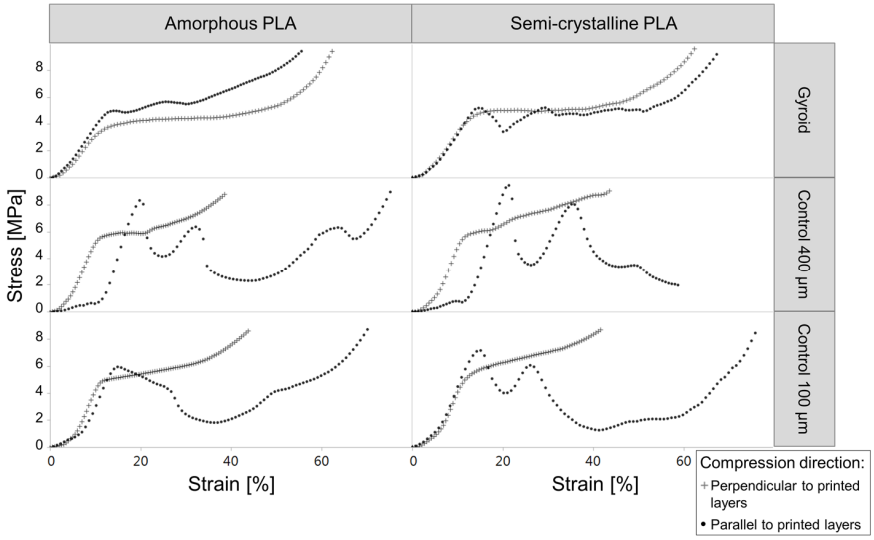


Figure 5: Stress-strain curves of amorphous (left) and semi-crystalline (right) gyroid (top) and control samples (middle and bottom) along two axes: perpendicular (+) and parallel (•) to printed layers. Results were obtained in triplicate but a single representative result is shown for the sake of clarity. All curves are available in Supporting Information (Figure SI1).

3.7 Impact of geometry, printing resolution and crystallinity of the structures on *in vitro* degradation kinetics

PLA mainly degrades by ester linkage hydrolysis, which occurs in presence of water and is catalyzed in acidic or basic conditions. Gyroid and control samples, in amorphous and semi-crystalline state, were immersed in phosphate buffered saline (PBS) during 84 weeks.

The mass of the samples was stable during about 50 weeks (Figure 6). From week 52, samples started to drastically degrade. The semi-crystalline control 100 µm, amorphous gyroid and amorphous control 100 µm were the most degraded at week 84, with a remaining mass of 20, 43 and 46% of the initial mass, respectively. The relative masses after 84 weeks were significantly higher for the 400 µm resolution samples (80% for amorphous and 73% for crystalline samples), meaning that thicker printed layers slow down the degradation process. Concerning the crystallinity, the effect seems less obvious. Indeed, annealing seems to weaken 400 µm and 100 µm control samples, but not the gyroid samples.

This sudden degradation is well known for PLA and described in literature. As water is able to penetrate the PLA bulk, hydrolysis happens throughout the

entire polymer matrix. This phenomenon is called “bulk degradation” and it has to be distinguished from “surface erosion” which happens in more hydrophobic polymers such as polycaprolactone. The bulk degradation of PLA is also the result of an autocatalytic process. When an ester bond is cleaved, a new carboxylic acid function is generated, the pH in the bulk decreases, and the degradation kinetic increases.[28, 53]

Felfel et al. and Serra et al. did not observe significant degradation of PLA films after 8 weeks at 37°C in PBS and simulated body fluid, respectively.[24, 54] Höglund et al. obtained a 75% relative mass for polylactide 3051D (NatureWorks LLC, USA) and 85% for 250 µm-thick PLLA films after 26 weeks of degradation at 37°C in PBS.[55] Ravi et al. worked on 3D printed porous sheets (800 µm thick) and measured relative masses between 76 and 89% after 26 weeks for the same polymer (PLLA, PURAC, The Netherlands) for distinct pore designs.[56] Both studies showed higher degradation rates compared to our study. However, both PLA source and sample geometry/dimensions were different. Indeed, several factors influence PLA degradation rate including the morphology, degree of crystallinity, molar mass, hydrophobicity, size and geometry of the samples, stereocomplex formation (*i.e.* formation of intermolecular complexes occurring due to non-covalent bonds between enantiomeric chains), and environmental conditions (pH and temperature).[55] In some cases, the complete degradation of PLA can take more than 3 years.[54] These differences in degradation time emphasize the importance of extended degradation studies on real or close-to-real sample sizes and geometries. A degradation environment (pH, redox potential, enzymatic content, fluid exchange, *etc.*) as close as possible to the one of the final implantation site of the scaffold would be ideal to obtain degradation kinetics relevant for the *in vivo* situation.

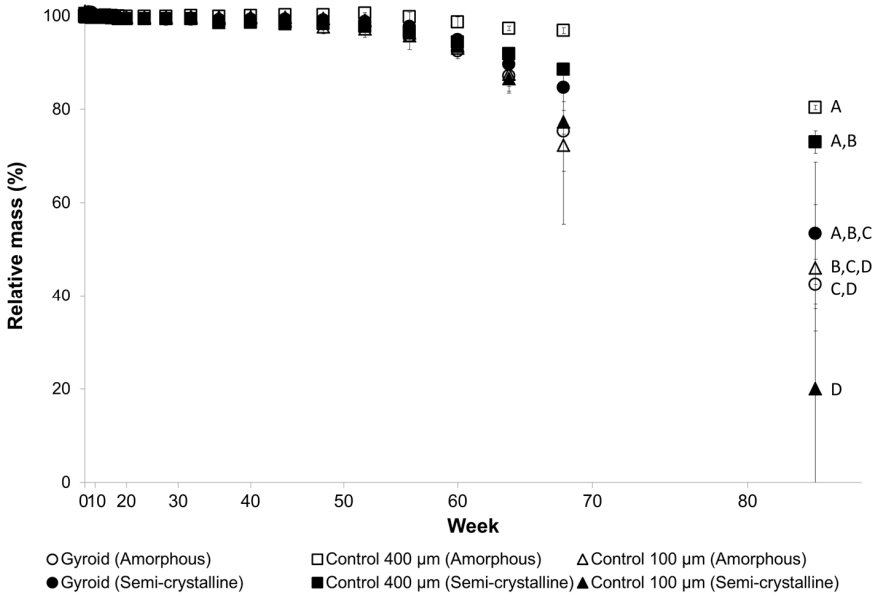


Figure 6: Degradation of not-annealed and annealed gyroid and control samples in phosphate buffered saline (PBS). For the sake of clarity, a non-linear x axis was used (the square of the number of weeks was used to build the scale) (error bar = standard deviation, n=4). Values not sharing the same letter are significantly different at week 84 (α=0.05).

Photographs of the degraded structures were taken at week 64 (Figure 7) and macroscopic changes are visible for amorphous scaffolds: a change in color, from clear and translucent to a milky white and completely opaque polymer. Although sample masses were stable for 50 weeks, this observation was already visible after 3 weeks. This has already been attributed to the swelling of PLA at an early stage of the bulk erosion process[56], which leads to a change in optical properties. In contrast, such change was not observed for semi-crystalline samples, which were less translucent initially.

Scaffold geometry also impacts degradation. Control scaffolds degrade by losing struts one after the other, whereas the gyroid structure tends to retain its integrity. This could be related to the inclination angles of the circular gyroid struts that continuously vary all over the structure. This results in slight changes in area and position between two adjacent layers.[32] The layers are then more interconnected in the case of the gyroid compared to the strut-based scaffold, which has only a few connection points between struts of different levels. However, in the case of the amorphous gyroid, cracks arise at the junctions of printed layers, resulting in elongation of the sample.

Therefore, the annealing process seems to have a positive effect on the cohesion of the printed layers of the gyroid samples.

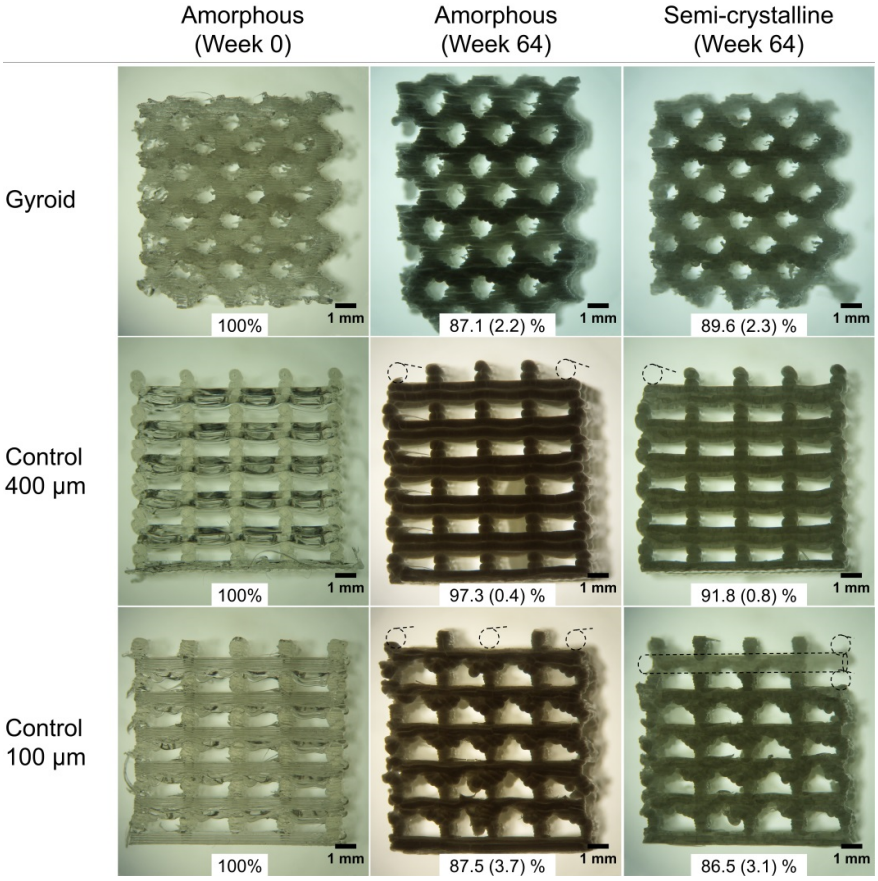


Figure 7: Pictures of gyroid (top) and control (middle – 400 µm and bottom – 100 µm) samples, as produced (left) or after 64 weeks of degradation (middle – amorphous samples, right – semi-crystalline samples). Semi-crystalline samples as produced (Week 0) are not shown on the picture as, except regarding the less translucent color, the samples looked similar to amorphous samples (Week 0). Dotted lines represent struts present at the beginning of the experiment that were lost due to structure degradation. Means of relative masses and standard deviations (n=4) are presented in white boxes.

The degradation seems affected only by printed layer thickness, a higher thickness reducing the speed of the process. Neither crystallinity nor mesh geometry affect significantly the degradation rate even though the change in mesh geometry will influence the detachment of pieces from the structures. Besides this, the annealing process improves layers attachment in the case of gyroid samples.

4 Conclusions

A complex gyroid scaffold was printed in PLA close to the resolution limit of fused deposition modeling, a simple and low-cost additive manufacturing technique. This geometry is particularly suitable for tissue engineering approaches given the large pore size, high porous fraction and mechanical robustness.

The reliability of the printing procedure was demonstrated based on a µCT scan, on porous fraction measurement and on surface topography analysis. PLA is a FDA- and EMA-approved biodegradable and implantable polymer. The water-soluble PVA support was shown to be important to obtain a controlled and well-defined shape of the gyroid structure, and it can be easily dissolved after printing. Annealing was used to increase the crystallinity fraction of the polymer, with a view to tune mechanical properties and degradation rate. Mechanical compression tests showed that crystallinity, layer resolution, and especially the structure design influence the stress-strain curves. Moreover, the gyroid structure presents an isotropic behavior regarding compression, in contrast with strut-based designs commonly reported in the literature. Degradation tests highlighted the faster degradation for thinner printed layers, whereas the gyroid geometry prevents the detachment of pieces from the structure upon degradation, and the annealing process increases layers attachment. Results, brought together, show that the gyroid design shows superior properties to be used for personalized implantable scaffolds for tissue engineering.

5 Supporting information

Impact of geometry, printing resolution and crystallinity of the structures on mechanical resistance

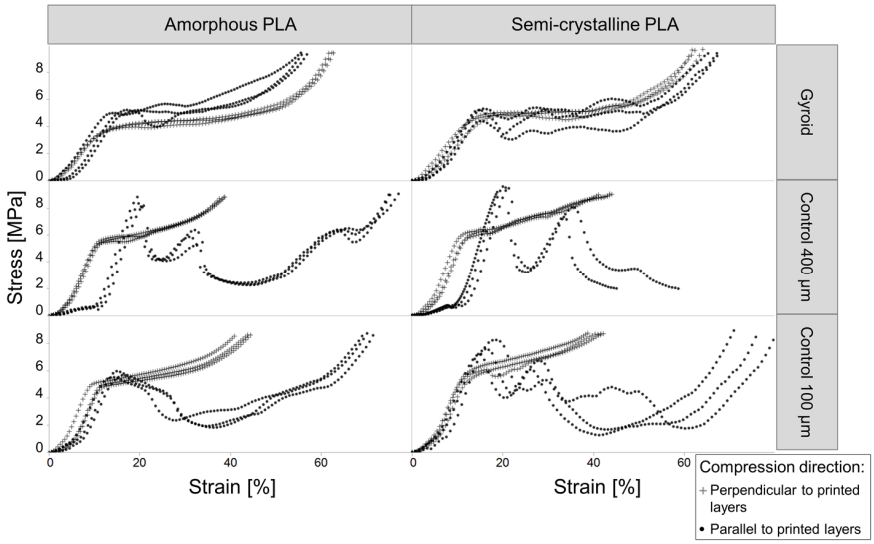


Figure SI1: Stress-strain curves of amorphous (left) and semi-crystalline (right) gyroid (top) and control samples (middle and bottom) along two axes: perpendicular (+) and parallel (•) to printed layers. Results were obtained in triplicate.

The compressed samples are porous and real moduli can therefore not be extracted. The values of the first significant slopes computed at the initial linear part of stress-strain curves (Figure SI2) can, however, give an apparent compression modulus of the structures and can be compared. The first slope until around 15% of compression for control 400 µm samples, compressed parallel to the printed layers (both amorphous and semi-crystalline), were not taken into account as they are a consequence of a printing artifact (small outgrows present at the edges of the main body of the sample). Comparing slopes (Figure SI3), three groups of close values can be highlighted: (i) amorphous and semi-crystalline gyroid samples compressed in both directions show the lowest moduli around 50 MPa; (ii) amorphous and semi-crystalline control 100 µm samples compressed in both directions as well as amorphous and semi-crystalline control 400 µm samples compressed perpendicular to the printed layers give intermediate values around 80 MPa; and (iii) amorphous and semi-crystalline control 400 µm samples compressed parallel to the printed layers show the highest values around 115 MPa. These results show that the mesh geometry has an effect on the apparent modulus

of the structure. The gyroid, owing to its spring shape, shows as expected a more deformable behavior. The layer thickness has an effect only in the case of a compression applied parallel to the printed layers, meaning that a smaller number of thick layers (400 µm) results in scaffolds that are less deformable than a higher number of thinner layers (100 µm). This can be attributed to the presence of a higher number of weak boundaries within the columns of the structures when the printed layer is thinner. The crystallinity, in opposition to expectations, does not have much influence on the apparent modulus.

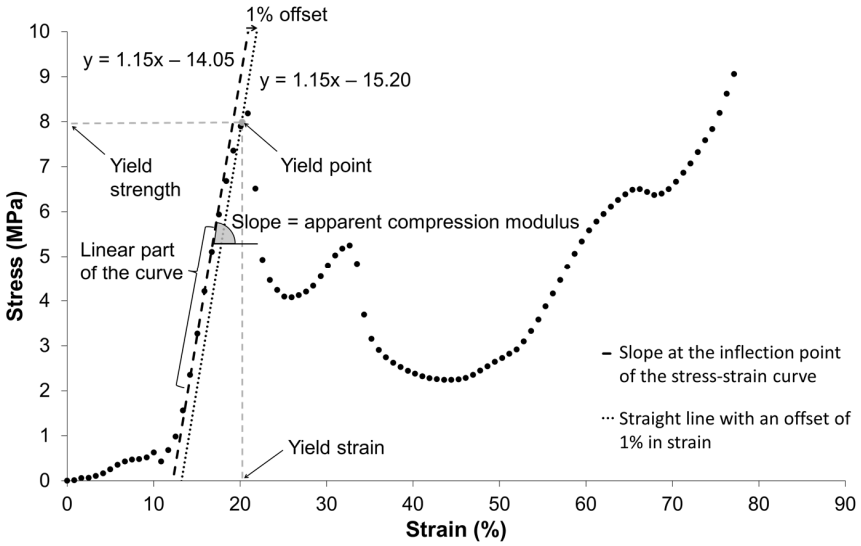


Figure SI2: Offset method applied to a stress-strain curve measured from the compression, applied parallel to printed layers, of an amorphous control 400 µm sample. Method followed to obtain (i) the apparent compression modulus, from the slope of the initial linear part of stress-strain curve, and (ii) yield strength, from the 1% translation in strain of the straight line resulting from the prolongation of the initial linear part. The intersection between this second straight line and the stress-strain curve gives the yield point. The y-value of the yield point gives the yield strength while the x-value gives the yield strain.

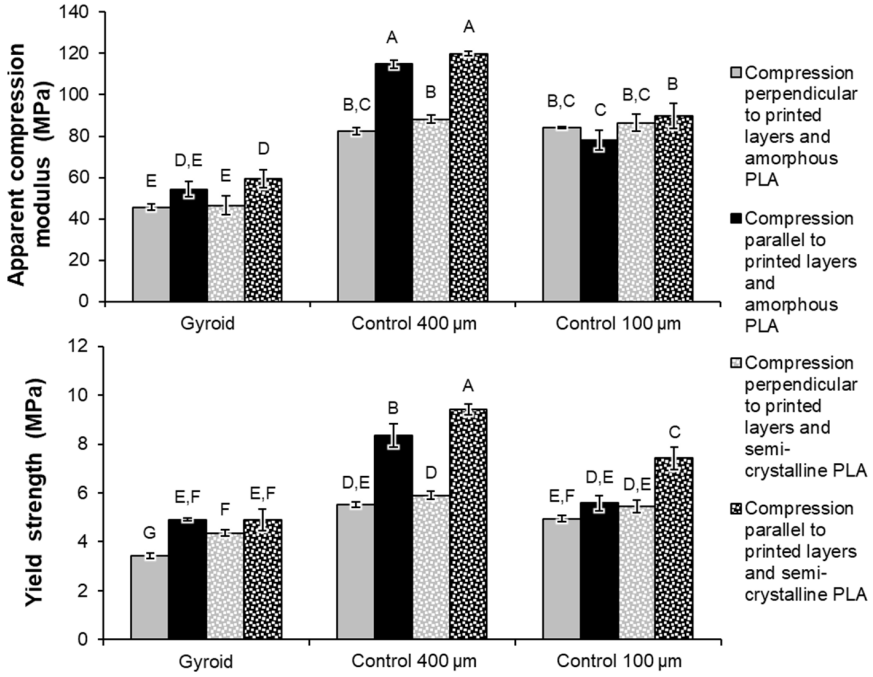


Figure SI3: Apparent compression modulus (obtained from the slope of the initial linear part of stress-strain curve) and yield strength (obtained from stress-strain curves with the offset method using a value of 1%) of amorphous and semi-crystalline gyroid and control samples along two axes: perpendicularly and parallel to printed layers (error bar= standard deviation, n=3). Values not sharing the same letter are significantly different (α=0.05).

6 References

1. Verhulsel, M.; Vignes, M.; Descroix, S.; Malaquin, L.; Vignjevic, D. M.; Viovy, J. L., A review of microfabrication and hydrogel engineering for micro-organs on chips. *Biomaterials* **2014,** *35* (6), 1816-1832.

2. Cox, S. C.; Thornby, J. A.; Gibbons, G. J.; Williams, M. A.; Mallick, K. K., 3D printing of porous hydroxyapatite scaffolds intended for use in bone tissue engineering applications. *Mater. Sci. Eng. C Mater. Biol. Appl.* **2015,** *47*, 237-247.

3. Pineda, E. T.; Nerem, R. M.; Ahsan, T., Differentiation patterns of embryonic stem cells in two- versus three-dimensional culture. *Cells Tissues Organs* **2013,** *197* (5), 399-410.

4. Tang, L.; Lu, X.; Zhu, R.; Qian, T.; Tao, Y.; Li, K.; Zheng, J.; Zhao, P.; Li, S.; Wang, X.; Li, L., Adipose-Derived Stem Cells Expressing the Neurogenin-

2 Promote Functional Recovery After Spinal Cord Injury in Rat. *Cell. Mol. Neurobiol.* **2016,** *36* (5), 657-667.
5. Gao, F.; Chiu, S. M.; Motan, D. A. L.; Zhang, Z.; Chen, L.; Ji, H. L.; Tse, H. F.; Fu, Q. L.; Lian, Q., Mesenchymal stem cells and immunomodulation: current status and future prospects. *Cell Death Dis.* **2016,** *7*, e2062.
6. Park, S.; Kim, G.; Jeon, Y. C.; Koh, Y.; Kim, W., 3D polycaprolactone scaffolds with controlled pore structure using a rapid prototyping system. *J. Mater. Sci. Mater. Med.* **2009,** *20* (1), 229-234.
7. Ahmed, T. A. E.; Dare, E. V.; Hincke, M., Fibrin: A versatile scaffold for tissue engineering applications. *Tissue Eng. Part B Rev.* **2008,** *14* (2), 199-215.
8. Lee, H.; Ahn, S.; Bonassar, L. J.; Kim, G., Cell(MC3T3-E1)-printed poly(ε-caprolactone)/alginate hybrid scaffolds for tissue regeneration. *Macromol. Rapid. Comm.* **2013,** *34* (2), 142-149.
9. Jung, J. W.; Park, J. H.; Hong, J. M.; Kang, H.-W.; Cho, D.-W., Octahedron pore architecture to enhance flexibility of nasal implant-shaped scaffold for rhinoplasty. *Int. J. Precis. Eng. Man.* **2014,** *15* (12), 2611-2616.
10. Trachtenberg, J. E.; Mountziaris, P. M.; Miller, J. S.; Wettergreen, M.; Kasper, F. K.; Mikos, A. G., Open-source three-dimensional printing of biodegradable polymer scaffolds for tissue engineering. *J. Biomed. Mater. Res. A* **2014,** *102* (12), 4326-4335.
11. Seyednejad, H.; Gawlitta, D.; Kuiper, R. V.; de Bruin, A.; van Nostrum, C. F.; Vermonden, T.; Dhert, W. J. A.; Hennink, W. E., *In vivo* biocompatibility and biodegradation of 3D-printed porous scaffolds based on a hydroxyl-functionalized poly(ε-caprolactone). *Biomaterials* **2012,** *33* (17), 4309-4318.
12. Gross, B. C.; Erkal, J. L.; Lockwood, S. Y.; Chen, C.; Spence, D. M., Evaluation of 3D printing and its potential impact on biotechnology and the chemical sciences. *Anal. Chem.* **2014,** *86* (7), 3240-3253.
13. Thrivikraman, G.; Athirasala, A.; Twohig, C.; Boda, S. K.; Bertassoni, L. E., Biomaterials for Craniofacial Bone Regeneration. *Dent. Clin. N. Am.* **2017,** *61* (4), 835-856.
14. Ho, L.; Hsu, S.-h., Cell reprogramming by 3D bioprinting of human fibroblasts in polyurethane hydrogel for fabrication of neural-like constructs. *Acta Biomater.* **2018,** *70*, 57-70.
15. Giuseppe, M. D.; Law, N.; Webb, B.; A. Macrae, R.; Liew, L. J.; Sercombe, T. B.; Dilley, R. J.; Doyle, B. J., Mechanical behaviour of alginate-gelatin hydrogels for 3D bioprinting. *J. Mech. Behav. Biomed. Mater.* **2018,** *79*, 150-157.
16. Walker, J. M.; Bodamer, E.; Krebs, O.; Luo, Y.; Kleinfehn, A.; Becker, M. L.; Dean, D., Effect of Chemical and Physical Properties on the *In Vitro*

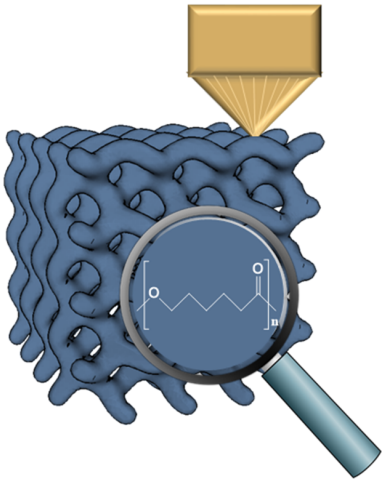
Degradation of 3D Printed High Resolution Poly(propylene fumarate) Scaffolds. *Biomacromolecules* **2017,** *18* (4), 1419-1425.
17. Teixeira, B. N.; Aprile, P.; Mendonca, R. H.; Kelly, D. J.; Thire, R., Evaluation of bone marrow stem cell response to PLA scaffolds manufactured by 3D printing and coated with polydopamine and type I collagen. *J. Biomed. Mater. Res. B Appl. Biomater.* **2019,** *107* (1), 37-49.
18. Barba, A.; Diez-Escudero, A.; Maazouz, Y.; Rappe, K.; Espanol, M.; Montufar, E. B.; Bonany, M.; Sadowska, J. M.; Guillem-Marti, J.; Öhman-Mägi, C.; Persson, C.; Manzanares, M.-C.; Franch, J.; Ginebra, M.-P., Osteoinduction by Foamed and 3D-Printed Calcium Phosphate Scaffolds: Effect of Nanostructure and Pore Architecture. *ACS Appl. Mater. Inter.* **2017,** *9* (48), 41722-41736.
19. Deng, C.; Yao, Q.; Feng, C.; Li, J.; Wang, L.; Cheng, G.; Shi, M.; Chen, L.; Chang, J.; Wu, C., 3D Printing of Bilineage Constructive Biomaterials for Bone and Cartilage Regeneration. *Adv. Funct. Mater.* **2017,** *27* (36), 1703117.
20. Kim, J. A.; Yun, H.-s.; Choi, Y.-A.; Kim, J.-E.; Choi, S.-Y.; Kwon, T.-G.; Kim, Y. K.; Kwon, T.-Y.; Bae, M. A.; Kim, N. J.; Bae, Y. C.; Shin, H.-I.; Park, E. K., Magnesium phosphate ceramics incorporating a novel indene compound promote osteoblast differentiation *in vitro* and bone regeneration *in vivo*. *Biomaterials* **2018,** *157*, 51-61.
21. Gao, F.; Xu, Z.; Liang, Q.; Liu, B.; Li, H.; Wu, Y.; Zhang, Y.; Lin, Z.; Wu, M.; Ruan, C.; Liu, W., Direct 3D Printing of High Strength Biohybrid Gradient Hydrogel Scaffolds for Efficient Repair of Osteochondral Defect. *Adv. Funct. Mater.* **2018,** *28*, 1706644.
22. Pati, F.; Ha, D.-H.; Jang, J.; Han, H. H.; Rhie, J.-W.; Cho, D.-W., Biomimetic 3D tissue printing for soft tissue regeneration. *Biomaterials* **2015,** *62*, 164-175.
23. Buyuksungur, S.; Endogan Tanir, T.; Buyuksungur, A.; Bektas, E. I.; Torun Kose, G.; Yucel, D.; Beyzadeoglu, T.; Cetinkaya, E.; Yenigun, C.; Tonuk, E.; Hasirci, V.; Hasirci, N., 3D printed poly(ε-caprolactone) scaffolds modified with hydroxyapatite and poly(propylene fumarate) and their effects on the healing of rabbit femur defects. *Biomater. Sci.* **2017,** *5* (10), 2144-2158.
24. Serra, T.; Ortiz-Hernandez, M.; Engel, E.; Planell, J. A.; Navarro, M., Relevance of PEG in PLA-based blends for tissue engineering 3D-printed scaffolds. *Mater. Sci. Eng. C Mater. Biol. Appl.* **2014,** *38*, 55-62.
25. Serra, T.; Planell, J. A.; Navarro, M., High-resolution PLA-based composite scaffolds via 3-D printing technology. *Acta Biomater.* **2013,** *9* (3), 5521-5530.

26. Silva, J. M.; Videira, M.; Gaspar, R.; Préat, V.; Florindo, H. F., Immune system targeting by biodegradable nanoparticles for cancer vaccines. *J. Control. Release* **2013,** *168* (2), 179-199.
27. Uzel, A. P.; Seris, E.; Henri, S.; Jouan, G.; Borget, P.; Daculsi, G., Preclinical and clinical cases of new absorbable composite interference screws in osteoarticular surgery. *Key Eng. Mater.* **2013,** *529-530*, 325-330.
28. Henton, D. E.; Gruber, P.; Lunt, J.; Randall, J., Polylactic Acid Technology. In *Natural Fibers, Biopolymers, and Biocomposites*, Group, T. F., Ed. CRC Press Boca Raton, 2005; pp 527-577.
29. Temple, J. P.; Hutton, D. L.; Hung, B. P.; Huri, P. Y.; Cook, C. A.; Kondragunta, R.; Jia, X.; Grayson, W. L., Engineering anatomically shaped vascularized bone grafts with hASCs and 3D-printed PCL scaffolds. *J. Biomed. Mater. Res. A* **2014,** *102* (12), 4317-4325.
30. Wang, F.; Shor, L.; Starly, B.; Darling, A.; Güçeri, S.; Sun, W. In *Fabrication of cellular poly-ε-caprolactone (PCL) scaffolds by precision extruding deposition process*, Bioengineering, Proceedings of the Northeast Conference, New Jersey, New Jersey, 2003; pp 181-182.
31. Dolan, J. A.; Wilts, B. D.; Vignolini, S.; Baumberg, J. J.; Steiner, U.; Wilkinson, T. D., Optical Properties of Gyroid Structured Materials: From Photonic Crystals to Metamaterials. *Adv. Opt. Mater.* **2015,** *3* (1), 12-32.
32. Yan, C.; Hao, L.; Hussein, A.; Raymont, D., Evaluations of cellular lattice structures manufactured using selective laser melting. *Int. J. Mach. Tool. Manu.* **2012,** *62*, 32-38.
33. Torres-Rendon, J. G.; Femmer, T.; De Laporte, L.; Tigges, T.; Rahimi, K.; Gremse, F.; Zafarnia, S.; Lederle, W.; Ifuku, S.; Wessling, M.; Hardy, J. G.; Walther, A., Bioactive gyroid scaffolds formed by sacrificial templating of nanocellulose and nanochitin hydrogels as instructive platforms for biomimetic tissue engineering. *Adv. Mater.* **2015,** *27* (19), 2989-2995.
34. Yánez, A.; Herrera, A.; Martel, O.; Monopoli, D.; Afonso, H., Compressive behaviour of gyroid lattice structures for human cancellous bone implant applications. *Mater. Sci. Eng. C Mater. Biol. Appl.* **2016,** *68*, 445-448.
35. Wang, Q.; Ren, L.; Li, X.; Zhang, S.; Sercombe, T. B.; Yang, K., Antimicrobial Cu-bearing stainless steel scaffolds. *Mater. Sci. Eng. C Mater. Biol. Appl.* **2016,** *68*, 519-522.
36. Luo, Y.; Dolder, C. K.; Walker, J. M.; Mishra, R.; Dean, D.; Becker, M. L., Synthesis and Biological Evaluation of Well-Defined Poly(propylene fumarate) Oligomers and Their Use in 3D Printed Scaffolds. *Biomacromolecules* **2016,** *17* (2), 690-697.
37. http://www.3dvia.com/content/DCA841D2E4F6C8DA (attached licence: http://creativecommons.org/licenses/by-nc/2.5/) (accessed July 2016).

38. Mauck, S. C.; Wang, S.; Ding, W.; Rohde, B. J.; Fortune, C. K.; Yang, G.; Ahn, S.-K.; Robertson, M. L., Biorenewable Tough Blends of Polylactide and Acrylated Epoxidized Soybean Oil Compatibilized by a Polylactide Star Polymer. *Macromolecules* **2016,** *49* (5), 1605-1615.
39. Schneider, C. A.; Rasband, W. S.; Eliceiri, K. W., NIH Image to ImageJ: 25 years of image analysis. *Nat. Methods* **2012,** *9* (7), 671-675.
40. Krotkỳ, J.; Honzíková, J.; Moc, P., Deformation of print PLA material depending on the temperature of reheating printing pad. *Manuf. Technol.* **2016,** *16* (1), 136-140.
41. Hong, J. H.; Yu, T.; Chen, Z.; Park, S. J.; Kim, Y. H., Improvement of flexural strength and compressive strength by heat treatment of PLA filament for 3D-printing. *Mod. Phys. Lett. B* **2019,** *33* (14-15), 1940025.
42. Guyot, Y.; Papantoniou, I.; Chai, Y. C.; Van Bael, S.; Schrooten, J.; Geris, L., A computational model for cell/ECM growth on 3D surfaces using the level set method: a bone tissue engineering case study. *Biomech. Model. Mechan.* **2014,** *13* (6), 1361-1371.
43. Guyot, Y.; Papantoniou, I.; Luyten, F. P.; Geris, L., Coupling curvature-dependent and shear stress-stimulated neotissue growth in dynamic bioreactor cultures: a 3D computational model of a complete scaffold. *Biomech. Model. Mechan.* **2016,** *15* (1), 169-180.
44. Janson, I. A.; Putnam, A. J., Extracellular matrix elasticity and topography: Material-based cues that affect cell function via conserved mechanisms. *J. Biomed. Mater. Res. A* **2015,** *103* (3), 1246-1258.
45. Dalby, M. J.; Riehle, M. O.; Yarwood, S. J.; Wilkinson, C. D. W.; Curtis, A. S. G., Nucleus alignment and cell signaling in fibroblasts: response to a micro-grooved topography. *Exp. Cell. Res.* **2003,** *284* (2), 274-282.
46. Charest, J. L.; García, A. J.; King, W. P., Myoblast alignment and differentiation on cell culture substrates with microscale topography and model chemistries. *Biomaterials* **2007,** *28* (13), 2202-2210.
47. Heinl, P.; Müller, L.; Körner, C.; Singer, R. F.; Müller, F. A., Cellular Ti-6Al-4V structures with interconnected macro porosity for bone implants fabricated by selective electron beam melting. *Acta Biomater.* **2008,** *4* (5), 1536-1544.
48. Guarino, V.; Marrese, M.; Ambrosio, L., Chemical and Physical Properties of Polymers for Biomedical Use. In *Advanced Polymers in Medicine*, Puoci, F., Ed. Springer International Publishing: Cham, 2015; pp 67-90.
49. Wu, W.; Geng, P.; Li, G.; Zhao, D.; Zhang, H.; Zhao, J., Influence of Layer Thickness and Raster Angle on the Mechanical Properties of 3D-Printed PEEK and a Comparative Mechanical Study between PEEK and ABS. *Materials* **2015,** *8* (9), 5834-5846.

50. Pia, G.; Brun, M.; Aymerich, F.; Delogu, F., Gyroidal structures as approximants to nanoporous metal foams: clues from mechanical properties. *J. Mater. Sci.* **2017,** *52* (2), 1106-1122.
51. Speirs, M.; Van Hooreweder, B.; Van Humbeeck, J.; Kruth, J. P., Fatigue behaviour of NiTi shape memory alloy scaffolds produced by SLM, a unit cell design comparison. *J. Mech. Behav. Biomed. Mater.* **2017,** *70*, 53-59.
52. Safai, L.; Cuellar, J. S.; Smit, G.; Zadpoor, A. A., A review of the fatigue behavior of 3D printed polymers. *Addit. Manuf.* **2019,** *28*, 87-97.
53. Woodruff, M. A.; Hutmacher, D. W., The return of a forgotten polymer - Polycaprolactone in the 21st century. *Prog. Polym. Sci.* **2010,** *35* (10), 1217-1256.
54. Felfel, R. M.; Hossain, K. M. Z.; Parsons, A. J.; Rudd, C. D.; Ahmed, I., Accelerated *in vitro* degradation properties of polylactic acid/phosphate glass fibre composites. *J. Mater. Sci.* **2015,** *50* (11), 3942-3955.
55. Höglund, A.; Odelius, K.; Albertsson, A.-C., Crucial Differences in the Hydrolytic Degradation between Industrial Polylactide and Laboratory-Scale Poly(L-lactide). *ACS Appl. Mater. Inter.* **2012,** *4* (5), 2788-2793.
56. Ravi, P.; Shiakolas, P. S.; Welch, T. R., Poly-l-lactic acid: Pellets to fiber to fused filament fabricated scaffolds, and scaffold weight loss study. *Addit. Manuf.* **2017,** *16*, 167-176.

Chapter 2: Optimization of poly(ε-caprolactone) 3D printing



In this second chapter, the potential use of poly(ε-caprolactone) (PCL) to produce gyroid scaffolds using fused deposition modeling was investigated. Printing parameters were optimized using two different supporting materials and a morphological evaluation was carried out. Besides, the porous fraction of the printed scaffolds was compared to the theoretical one. Mechanical properties of the PCL gyroid scaffolds were compared to the ones of common strut-based scaffolds presenting the same porous fraction. The spring shape structure of the gyroid was accurately printed and pore interconnectivity was demonstrated by micro-CT. The porous fraction of the gyroid scaffolds was 69% as expected from the model. Resistance against compression did not show the isotropic behavior expected for a gyroid design. Apparent compression moduli between 6 and 12 MPa were measured, which makes the PCL gyroid scaffold a good candidate for cartilage regeneration.

We sincerely thank Robin Verheyen[1], Prof. Aart Willem Van Vuure (KUL), Carlos A. Fuentes Rojas (KUL), Prof. Yves Dufrêne, Sylvie Derclaye, Prof. Julian Leprince, Prof. Arnaud Delcorte and Claude Poleunis for their contribution to the work presented in this chapter.

1 Introduction

Like PLA, poly(ε-caprolactone) (PCL) is a biocompatible polymer broadly used in regenerative medicine and drug delivery. It is a hydrophobic and semi-crystalline polymer and, like PLA, it belongs to the aliphatic polyester family. This thermoplastic polymer has a low melting point (59-64°C) and a low glass transition temperature (-60°C). It can be tailored to adjust its degradation kinetics and its mechanical properties, which is a strong asset. Furthermore, it can be functionalized to increase hydrophilicity, adhesion and bioactivity, with a view to foster cell response. PCL has superior rheological and viscoelastic properties and is easy to manufacture into a large range of implants and devices. Its main disadvantages are its slow degradation rate and its mechanical properties that are not suited for load-bearing applications. Depending on the application, PLA, PGA or their copolymers may be preferred for their faster degradation rate. In addition, PLA presents more suitable mechanical properties for the production of implantable and biodegradable plates and screws. However, PCL is appropriate to produce devices, such as degradable sutures, that provide a long-term release of molecules loaded in their matrix.[2] In tissue engineering, PCL is used for cartilage repair (nose, ears, trachea,…)[3] owing to its higher elasticity at body temperature compared to PLA[4, 5] and its longer resorption time compared to PGA[6].

PCL printing, using fused deposition modelling (FDM) or other extrusion-based printing techniques to produce strut-based scaffolds, was well studied in literature. The melt flow behavior of PCL[7] in such printing techniques and the effect of process parameters (extrusion temperature, deposition velocity, slice thickness,…) on morphological and mechanical properties of the printed scaffold[8] were evaluated. Strut-based scaffolds presenting different strut sizes, strut diameters, strut orientations and pore sizes were produced and the effect of these geometries on scaffold mechanical properties was investigated[9-11]. Many modifications were proposed to improve PCL scaffolds mechanical properties, hydrophilicity and bioactivity. PCL was blended with PLA[4, 12] or PLGA[13, 14], and/or filled with nano-hydroxyapatite[15-17], tricalcium phosphate[13, 14], bioactive glass[18] or graphene oxide particles[16]. PCL copolymers were also proposed to control scaffold degradation rate.[18, 19] Printed scaffold surface modifications were performed using nano-hydroxyapatite and poly(propylene fumarate) to improve surface

hydrophilicity and promote osteoconductivity.[20] Natural polymers such as collagen[21], alginate[22], chitosan[23] and hyaluronic acid[24] were added to printed PCL scaffolds to produce natural/synthetic hybrid scaffolds. They combine the mechanical properties of a synthetic polymer with the bioactivity of a natural polymer. *In vitro* degradation of PCL scaffolds[25] and their effect on adipose-derived mesenchymal stem cell osteogenic and adipogenic differentiation were studied[26]. *In vivo* implantation of PCL scaffolds was evaluated to produce goat tissue-engineered trachea[27] and to repair canine sternal defects[28]. All these studies were achieved on simple strut-based scaffolds, which reflects the lack in complex meshes to produce PCL scaffolds by extrusion-based printing methods.

To our knowledge, only one recent study proposed a sheet-based gyroid design as scaffold mesh (Figure 1 A and B).[29] However, mechanical properties of the scaffold were not studied.

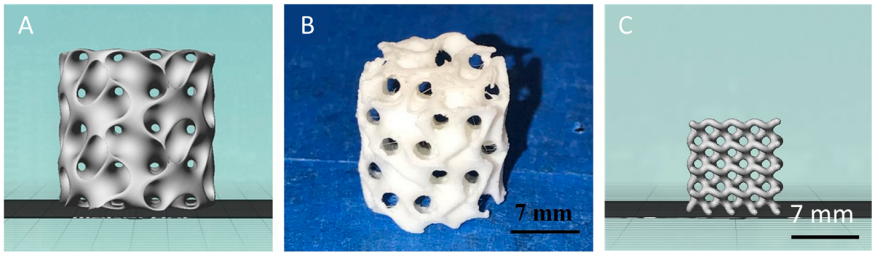


Figure 1: (A) Sheet-based gyroid model and (B) PCL-printed sheet-based gyroid scaffold and (C) skeletal-based gyroid model. Adapted from [29].

In this second chapter, PCL printing parameters are optimized and pushed to the resolution limit of FDM to achieve the challenging 3D printing of skeletal-based gyroid scaffolds (Figure 1 C). The gyroid presents an isotropic geometry, which is much more complex than strut-based scaffolds commonly seen in literature. Furthermore, mechanical properties of both kinds of scaffolds are compared.

2 Materials and methods

2.1 PCL scaffold model and 3D printing

The obtention of the CAD models was already discussed in Chapter 1 of this Part. Briefly, the gyroid model was downloaded and was made four times thicker to allow printing using FDM. The strut-based model (control) was

designed to have similar strut diameter and porous fraction as the gyroid model. The gyroid model was printed in PCL (Makerbot, Germany), and High Impact Polystyrene (HIPS) (Makerbot, Germany) was first used as supporting material. HIPS was removed using (R)-+-Limonene. The use of water-soluble poly(vinyl alcohol) (PVA) as supporting material replaced the use of HIPS to avoid treatment with an organic solvent and to better fit clinical requirements. The HIPS-supported gyroid was sliced using the MakerWare program V2.4 (Makerbot Software, Team in Brooklyn, NY, USA) while the PVA-supported gyroid was sliced using the Makerbot Desktop program V3.9 (Makerbot Software, Team in Brooklyn, NY, USA).

Gyroids were imported and duplicated to print 18 scaffolds (when HIPS-supported) (Figure 2) or 6 scaffolds (when PVA-supported) in parallel (Table 1). Scaffolds were printed using a concentric pattern with a full infill. The vertical resolution was set to 100 µm while the horizontal resolution was imposed by the nozzle diameter (400 µm). Extrusion temperatures of 95°C, 250°C and 205°C were used for PCL, HIPS and PVA, respectively. PVA was dried overnight at 80°C before use. Printing speed was set to 40 mm/s with the enabled dynamic speed option when HIPS-supported and was set to 10 mm/s when PVA-supported (the dynamic speed option being no more available in the slicing program). The dynamic speed option automatically reduces the printing speed on tight curves. The support was printed 0.4 mm away from the scaffold and its density was set to 0.5 for HIPS-supported gyroids and 0.7 for PVA-supported gyroids. Purge walls and rafts were printed. For HIPS-supported scaffolds, the printer was placed in a cold room (4°C) during printing to allow a faster cooling of the polymer after deposition. Printing of PVA-supported gyroids was performed at room temperature and using a fan placed in front of the printer. After printing, the supporting material (HIPS or PVA) was dissolved (using limonene or water, respectively). Control strut-based scaffolds were printed in similar conditions (Table 1) but without supporting material, using a vertical resolution of 300 µm and a printing speed of 30 mm/s.

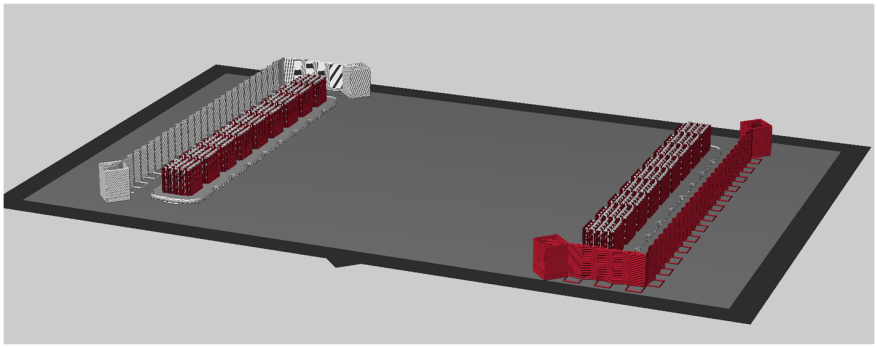


Figure 2: Print preview of the 18 gyroid scaffolds printed in parallel. PCL in white and supporting material in red.

Table 1: Main printing parameters used for the printing of HIPS- or PVA-supported gyroid scaffolds as well as for strut-based control scaffolds.

	Gyroid scaffold		Strut-based scaffold
Supporting material	HIPS	PVA	No support
Number of scaffolds printed in parallel	18	6	6
Raft	Yes	Yes	Yes
Purge wall	Yes	Yes	Yes
Pattern	Concentric	Concentric	Concentric
Infill	100%	100%	100%
Vertical resolution (Z)	100 µm	100 µm	300 µm
Lateral resolution (XY)	400 µm	400 µm	400 µm
Extrusion temperature	PCL: 95°C HIPS: 250°C	PCL: 95°C PVA: 205°C	PCL: 95°C
Printing speed	40 mm/s	10 mm/s	30 mm/s
Dynamic speed option	Enabled	No longer available	No longer available
Support-to-model distance	0.4 mm	0.4 mm	No support
Support density	0.5	0.7	No support
Temperature of printing environment	4°C	Room temperature with external ventilation	Room temperature with external ventilation

2.2 Morphological characterization

Morphological characterization of the 3D-printed scaffolds was achieved using three different techniques. A first rough evaluation was performed using a low magnification microscope to observe the general structure and printing defects. Then, the inside of the scaffold and printing patterns were studied owing to a 3D reconstruction of the PCL gyroid scaffold using micro-computed tomography (µCT) scans. Finally, boundaries and surface topography of the samples were imaged using a profilometer.

After printing and support removal, scaffolds were observed using a low magnification microscope (Zeiss Stemi DV4 Stereomicroscope, Carl Zeiss MicroImaging GmbH, Germany) using 12X, 16X and 32X magnifications.

The µCT scan was acquired at the KULeuven using a Phoenix NanoTom X-ray computed tomography equipment (General Electric Company, Fairfield, USA) as already described in Chapter 1 of this Part. Briefly, the applied voltage and current were 40 kV and 620 µA, respectively. A molybdenum target was used and the exposure time was 500 ms. The obtained voxel size was 6.1 µm³. The stack of scan images was then thresholded with the CTVox software (Bruker microCT, Kontich, Belgium) to differentiate the polymer from the pores.

Sample topography was evaluated using a Dektak XT (Bruker, USA) profilometer equipped with a needle presenting a 0.7 µm curvature radius and using the Vision64 acquisition software (V5.40). As explained in Chapter 1 of this Part, to prevent the needle to get stuck and break inside a pore, the gyroid model was modified to have the most external 0.5 mm of the structure printed on the sides of a plain cube. Areas of 6.7x4.4 mm² and 8.4x4.7 mm² were scanned at the top and the side of the printed structure, respectively. Scanned lines were separated by 5 µm for both top and side faces and the linear resolution was 0.36 µm/pt and 0.47 µm/pt, respectively. On both top and side faces, a mass of 0.5 mg was applied on the needle.

2.3 Porous fraction evaluation

PCL gyroid scaffolds printed with PVA support (n=6) as well as strut-based scaffolds (n=6) were weighed, and their length, width and depth dimensions were measured after PVA dissolution in water (if any). As already described in Chapter 1 of this Part, the mass and volume of the samples were used to evaluate the porous fraction. Briefly, equation (1) was used to compare the

porous fraction of the gyroid scaffolds to the porous fraction of the strut-based scaffold:

$$Porous\ fraction\ [\%] = \frac{V_{obj}[m^3] - \frac{m\ [kg]}{\rho_{PCL}[kg/m^3]}}{V_{obj}[m^3]} x100 \quad (1)$$

Where:

V_{obj} represents the entire volume of the object, based on its dimensions;

m is the mass of the object;

ρ_{PCL} is the density of PCL, equal to 1145 kg/m^3.[8, 30]

Porous fractions of both kind of 3D-printed scaffolds were also compared to their respective theoretical value, which were determined using Netfabb basic 7.4.0 (Netfabb GmbH, Germany) based on the CAD models.

2.4 Compression tests

Stress-strain curves were obtained as previously described (Chapter 1 of this part) to evaluate the effect of the geometry of 3D-printed PCL scaffolds on resistance against compression. Briefly, the force required to keep a constant compression speed of 1 mm/min as well as displacements were recorded using a LRX plus (Lloyd Instruments, max load=1 kN) testing machine. Forces and displacements were converted into stress and strain using sample dimensions. Measurements were performed for vertical compressions (VC, *i.e.* force applied perpendicular to printed layers, n=3) and lateral compressions (LC, *i.e.* force applied parallel to printed layers, n=3). Compression modulus and yield strength were determined as presented in Supporting information of Chapter 1 and in Zein and coworkers.[9] Briefly, the compression modulus was defined as the slope of the initial linear region of the stress-strain curve and the yield strength was defined as the stress at the intersection between the stress-strain curve and the modulus slope with 1% offset. The yield strain corresponds to the strain at which the yield strength occurs. It is important to mention that for logistics reasons, the tested gyroid scaffolds were only 3D-printed at 90% (*i.e.* the 10 upper layers were missing on a total of 106 layers for the entire scaffold). However, as dimensions are taken into account in data processing and as the change in height is low compared to the size of the entire scaffold, the results obtained are relevant and will be presented. At worst, a higher compressive modulus and a higher

yield strength for lateral compression should be expected, which does not change the discussion about these results.

3 Results and discussion

3.1 PCL gyroid scaffold printed with HIPS support

PCL gyroid scaffolds were first printed using HIPS as supporting material. Due to the large difference in printing temperature of the two polymers (extruder temperature: 95°C and 250°C, respectively), the printing was performed in a cold room to ensure a quick cooling of HIPS when deposited. Indeed, the close presence of a polymer heated at a much higher temperature than the melting point of PCL showed to affect the shape of the PCL layer that was already printed. After HIPS removal using limonene bathes, the top, bottom, and side faces of gyroid scaffolds were imaged (Figure 3) and a µCT scan of the scaffold was obtained (Figure 4). Pictures showed that top and bottom faces are similar while side faces significantly differed from the two others. The side faces were more open than both other faces, which was not consistent with the model used for printing. This result was also observed for PLA (data not shown). It can be explained by the difference between the horizontal (400 µm) and vertical (100 µm) resolution of the printer. Hence, horizontal features cannot be as well defined as vertical features. However, the µCT scan showed that this does not affect the interconnectivity of the pores inside the scaffold. Moreover, it was shown for PLA that the isotropy of the structure regarding mechanical properties was not affected either (Chapter 1 of this Part). Both images as well as the µCT scan showed that the spring shape of the gyroid structure was respected, pores were well defined and pore projections were circular.

Even though the gyroid structure was respected, some PCL sheets expanded in the porous space. The shape of these PCL projections was quite different from traditional oozing, frequently seen in FDM. Oozing, also named stringing, consists in the formation of tiny strings of polymers that ooze out of the nozzle while the head is travelling in the void without printing between two printed areas. These strings give a “hairy” object, that can be post-treated to remove these imperfections. Some examples of oozing will be shown in section 2.2 of this chapter). Sheet-shaped PCL projections found here outside the object boundaries did not seem to match with the usual

definition of oozing. A hypothesis would be that the 250°C hot nozzle used for supporting material deposition came into contact with PCL when moving over printed PCL regions, melted it and extended it into the void, resulting in PCL sheets in the macroporosity.

A cross-section of the printed scaffold was isolated from the µCT scan and compared to a cross-section of the model (Figure 4 c and d). Both cross-sections were in close agreement. Bean shaped units representing the pillars of the gyroid structure were correctly printed. Furthermore, the cross-section image of the printed sample again emphasized the large pore size and the high interconnectivity of the pores. The advantages of such features for a scaffold were already largely described in Context of research as well as in Chapter 1 of this part and will not be further discussed here.

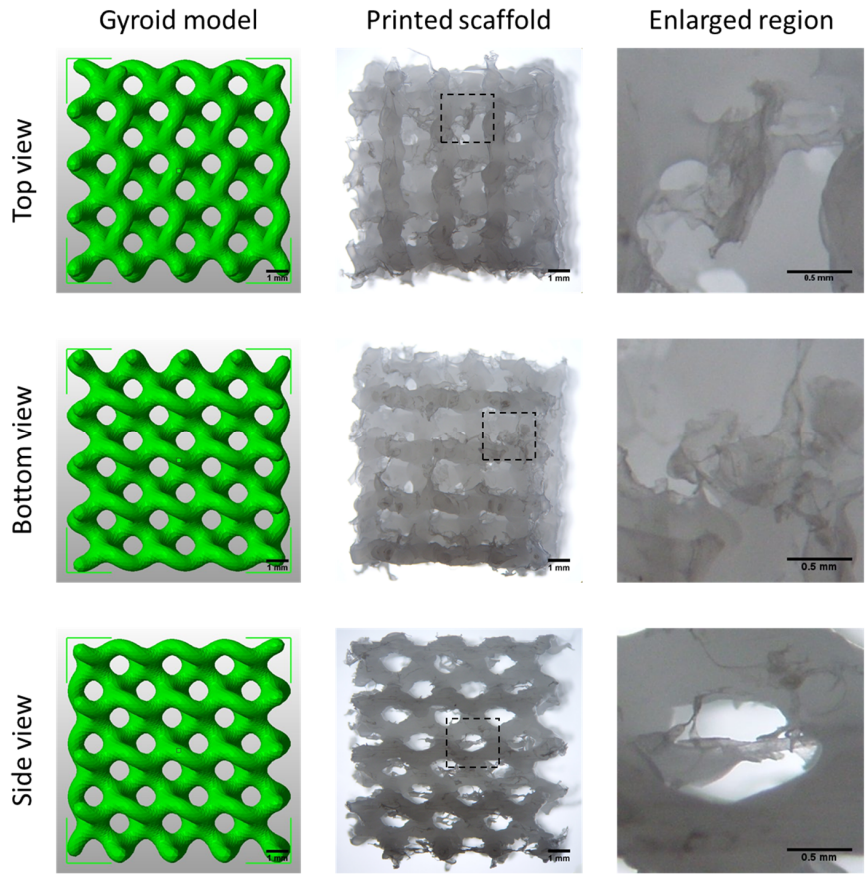


Figure 3: Top, bottom and side views of the model used for printing (left) and of a PCL scaffold printed with HIPS support then observed using optical microscopy (middle). Optical microscope images at higher magnification (right) highlight the presence of sheet-shaped PCL projections outside object boundaries.

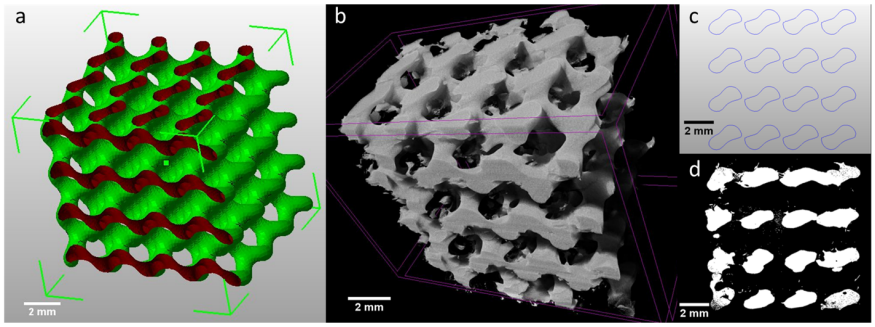


Figure 4: (a) Model used for 3D printing and (b) µCT scan of a PCL gyroid scaffold 3D-printed with HIPS support, both cropped at the front and the top of the structure for the sake of visualization. (c) Model and (d) µCT scan of the corresponding printed cross-sections.

3.2 PCL gyroid scaffold printed with PVA support

To get closer to a potential use of the scaffold for tissue engineering in clinics, the HIPS support was replaced by water-soluble PVA. It avoids the use of organic solvent for supporting material removal to move towards a "solvent-free" system. In addition, the extrusion temperature of PVA is lower to the one of the HIPS (205°C and 250°C, respectively). A reduced gap between PCL melting point and supporting material temperature could improve scaffold printing. The adaptation of the printing protocol to use PVA instead of HIPS was quite challenging due to hygroscopic behavior of PVA. Indeed, hygroscopic polymers tended to clog the extruding nozzle if they were not sufficiently dried. Therefore, PVA was well dried each time before being printed. Due to the high affinity of PVA for water, the polymer however absorbed moisture from the air during printing, which resulted in a clogged nozzle if the printing session was too long. The rate of water absorption by PVA is proportional to the relative humidity of the air. Hence, it prevented the use of a cold room for printing as it was done for HIPS since the relative humidity is then much higher than at room temperature.

On the one hand, to be printed accurately, PCL needs cold air and time for cooling (low printing speed, printing of many samples in parallel to lengthen the time before deposition of the next printed layer,…) especially if it is printed together with another polymer presenting a higher melting point. On the other hand, PVA needs a dry environment (low relative humidity) and fast printing to avoid moisture reabsorption. The requirements for each polymer are thus contradictory and compromises have to be found in terms of printing conditions. Consequently, printing was performed at room temperature, six samples were printed in parallel and a fan was placed in front of the printer to improve cooling. Figure 5 shows pictures of the gyroid scaffold after PVA support removal and pictures of the control strut-based scaffold printed without support. The gyroid scaffold seemed less well printed when PVA was used instead of HIPS. The spring-shape structure characterizing the gyroid was clearly observable, though pores were obstructed by many PCL strings (grey arrows) and sheets (black arrows). Besides, pore projections, observable in the side view, were more elliptical than circular. This could be explained by a subsidence of the structure during printing. It is hard to say if the less accurate printing was due to the change in parameters to allow PVA printing or due to the supporting material nature itself.

Strut-based scaffolds were correctly printed and were made of straight struts even when the polymer was printed in the void between two struts of the underlying layer. Bending struts would constitute weak points, which could have compromised further compression testing. However, oozing could not be eliminated completely and was also present in the scaffold and at the edges (grey arrows). The 0.3 mm thick printed layers were clearly visible. The printed surface was smoother than the one of the gyroid scaffold and no PCL sheets were observed. This can be attributed to the fact that the structure is much simpler to print as it is constituted of simple struts. Moreover, no PVA was used and the second nozzle usually used for supporting material printing was not heated. Hence, printed PCL was not in contact with a heat source, which could have melted and deformed it. It is worth noting that some struts were made of two layers while most of them were made of three layers. It is explained by the chosen vertical resolution (0.3 mm) and strut diameter of the structure in the model (0.8 mm). Indeed, as 0.8 mm is not a multiple of 0.3 mm, the slicing program takes 3 layers of 0.3 mm (0.9 mm) and compensates the exceeding 0.1 mm by removing one layer after 3 printed struts. Therefore, the dimensions of the model as well as dimensions of features in the model should be considered when the vertical resolution is chosen, for enhanced printing accuracy.

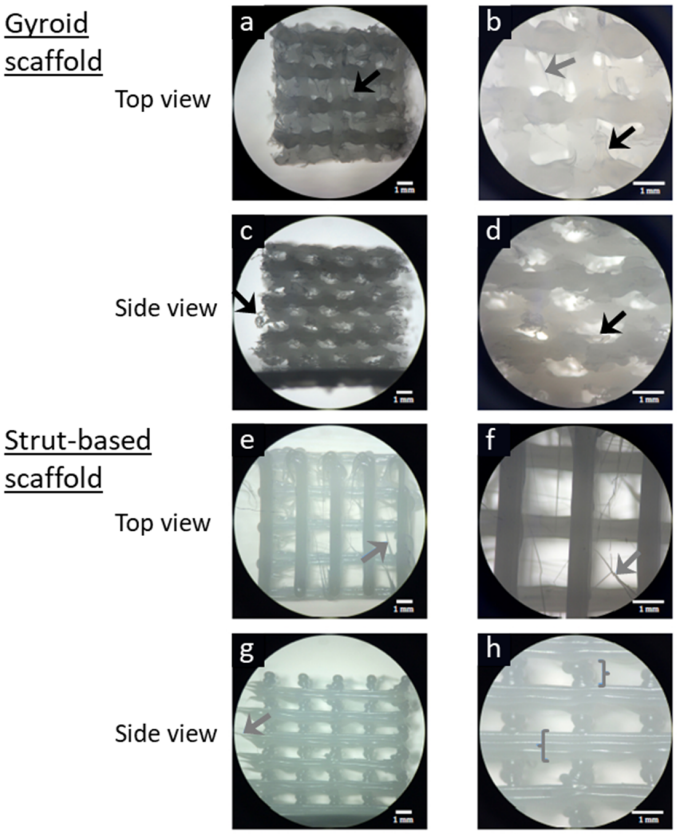


Figure 5: Pictures of (a to d) gyroid and (e to h) strut-based scaffolds using a low-magnification optical microscope. Gyroid scaffolds were printed with PVA as supporting material. Left column shows 16x magnifications of (a, e) top and (c, g) side views of both scaffolds, while right columns shows 32x magnifications of (b, f) top and (d, h) side views. Black arrows highlight sheet-shaped PCL projections outside object boundaries. Grey arrows indicate the strings formed owing to oozing. Grey brackets show the three printed layers that form one strut of the strut-based scaffold.

3.3 PCL scaffold topography

Profilometry analysis was performed on the top and the side of the modified samples printed without support (Figure 6). Such structures are much easier to print and do not reflect the porous gyroid scaffold as the latter is printed together with a supporting material. Nevertheless, it gives an idea of the result that could be expected if PCL sheet formation was prevented. The images acquired by profilometry showed that the general expected shape was respected even though the summits of the hills on the side face did not perfectly match with the model used for printing. A closer examination of the

recorded profiles confirmed that the resolution of 100 µm was correctly applied and that no significant roughness was detected at the micrometer-scale (data not shown). As already explained in the Context of research as well as in Chapter 1 of this part, cells are sensitive to surface topography. Hence, microtopography has to be studied and, if needed, modified to ensure an adequate cell behavior.

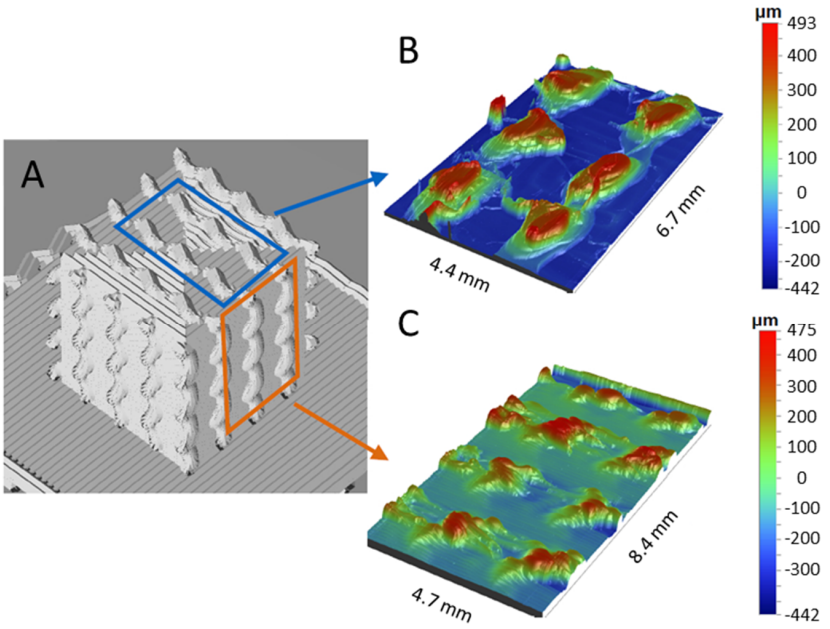


Figure 6: (A) Model used to obtain a simplified geometry suitable for profilometry analysis and topographic scans obtained by profilometry of framed areas on (B) the top and (C) the side of the 3D-printed sample.

3.4 Scaffold porosity

In tissue engineering, scaffold porosity is one of the major concerns as a high porous fraction will allow better oxygen, nutrient and metabolite diffusion. Besides, more space will be available for cells to migrate and secrete their own ECM. However, a too high porous fraction will affect the mechanical resistance of the scaffold. The porous fraction of PCL gyroid scaffolds printed using PVA as supporting material was evaluated using the mass and dimensions of the 3D-printed samples (Table 2). The gyroid and the strut-based scaffolds featured a similar porous fraction of approximately 69%. Therefore, the mechanical properties of the two designs could be compared. Even though the porous fraction of the printed gyroid scaffold was

significantly lower than the theoretical one computed based on the model used for printing ($p < 0.05$), a difference of 4% was satisfactory considering the complexity of the model. Such deviation was not observed for the strut-based scaffold, which displays a simpler geometry.

Table 2: Printed gyroid and strut-based scaffold porous fraction computed from masses and dimensions of printed scaffolds (n=6; standard deviation) and compared to the theoretical value extracted from the model used for printing.

	Gyroid scaffold	**Strut-based scaffold**
Theoretical porous fraction (%)	72.7	69.1
Measured porous fraction (%)	68.9 (1.2)	69.3 (2.1)

3.5 Impact of mesh geometry on mechanical resistance

Stress-strain curves obtained for PCL gyroid scaffolds printed using PVA as supporting material (after PVA removal) and for control strut-based scaffolds are presented in Figure 7. For each scaffold, the compression was performed vertically (VC, perpendicular to printed layers) and laterally (LC, parallel to printed layers). Compression modulus, yield strength and yield strain were extracted from the initial part of the curve (between 0% and 20% of strain) and are presented in Figure 8. Contrary to what was observed for PLA in Chapter 1 of this part, curves for LC and VC of the gyroid scaffold did not match. Similarly, the extracted compression modulus and yield strength were higher for LC compared to VC. This could be explained by two hypotheses. First, it was shown for gyroids printed in titanium using electron beam melting that the eccentricity of pore projection was affecting the mechanical properties of the scaffold.[31] If pore projections are elliptical and elongated parallel to the applied force, the compressive modulus as well as the yield strength are higher compared to a circular pore projection. In contrast, if pore projections are elongated perpendicular to the applied force, the compressive modulus as well as the yield strength are lower compared to a circular pore projection. As it was observed in section 2.2. of this chapter, pore projection of the gyroid scaffolds printed using PVA as supporting material were rather elliptical than circular. Pores were elongated in the lateral direction, which matched with the higher compressive modulus and yield strength observed for LC compared to VC. A second hypothesis rests on the fact that the layer-by-layer building of the structure attenuated its isotropic behavior and that the level of this attenuation is a function of

the intrinsic properties of the material used, resulting in a more marked effect for PCL compared to PLA.

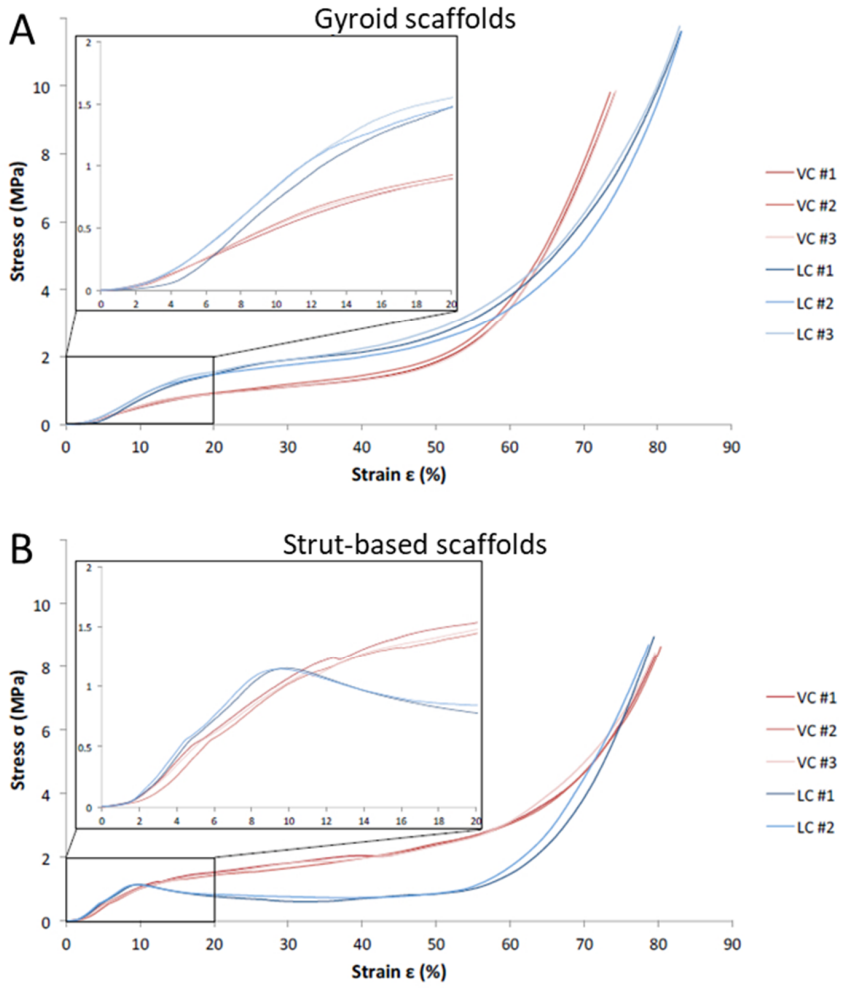


Figure 7: Stress-strain curves from vertical compression (VC) and lateral compression (LC) of (A) gyroid and (B) strut-based samples. Gyroid scaffolds were printed with PVA as supporting material. Results were obtained in triplicate except for LC of strut-based scaffold for which one curve was removed owing to aberrant values. For each scaffold type, the initial part of the curve is enlarged.

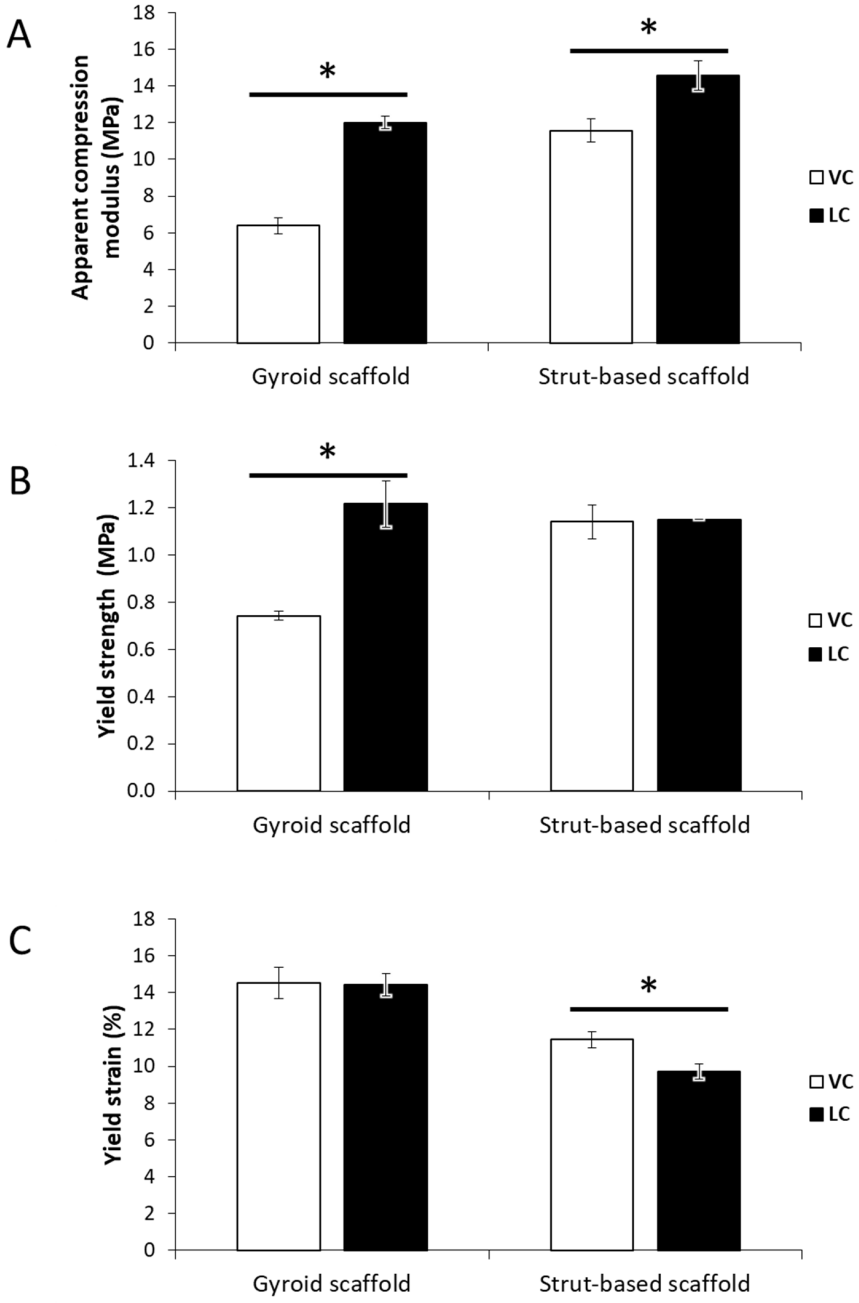


*Figure 8: (A) Apparent compression modulus (obtained from the slope of the initial linear part of stress-strain curve), (B) yield strength and (C) yield strain (both obtained from stress-strain curves with the offset method using a value of 1%) of PCL gyroid printed with PVA as supporting material and strut-based samples measured for VC and LC (error bars show the standard deviations, n=3). Bars with * represent significant differences (Student t-tests, $p < 0.05$).*

Regarding strut-based scaffolds, similar results were obtained for PLA and PCL. A peak was observed in LC corresponding to the buckling of columns (struts) placed parallel to the applied force. This peak was not observed in VC as all struts are placed perpendicular to the applied force. Besides, the compression modulus was higher for LC as it was the case for PLA. However, though occurring at different strain, the yield strength of PCL was not significantly different depending on the orientation of compression unlike for PLA.

Both scaffold compressive moduli were in the range of elastic moduli measured for cartilage from distinct areas of lower limb joints (2-20 MPa).[32] That makes the PCL gyroid scaffold a good candidate for cartilage tissue engineering.

4 Conclusion and future prospects

This chapter shows the capacity of FDM technology to produce PCL skeletal-based gyroid scaffolds, and, for the first time, mechanical properties of these PCL complex structures were compared to PCL strut-based structures used in many other studies.

Printing parameters were optimized to print PCL gyroid scaffolds first using HIPS, then PVA as supporting material. Pictures and a µCT scan of PCL-printed samples showed that the gyroid geometry was respected. Furthermore, profilometry gave us information about the smooth scaffold surface topography and confirmed the 100 µm vertical resolution. The porous fraction of printed PCL gyroid scaffolds was about 70% and their mechanical properties were compared to the ones of strut-based scaffolds presenting the same porous fraction. The isotropic behavior of the gyroid scaffold regarding resistance against compression according to its orientation was not observed in the case of PCL, even though the gyroid model is isotropic. Hypotheses to explain this unexpected result are either (i) a subsidence of the structure, which elongates the pore shape which, in turn, affects the vertical and lateral mechanical properties or (ii) an artifact resulting from the layer-by-layer construction.

As it was achieved for PLA, improvement could be performed for a more accurate printing. PCL-PVA printing could be carried out in a controlled environment presenting a low temperature and a low relative humidity. This

would allow a quick cooling of PCL and PVA to avoid structure subsidence after printing. Moreover, water absorption by PVA would be reduced to prevent nozzle clogging. The slicing program as well as the version of the program used is crucial to ensure printing quality.[33] Other slicing programs or versions could be tested.

As FDM field is evolving quite rapidly, other features proposed by new 3D printers could also improve the accuracy of printing. The main issue encountered with PVA- or HIPS-supported PCL printing is the presence of PCL sheets. The second nozzle of the printer is suspected to be the reason of their formation. It seems that the second nozzle comes into contact with the printed PCL, melts it and extends it in unwanted places. In some printers, it is possible to retract the nozzle that is not printing. Hence, a distance between the nozzle and the printed model is ensured. At the end of a layer, if the second nozzle is needed, the first nozzle is retracted and the second nozzle is put back at the right distance for printing. Nozzles switching continues until the end of printing. In addition to nozzle alignments, nozzles-to-platform distances are critical for a good deposition of the polymer. With the printer used in the present work, the calibration method was manual and rather approximative. A paper card was placed between the platform and the nozzles. The platform was approached until a friction was felt when moving the card between the nozzles and the platform. Printers with automatic alignment exist and could be tested. These are two examples amongst many other features available with new 3D printers.

Once the gyroid scaffold is printed with accuracy and presents circular pore projections, new mechanical testing could be carried out to confirm the hypothesis of pore eccentricity that would prevent the mechanical properties to be isotropic. A degradation study could be conducted to compare gyroid and strut-based PCL scaffolds as it was done for PLA in Chapter 1. However, this experiment could take several years if carried in the same conditions. Indeed, PCL is reported to be much more stable owing to its high hydrophobicity.[5, 34]

5 References

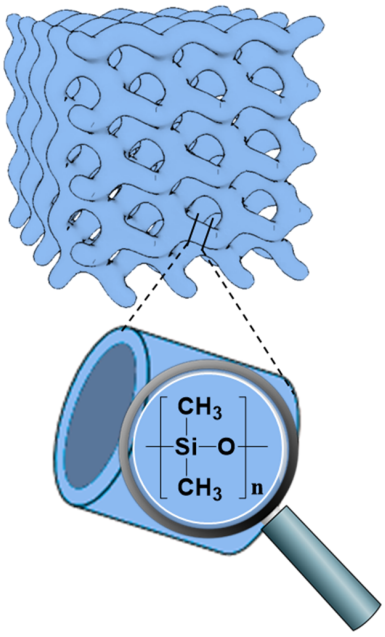
1. Verheyen, R. 3D printing and surface modification of poly(ε-caprolactone) scaffolds for tissue engineering applications. Master thesis, UCLouvain, Louvain-la-Neuve, Belgium, 2016.

2. Woodruff, M. A.; Hutmacher, D. W., The return of a forgotten polymer - Polycaprolactone in the 21st century. *Prog. Polym. Sci.* **2010,** *35* (10), 1217-1256.
3. Siddiqui, N.; Asawa, S.; Birru, B.; Baadhe, R.; Rao, S., PCL-Based Composite Scaffold Matrices for Tissue Engineering Applications. *Mol. Biotechnol.* **2018,** *60* (7), 506-532.
4. Patrício, T.; Domingos, M.; Gloria, A.; Bártolo, P., Characterisation of PCL and PCL/PLA Scaffolds for Tissue Engineering. *Proc. CIRP* **2013,** *5*, 110-114.
5. Zhang, X.; Peng, X.; Zhang, S. W., 7 - Synthetic biodegradable medical polymers: Polymer blends. In *Science and Principles of Biodegradable and Bioresorbable Medical Polymers*, Zhang, X., Ed. Woodhead Publishing: 2017; pp 217-254.
6. Park, J. H.; Yoon, J. K.; Lee, J. B.; Shin, Y. M.; Lee, K. W.; Bae, S. W.; Lee, J. H.; Yu, J. J.; Jung, C. R.; Youn, Y. N.; Kim, H. Y.; Kim, D. H., Experimental Tracheal Replacement Using 3-dimensional Bioprinted Artificial Trachea with Autologous Epithelial Cells and Chondrocytes. *Sci. Rep.* **2019,** *9* (1), 2103.
7. Ramanath, H. S.; Chua, C. K.; Leong, K. F.; Shah, K. D., Melt flow behaviour of poly-ε-caprolactone in fused deposition modelling. *J. Mater. Sci. Mater. Med.* **2008,** *19* (7), 2541-2550.
8. Domingos, M.; Chiellini, F.; Gloria, A.; Ambrosio, L.; Bartolo, P.; Chiellini, E., Effect of process parameters on the morphological and mechanical properties of 3D Bioextruded poly(ε-caprolactone) scaffolds. *Rapid Prototyping J.* **2012,** *18* (1), 56-67.
9. Zein, I.; Hutmacher, D. W.; Tan, K. C.; Teoh, S. H., Fused deposition modeling of novel scaffold architectures for tissue engineering applications. *Biomaterials* **2002,** *23* (4), 1169-1185.
10. Ribeiro, J. F. M.; Oliveira, S. M.; Alves, J. L.; Pedro, A. J.; Reis, R. L.; Fernandes, E. M.; Mano, J. F., Structural monitoring and modeling of the mechanical deformation of three-dimensional printed poly(ϵ-caprolactone) scaffolds. *Biofabrication* **2017,** *9* (2), 025015.
11. Rotbaum, Y.; Puiu, C.; Rittel, D.; Domingos, M., Quasi-static and dynamic *in vitro* mechanical response of 3D printed scaffolds with tailored pore size and architectures. *Mater. Sci. Eng. C Mater. Biol. Appl.* **2019,** *96*, 176-182.
12. Patrício, T.; Domingos, M.; Gloria, A.; D'Amora, U.; Coelho, J. F.; Bártolo, P. J., Fabrication and characterisation of PCL and PCL/PLA scaffolds for tissue engineering. *Rapid Prototyping J.* **2014,** *20* (2), 145-156.
13. Idaszek, J.; Bruinink, A.; Swieszkowski, W., Ternary composite scaffolds with tailorable degradation rate and highly improved colonization by human bone marrow stromal cells. *J. Biomed. Mater. Res. A* **2015,** *103* (7), 2394-2404.

14. Pati, F.; Song, T. H.; Rijal, G.; Jang, J.; Kim, S. W.; Cho, D. W., Ornamenting 3D printed scaffolds with cell-laid extracellular matrix for bone tissue regeneration. *Biomaterials* **2015,** *37*, 230-241.
15. Ronca, D.; Langella, F.; Chierchia, M.; D'Amora, U.; Russo, T.; Domingos, M.; Gloria, A.; Bartolo, P.; Ambrosio, L., Bone Tissue Engineering: 3D PCL-based Nanocomposite Scaffolds with Tailored Properties. *Proc. CIRP* **2016,** *49*, 51-54.
16. Wang, H.; Domingos, M.; Scenini, F., Advanced mechanical and thermal characterization of 3D bioextruded poly(ε-caprolactone)-based composites. *Rapid Prototyping J.* **2018,** *24* (4), 731-738.
17. Yao, Q.; Wei, B.; Guo, Y.; Jin, C.; Du, X.; Yan, C.; Yan, J.; Hu, W.; Xu, Y.; Zhou, Z.; Wang, Y.; Wang, L., Design, construction and mechanical testing of digital 3D anatomical data-based PCL-HA bone tissue engineering scaffold. *J. Mater. Sci. Mater. Med.* **2015,** *26* (1), 5360.
18. Korpela, J.; Kokkari, A.; Korhonen, H.; Malin, M.; Narhi, T.; Seppala, J., Biodegradable and bioactive porous scaffold structures prepared using fused deposition modeling. *J. Biomed. Mater. Res. B Appl. Biomater.* **2013,** *101* (4), 610-619.
19. Seyednejad, H.; Gawlitta, D.; Kuiper, R. V.; de Bruin, A.; van Nostrum, C. F.; Vermonden, T.; Dhert, W. J. A.; Hennink, W. E., *In vivo* biocompatibility and biodegradation of 3D-printed porous scaffolds based on a hydroxyl-functionalized poly(ε-caprolactone). *Biomaterials* **2012,** *33* (17), 4309-4318.
20. Buyuksungur, S.; Endogan Tanir, T.; Buyuksungur, A.; Bektas, E. I.; Torun Kose, G.; Yucel, D.; Beyzadeoglu, T.; Cetinkaya, E.; Yenigun, C.; Tonuk, E.; Hasirci, V.; Hasirci, N., 3D printed poly(ε-caprolactone) scaffolds modified with hydroxyapatite and poly(propylene fumarate) and their effects on the healing of rabbit femur defects. *Biomater. Sci.* **2017,** *5* (10), 2144-2158.
21. Shim, J. H.; Kim, A. J.; Park, J. Y.; Yi, N.; Kang, I.; Park, J.; Rhie, J. W.; Cho, D. W., Effect of solid freeform fabrication-based polycaprolactone/poly(lactic-co-glycolic acid)/collagen scaffolds on cellular activities of human adipose-derived stem cells and rat primary hepatocytes. *J. Mater. Sci. Mater. Med.* **2013,** *24* (4), 1053-1065.
22. Lee, H.; Ahn, S.; Bonassar, L. J.; Kim, G., Cell(MC3T3-E1)-printed poly(ε-caprolactone)/alginate hybrid scaffolds for tissue regeneration. *Macromol. Rapid. Comm.* **2013,** *34* (2), 142-149.
23. Dong, L.; Wang, S.-J.; Zhao, X.-R.; Zhu, Y.-F.; Yu, J.-K., 3D-Printed Poly(ε-caprolactone) Scaffold Integrated with Cell-laden Chitosan Hydrogels for Bone Tissue Engineering. *Sci. Rep.* **2017,** *7* (1), 13412.
24. Stichler, S.; Böck, T.; Paxton, N.; Bertlein, S.; Levato, R.; Schill, V.; Smolan, W.; Malda, J.; Teßmar, J.; Blunk, T.; Groll, J., J., Double printing of

hyaluronic acid/poly(glycidol) hybrid hydrogels with poly(ε -caprolactone) for MSC chondrogenesis. *Biofabrication* **2017,** *9* (4), 044108.
25. Ferreira, J.; Gloria, A.; Cometa, S.; Coelho, J. F. J.; Domingos, M., Effect of *in Vitro* Enzymatic Degradation on 3D Printed Poly(ε-Caprolactone) Scaffolds: Morphological, Chemical and Mechanical Properties. *J. Appl. Biomater. Funct. Mater.* **2017,** *15* (3), 185-195.
26. Caetano, G. F.; Bártolo, P. J.; Domingos, M.; Oliveira, C. C.; Leite, M. N.; Frade, M. A. C., Osteogenic Differentiation of Adipose-derived Mesenchymal Stem Cells into Polycaprolactone (PCL) Scaffold. *Procedia Engineer.* **2015,** *110*, 59-66.
27. Xia, D.; Jin, D.; Wang, Q.; Gao, M.; Zhang, J.; Zhang, H.; Bai, J.; Feng, B.; Chen, M.; Huang, Y.; Zhong, Y.; Witman, N.; Wang, W.; Xu, Z.; Zhang, H.; Yin, M.; Fu, W., Tissue-engineered trachea from a 3D-printed scaffold enhances whole-segment tracheal repair in a goat model. *J. Tissue Eng. Regen. Med.* **2019,** *13* (4), 694-703.
28. Xuan, Y.; Tang, H.; Wu, B.; Ding, X.; Lu, Z.; Li, W.; Xu, Z., A specific groove design for individualized healing in a canine partial sternal defect model by a polycaprolactone/hydroxyapatite scaffold coated with bone marrow stromal cells. *J. Biomed. Mater. Res. A* **2014,** *102* (10), 3401-3408.
29. Hernandez, I.; Kumar, A.; Joddar, B., A Bioactive Hydrogel and 3D Printed Polycaprolactone System for Bone Tissue Engineering. *Gels* **2017,** *3* (3), 26.
30. Rabionet, M.; Polonio, E.; Guerra, A. J.; Martin, J.; Puig, T.; Ciurana, J., Design of a scaffold parameter selection system with additive manufacturing for a biomedical cell culture. *Materials* **2018,** *11* (8), 1427.
31. Yánez, A.; Herrera, A.; Martel, O.; Monopoli, D.; Afonso, H., Compressive behaviour of gyroid lattice structures for human cancellous bone implant applications. *Mater. Sci. Eng. C Mater. Biol. Appl.* **2016,** *68*, 445-448.
32. Shepherd, D. E. T.; Seedhom, B. B., The 'instantaneous' compressive modulus of human articular cartilage in joints of the lower limb. *Rheumatol.* **1999,** *38* (2), 124-132.
33. Evans, B., 3D Printer Toolchain. In *Practical 3D Printers*, Apress: Berkeley, CA, 2012; pp 27-47.
34. Cameron, R. E.; Kamvari-Moghaddam, A., 5 - Synthetic bioresorbable polymers. In *Durability and Reliability of Medical Polymers*, Jenkins, M.; Stamboulis, A., Eds. Woodhead Publishing: 2012; pp 96-118.

Chapter 3: PDMS coating optimization and preliminary studies



In order to modify the surface mechanical properties of the scaffold, a poly(dimethylsiloxane) (PDMS) coating was applied. A method based on the formation of a semi-interpenetrating polymer network (SIPN) was proposed to coat both PLA and PCL structures. The surface of the structure is swollen, leading to the interpenetration of PDMS and PLA or PCL linear chains. PDMS is then crosslinked around these linear chains. The effect of the composition of the mixture of solvents and PDMS used for coating PLA and PCL as well as coating thickness were first studied on model structures (flat substrates, cylinders, *etc*.). The surface chemistry of PLA and PCL-coated samples was examined using water contact angle measurements in dynamic conditions and X-ray photoelectron spectroscopy. Coating thickness was then evaluated using scanning electron microscopy. The coating protocol and its parameters were finally adapted to the macroporous gyroid scaffolds. Both water contact angle measurements and XPS revealed the presence of the PDMS coating on model surfaces. PDMS coating thickness on PLA and PCL cylinders varied between 14 and 41 µm. Once the protocol was adapted for gyroid scaffolds, it was further modified to reach coating thicknesses around 100 µm. A new method was thus developed to successfully coat microporous scaffolds with a PDMS layer, whose mechanical properties can be tuned by adjusting the crosslinking density. Coating through the formation of a SIPN is shown to be particularly adapted to macroporous scaffolds presenting a complex geometry, as it ensures a good homogeneity and adhesion of the coating to the scaffold material.

We sincerely thank Mirasbek Kuterbekov[1], Robin Verheyen[2], Nicola Gossart[3], Yasmine Adriaensen, Pierre Eloy, Delphine Magnin, Pascale Lipnik, Cecile D'Haese, Colette Douchamps, Prof. Yves Dufrêne and Sylvie Derclaye for their contribution to the work presented in this chapter.

1 Introduction

Cell behavior is not the same whether it is grown on a 2D substrate or encapsulated in a 3D scaffold. It was shown that the same modifications (chemical or mechanical) applied to a 2D substrate or in to 3D scaffold were not affecting cells in the same manner.[4, 5] Between 2D substrates and 3D scaffolds in which cells are embedded, macroporous scaffolds can be considered as a third configuration. Indeed, inside macroporous scaffolds, cells lay flat and spread as they do on 2D substrates. Cells only have a basal attachment and do not feel a matrix surrounding them. However, cells are able to sense pore geometry.[6] For example, concave curvatures with radii largely above cell size were shown to influence cell behavior such as attachment rate, migration, secretion and morphology. We may thus wonder if cells seeded in macroporous scaffolds react as they do on 2D substrates or rather as they would inside 3D scaffolds. Cell mechanotransduction was mainly studied on 2D substrates.[5] Some 3D systems such as hydrogels were also studied but, to our knowledge, mechanotransduction was not studied on cells seeded inside macroporous scaffolds. Here, to study cell mechanotransduction inside a macroporous scaffold, a polymer coating was applied to selectively modify the surface mechanical properties of the scaffold. Using a coating, cell behavior should be affected while the global morphological and mechanical properties of the scaffold will remain constant.

The specifications for this coating are as follows. First, the polymer coating should allow easy and reproducible change in mechanical properties. Then, the change in mechanical properties should not affect coating chemistry. Indeed, chemistry also affects cell behavior. If chemistry varies with mechanical properties, changes in cell behavior cannot be attributed to modifications of mechanical properties solely. Finally, the coating should be thick enough to hide the underlying mechanical properties to the cells. Indeed, cells are able to sense mechanical properties of a material present under a soft coating.[7, 8] This topic will be further discussed in Chapter 5 of this Part. The minimal coating thickness to prevent cells from feeling the hard material located under the coating is discussed in the literature.[7, 8] It was decided to aim for a coating thickness of at least 20 µm, which is a good compromise between feasibility and masking efficiency.

Sylgard 184, a crosslinkable poly(dimethylsiloxane) (PDMS), is a good candidate to elaborate such coating. This polymer is provided in a kit

containing two reagents, the base and the curing agent. Mixing these two compounds in different ratio and curing the obtained material using heat treatement will provide polymers with different crosslinking degrees. Therefore, the mechanical properties are easily varied and controlled. Besides, chemistry is kept constant whatever the mechanical properties of the coating. PDMS has been already often use for mechanotransduction studies on 2D substrates.[9]

Unfortunately, the PDMS used (Sylgard 184) is viscous and dip coating of complex macroporous structures results in pore clogging (Figure 1). To overcome this issue, a protocol based on the formation of a semi-interpenetrating polymer network (SIPN)[10] was tested and optimized to get a thick coating on complex structures. SIPN are polymer networks composed of at least one polymer that interpenetrates with and is crosslinked around at least one linear or branched polymer.[11, 12] The PLA or PCL structure to be coated is plunged in a mixture of solvent and non-solvent of this structure containing PDMS base and curing agent (see Figure 7 in Part III Aim and strategy). The mixture swells structure surface and allows uncured PDMS chains to interpenetrate with PLA or PCL chains. The structure is rinsed in the non-solvent to deswell the surface and trap PDMS chains. Finally, PDMS chains are crosslinked to stiffen the coating. The interpenetration of PDMS with PLA or PCL allows a good adhesion of the coating on the structure.

To our knowledge, the use of a method based on the formation of a SIPN to achieve micrometer-sized coatings on polymer macroporous scaffold for tissue engineering is underexplored. Optimizations of this protocol for PLA and PCL are presented in this chapter.

"*God made the bulk; surfaces were invented by the devil.*" (Wolfgang Pauli)

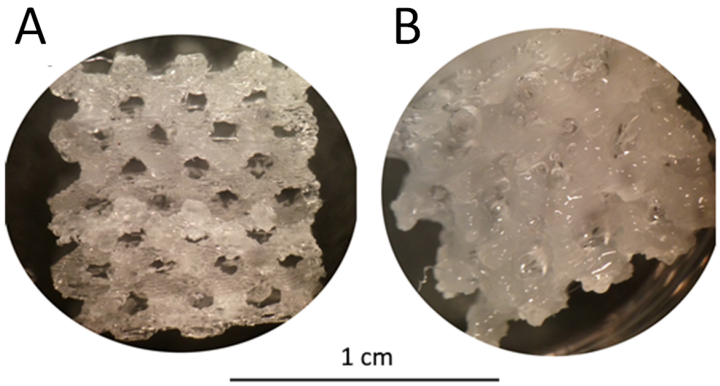


Figure 1: (A) 3D-printed PLA gyroid scaffold. (B) PLA gyroid scaffold dipped in a mixture of PDMS base and curing agent (10:1 ratio) and cured at 85°C overnight. Pores are completely clogged due to PDMS high viscosity.

2 Coating through the formation of a SIPN and optimizable parameters

A coating protocol using the formation of a SIPN was proposed by Nguyen and coworkers to coat PDMS on PLA.[10] This method does not require the presence of reactive groups on the substrate to be coated and is quite versatile. Figure 2A represents the different steps of the protocol. The PLA structure is plunged in a mixture of solvent (1,4-dioxane) and non-solvent (n-hexane) of PLA containing the PDMS base as well as the curing agent. For the sake of clarity, even though four compounds are present in the mixture, PDMS base and curing agent solution will be considered as one compound. Hence, the notion of ternary mixture will be used instead of the one of quaternary mixture. This ternary mixture provokes structure surface swelling and uncured PDMS chains interpenetrate with the swollen surface. An increased residence time in the mixture was shown to increase coating thickness. This step can be performed at room temperature or at higher temperature to start PDMS crosslinking in the ternary mixture, increasing coating thickness. The structure is rinsed in n-hexane (PLA non-solvent) to deswell the surface and trap PDMS chains. Finally, the sample is heated to cure the PDMS coating.

A second coating cycle can be added to increase coating thickness (Figure 2B). This second cycle was used by Nguyen and coworkers to increase coating

thickness on 3D-printed structures presenting centimeter-size pores. In this case, the surface to swell is the first deposited PDMS coating. Therefore, the composition of the ternary mixture is adapted. The PDMS-coated PLA structure is immersed in a mixture of n-hexane (solvent of PDMS) and isopropanol (non-solvent of PDMS) containing PDMS base and curing agent. The already formed PDMS layer swells and interpenetrates with uncured PDMS chains present in the mixture. The authors did not report a rinsing step for this cycle. It was assumed that the coated structure is rinsed in the non-solvent of PDMS (isopropanol). The sample is heated to cure the PDMS. Such a cycle can be repeated to further increase PDMS coating thickness.

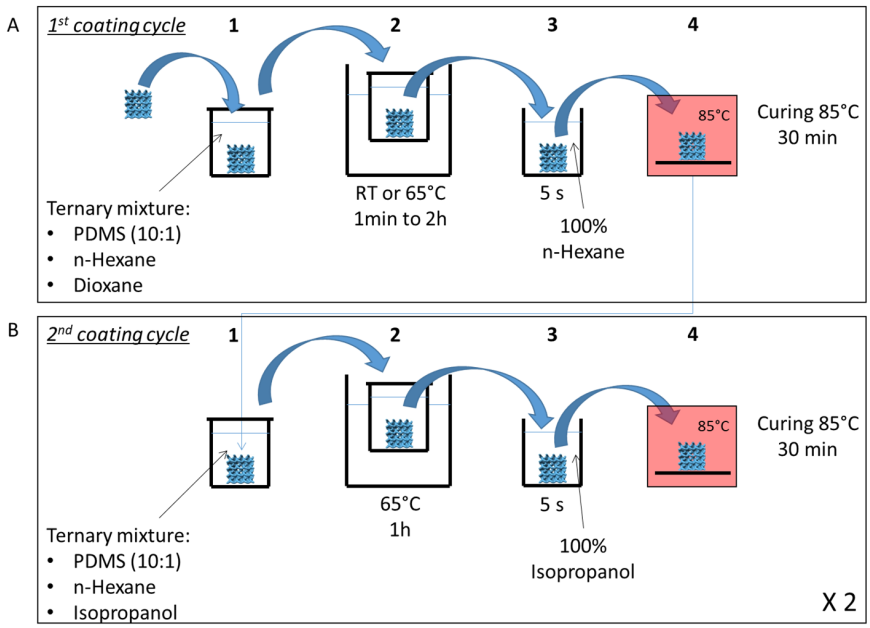


Figure 2: Schematic of the different steps in coating protocol through the formation of a SIPN proposed by Nguyen and coworkers.[10] (A) First and (B) subsequent coating cycles are illustrated. 1. Insertion of the structure in the ternary mixture containing solvent and non-solvent of the structure as well as PDMS base and curing agent. 2. The structure remains in ternary mixture for a defined period of time at a given temperature. This step allows surface swelling and uncured PDMS interpenetration with structure polymer chains. 3. Rinsing step in non-solvent of the structure shrinks back the swollen surface and traps PDMS. 4. Curing of PDMS coating.

Many parameters of this protocol are expected to have an effect on coating success as well as on coating thickness:

- **Composition of ternary mixture:** Solvents used and proportions influence structure swelling in the mixture.

- **Temperature and residence time in the ternary mixture:** Higher residence time and higher temperature are supposed to result in thicker swollen surface layers. Besides, both parameters influence PDMS crosslinking inside the mixture.
- **Rinsing step:** Used to shrink the surface layer and entrap PDMS chains. However, it also removes a part of the deposited PDMS.
- **Curing time and temperature between cycles:** Higher temperature and longer curing will increase the degree of crosslinking. Curing is used to anchor the deposited PDMS. However, the more crosslinks are made, the less functions will remain available to crosslink with uncured PDMS chains in further cycles.

Using this protocol, different ratios between PDMS base and curing agent were tested to vary the mechanical properties of the coating. Ratio between PDMS base and curing agent will be presented as follows: PDMS(X:Y). X will refer to the amount in mass of PDMS base for an amount in mass Y of curing agent.

3 Selection of the coating mixture

The composition of the n-hexane, 1,4-dioxane and PDMS mixture was shown to influence coating thickness.[10] However, a too high amount of solvent compared to non-solvent will provoke structure deformation or complete dissolution. The concept of ternary phase diagram usually refers to the solubility of a compound in a mixture of two other compounds. In the present study, the ternary phase diagram will describe the solubility of PCL or PLA in the ternary mixture. Different ternary mixtures were tested to define boundary conditions inside which structure shape is conserved. Based on these information, ternary phase diagrams were drawn for PLA and PCL in the ternary mixture. Both PLA and PCL are soluble in 1,4-dioxane (used as solvent) and insoluble in n-hexane (used as non-solvent).

3.1 Materials and methods

Printed **PLA** cylinders (1.2 mm diameter; 20 mm length, n=3) were immersed in 20 ml of the mixtures containing different volume proportions of 1,4-dioxane, n-hexane and uncured PDMS solution. Uncured PDMS solution was

prepared by mixing base and curing agent in 10:1 (w:w) proportions. Immersion was carried out for 1 h at 65°C.

Regarding **PCL**, the experiment was undertaken in the frame of two different master theses. The used protocol was identical but the coated structures were different. Printed PCL cylinders (1.2 mm diameter; 20 mm length, n=3) and diamond-shaped 3D structures (Figure 3) were immersed in mixtures (20 and 5 ml, respectively) prepared as previously mentioned for PLA. Immersion was performed for 2 h at 37°C.

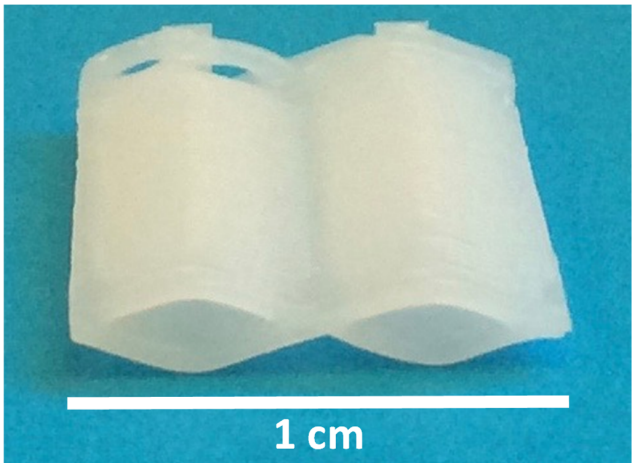


Figure 3: Picture of the diamond-shaped 3D structure in PCL.

3.2 Results and discussions

Ternary maps of the conditions tested for PLA and PCL as well as the resulting qualitative effect on structure dissolution state are presented in Figure 4.

A ternary solubility phase diagram of PLA in n-hexane, 1,4-dioxane and PDMS was also established by Nguyen and coworkers.[10] However, their study was performed using PLA cylinders with a diameter of 300 µm and immersion at room temperature for 1 h. The solid line drawn in Figure 4 A represents the limit above which a partial or total dissolution of the structure was observed in their study. In our study, mixtures above and below this line were tested for PLA cylinders with a diameter of 1.2 mm and immersion for 1 h at 65°C. Our results confirmed this limit of dissolution. Below this limit, a working zone of 9 different compositions of the mixture (Table 1) was selected for subsequent coating thickness measurements (section 4.2 of this chapter).

Table 1: Composition in volume proportion of the selected mixtures for subsequent coating thickness measurement on PLA.

Mixture	PDMS (%)	n-hexane (%)	1,4-dioxane (%)
1	40	40	20
2	30	50	20
3	20	60	20
4	35	35	30
5	25	45	30
6	15	55	30
7	30	30	40
8	20	40	40
9	10	50	40

To our knowledge, PCL coating with PDMS using the formation of a SIPN using these solvents had never been tested before. Consequently, the corresponding ternary solubility phase diagram had to be established without prior knowledge of the system behavior. Diamond-shaped 3D-printed structures were used as models to test a broad range of n-hexane, 1,4-dioxane and PDMS proportions covering the whole phase diagram. Step by step, the proportions were narrowed down to a range of proportions offering a working zone in which PCL does not dissolve. Four different regions of the ternary map were evidenced (Figure 4 B):

- The 3D structure was completely dissolved for mixtures containing more than 50% of 1,4-dioxane.
- The 3D structure was partially or totally lost for mixtures containing between 15 and 40% of 1,4-dioxane.
- The 3D structure was conserved but pores were clogged by the PDMS coating for mixtures containing less than 10% of 1,4-dioxane and more than 80% of PDMS. This result will probably vary with pore size as small pores are more susceptible to be clogged.
- The 3D structure was conserved and pores were not clogged by the PDMS coating for mixtures containing less than 10% of 1,4-dioxane as well as less than 65% of PDMS.

These results were confirmed using PCL cylinders. The same regions were observed in the ternary diagram and the limit between conservation and loss of the structure was more precisely placed at 13% of 1,4-dioxane in the mixture. As for PLA, a working zone of 9 different compositions of the

mixture (Table 2) was selected for subsequent coating thickness measurement (section 5 of this chapter).

Table 2: Composition in volume proportion of the selected mixtures for subsequent coating thickness measurement on PCL.

Mixture	PDMS (%)	n-hexane (%)	1,4-dioxane (%)
1	60	40	0
2	40	60	0
3	20	80	0
4	54	40	6
5	37	57	6
6	20	74	6
7	48	40	12
8	34	54	12
9	20	68	12

It has to be emphasized that these ternary diagrams are valid for the temperature and the residence time tested. An increase in temperature could increase the solubility of PLA or PCL and hence, could move the solubility boundaries. In the case of longer residence time, more time is allowed for PLA or PCL to dissolve. Furthermore, the ratio between the mass of the sample and the total volume of the mixture as well as sample dimensions and its geometry also influence structure solubility. Indeed, a low volume of ternary mixture will dissolve a low amount of PLA (or PCL) before reaching saturation, while the surface/volume ratio will influence dissolution kinetics.

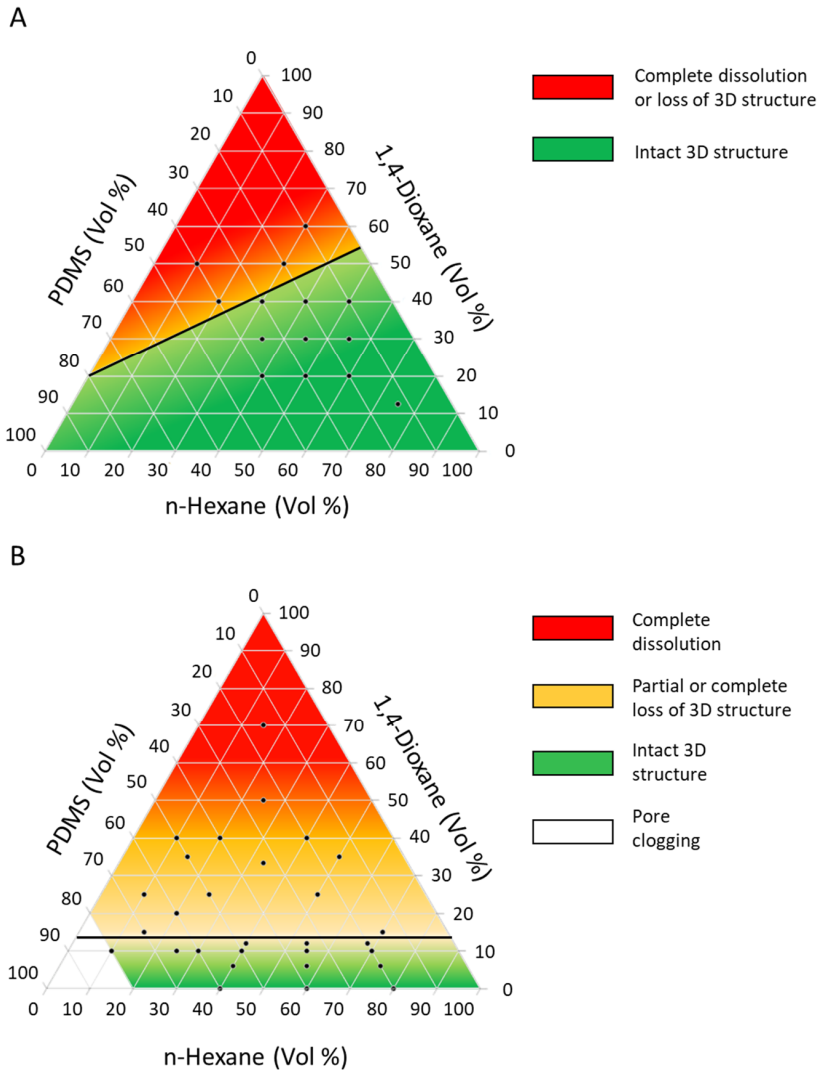


Figure 4: Ternary phase diagram of (A) PLA and (B) PCL in ternary mixtures of n-Hexane, 1,4-Dioxane and PDMS(10:1). Black dots correspond to tested conditions. The black solid line represents the limit over which the 3D structure is partially or totally lost. For PLA, this limit was observed by Nguyen and coworkers.[10] The same limit was obtained in our work. Solvent proportions were tested with a residence time of 1h at 65°C for PLA and with a residence time of 2h at 37°C for PCL.

4 Coating characterization through surface chemical analysis

The presence of the coating was first evidenced by analyzing the surface chemical composition of model cylinders and flat substrates. Water contact angle measurements were used to evaluate surface hydrophobicity, while X-ray photoelectron spectroscopy (XPS) allowed the surface chemical composition to be determined.

4.1 Materials and methods

PLA cylinders (1 mm diameter; 30 mm length) and disks (12 mm diameter; 0.5 mm thick) were printed and coated with PDMS. PDMS base and curing agent were mixed in 10:0.15, 10:0.3 and 10:1 proportions. PLA cylinders and discs were immersed in 5 ml of the PDMS/n-hexane/1,4-dioxane (12.5:75:12.5) mixtures for 1 h at 65°C. Samples were rinsed for 5 s in hexane and the PDMS coating was cured overnight at 55°C.

PCL cylinders (0.4 to 0.5 mm diameter; 25 mm length) and rectangular substrates (5x10 mm², 1 mm thick) were printed and coated with PDMS. PDMS base and curing agent were mixed in 10:1 proportions. PCL cylinders and discs were immersed in 5 ml PDMS/n-hexane/1,4-dioxane mixtures for 2 h at 37°C. The tested mixture ratios were (20:70:10), (35:55:10), (50:40:10) and (65:25:10). Samples were rinsed for 5 s in hexane and the PDMS coating was cured overnight at 55°C.

Water contact angle measurements in dynamic conditions were achived using a Krüss K100 tensiometer (KRÜSS GmbH, Germany). Uncoated and PDMS-coated PLA and PCL cylindrical samples were immersed in and withdrawn from ultrapure water (n=3). Water density and viscosity were set to 0.998 and $1.002.10^{-3}$ Pa.s, respectively (parameters for water at 20°C). Three or four cycles of wetting/dewetting were performed at a speed of 3 mm/min on a distance of at least 10 mm.

XPS analysis on PLA and PDMS-coated PLA disks (n=1, two locations on the sample) were carried out using a Kratos Axis Utra spectrometer (Kratos Analytical, UK) equipped with a monochromatized aluminium X-ray source (powered at 10 mA and 15 kV). The samples were fixed on a standard stainless steel multispecimen holder by using a piece of double-sided insulating tape. The pressure in the analysis chamber was about 10^{-6} Pa. The

angle between the normal to the sample surface and the direction of photoelectrons collection was about 0°. Analyses were performed in the hybrid lens mode with the slot aperture, the resulting analysed area was 700 µm x 300 µm. The pass energy was set at 160 eV for the survey scan and 40 eV for narrow scans. In the latter conditions, the full width at half maximum (FWHM) of the Ag $3d_{5/2}$ peak of a standard silver sample was about 0.9 eV. Charge stabilisation was achieved by using the Kratos Axis device.

XPS analysis on PCL and PDMS-coated PCL substrates (n=1, three locations on the sample) were carried out using a SSX 100/206 photoelectron spectrometer (Surface Science Instruments, USA) using a Al X-ray source (20 mA, 10 kV). The pressure in the analysis chamber was around 10^{-6} Pa. The angle between the surface normal and the axis of the analyzer lens was 55°. The analyzed area was approximately 1.4 mm^2 and the pass energy was set at 150 eV for the survey spectra. In these conditions, the FWHM of the Au $4f_{7/2}$ peak of a clean gold standard sample was about 1.6 eV. A flood gun set at 8 eV and a Ni grid placed 3 mm above the sample surface were used for charge stabilization.

4.2 Results and discussions

4.2.1 Water contact angle in dynamic conditions

Dynamic water contact angle measurements were performed on uncoated and PDMS-coated PLA or PCL cylinders.

For **PLA**, cylinders coated with different ratio between PDMS base and curing agent were compared to uncoated PLA (Figure 5 A). PDMS(10:1)-coated PLA showed higher values for both advancing and receding contact angles compared to uncoated samples. This result confirmed the presence of a PDMS coating layer at the surface of cylinders. PDMS indeed features a higher hydrophobicity than PLA.[13, 14] The values for PDMS(10:0.15) could not be considered different from neither PDMS(10:1) nor uncoated PDMS, as larger standard deviations were observed. Therefore, for this ratio, no definitive conclusions could be drawn. Besides, water contact angle hysteresis was higher for PDMS(10:0.15) compared to the other tested samples. This might reflect a non-uniform coating, a higher surface roughness or both in the case of PDMS(10:0.15).

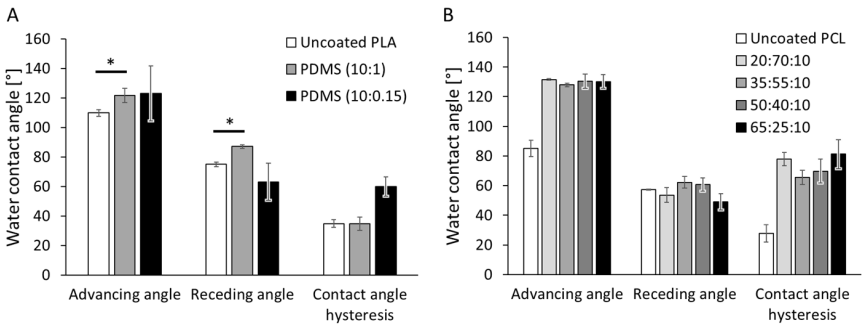


*Figure 5: Water advancing contact angles, receding angles and contact angle hysteresis for uncoated and PDMS-coated (A) PLA and (B) PCL. For PLA, coatings with different proportions between PDMS base and curing agent were evaluated. For PCL, coatings prepared using different volume fractions of PDMS:n-Hexane:1,4-Dioxane in the ternary mixture used to deposit the coating were analyzed (n=3; error bars show the standard deviations; * Student's t-test, α=0.05).*

A water contact angle hysteresis around 20°-35° is expected for PDMS and is explained by its chemistry.[13, 15] PDMS chains are mobile owing to a low glass transition temperature (T_g around -120°C). When PDMS is in contact with air, methyl groups from PDMS are exposed at the air-polymer interface. This accounts for the measurement of high advancing contact angle values. When PDMS is immersed in water, a surface reorganization occurs and the polymer chains tend to expose oxygen atoms from the backbone at water-polymer interface (Figure 6). This results in a more hydrophilic surface and hence, in receding contact angle values that are lower than the advancing ones.

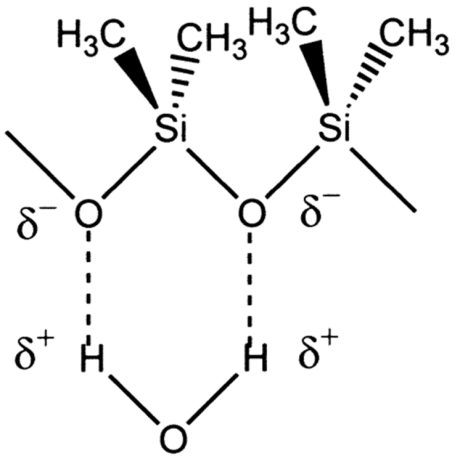


Figure 6: Exposition of the oxygen atoms from the backbone of PDMS at the water-polymer interface.[15]

In the case of **PCL**, whatever the coating mixture used, the same trends were observed (Figure 5 B). Advancing contact angles were significantly higher for coated samples compared to uncoated PCL, which reflected a higher surface hydrophobicity and hence, PDMS presence. However, the receding contact angles of coated samples were not significantly different from the one of the uncoated sample. As a result, contact angle hysteresis was higher for coated samples compared to uncoated PCL. Besides surface reorganization of PDMS chains, this could again suggests the presence of chemical heterogeneities, surface roughness or both.

Advancing and receding contact angle for uncoated PCL were consistent with values from the literature (around 85° and 60°, respectively).[14, 16] However, the higher contact angle values observed for PLA compared to PCL were not consistent with the fact that PCL possess a higher carbon-to-oxygen ratio than PLA. Values of advancing contact angles around 80° are indeed reported in the literature for PLA.[14] However, contact angle values may be influenced by the manufacturing process and/or by the possible presence of additives.

The advancing contact angle values of PLA and PCL coated samples were consistent with each other. The high advancing contact angle indicated the presence of the PDMS coating. Its value was also consistent with values found in the literature for PDMS, which are around 120°.[13, 15] The receding contact angle of PDMS was expected to be around 90°. This was in agreement with the measurements made on PDMS(10:1)-coated PLA while lower values were recorded for PDMS(10:0.15)-coated PLA and for all PDMS-coated PCL samples. Furthermore, high water contact angle hysteresis in the case of PDMS-coated PCL and PLA coated with PDMS(10:0.15) raised some suspicions about the presence of chemical heterogeneities.

4.2.2 XPS analysis

The elemental composition of the extreme surface was evaluated for uncoated and PDMS-coated PLA and PCL using XPS. Oxygen, carbon and silicon were detected and their relative fractions at the surface are presented in Figure 7.

The surface elemental composition of PDMS-coated PLA samples was similar whatever the ratio between base and curing agent used. Moreover, this composition was in close agreement with the 2:1:1 theoretical fraction of carbon, silicon and oxygen of the PDMS monomer. This corroborated the

results obtained with water contact angle measurements and further highlighted PDMS coating presence. However, the elemental composition determined for uncoated PLA deviated significantly from the expected 3:2 ratio for carbon and oxygen, respectively. An excess of carbon was indeed recorded. This could be explained by the surface deposition of carbon-containing contamination.

XPS measurements were also performed on PCL, either as such or coated with PDMS(10:1) using different mixtures of PDMS, n-hexane and 1,4-dioxane. In contrast with uncoated PLA, the elemental composition of uncoated PCL was close to the theoretical 3:1 ratio of carbon and oxygen for this polymer. A small silicon fraction was observed, which was attributed to contamination. To keep the exact same conditions, uncoated samples were placed in the same oven during PDMS crosslinking. This could have resulted in the transfer of volatile silicon-based contamination. Besides, silicone lubricant used for 3D printer parts could have contaminated the samples during printing. Regarding PDMS-coated PCL, the high amount of detected silicon highlighted the presence of PDMS and the proportions of carbon, silicon and oxygen approached the theoretical ones for this polymer (2:1:1). However, the oxygen fraction tended to be slightly higher (30% rather than 25%) while the carbon fraction was slightly lower (45% instead of 50%) than expected. This could be partially explained by the presence of silica nanoparticles used as filler in the PDMS matrix.[17-19]

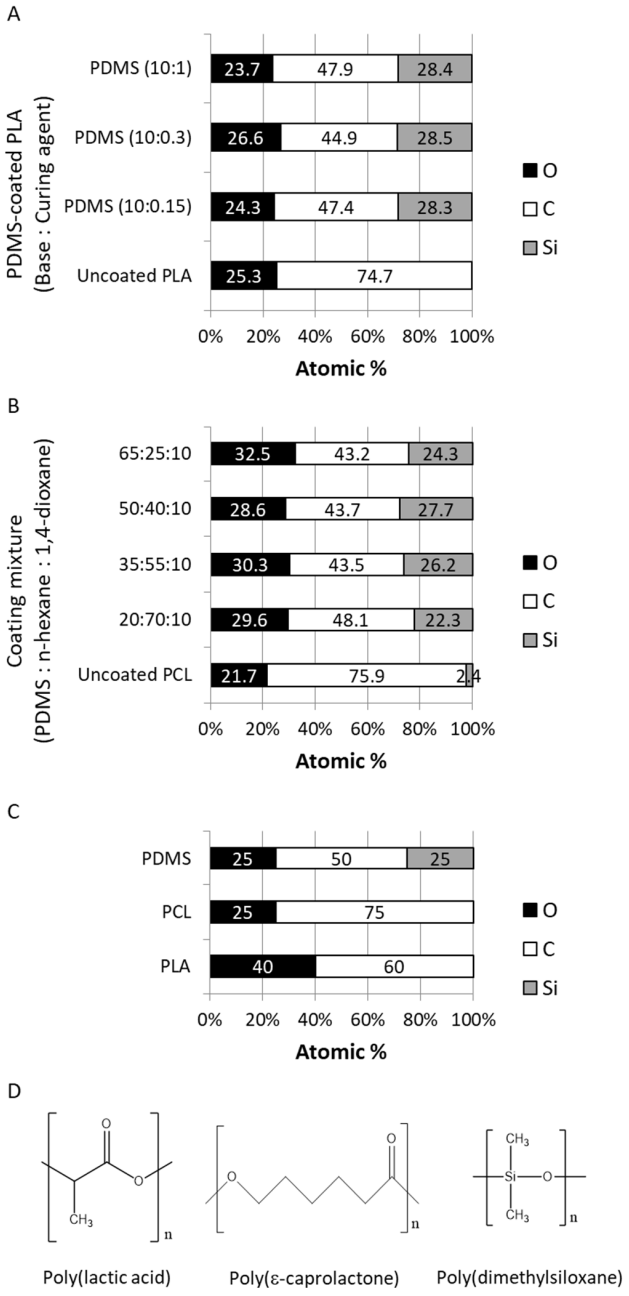


Figure 7: Surface elemental composition of uncoated and PDMS-coated (A) PLA and (B) PCL. For PLA, coating with different proportions between PDMS base and curing agent were evaluated. For PCL, coating prepared using different volume fraction of PDMS:n-Hexane:1,4-Dioxane in the ternary mixture were analyzed. (C) The expected surface elemental composition is given for each material, and was computed according to (D) the given molecular formula.

5 Influence of the coating mixture composition on coating thickness

Section 3 of this chapter gave information about surface chemistry of coated samples. The analyses showed the presence of PDMS for the tested conditions. No information was however obtained regarding coating thickness. As shown in the ternary solubility phase diagrams (Figure 4), different fractions of the constituents (PDMS, n-hexane and 1,4-dioxane) of the coating mixture were tested. Regions preventing the deformation and dissolution of PLA or PCL structures were identified. Within these working zones, the effect of the fraction of each constituent of the mixture on coating thickness was evaluated. PCL and PLA cylinders were coated with PDMS and were cut transversally. The obtained cross-sections were imaged using scanning electron microscopy and the coating thickness was measured on these pictures.

5.1 Materials and methods

Printed **PLA** and **PCL** cylinders (1.2 mm diameter; 20 mm length, n=3) were immersed in 20 ml of the mixtures containing different volume fractions of 1,4-dioxane, n-hexane and uncured PDMS solution. Uncured PDMS solution was prepared by mixing the base and the curing agent in 10:1 mass fraction. PLA treatment was performed by immersion in the mixture for 1 h at 65°C, while this was done for 2h at 37°C in the case of PCL. Treated cylinders were rinsed in hexane for 5 s. PDMS coatings were then crosslinked overnight at 85°C and 55°C for PLA and PCL, respectively.

Cylinders (n=3 per condition) were cut transversally using a razor blade and samples were imaged with a JSM-7600F (JEOL, Belgium) scanning electron microscope (SEM) at 5 keV and using the low magnification mode and a probe current of 2 nA. Energy-dispersive X-ray spectroscopy (EDX) was used to determine the chemical composition of the samples with a view to confirm the identification of the PDMS coating areas (data not shown). Coating thickness was then evaluated on SEM images (1 image per sample) by converting the distance in pixels into a distance in µm (Figure 8). Conversion factor between pixel and distance is determined by the number of pixels that compose the scale bar of the picture. This conversion was achieved using Paint.net (version 4.0.9).

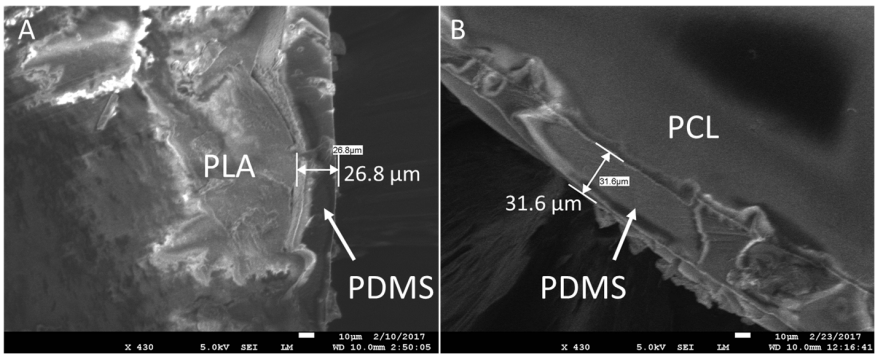


Figure 8: SEM images of PDMS-coated (A) PLA and (B) PCL cylinders and measurement of coating thickness.

5.2 Results and discussions

Figure 9 shows the thickness of the PDMS coating prepared on PLA and PCL cylinders (1.2 mm diameter) depending on coating mixture composition.

The average thickness of the PDMS coating on PLA varied between 14 and 41 µm (Figure 9 A). For all except two conditions, the PDMS layer thickness was above 20 µm. As explained at the beginning of this chapter, 20 µm is the threshold value that was considered as satisfying to hide the PLA structure mechanical properties in such a way that cell behavior can be governed by PDMS mechanical properties. Even though significant differences among coating thicknesses were observed, trends regarding the effect of coating mixture composition were difficult to highlight. All observed coating thicknesses were higher than the ones reported by Nguyen and coworkers.[10] Layer thicknesses from 0 to 2.5 µm were indeed obtained for 0.3 mm cylinders and 1 h of immersion at room temperature in their study. Besides, they reported an increase of coating thickness from 1 to 4 µm for increasing cylinder diameter between 0.1 mm to 0.4 mm. Hence, the thicker PDMS layers obtained in our study could be the result of larger cylinder diameter, higher immersion temperature or both.

Similar results were obtained for PCL (Figure 9 B). PDMS layer thickness varied from 17 to 43 µm. For all except one condition, the PDMS layer thickness was above 20 µm. Again, no trend could be highlighted as a function of the coating mixture composition in spite of some significant differences.

The lack of trend according to the mixture composition could be explained by the low number of samples and measurements on the same sample (3 samples per condition; 1 measurement per sample) while variability of the thickness was high. Moreover, other uncontrolled parameters could have influenced the PDMS coating thickness (sample drying, drainage, time between rinsing and curing,…).

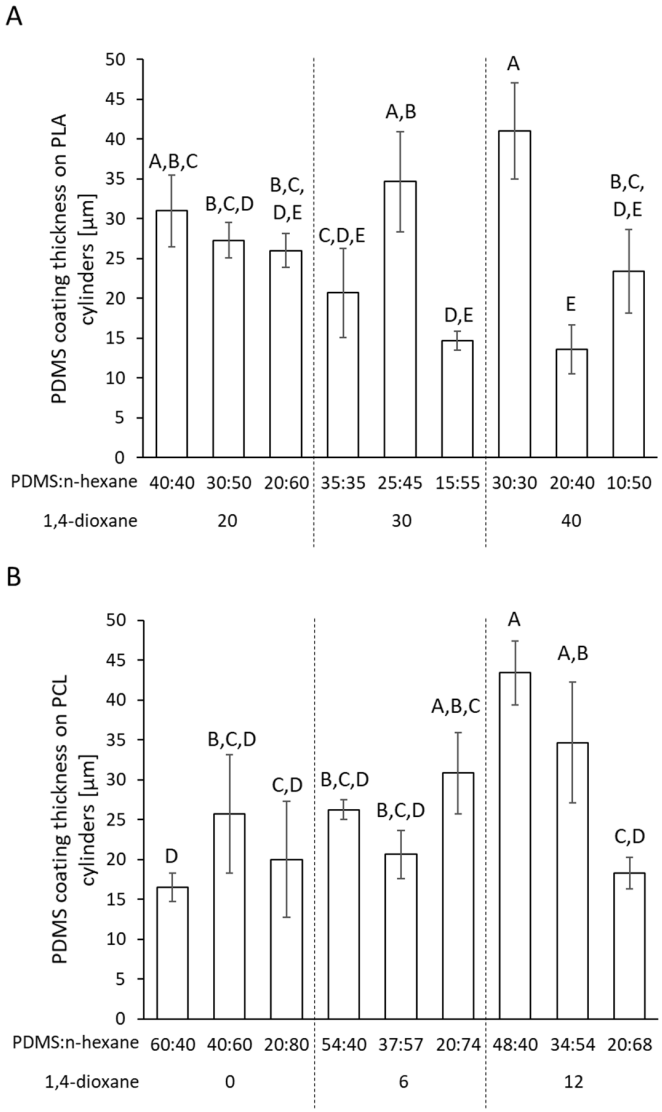


Figure 9: PDMS coating thickness measured on (A) PLA and (B) PCL cylinders depending on the ternary mixture used for coating (n=3; error bars show the standard deviations). Values not sharing the same letter are significantly different (α=0.05).

To get closer to the dimensions of the pillar of the gyroid scaffold, the experiment was repeated for PLA cylinders with smaller diameters (0.9 mm diameter instead of 1.2 mm). The same coating protocol and same coating mixtures were used. These thinner cylinders were completely dissolved in solutions presenting the highest fraction of 1,4-dioxane (40% of the mixture). The remaining cylinders did not show significant coatings. This result could be attributed to the higher surface/volume ratio of thin cylinders, which speeded up the swelling process and sample dissolution. Therefore, the entire ternary solubility phase diagram could have changed or could be shifted owing to structure dimensions. The ternary solubility phase diagram of PLA was obtained for cylinders of 1.2 mm diameter and results were similar to the results of Nguyen and coworkers for PLA cylinders of 0.3 mm.[10] However, the coatings were deposited at room temperature by Nguyen and coworkers, while our coatings were prepared at 65°C. An increase in temperature will result in an increase of solubility and dissolution rate. The lower surface/volume ratio of 1.2 mm diameter cylinder may have compensated the change of temperature, while the surface/volume ratio of 0.9 mm did not.

6 Development of other coating methods

While results obtained for PLA coating were promising, protocols were not adapted to the complex 3D scaffold with pillars presenting diameters around 0.9 mm as developed in this thesis. It was decided to test other coating methods. From this section, the study was only focused on PLA coating. A summary of the tested techniques and conditions as well as some obtained results are described below. Detailed protocols and results are presented in the Annex.

In addition to the coating through the formation of a SIPN proposed by Nguyen and coworkers, four other techniques were tested:

- **Coating by centrifugation:** As uncured Sylgard 184 is viscous and as scaffold pore sizes are small (diameter of pore projection around 1 mm), its penetration inside the scaffold for coating and the removal of the material in excess is difficult. Centrifugation was therefore used to help PDMS penetration within the scaffold and promote the removal of PDMS in excess. Scaffolds were inserted in 15 ml Falcon

tubes along with PDMS. After centrifugation followed by curing, no significant coating deposition was observed.

- **Dip coating:** To reduce its viscosity, PDMS can be diluted in n-hexane. Model cylinders and gyroid scaffolds were dipped in solutions containing different PDMS concentrations (5% to 50%) and PDMS was cured. Dipping was also repeated after curing on the same samples to increase coating thickness. Among the tested conditions for cylinders, 5 dip coating steps in 5% PDMS in n-hexane, with a curing step between each dip coating, gave the thickest PDMS layer (around 100 µm) (Figure 10 A). The same protocol was applied on gyroid scaffolds (Figure 10 B). Even though more analysis of the coating would have be needed, results were less convincing. A coating layer was visible, though no conclusion regarding coating homogeneity could be drawn. For both cylinders and gyroid, the coating was loosely attached to the PLA surface.

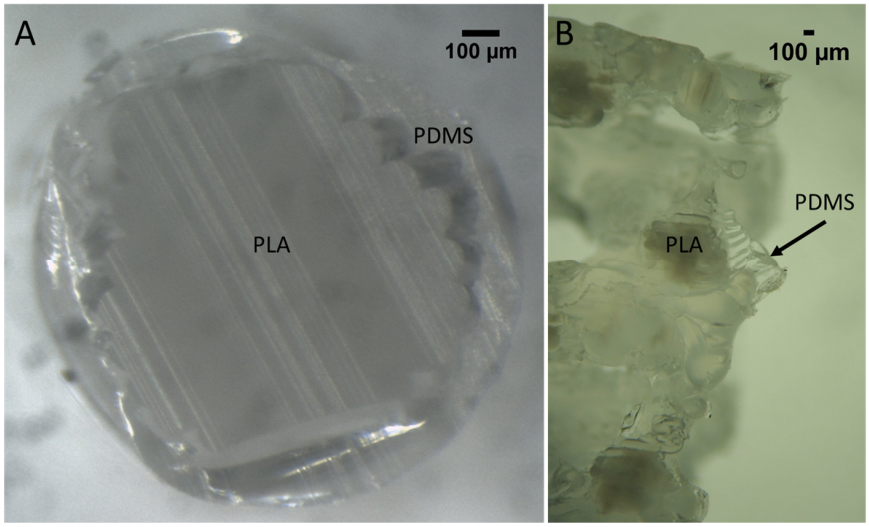


Figure 10: Low magnification pictures of (A) a PLA cylinder and (B) a PLA gyroid scaffold coated with PDMS using 5 dip coating steps in 5% PDMS in n-hexane.

- **Coating using sacrificial templating (molding):** To form a thick and homogeneous coating, a template can be printed that fits the scaffold, leaving a small template-scaffold interspace that can be filled to form the coating (Figure 11). The interspace is filled with uncured PDMS containing the curing agent. After curing, the templating material is selectively dissolved, leaving a homogeneous coating on the scaffold. This method is versatile as other coating

materials could be used. Though the template structure was successfully designed, the printed gyroid scaffold and this template were overlapping at some places. As the models were aligned, this could be the consequence of a too high amount of deposited polymer, too large nozzles or a wrong alignment of printed structures or nozzles during printing. Like for dip coating, the PDMS is deposited around the PLA scaffold. Hence, a loose attachment of the coating to the scaffold could be expected.

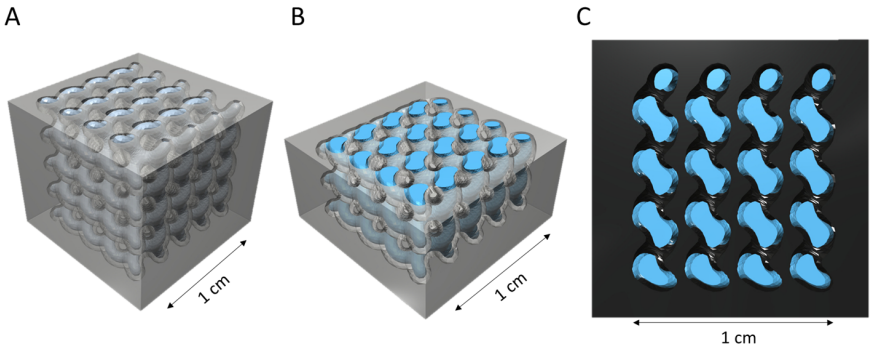


Figure 11: Templating structure model (translucent grey or black) designed around the gyroid scaffold model (blue) with a small interspace for coating molding. (A) Diagonal view of full model, (B) diagonal view of model virtually cut in the middle and (C) top view of the virtually cut model.

- **Coating through solvogel formation**: PLA gyroids were immersed in a mixture of PDMS:n-hexane:1,4-dioxane. Vials were hermetically sealed and PDMS was crosslinked during 7 days at room temperature. As the vials are sealed, solvent cannot evaporate and PDMS crosslinks in the solvent to form a gel. As the liquid phase is an organic solvent, the gel is called “solvogel” (in contrast with “hydrogels”, in which water forms the liquid phase). Once crosslinked, the gel around the scaffold was trimmed and solvent was evaporated at room temperature. As solvent evaporates, PDMS shrinks around the PLA structure and forms a smooth and rather homogeneous coating (Figure 12). When the solvent was completely evaporated, PDMS was fully cured overnight at 85°C. A higher temperature can be used for gel formation to speed up the process, though too high temperatures could lead to bubble formation. Theoretically, the layer thickness could be controlled by varying the PDMS fraction in the mixture. Here, the results were obtained for

PDMS(10:1). Similar results could not be obtained for PDMS(10:0.2) as PDMS did crosslinked neither at room temperature nor at 40°C.

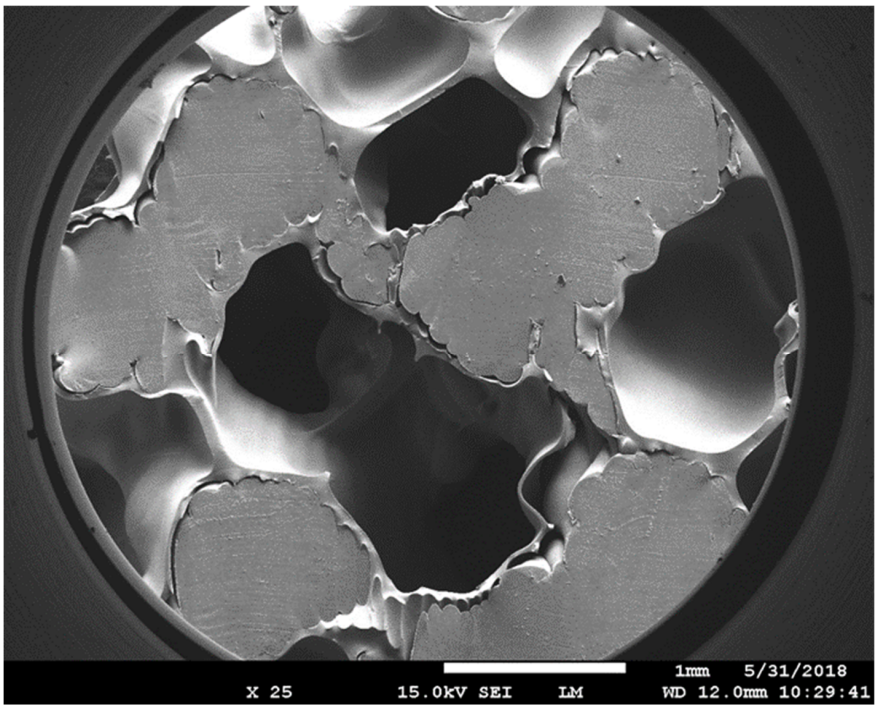


Figure 12: SEM image of a PLA gyroid scaffold (dark grey) coated through solvogel formation with PDMS(10:1) (light grey).

7 Further tentative developments to adapt the coating protocol using the formation of a SIPN to PLA macroporous scaffolds

As coating thickness or attachment using the aforementioned methods were not satisfying, the coating through the formation of a SIPN proposed by Nguyen and coworkers was further studied.[10] This protocol presents the advantage of improving coating adhesion owing to the interpenetration of PDMS chains with PLA chains. Temperature could have been adapted, and coating mixture composition could have been again optimized. However, as the relation between coating thickness and mixture proportions was unclear, it was chosen to vary other parameters. Hence, starting from the conditions that Nguyen and coworkers employed to coat 3D-printed structures and

keeping constant their coating mixture composition (12.5:75:12.5 for PDMS, n-hexane and 1,4-dioxane, respectively), different protocols and parameters were tested. Further information on protocols and results is detailed in the Annex.

- **Formation of a SIPN combined with dip coating:** The first coating cycle was performed as mentioned by Nguyen and coworkers. After PDMS curing, scaffolds were dipped in 5% PDMS in n-hexane and deposited on a glass substrate for solvent evaporation. Dipping was carried out 5 times with curing between cycles. The resulting coating was relatively thin (Figure 13). It has to be mentioned that for the first cycle, before and after the rinsing step, the excess of solvent retained in the scaffold by capillarity was drained using paper towel. Drainage as well as rinsing step in hexane were suspected to reduce coating thickness. Indeed, during these steps, PDMS was removed from the scaffold. In addition, when the scaffold was deposited on a flat substrate, the coating solution was sucked out of the scaffold. This further reduced the amount of PDMS deposited on the scaffold.

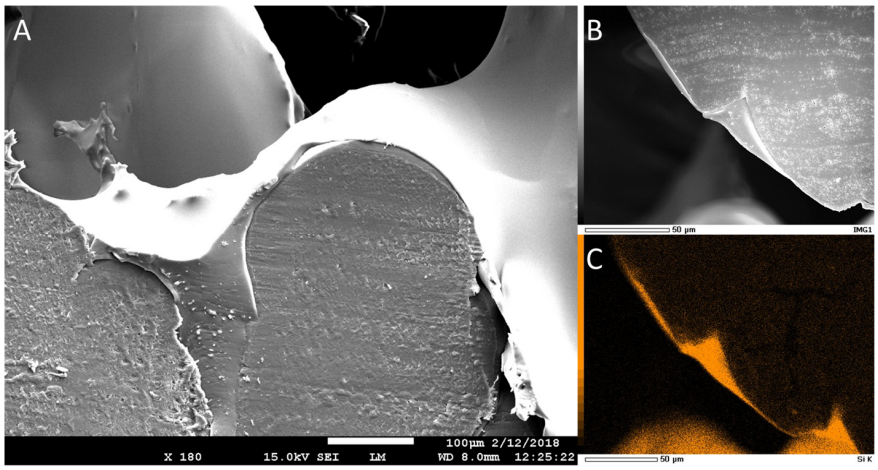


Figure 13: PLA gyroid scaffold (dark grey) coated with PDMS (light grey and yellow) through the formation of a SIPN combined with dip coating. (A) SEM image of a wide region of the sample, (B) SEM image of an enlarged region and (C) the corresponding Si signal (yellow) detected by EDX.

- **Formation of a SIPN with repeated cycles:** The first and second cycles were conducted as mentioned by Nguyen and coworkers. The first cycle swells PLA to entrap PDMS chains while the second cycle swells the PDMS layer deposited during the first cycle to provide a

better anchorage to the second deposited PDMS layer. As illustrated in Figure 14, a series of experiments with and without rinsing steps, exceeding content drainages and curing between cycles were carried out. The effect of either scaffold deposition on a flat substrate or scaffold hanging for solvent evaporation was also evaluated. Finally, isopropanol, used as non-solvent of PDMS to prevent complete dissolution, was no more added to the ternary mixture. Indeed, once PDMS is crosslinked, PDMS dissolution does not occur. Though PDMS swelling is possible, polymer chains cannot be completely separated due to covalent crosslinks, which maintain chains together. Then, without isopropanol, PDMS swelling should be maximum.

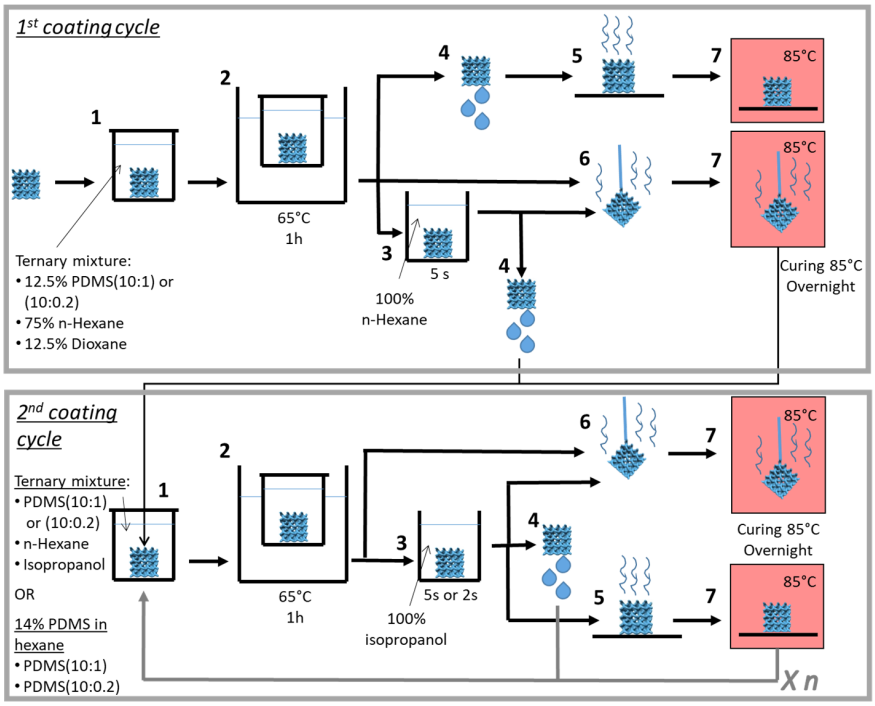


Figure 14: Schematic of the different steps and tested modifications in coating protocol through the formation of a SIPN. 1. Insertion of the scaffold in the ternary mixture or in n-hexane containing PDMS base and curing agent. 2. Scaffold remains in coating mixture for a defined period of time at a given temperature. This step allows surface swelling and uncured PDMS interpenetration with scaffold polymer chains. Besides, PDMS starts to crosslink. 3. Rinsing step in non-solvent of the scaffold shrinks back the swollen surface and traps PDMS. 4. Drainage of excess solvent retained by capillarity in the scaffold. 5. Deposition of the scaffolds on a glass substrate for solvent evaporation. 6. Hanging of scaffolds for solvent evaporation. 7. Curing of PDMS coating.

The best results were obtained using the **coating protocol through the formation of a SIPN with repeated cycles** when neither draining nor rinsing steps were applied. Moreover, scaffolds should be hanged for solvent evaporation to avoid solvent suction that happens when a scaffold is deposited after removal from the coating mixture. In the second and subsequent cycles, no isopropanol was added in coating mixture. Deposition cycles have to be repeated until a sufficient amount of PDMS is coated. Rather homogeneous coating were observed for both PDMS(10:1) and PDMS(10:0.2) (Figure 15). However, a total of 3 coating cycles was sufficient to obtain a thickness of around 100 µm for PDMS(10:1), while 5 cycles were necessary to achieve a thickness around 60 µm for PDMS(10:0.2).

Drainage or suction of the solvent out of the scaffold was prevented (no drainage using paper towel and no deposition on a 2D substrate). However, drainage of the solvent to the bottom of the macroporous scaffolds owing to gravity could not be avoided. Consequently, thicker PDMS layers or even clogged pores were observed in the bottom of the scaffolds.

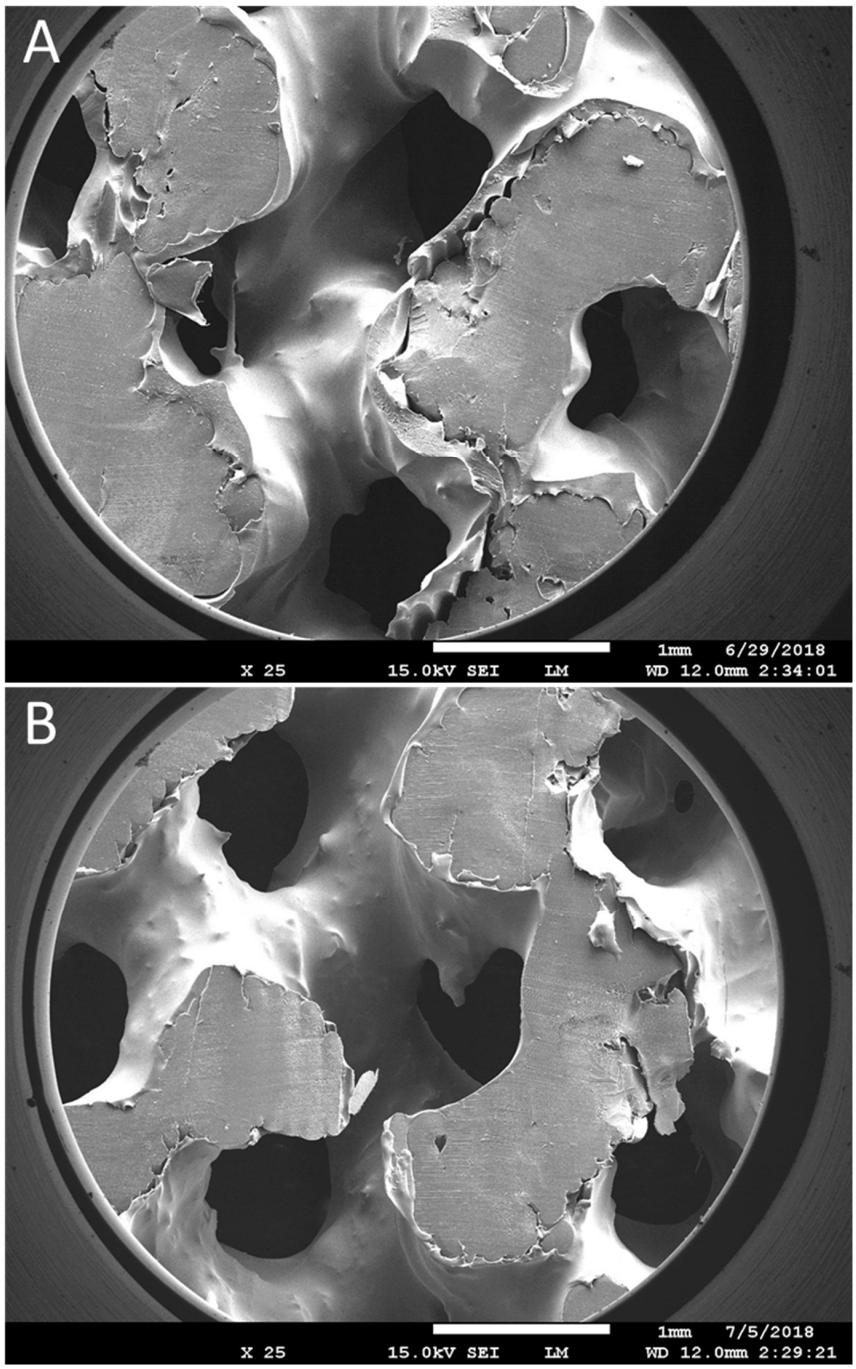


Figure 15: SEM images of PLA gyroid scaffolds (dark grey) coated with PDMS (light grey) through SIPN formation with repeated cycles. (A) PDMS(10:1) and (B) PDMS(10:0.2) were coated using a total of 3 and 5 cycles, respectively.

8 Conclusion and future prospects

PDMS with two different crosslinking densities were successfully deposited on PLA macroporous scaffolds. Thick PDMS layers between 60 µm and 100 µm were obtained. Besides, similar coatings were achieved on PCL model structures.

PLA and PCL model structures and scaffolds were coated with crosslinked PDMS using a protocol developed based on a method described in the literature. Briefly, a mixture of solvent and non-solvant of the structure is used to swell its surface and form a SIPN with the PDMS present in the mixture. The ratio between base and curing agent can be adapted to modify the surface mechanical properties. The coating presence was assessed through water contact angle measurements in dynamic conditions and XPS analysis. For PLA, water contact angles were higher for PDMS(10:1)-coated compared to uncoated PLA. This reflected a higher hydrophobicity of the surface after coating and confirmed PDMS presence. However, PDMS(10:0.15)-coated samples did not show significant differences compared to uncoated PLA. In addition, contact angle hysteresis was higher for that sample, which indicated an inhomogeneous surface chemistry, a higher surface roughness or both. Regarding XPS results, surface elemental composition matched the one expected for PDMS. Furthermore, no significant differences were observed between coated samples. For PCL, whatever the ternary mixture composition used, water contact angles were higher for coated samples, which again indicated PDMS coating presence. For all samples, contact angle hysteresis was high and inhomogeneity in chemistry and/or surface roughness are expected. XPS analysis highlighted silicon presence on coated samples, which confirmed PDMS presence.

The effect of the ternary mixture composition used for coating on coating thickness was assessed on model samples. A working domain in the ternary diagram that prevents complete sample dissolution or sample clogging was delimited for PLA and PCL. PDMS coating thickness for coated PLA and PCL cylinders varied from 14 to 43 µm. Even though some significant differences in thickness were observed, no trends relative to ternary mixture composition could be established. Besides, the ternary solubility phase diagram obtained for PLA at 65°C showed to be highly dependent on sample size. Indeed, results could not be reproduced for the coating of smaller cylinders.

As the coating protocol developed for model structure was not scalable to our gyroid scaffold, many other coating techniques were proposed and tested: coating using centrifugation, sacrificial templating, dip coating and coating through solvogel formation. Even though some of them were promising, technical issues, insufficient crosslinking or coating detachment prevented their use. Hence, it was decided to come back to the first method. Developments were again focused on coating through the formation of a SIPN. Many parameters were varied starting from the protocol proposed by Nguyen and coworkers. The performed experiments highlighted the detrimental effects of rinsing steps and solvent drainage (paper towel or suction by deposition of the sample on a flat substrate).

Drainage to the bottom of the scaffold owing to gravity could not be avoided resulting in thicker PDMS layers or clogged pores. This issue could be solved to improve coating homogeneity throughout the scaffolds. Slow rotation of the scaffold to be coated or quick solvent evaporation could be used to reduce this effect. If a quick evaporation is used, attention should be paid to avoid blowing of cured PDMS and prevent bubble formation. Moreover, variation of the residence time as well as of the temperature of the ternary mixture could also be important parameters to study and to optimize.

The **coating protocol through the formation of a SIPN with repeated cycles** was used for further experiments. A better adhesion of the coating was observed compared to many other tested methods, which is a macroscopic proof of the formation of the SIPN. Neither rinsing nor drainage steps were further used and structure were hanged to ensure a maximal coating thickness.

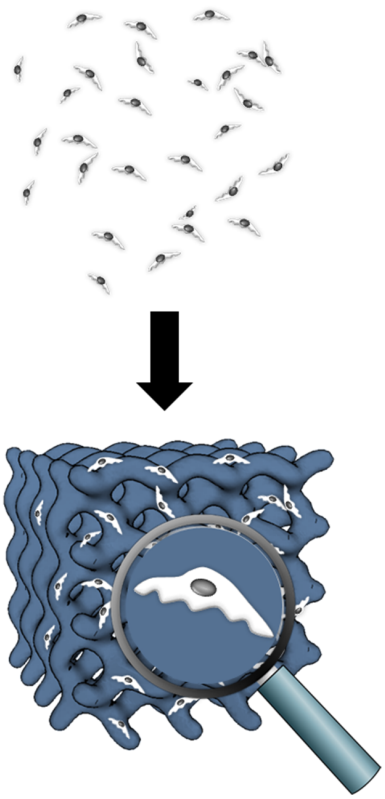
9 References

1. Kuterbekov, M. 3D-printed model substrates for tissue engineering applications. Master thesis, UCLouvain, Louvain-la-Neuve, Belgium, 2015.
2. Verheyen, R. 3D printing and surface modification of poly(ε-caprolactone) scaffolds for tissue engineering applications. Master thesis, UCLouvain, Louvain-la-Neuve, Belgium, 2016.
3. Gossart, N. Modification des propriétés mécaniques de surface de structures imprimées par 3D printing afin d'orienter la différenciation de cellules souches. Master thesis, UCLouvain, Louvain-la-Neuve, Belgium, 2017.

4. Duval, K.; Grover, H.; Han, L. H.; Mou, Y.; Pegoraro, A. F.; Fredberg, J.; Chen, Z., Modeling physiological events in 2D vs. 3D cell culture. *Physiology* **2017,** *32* (4), 266-277.
5. Chen, G.; Lv, Y.; Guo, P.; Lin, C.; Zhang, X.; Yang, L.; Xu, Z., Matrix mechanics and fluid shear stress control stem cells fate in three dimensional microenvironment. *Curr. Stem Cell Res. Ther.* **2013,** *8* (4), 313-323.
6. Zadpoor, A. A., Bone tissue regeneration: The role of scaffold geometry. *Biomater. Sci.* **2015,** *3* (2), 231-245.
7. Maloney, J. M.; Walton, E. B.; Bruce, C. M.; Van Vliet, K. J., Influence of finite thickness and stiffness on cellular adhesion-induced deformation of compliant substrata. *Phys. Rev. E Stat. Nonlin. Soft. Matter. Phys.* **2008,** *78* (4), 041923.
8. Tusan, C. G.; Man, Y. H.; Zarkoob, H.; Johnston, D. A.; Andriotis, O. G.; Thurner, P. J.; Yang, S.; Sander, E. A.; Gentleman, E.; Sengers, B. G.; Evans, N. D., Collective Cell Behavior in Mechanosensing of Substrate Thickness. *Biophys. J.* **2018,** *114* (11), 2743-2755.
9. Janson, I. A.; Putnam, A. J., Extracellular matrix elasticity and topography: Material-based cues that affect cell function via conserved mechanisms. *J. Biomed. Mater. Res. A* **2015,** *103* (3), 1246-1258.
10. Nguyen du, T.; Kleiman, M.; Ryu, K. A.; Hiew, S.; Brubaker, K.; Mughnetsyan, R.; Truong, R.; Dolan, B.; Tackett, E.; Esser-Kahn, A. P., Three-dimensional conformal coatings through the entrapment of polymer membrane precursors. *ACS Appl. Mater. Inter.* **2014,** *6* (4), 2830-2835.
11. Sperling, L. H., Interpenetrating Polymer Networks: An Overview. In *Interpenetrating Polymer Networks*, American Chemical Society: 1994; Vol. 239, pp 3-38.
12. Ye, Y.-S.; Rick, J.; Hwang, B.-J., Water Soluble Polymers as Proton Exchange Membranes for Fuel Cells. *Polymers* **2012,** *4* (2), 913-963.
13. Oláh, A.; Hillborg, H.; Vancso, G. J., Hydrophobic recovery of UV/ozone treated poly(dimethylsiloxane): Adhesion studies by contact mechanics and mechanism of surface modification. *Appl. Surf. Sci.* **2005,** *239* (3-4), 410-423.
14. Yoon, J. S.; Jung, H. W.; Kim, M. N.; Park, E. S., Diffusion coefficient and equilibrium solubility of water molecules in biodegradable polymers. *J. Appl. Polym. Sci.* **2000,** *77* (8), 1716-1722.
15. Uilk, J. M.; Mera, A. E.; Fox, R. B.; Wynne, K. J., Hydrosilation-cured poly(dimethylsiloxane) networks: Intrinsic contact angles via dynamic contact angle analysis. *Macromolecules* **2003,** *36* (10), 3689-3694.
16. Zhu, Y.; Gao, C.; Liu, X.; Shen, J., Surface modification of polycaprolactone membrane via aminolysis and biomacromolecule immobilization for promoting cytocompatibility of human endothelial cells. *Biomacromolecules* **2002,** *3* (6), 1312-1319.

17. Degand, S. Design of surfaces with mechanical nanoheterogeneities for a better control of cell-material interactions. PhD thesis, UCLouvain, Louvain-la-Neuve, Belgium, 2013.
18. Efimenko, K.; Wallace, W. E.; Genzer, J., Surface modification of Sylgard-184 poly(dimethyl siloxane) networks by ultraviolet and ultraviolet/ozone treatment. *J. Colloid Interf. Sci.* **2002,** *254* (2), 306-315.
19. Lee, J. N.; Jiang, X.; Ryan, D.; Whitesides, G. M., Compatibility of mammalian cells on surfaces of poly(dimethylsiloxane). *Langmuir* **2004,** *20* (26), 11684-11691.

Chapter 4: Preliminary cell culture studies



Before studying stem cell behavior on PDMS-modified macroporous scaffolds, preliminary studies were performed to determine suitable seeding conditions for adipose-derived mesenchymal stem cells (AMSC) and stem cells from the apical papilla (SCAP). The deposition of different adhesion proteins on uncoated and PDMS-coated PLA disks were tested to foster AMSC adhesion. Dynamic and static seeding methods were then explored to favor AMSC and SCAP seeding on 3D-printed PLA scaffolds. Besides, cell seeding and proliferation on 3D scaffolds were compared to the ones of cells on 2D substrates. Cell number and volume of cell suspension were optimized to reduce the number of cells lost upon seeding. Fibronectin was shown to significantly improve AMSC adhesion on uncoated and PDMS-coated PLA disks. No significant difference on AMSC seeding efficiency was observed whether seeding was performed in dynamic or static condition. SCAP were successfully seeded on 3D scaffolds and displayed a lower proliferation rate on these scaffolds compared to 2D substrates. The optimal number of SCAP and volume of cell suspension in gyroid scaffolds were determined to be 10^5 cells in 60 µl. Even though cell seeding on macroporous samples is challenging owing to the large pore size, parameters were determined to successfully seed and culture SCAP on 3D scaffolds.

We sincerely thank Mirasbek Kuterbekov[1], Audrey Smith, Bernard Ucakar, Kevin Vanvarenberg, Nathalie Lecouturier, Pauline de Berdt, Prof. Françoise Van Bambeke, Prof. Denis Dufrane and Prof. Anibal Diogenes for their contribution to the work presented in this chapter.

1 Introduction

Before cell seeding on complex coated samples, preliminary studies were performed to evaluate how the PDMS coating and the PLA gyroid scaffold impact stem cell adhesion and proliferation. These preliminary studies helped us to set up experiments such as cell seeding and surface modification to improve cell adhesion. Indeed, PDMS is known to be inadequate for cell adhesion owing to its hydrophobicity.[2] Hence, PDMS surface modifications such as protein deposition[2, 3] or chemical immobilization[4, 5] , and plasma treatment are often required to increase hydrophilicity[6, 7].

Cell seeding efficiency in macroporous strut-based scaffold can be relatively low and is influenced by pore size and mesh architecture.[8] Cell seeding efficiency on scaffolds with 700 µm pore size was lower than the one on scaffolds with 100 µm pore size (30% and 40%, respectively). Furthermore, similar scaffolds presenting heterogeneous pore size improved cell seeding efficiency. These results are attributed to the difference in architecture and to scaffold surface area, which depends on pore size.

In this chapter, two different cell types were used: adipose-derived mesenchymal stem cells (AMSC) and stem cells from the apical papilla (SCAP). AMSC are replacing bone marrow stem cells as the preferred source of mesenchymal stem cells (MSC) for tissue engineering strategies.[9] They are isolated from the adipose tissue harvested by liposuction. Those tissues are present in the body the entire life span and their use does not raise ethical concerns. Like other MSC, AMSC can differentiate into many cell types such as adipo-, osteo-, chondro-, myo- and neurolineages.[10] SCAP were described in the section 6 of Strategy of the thesis (Part III). Briefly, these cells are easily harvested from the apical papilla of immature wisdom teeth and have a high proliferation rate.[11] *In vitro*, SCAP can differentiate into osteo-, odonto-, chondro-, adipo- and neurolineages.[11-14] These cells have been extensively studied in our laboratory and present many advantages such as a resistance to hypoxic condition and ability to secrete proangiogenic factors.[14-17]

This chapter aims at improving stem cell adhesion on both PLA and PDMS materials. Besides, cell seeding is optimized on PLA gyroid scaffolds. This step is challenging owing to the millimeter pore size of the structure.

2 Impact of adhesion protein adsorption on AMSC adhesion

To improve cell adhesion on PLA and PDMS substrates, four different protein or polypeptide depositions were tested and compared. Collagen[18], fibronectin[19], Matrigel® [20] and poly-l-lysine[21] have already been tested with success on PDMS. Both collagen and fibronectin are proteins present in natural extracellular matrix. They possess signal peptides recognized by integrins that allow cell adhesion.[22] Matrigel® is a commercialized protein mixture mainly composed of laminin, collagen IV and entactin. This matrix is secreted by Engelbreth-Holm-Swarm mouse sarcoma cells.[23] Poly-l-lysine is a homopolypeptide positively charged at neutral pH owing to the presence of amino groups. The presence of positive charges (while cell membranes are negatively charged) improves cell adhesion.[2]

2.1 Materials and methods

Instead of complex gyroid structures, simpler flat substrates were used as models to simplify microscope analysis. PLA discs (12 mm in diameter and 0.5 mm thick) were printed and coated with PDMS(10:0.3) according to the protocol proposed by Nguyen and coworkers.[24] Briefly, PDMS base and curing agent were mixed in 10:0.3 (v:v) proportions. PLA disks were immersed in PDMS(10:0.3)/hexane /dioxane (12.5:75:12.5) mixture for 1 h at 65°C. Disks were rinsed for 5 s in hexane and PDMS coating was cured overnight at 55°C. Samples were disinfected in ethanol 70% (v:v in water) and dried.

Protein depositions on bare PLA disks and PDMS-coated disks were built by simple adsorption using conventional protocols. Briefly, disks were immersed in the protein solution (concentrations are presented in Table 1), incubated for 1 h (5 min for poly-l-lysine) at room temperature and removed from the protein solution. Fibronectin-modified and poly-l-lysine-modified samples were rinsed using PBS.

Table 1: Protein concentrations used for surface deposition

Protein/polypeptide	Solution concentration (µg/ml)
Collagen	100
Fibronectin	10
Matrigel®	83
Poly-l-lysine	100

AMSC isolated from lipoaspirate were cultured in Gibco DMEM medium (containing glucose, L-glutamine and without pyruvate) supplied with 10% (v:v) of fetal bovine serum, 1% (v:v) of L-glutamine and 1% (v:v) of Penicilin-Streptomicin mixture. AMSC were used at passage 5 and seeded at 5000 cells per disk. Three days after seeding, cells were fixed using paraformaldehyde (4%) and were stained for cytoskeleton using rhodamine-phalloidin. Images were acquired using a Olympus IX71 fluorescence microscope and cells were counted on three pictures (1.39x1.05 mm^2) per condition. Only one sample per condition was imaged but in total 3 samples were prepared and checked to verify reproducibility of reported trends.

2.2 Results and discussions

Fibronectin supported a significantly higher cell adhesion for both conditions compared to other proteins (Figure 1). Poly-l-lysine also supported cell adhesion for uncoated PLA. However, cell adhesion on PDMS-coated substrates was not different than the one on observed on samples without protein deposition. Pictures presented in Figure 2 illustrate cell morphology for uncoated and PDMS-coated PLA with and without fibronectin deposition. As presented in Figure 1, more cells were present on fibronectin-modified substrates. Furthermore, cells presented a larger area of spreading on fibronectin than on bare substrates.

As poly-l-lysine is positively charged, it is quite hydrophilic, while PDMS is more hydrophobic than PLA. This could explain a lower adsorption of poly-l-lysine on PDMS and, hence, a low cell adhesion. The larger area of spreading observed for cells on fibronectin is a sign of good adhesion. Success of fibronectin at improving cell adhesion compared to other proteins is hard to explain. Indeed, each protein deposition relied on simple physisorption and the concentration used for the deposition of fibronectin was the lowest used (10 µg/ml for fibronectin compared to 80-100 µg/ml for other proteins). Besides, deposition of fibronectin on silicone substrates for cell culture is rather low.[25] Nevertheless, fibronectin was extensively and successfully used for many cell culture experiments on PDMS.[26-28] Based on these results, fibronectin deposition was performed on both coated and uncoated PLA samples before each cell study to improve cell adhesion.

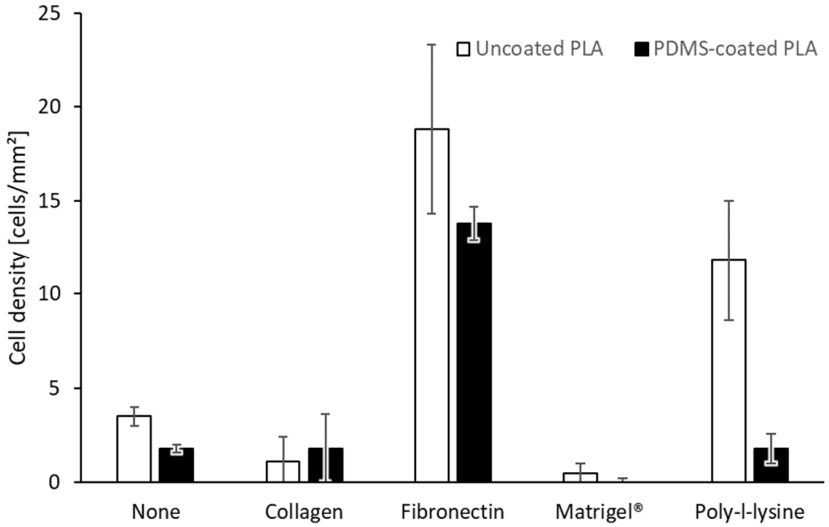


Figure 1: Effect of adhesion-supporting protein (or polypeptide) deposition on the adhesion of AMSC. Density of AMSC attached on uncoated PLA and PDMS-coated PLA disks modified with collagen, fibronectin, Matrigel® and poly-l-lysine. (n=3; error bars show the standard deviations).

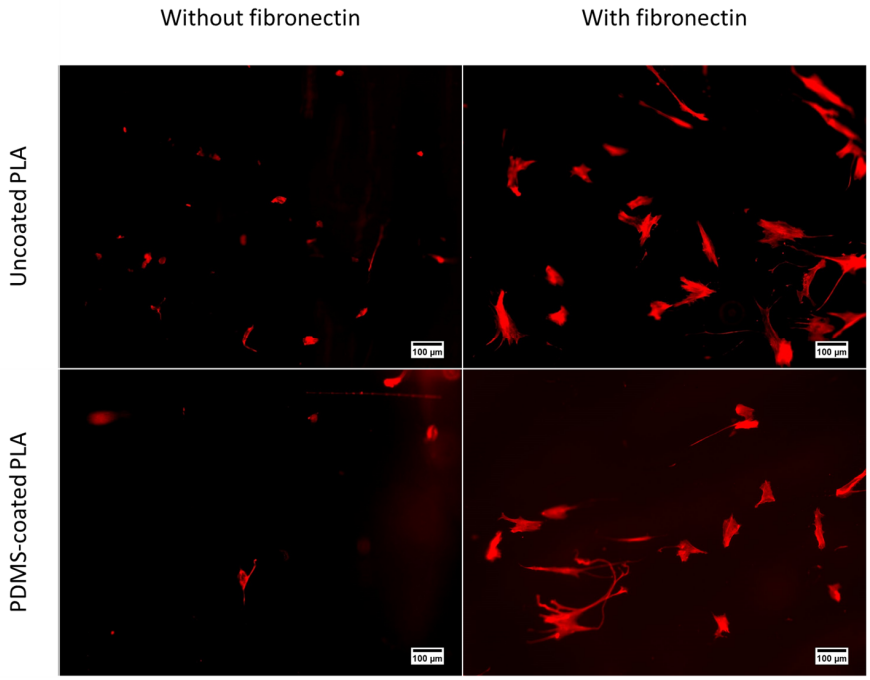


Figure 2: Improvement of AMSC adhesion using fibronectin deposition. Immunofluorescence images of AMSC on uncoated PLA and PDMS-coated PLA with and without fibronectin deposition. Fibronectin supported cell anchorage.

3 Impact of cell seeding method on AMSC adhesion

Cells can be seeded on a scaffold using many different protocols. Three different protocols using an orbital shaker, a rocking shaker or gravity (*i.e.* cell seeding at the top of the scaffold) were tested to seed AMSC on PLA gyroid scaffolds. Seeding and proliferation were compared to tissue culture-treated or not-treated flat polystyrene substrates from 12-well plates.

3.1 Materials and methods

To allow the comparison between 3D structures and 2D substrates, parts of gyroid scaffolds were designed and printed to possess a theoretical surface area of 3.26 cm^2 (Figure 3 A), which is quasi equivalent to the surface developed by wells from 12-well plates (3.8 cm^2). Samples were disinfected in ethanol 70% and dried. Fibronectin was deposited on PLA substrates before seeding (10 µg/ml, 1 ml). AMSC were used at passage 10.

The three protocols used were the following:

- Part of gyroid scaffolds were placed in 24 well plates (n=4). One ml of AMSC suspension containing 10^4 cells was added to the well. The plate was placed on an orbital shaker in the incubator for 3 hours at 100 rpm (orbit: 1.9 cm). After seeding, scaffolds were placed in a new plate and 1 ml of fresh medium was added.
- Part of gyroid scaffolds were placed in 24 well plates (n=4). One ml of AMSC suspension containing 10^4 cells was added to the well. The plate was placed on a rocking shaker in the incubator for 3 hours at a speed of 13 oscillations/min (tilting angle: 6°). After seeding, scaffolds were placed in a new plate and 1 ml of fresh medium was added.
- Part of gyroid scaffolds were placed in 24 well plates (n=4). Fifty µl of AMSC suspension containing 10^4 cells were deposited on top of the scaffolds. After 3 hours of incubation, scaffolds were placed in a new plate and 1 ml of fresh medium was added. This technique will be referred as the “top seeding” method.

2D controls used for comparison were:

- PLA disks (n=4): PLA disks perfectly fitting in wells from 12-well plates were printed and coated with fibronectin before seeding.
- Polystyrene (PS) substrates (12-well plate) (n=4): Polystyrene 12-well plates that were not plasma-treated for cell culture were used as negative control. Indeed, untreated polystyrene does not allow a good cell adhesion due to its hydrophobicity.
- Tissue culture-treated polystyrene (TCPS) (12-well plate) substrates (n=4): Tissue culture treated 12-well plates were used as positive control.

For each control, 1 ml of AMSC suspension containing 10^4 cells was added to the well.

At day 2, 7 and 14 after seeding, a resazurin-based *in vitro* toxicology assay was performed to evaluate cell metabolic activity. Medium was removed and 2D and 3D samples were rinsed with PBS. 1 ml of fresh medium containing 5% of resazurin (*in vitro* toxicology assay kit, VWR) was added to the wells. Plates were incubated for 4 h at 37°C. Supernatant was collected and fluorescence was measured (excitation wavelength: 560 nm; emission wavelength: 590 nm). As the test is not destructive, samples were rinsed twice with PBS and were incubated for measurements at later time points.

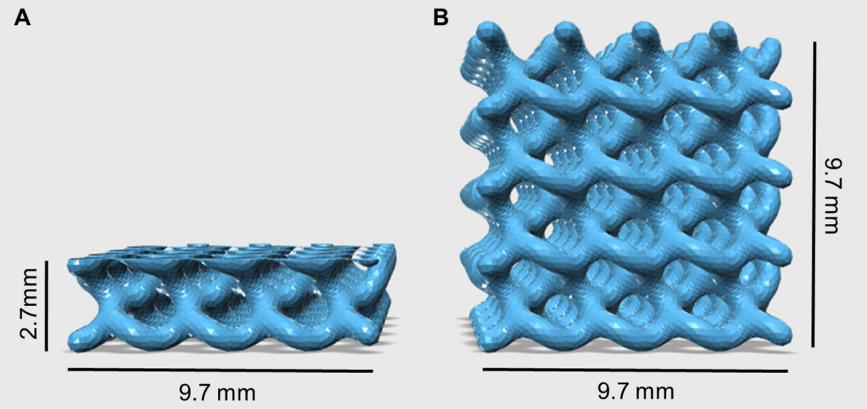


Figure 3: (A) Part of gyroid model and (B) full gyroid model presenting theoretical surface areas of 3.26 cm² and 10.76 cm², respectively.

3.2 Results and discussions

Metabolic activity data measured for each condition at day 2, 7 and 14 after seeding are presented in Figure 4. Cell metabolic activity decreased with culture time for 3D samples and PLA disks while it increased for TCPS. AMSC metabolic activity at day 2 reflects the number of cells that were effectively seeded on the samples. Among 2D substrates, a high metabolic activity was obtained for TCPS at day 2, while metabolic activity for PS was low. These results were confirmed by microscopy. A high cell density and a low cell density were observed for TCPS and PS, respectively (data not shown). Besides, cells presented a high spreading area on TCPS, which was not the case for cells on PS. Metabolic activity measured for PLA disks was lower than for TCPS but higher than for PS. Compared to positive control, about 75% of the cells adhered to PLA disks. However, the metabolic activity for 3D samples was as low as PS 2D substrates whatever the seeding protocol used.

An insufficient cell number effectively adhered to the 3D scaffolds in spite of fibronectin deposition. Surface chemistry of the scaffold cannot explain these low values as results for PLA disks were satisfying. One of the main factors influencing cell seeding is the probability of the cell to encounter the surface and to attach on it. On 2D substrates, all the cells sediment and finally get a chance to touch and adhere on the surface. This is not the case for 3D samples. If cells sediment, the chance to touch the scaffold and to adhere on its surface can be lower than the chance to reach the bottom of the well depending on pore size. Therefore, orbital and rocking shaker were used to maintain cells in suspension during seeding time. However, applied movement could have been insufficient to maintain cells in suspension because of the small diameter of the wells used for seeding (15.6 mm). This could have been resulted in low seeding efficiency.

Regarding cells seeded on scaffolds by top seeding, a small volume containing a high number of cells was deposited on the top of scaffolds to maximize the probability of cell-scaffold contact. However, the volume was still too high and the medium was sucked by capillarity to the bottom of the well.

Parameters that could be optimized to improve seeding efficiency are the following:

- Increase cell density per scaffold;

- Decrease the volume of medium used to avoid suction by capillarity at the bottom of the well;
- Increase seeding time as it could have been a limited factor. Indeed, 3 h of seeding could have been too short for cells to adhere.

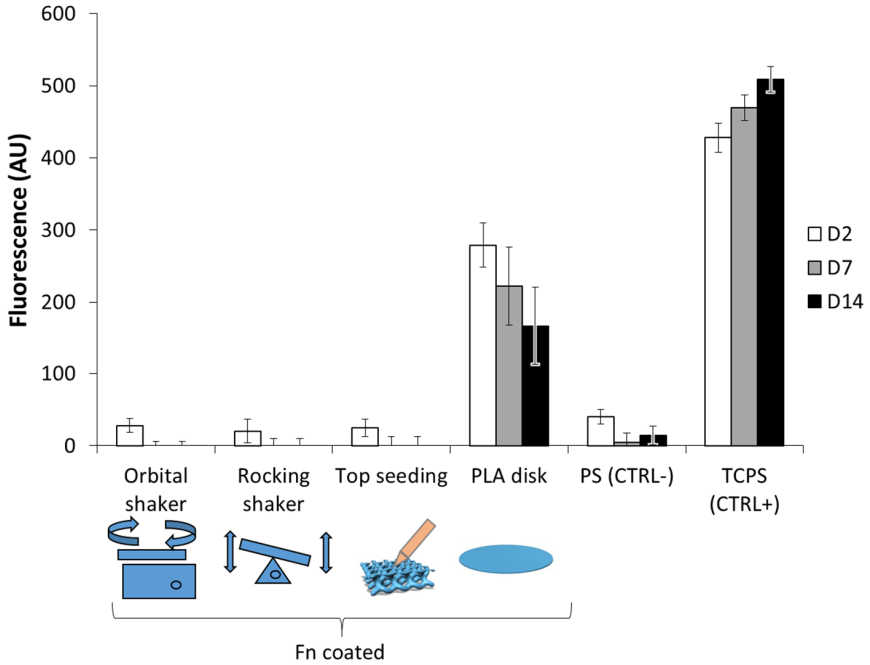


Figure 4: AMSC seeding and proliferation on 3D scaffolds and 2D substrates: AMSC metabolic activity 2, 7 and 14 days after seeding. Seeding were performed using different seeding methods. 3D structures are compared to 2D substrates (n=4; error bars show the standard deviations).

The decrease in metabolic activity for PLA samples at day 7 and 14 was quite unexpected. Cells seemed to die whatever the conditions except for TCPS. Moreover, AMSC cultured in T-flasks showed unexpected behavior such as a slowed or even stopped proliferation. This was observed for AMSC from two different donors. To avoid further issues it was decided to work with SCAP, which present similar advantages to AMSC and which have been well studied in our laboratory.

Subsequently, it was hypothesized that the addition of too much L-glutamine (amino acid commonly supplemented to mammalian cell culture media and used as energy source[29, 30] or source of nitrogen[31]) in the medium already containing L-glutamine could have been toxic for the cells. Indeed, L-

glutamine spontaneously degrades in ammonia and pyrrolidone carboxylic acid.[32] A too high concentration of L-glutamine would have led more rapidly to a medium containing toxic levels of ammonia.

4 SCAP adhesion on gyroid scaffolds

Following the results obtained with AMSC, a similar study was carried out for SCAP. Owing to the small number of cells attaching to the scaffold, the number of seeded cells and the seeding time before to add fresh medium were increased. As no significant differences were obtained between methods for AMSC seeding, it was decided to focus on the top seeding method. Cell adhesion on part and full gyroid scaffolds were compared to determine whether the structure size was affecting the seeding.

4.1 Materials and methods

SCAP were cultured in Minimum Essential Medium (Sigma-Aldrich, Belgium) supplemented with 10% bovine serum (Sigma-Aldrich, Belgium), 1% of L-glutamine (Life Technologies, Belgium) and 1% of Penicillin-Streptomycin mixture (Life Technologies, Belgium). Passages were achieved using Accutase (Life Technologies, Belgium) when cells reached around 90% confluence. SCAP were used at passage 7.

PLA gyroid scaffolds as well as PLA disks were disinfected in ethanol 70%, dried and then coated with fibronectin before seeding (10 µg/ml, 1 ml for part of gyroid scaffolds and PLA disks and 2 ml for full gyroid scaffolds). For gyroid scaffolds (part and full; n=3 for each), cells were suspended to reach a cell density of $1.3x10^7$ cells/ml. Thirty µl ($4x10^5$ cells) and 60 µl ($8x10^5$ cells) were placed at the top of part of gyroid scaffolds and full gyroid scaffolds, respectively. After 5 hours of incubation, 1 ml and 2 ml of fresh medium were added, respectively. For 2D substrates (PLA disks, PS and TCPS; n=3 for each), 1 ml of medium containing $2x10^4$ cells was seeded into each well.

Resazurin-based *in vitro* toxicology assays were performed as previously described (section 2.1 of this chapter) at day 2, 4, 7 and 11 after seeding to measure cell metabolic activity. For full gyroid scaffolds, 2 ml of reactive medium was used instead of 1 ml to completely immerse the scaffolds. At day 11, cells were detached from all samples using Accutase and DNA was quantified using a CyQUANT Cell Proliferation Assay Kit (Thermo Fisher

Scientific, Belgium) according to manufacturer protocol. Briefly, cells were lysed using lysis buffer to release DNA. DNA in lysis buffer was mixed to the dye in a black 96 well-plate and fluorescence was measured (excitation wavelength: 480 nm; emission wavelength: 520 nm). The fluorescence signal was converted in number of cells using a calibration curve obtained with dilutions of a known number of cells in the same 96-well plate. The first part of the process (cell culture, resazurin-based *in vitro* toxicology assay) was performed in duplicate, while the CyQUANT assay was executed only for one replicate.

4.2 Results and discussions

For all samples, SCAP metabolic activity increased with culture time (Figure 5 A). Regarding 2D substrates, for each time point, the highest value was observed for TCPS. However, an insignificant difference was observed for TCPS samples between day 7 and day 11. SCAP metabolic activity on PLA disks and PS were similar for each time point and lower than the one of TCPS. For each time point, similar values were observed for full gyroid scaffolds and parts of gyroid scaffolds. At day 2, both 3D scaffolds showed significantly higher values compared to 2D substrates. However, if we compare 2D substrates and the part of gyroid scaffolds (which were both presenting a similar surface area), the increase in metabolic activity with culture time was faster for 2D substrates.

Metabolic activity is not always directly correlated to the number of cells. Indeed, a low number of cells could present a high metabolic activity if highly active, while a large number of cells with a lower metabolic activity (if quiescent for instance) could show similar measured metabolic activity. Hence, to confirm the results obtained for metabolic activity, the number of SCAP was quantified (Figure 5 B) and normalized by the number of seeded cells (Figure 5 C). On 2D substrates, cells proliferated to reach at least 10 times the number of seeded cells whatever the condition. The number of cells obtained for full gyroid scaffolds was twice the number obtained for part of gyroid scaffolds. Besides, for both gyroid scaffolds, the number of cells obtained after 11 days was three times lower than the number of cells engaged for seeding.

Metabolic activity measurements showed that SCAP were able to adhere and proliferate whatever the conditions. This result was confirmed by the increased number of cells on 2D substrates after 11 days. Cells adhered

easier on TCPS compared to both PLA and PS substrates but adhesion on PLA and PS seemed similar. The small difference in metabolic activity observed for TCPS between day 7 and day 11 could be the consequence of cell confluence. Indeed, cell confluence was observed at day 7 using an inverted microscope (data not shown). Once the confluence is reached, cells stop to proliferate[33] and the overall metabolic activity is maintained.

Part and full gyroid scaffolds showed similar fluorescence measurements throughout the culture time. Considering that two times the volume of assay reagent was used for full gyroid scaffolds compared to part of gyroid scaffolds, this was coherent with the fact that two times the number of cells was seeded on full gyroid scaffolds compared to part of gyroid scaffolds. This result was confirmed by the two times higher number of cells at day 11 for full gyroid scaffolds compared to part of gyroid scaffolds. Based on those results, seeding efficiency does not seem to be influenced by gyroid scaffold size as proportions were respected.

At least twenty times more cells were seeded on the gyroids scaffolds compared to 2D substrates, which was consistent with the higher metabolic activity observed at a day 2. Even though a small number of cells were observed at day 11 compared to the seeded number of cells, the latter result showed that a sufficient number of cells were successfully seeded. The faster increase in metabolic activity observed for 2D substrates indicated that proliferation rates were higher for 2D substrates compared to 3D macroporous samples. This difference was observed even though the pore size of the macroporous scaffold was sufficient for the cells to spread on pore walls as they do on 2D substrates. This would indicate that even if cells seemed to spread like on 2D substrates, they still felt the 3rd dimension or the curvatures of the scaffold. In literature, proliferation rate is usually different in 2D and in 3D.[34, 35] The configuration giving the higher proliferation rate is cell line and matrix dependent. Proliferation rate of some cell lines will be higher in 3D than in 2D while proliferation rate of other cell lines will be higher in 2D.

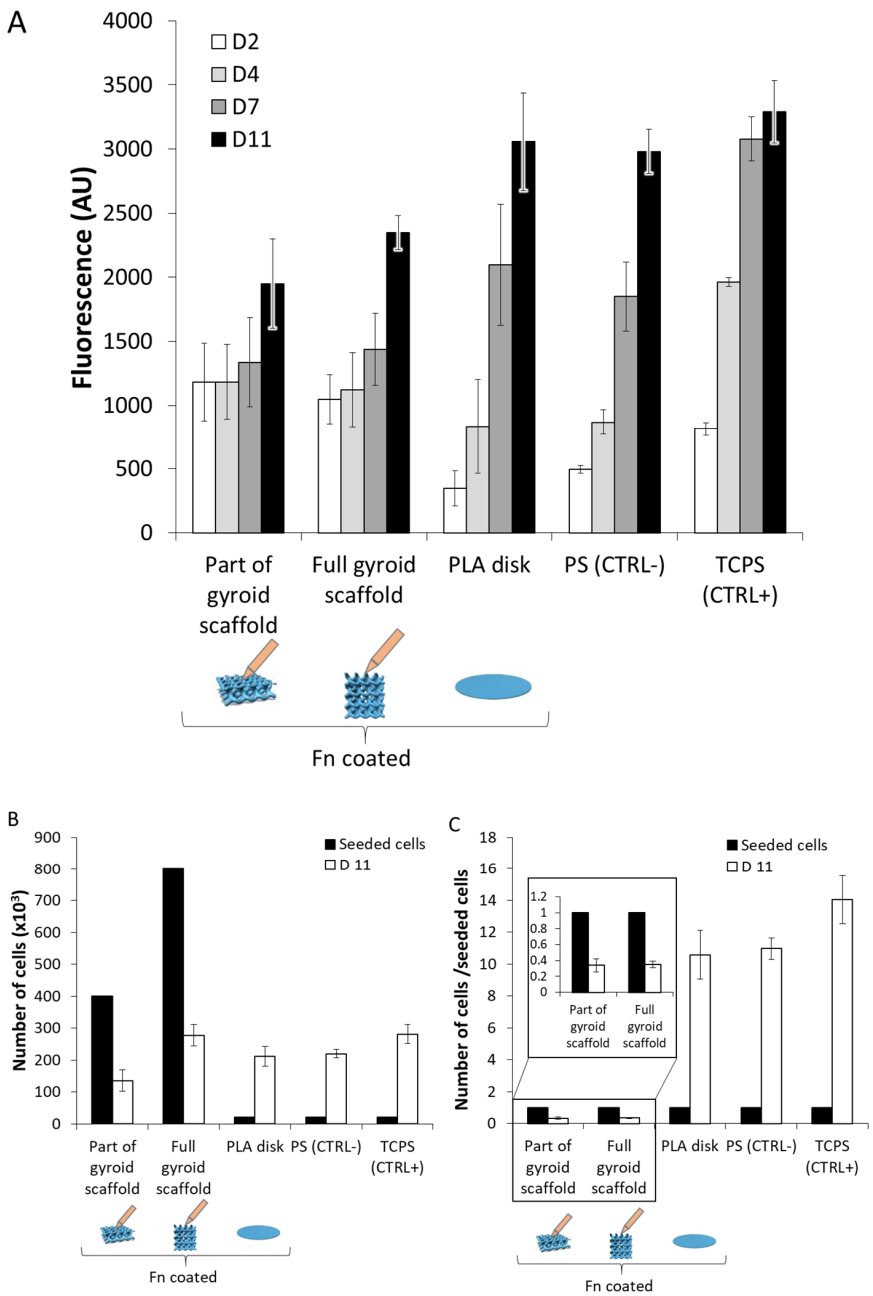


Figure 5: SCAP seeding and proliferation on 3D scaffolds and 2D substrates: (A) SCAP metabolic activity 2, 5, 7 and 11 days after seeding and (B) number of cells 11 days after seeding (C) normalized by the number of seeded cells. Fn= Fibronectin (n=2x3 for metabolic activity and n=1x3 for DNA quantification; error bars show the standard deviations).

SCAP were successfully seeded on 3D macroporous scaffolds and were able to proliferate. However, proliferation was lower on 3D scaffolds compared to 2D substrates. Even though a small number of cells seemed to adhere on the 3D scaffolds, their size did not influence the seeding.

5 Improvement of SCAP adhesion yield by adjustment of cell density

5.1 Materials and methods

During seeding, a high number of SCAP did not attach on the scaffolds. To reduce cell loss, different seeding densities were tested: $2x10^5$, 10^5, $5x10^4$, $2x10^4$ cells in 30 µl of medium were seeded on part of gyroid scaffolds (n=3) as previously described (section 3.1. of this chapter). The next day, metabolic activity was measured using the resazurin-based *in vitro* toxicology assay kit as described in part 2.1 of this capter. Cells were detached from the structures using Accutase and DNA was quantified using the CyQUANT assay kit as described in part 3.1. PLA disks (n=3) and TCPS (n=3) were used as positive controls (seeding density was $2x10^4$ cells/sample) as described in part 3.1. SCAP were used at passage 7.

5.2 Results and discussions

Both PLA disks and TCPS showed similar values of metabolic activity, while the number of cells was close to the seeded number (Figure 6 A and B). SCAP metabolic activity as well as the number of cells effectively seeded decreased along with the number of cells seeded on the 3D scaffolds. Between 40% and 70% of seeded cells attached on the scaffolds but no clear trends were observed between the percentage of seeded cells and the number of seeded cells (Figure 6 C). An initial seeding of $50x10^3$ cells allowed an effective seeding of about $30x10^3$ cells on the scaffold, which was quite close to the number of cells seeded on the control ($25x10^3$ cells). Furthermore, metabolic activity for both samples were similar. Hence, it was decided to seed $50x10^3$ cells on part of gyroid scaffolds and $100x10^3$ cells on full gyroid scaffold as it is a good compromise between the number of cells used and a sufficient number of cells effectively seeded on the scaffold.

Data of metabolic activity were normalized by the number of cells. Figure 6 D shows metabolic activity for $20x10^3$ cells in each condition. Metabolic activity per cell decreased for increased number of cells. This showed that the number of cells was not linearly correlated to the measured metabolic activity.

This experiment allowed to find the optimal number of cells to engage to have an effective seeding close to the one achieved on control substrates. Thereafter, it was decided to engage $50x10^3$ cells in 30 µl for the seeding of part of gyroid scaffolds and $100x10^3$ cells in 60 µl for the seeding of full gyroid scaffolds.

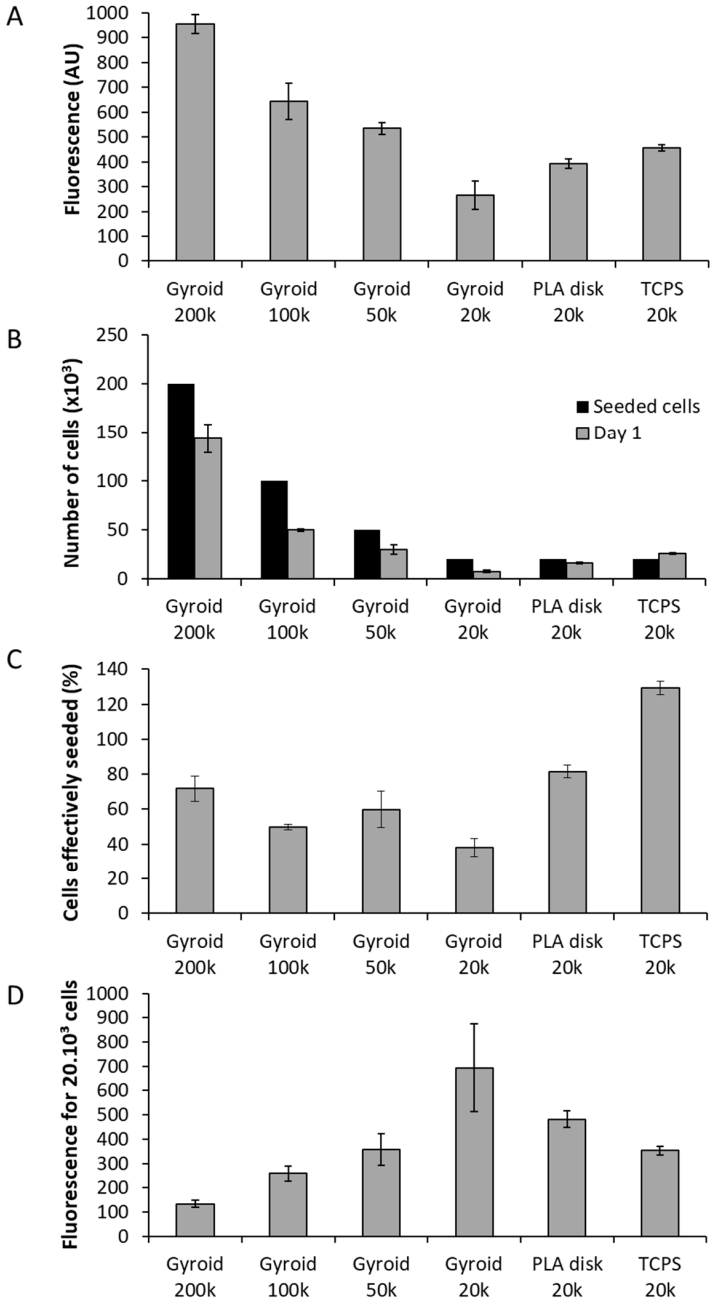


Figure 6: SCAP seeding optimization: (A) SCAP metabolic activity and (B) number of cells measured on parts of gyroids, PLA disks and tissue culture polystyrene (TCPS) substrates one day after seeding. 200k, 100k, 50k and 20k refers to the number of cells seeded in thousand. Based on these two graphs, (C) percentage of cells effectively seeded and (D) metabolic activity normalized for 20x10³ cells were computed (n=3; error bars show the standard deviations).

6 Conclusion and future prospects

Cell adhesion was improved on both PLA and PDMS by fibronectin deposition. Besides, SCAP initial seeding conditions were defined in order to obtain a sufficient number of adherent cells on gyroid scaffolds presenting millimeter pore size.

Results from this chapter allowed to set up *in vitro* experiments. Surfaces were modified using different proteins and polypeptides. Fibronectin significantly improved AMSC attachment on both uncoated and PDMS-coated PLA. Different cell seeding techniques on 3D scaffolds were tested. Seeding efficiency was low compared to 2D substrates whatever the seeding technique. This could be explained by cell sedimentation and the low probability for cells to meet the scaffold surface and attach to it. AMSC from two different donors were not proliferating or were even dying, it was therefore decided to work with SCAP as this cell type was well studied in our laboratory and seemed to encounter less adherence and proliferation problems than AMSC. The study was then focused on the top seeding method. A high number of cells was seeded in a small volume to increase the probability for cells to meet the surface and attach on it. Cells were successfully seeded on PLA gyroid scaffolds and the size of the structure did not affect the seeding efficiency. SCAP proliferated during the tested period and proliferation rates were higher for 2D substrates than for 3D macroporous scaffolds. However, the number of cells engaged for initial seeding was really high compared to the number of cells on the scaffold after 11 days. Hence, lower numbers of cells were seeded to increase the yield. Seeding efficiency was between 40 and 70% for all seeding densities tested. The seeding density used for further experiments was then $50x10^3$ cells in 30 µl, for seeding on part of gyroid scaffolds as the number of SCAP attached to the scaffold was close to the value obtained for TCPS. For full gyroid scaffolds, the same cell density was used but resuspended in 60 µl instead of 30 µl.

Some improvements could be proposed for cell seeding. Indeed, top seeding is expected to seed cells mainly at the top of the scaffold, resulting in heterogeneous cell distribution. The two other methods tested using orbital and rocking shakers could be further optimized. Perspectives for further studies would be to use higher seeding densities, while well diameters and shaking speeds could be optimized.[36] Cycles of shaking periods and rests as well as the use of ultra-low-attachment plates could be tested like it is performed for microparticle seeding.[37] Indeed, ultra-low-attachment plate

prevents protein adhesion and prevents cell adhesion on well surfaces.[38] Thereupon, cells preferentially adhere on the scaffold. In addition, other dynamic seeding techniques such as perfusion do exist.[39, 40] The scaffold is placed in a closed chamber and medium containing cells is pushed through the scaffold. A uniaxial flow has a poor seeding efficiency for open regular porous geometries.[41, 42] However, to improve cell seeding, medium containing cells can be recycled and reinjected until a sufficient number of cells has attached on the scaffold. Even though special equipment are usually employed, it could have been achieved in our laboratory either using a closed loop and a peristaltic pump (Figure 7 A) or using two syringes placed on both sides of the scaffold (Figure 7 B).

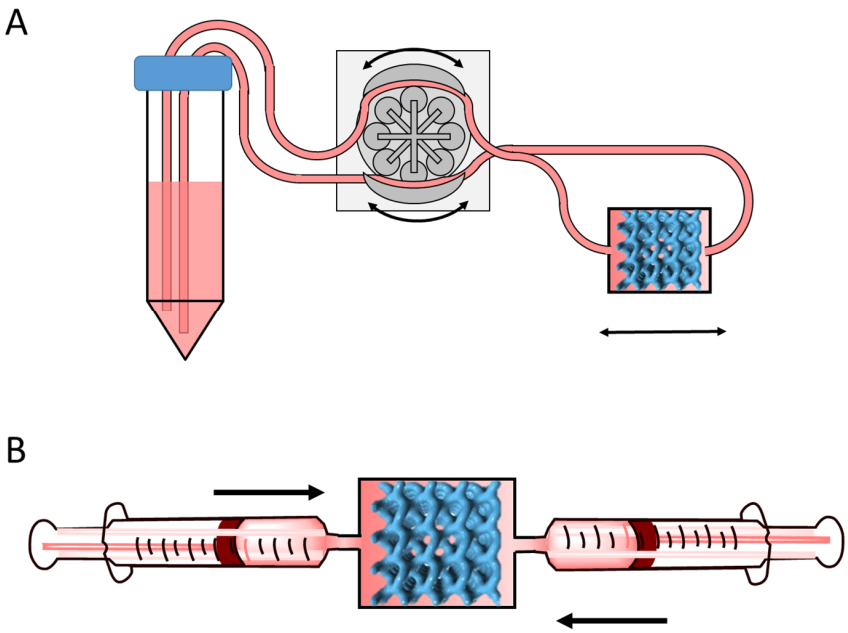


Figure 7: Schematic of the equipment for dynamic cell seeding in a 3D scaffold. Seeding (A) using a peristaltic pump or (B) using two syringes placed on both sides of the scaffold.

7 References

1. Kuterbekov, M. 3D-printed model substrates for tissue engineering applications. Master thesis, UCLouvain, Louvain-la-Neuve, Belgium, 2015.
2. Wang, L.; Sun, B.; Ziemer, K. S.; Barabino, G. A.; Carrier, R. L., Chemical and physical modifications to poly(dimethylsiloxane) surfaces

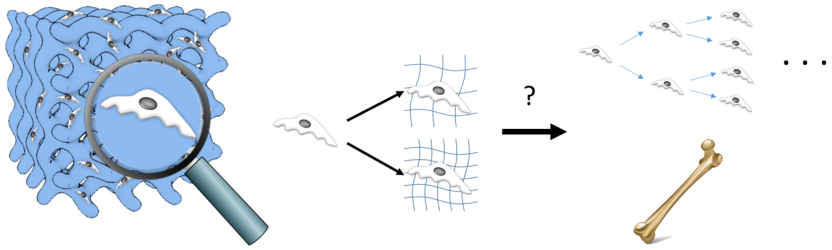
affect adhesion of Caco-2 cells. *J. Biomed. Mater. Res. Part A* **2010,** *93* (4), 1260-1271.
3. Chumbimuni-Torres, K. Y.; Coronado, R. E.; Mfuh, A. M.; Castro-Guerrero, C.; Silva, M. F.; Negrete, G. R.; Bizios, R.; Garcia, C. D., Adsorption of proteins to thin-films of PDMS and its effect on the adhesion of human endothelial cells. *RSC Adv.* **2011,** *1* (4), 706-714.
4. Nishikawa, M.; Yamamoto, T.; Kojima, N.; Kikuo, K.; Fujii, T.; Sakai, Y., Stable immobilization of rat hepatocytes as hemispheroids onto collagen-conjugated poly-dimethylsiloxane (PDMS) surfaces: Importance of direct oxygenation through PDMS for both formation and function. *Biotechnol. Bioeng.* **2008,** *99* (6), 1472-1481.
5. Rezaei, S. M.; Mohd Ishak, Z. A., The biocompatibility and hydrophilicity evaluation of collagen grafted poly(dimethylsiloxane) and poly (2-hydroxyethylmethacrylate) blends. *Polym. Test.* **2011,** *30* (1), 69-75.
6. Fuard, D.; Tzvetkova-Chevolleau, T.; Decossas, S.; Tracqui, P.; Schiavone, P., Optimization of poly-di-methyl-siloxane (PDMS) substrates for studying cellular adhesion and motility. *Microelectron. Eng.* **2008,** *85* (5-6), 1289-1293.
7. Pan, F.; Zhang, M.; Wu, G.; Lai, Y.; Greber, B.; Schöler, H. R.; Chi, L., Topographic effect on human induced pluripotent stem cells differentiation towards neuronal lineage. *Biomaterials* **2013,** *34* (33), 8131-8139.
8. Sobral, J. M.; Caridade, S. G.; Sousa, R. A.; Mano, J. F.; Reis, R. L., Three-dimensional plotted scaffolds with controlled pore size gradients: Effect of scaffold geometry on mechanical performance and cell seeding efficiency. *Acta Biomater.* **2011,** *7* (3), 1009-1018.
9. O'Halloran, N.; Courtney, D.; Kerin, M. J.; Lowery, A. J., Adipose-Derived Stem Cells in Novel Approaches to Breast Reconstruction: Their Suitability for Tissue Engineering and Oncological Safety. *Breast Cancer Basic Clin. Res.* **2017,** *11*, 1178223417726777.
10. Dai, R.; Wang, Z.; Samanipour, R.; Koo, K. I.; Kim, K., Adipose-Derived Stem Cells for Tissue Engineering and Regenerative Medicine Applications. *Stem Cells Intl.* **2016,** *2016*, 6737345.
11. Zhang, W.; Zhang, X.; Li, J.; Zheng, J.; Hu, X.; Xu, M.; Mao, X.; Ling, J., Foxc2 and BMP2 induce osteogenic/odontogenic differentiation and mineralization of human stem cells from apical papilla. *Stem Cells Intl.* **2018,** *2018*, 2363917.
12. Huang, G. T. J.; Gronthos, S.; Shi, S., Critical reviews in oral biology & medicine: Mesenchymal stem cells derived from dental tissues vs. those from other sources: Their biology and role in Regenerative Medicine. *J. Dent. Res.* **2009,** *88* (9), 792-806.

13. Zhu, Y.; Zhang, P.; Gu, R. L.; Liu, Y. S.; Zhou, Y. S., Origin and Clinical Applications of Neural Crest-Derived Dental Stem Cells. *Chin. J. Dent. Res.* **2018,** *21* (2), 89-100.
14. Vanacker, J.; Viswanath, A.; De Berdt, P.; Everard, A.; Cani, P. D.; Bouzin, C.; Feron, O.; Diogenes, A.; Leprince, J. G.; des Rieux, A., Hypoxia modulates the differentiation potential of stem cells of the apical papilla. *J. Endod.* **2014,** *40* (9), 1410-1418.
15. De Berdt, P.; Bottemanne, P.; Bianco, J.; Alhouayek, M.; Diogenes, A.; Llyod, A.; Gerardo-Nava, J.; Brook, G. A.; Miron, V.; Muccioli, G. G.; Rieux, A., Stem cells from human apical papilla decrease neuro-inflammation and stimulate oligodendrocyte progenitor differentiation via activin-A secretion. *Cell. Mol. Life Sci.* **2018,** *75* (15), 2843-2856.
16. Germain, L.; De Berdt, P.; Vanacker, J.; Leprince, J.; Diogenes, A.; Jacobs, D.; Vandermeulen, G.; Bouzin, C.; Préat, V.; Dupont-Gillain, C.; Des Rieux, A., Fibrin hydrogels to deliver dental stem cells of the apical papilla for regenerative medicine. *Regen. Med.* **2015,** *10* (2), 153-167.
17. Viswanath, A.; Vanacker, J.; Germain, L.; Leprince, J. G.; Diogenes, A.; Shakesheff, K. M.; White, L. J.; des Rieux, A., Extracellular matrix-derived hydrogels for dental stem cell delivery. *J. Biomed. Mater. Res. Part A* **2017,** *105* (1), 319-328.
18. Palchesko, R. N.; Zhang, L.; Sun, Y.; Feinberg, A. W., Development of Polydimethylsiloxane Substrates with Tunable Elastic Modulus to Study Cell Mechanobiology in Muscle and Nerve. *PLOS ONE* **2012,** *7* (12), e51499.
19. Zhang, W.; Choi, D. S.; Nguyen, Y. H.; Chang, J.; Qin, L., Studying cancer stem cell dynamics on PDMS surfaces for microfluidics device design. *Sci. Rep.* **2013,** *3*, 2332.
20. Kamei, K. I.; Hirai, Y.; Yoshioka, M.; Makino, Y.; Yuan, Q.; Nakajima, M.; Chen, Y.; Tabata, O., Phenotypic and Transcriptional Modulation of Human Pluripotent Stem Cells Induced by Nano/Microfabrication Materials. *Adv. Healthc. Mater.* **2013,** *2* (2), 287-291.
21. Wu, M. H., Simple poly(dimethylsiloxane) surface modification to control cell adhesion. *Surf. Interface Anal.* **2009,** *41* (1), 11-16.
22. Hynes, R. O., Integrins: Bidirectional, allosteric signaling machines. *Cell* **2002,** *110* (6), 673-687.
23. Hughes, C. S.; Postovit, L. M.; Lajoie, G. A., Matrigel: a complex protein mixture required for optimal growth of cell culture. *Proteomics* **2010,** *10* (9), 1886-1890.
24. Nguyen du, T.; Kleiman, M.; Ryu, K. A.; Hiew, S.; Brubaker, K.; Mughnetsyan, R.; Truong, R.; Dolan, B.; Tackett, E.; Esser-Kahn, A. P., Three-dimensional conformal coatings through the entrapment of polymer membrane precursors. *ACS Appl. Mater. Inter.* **2014,** *6* (4), 2830-2835.

25. Cunningham, J. J.; Nikolovski, J.; Linderman, J. J.; Mooney, D. J., Quantification of fibronectin adsorption to silicone-rubber cell culture substrates. *BioTechniques* **2002,** *32* (4), 876-887.
26. Cornelissen, C. G.; Dietrich, M.; Gromann, K.; Frese, J.; Krueger, S.; Sachweh, J. S.; Jockenhoevel, S., Fibronectin coating of oxygenator membranes enhances endothelial cell attachment. *Biomed. Eng. Online* **2013,** *12* (1), 7.
27. Seo, J. H.; Sakai, K.; Yui, N., Adsorption state of fibronectin on poly(dimethylsiloxane) surfaces with varied stiffness can dominate adhesion density of fibroblasts. *Acta Biomater.* **2013,** *9* (3), 5493-5501.
28. Degand, S.; Knoops, B.; Dupont-Gillain, C. C., Design and characterization of surfaces presenting mechanical nanoheterogeneities for a better control of cell-material interactions. *Colloids Surf. A Physicochem. Eng. Asp.* **2013,** *442*, 164-172.
29. Zhao, M. H.; Kim, N. H.; Cui, X. S., GlutaMAX prolongs the shelf life of the culture medium for porcine parthenotes. *Theriogenology* **2016,** *85* (3), 368-375.
30. Salehinejad, P.; Alitheen, N. B.; Nematollahi-Mahani, S. N.; Ali, A. M.; Omar, A. R.; Janzamin, E.; Hajghani, M., Effect of culture media on expansion properties of human umbilical cord matrix-derived mesenchymal cells. *Cytotherapy* **2012,** *14* (8), 948-953.
31. Thermofisher L-Glutamine & GlutaMAX Cell Culture Supplements. https://www.thermofisher.com/be/en/home/life-science/cell-culture/mammalian-cell-culture/media-supplements/glutamax-media.html (accessed June 26, 2019).
32. Tritsch, G. L.; Moore, G. E., Spontaneous decomposition of glutamine in cell culture media. *Exp. Cell. Res.* **1962,** *28* (2), 360-364.
33. Hutson, T. B.; Mitchell, M. L.; Keller, J. T.; Long, D. J.; Chang, M. J. W., A technique for monitoring mammalian cell growth and inhibition *in situ* via Fourier transform infrared spectroscopy. *Anal. Biochem.* **1988,** *174* (2), 415-422.
34. Edmondson, R.; Broglie, J. J.; Adcock, A. F.; Yang, L., Three-dimensional cell culture systems and their applications in drug discovery and cell-based biosensors. *Assay Drug Dev. Techn.* **2014,** *12* (4), 207-218.
35. Duval, K.; Grover, H.; Han, L. H.; Mou, Y.; Pegoraro, A. F.; Fredberg, J.; Chen, Z., Modeling physiological events in 2D vs. 3D cell culture. *Physiology* **2017,** *32* (4), 266-277.
36. Bueno, E. M.; Laevsky, G.; Barabino, G. A., Enhancing cell seeding of scaffolds in tissue engineering through manipulation of hydrodynamic parameters. *J. Biotechnol.* **2007,** *129* (3), 516-531.

37. de Soure, A. M.; Fernandes-Platzgummer, A.; da Silva, C. L.; Cabral, J. M. S., Scalable microcarrier-based manufacturing of mesenchymal stem/stromal cells. *J. Biotechnol.* **2016,** *236*, 88-109.
38. Amaral, R. L. F.; Miranda, M.; Marcato, P. D.; Swiech, K., Comparative analysis of 3D bladder tumor spheroids obtained by forced floating and hanging drop methods for drug screening. *Front. Physiol.* **2017,** *8*, 605.
39. Beşkardeş, I. G.; Aydın, G.; Bektaş, Ş.; Cengiz, A.; Gümüşderelioğlu, M., A systematic study for optimal cell seeding and culture conditions in a perfusion mode bone-tissue bioreactor. *Biochem. Eng. J.* **2018,** *132*, 100-111.
40. Schmid, J.; Schwarz, S.; Meier-Staude, R.; Sudhop, S.; Clausen-Schaumann, H.; Schieker, M.; Huber, R., A perfusion bioreactor system for cell seeding and oxygen-controlled cultivation of three-dimensional cell cultures. *Tissue Eng. Part C Methods* **2018,** *24* (10), 585-595.
41. Campos Marín, A.; Brunelli, M.; Lacroix, D., Flow perfusion rate modulates cell deposition onto scaffold substrate during cell seeding. *Biomech. Model. Mechan.* **2018,** *17* (3), 675-687.
42. Ali, D., Effect of scaffold architecture on cell seeding efficiency: A discrete phase model CFD analysis. *Comput. Biol. Med.* **2019,** *109*, 62-69.

Chapter 5: The crosslinking density of a PDMS coating on macroporous scaffolds influences the proliferation of stem cells from the apical papilla but not their osteogenic differentiation



It is well known that cell behavior, such as their adhesion, proliferation and differentiation, is influenced by the mechanical properties of their environment. The impact of mechanical properties on cell behavior was largely studied on 2D substrates, while the one on cells encapsulated in a 3D matrix starts to be clarified. In between, mechanotransduction of cells inside macroporous scaffolds is rather unexplored but is yet clinically relevant. This study aimed at exploring the behavior of stem cells from the apical papilla (SCAP) inside macroporous scaffolds presenting environments with different mechanical properties. To this end, the surface mechanical properties of 3D-printed macroporous scaffolds were successfully modified employing a crosslinkable poly(dimethylsiloxane) (PDMS) coating. Rotational rheometry analysis showed that PDMS stiffness increased for increased amount of PDMS curing agent, *i.e.* increased crosslinking density. The thickness of PDMS coatings, presenting different mechanical properties, on PLA scaffolds was evaluated by scanning electron microscopy; it was around 50 µm. Proliferation and osteogenic differentiation of SCAP cultured on these scaffolds were monitored. Even though SCAP proliferation was reduced on softer PDMS coatings, PDMS stiffness did not influence their osteogenic differentiation. Differentiation results differ from the ones obtained on conventional 2D culture substrates and highlight how essential is the study of mechanotransduction in 3D macroporous scaffolds.

To be published as: Germain, L.; Mwema, A.; Dupont-Gillain, C.; des Rieux, A., The crosslinking density of a PDMS coating on macroporous scaffolds influences the proliferation of stem cells from the apical papilla but not their osteogenic differentiation. (Manuscript in preparation)

We sincerely thank Yasmine Labrak, Viridiane Gratpain, Kevin Vanvarenberg, Bernard Ucakar, Prof. Françoise Van Bambeke, Nicola Gossart, Flanco Zhuge, Prof. Evelyne Van Ruymbeke, Eléana Somville, Karine Glinel, Delphine Magnin and Prof. Anibal Diogenes for their contribution to the work presented in this chapter.

1 Introduction

Tissue engineering is the science aiming at tissue reconstruction using a combination of cells, scaffolds and bioactive factors[1] that is optimized to mimic cell environment of the desired tissue[2, 3]. Conventional scaffolding techniques (*e.g.* particulate leaching, thermally induced phase separation, gas foaming,…)[4-7] present severe limitations such as the lack of control regarding pore size, morphology, distribution and interconnectivity as well as the poor reproducibility of the scaffolds.[5] Additive manufacturing techniques working according to a layer-by-layer construction of the scaffold allow a high tunability of scaffold architecture to fit patient-to-patient variability.[5] Moreover, required scaffold properties as well as biological performances can be easily balanced.[5, 6]

Among additive manufacturing techniques, Fused deposition modelling (FDM) is a low cost and user-friendly technique.[8] Using FDM, we were previously able to produce well defined gyroid scaffolds in poly(lactic acid) (PLA).[9] Visually, the gyroid looks like a mesh composed of vertical and horizontal springs joining each other at nodal points. The gyroid presented interesting mechanical properties for tissue engineering, as it possesses a high fatigue life and a high specific stiffness to weight ratio while maintaining isotropy.[10-12] The high pore accessibility of the gyroid allows a good permeability to nutrients and metabolites.[13] Furthermore, concave curvatures with radii larger than cell size, abundantly present in the gyroid structure, improved tissue regeneration *in vitro* as well as *in vivo*.[14]

Cells are able to sense chemistry, topography and mechanical properties of their environment and convert them into biochemical signals. This process is known as mechanotransduction.[15-17] Hence, cell-material interactions are of upmost importance to understand and optimize as it will orient cell behavior and will determine the success of a graft.[18] Cell environments presenting stiffness similar to native tissue can improve the efficacy of biochemical stimuli and favor the regeneration of the corresponding new tissue.[19]

Mechanical properties of cell environment can be characterized by viscoelastic properties. While the effect of elastic modulus on cell behavior has been extensively studied, the effect of viscous modulus is relatively unexplored.[20, 21] Cameron and coworkers isolated the effect of viscous modulus on cell behavior using tailored polyacrylamide (PAA) systems.[22] For constant elastic moduli and complex moduli, an increase in viscous modulus

of PA gels increased human mesenchymal stem cells spreading area and proliferation and improved cell differentiation towards several lineages.

Owing to their large pore sizes, macroporous scaffolds are advantageous for clinical applications compared to microporous materials such as hydrogels. Indeed, nutrients and metabolites transfer is high and substrate remodeling is not necessary for cell motility, which improves transplanted and endogenous cells migration.[23] However, the majority of the studies focused on the effect of matrix stiffness on cells were performed on 2D substrates, although some work has been done in 3D using cells encapsulated in hydrogels.[19] Compared to hydrogel however, the macroporous scaffold brings a third configuration, which lies between the 2D and 3D culture. Cells spread in the pores as they do on a 2D substrates, but inside a 3D scaffold. The use of this configuration to study the effect of mechanical properties is relatively unexplored but clinically relevant.[24]

Polymers used to study cell mechanotransduction in 2D were mainly poly(dimethylsiloxane) (PDMS) elastomers, and PAA hydrogels.[20, 21, 25, 26] The desired mechanical properties are obtained varying the amount of polymer or crosslinker. The molecular weight also influences mechanical properties.[20] Coating those polymers on flat substrates is relatively simple. Dip coating or spin coating allow to form a uniform and sufficiently thick layer. In contrast, the coating of complicate macroporous structure is much more challenging and few techniques are effective.[27] Spin coating is used for flat substrates[28], while dip coating, depending on coating polymer hardening process[28], could provoke pore clogging or inhomogeneous coating distribution due to capillarity forces that retain the liquid inside the pores. Besides, vapor deposition, atomic layer deposition, solution deposition and layer-by-layer technique produce coating of nanometer thicknesses.[27] However, the thickness is not sufficient to hide the underneath substrate to the cells. Indeed, cells are able to sense the material present under coatings if coating thickness is not sufficient.[26, 29] Nguyen and coworkers proposed a new coating technique based on the formation of a semi-interpenetrating polymer network (SIPN).[27] Their technique is applicable to a wide variety of materials and they were able to obtain coatings presenting up to 10 µm thicknesses.

Adult stem cells are present in niches all over the body and naturally contribute to tissue repair.[21] They are, hence, a promising tool for tissue therapy.[19] Stem cells from the apical papilla (SCAP) are adult mesenchymal

stem cells isolated from the apex of wisdom teeth roots in formation.[30] SCAP present higher proliferation rate than dental pulp stem cells[31] and this proliferation rate is not influenced by hypoxic conditions[32]. This is of great interest as at first stages of scaffold implantation, oxygen supply could be low until first blood capillary network formation. Additionally, neuro- and osteospecific genes as well as proangiogenic factors are up-regulated in hypoxia compared to normoxia.[32]

This work aims at coating complex 3D-printed macroporous structures in order to locally change the mechanical properties at the surface of the scaffold. PDMS coatings were crosslinked with different concentrations in curing agent to tune mechanical stiffness of 3D-printed gyroid scaffolds. The impact of gyroid scaffolds presenting two different PDMS surface moduli was evaluated on SCAP adhesion, proliferation and osteogenic differentiation.

2 Materials and methods

2.1 PDMS mechanical properties

Linear viscoelastic properties of Sylgard 184 (Dow, Belgium) formed with different ratio of base and curing agent were studied by small amplitude oscillatory shear rheology. Sylgard 184 base and curing agent were mixed with ratios (w:w) of 10:3.5, 10:1, 10:0.3 and 10:0.2. Mixes were degassed and poured in Teflon molds to form sheets of 3 mm thickness. Crosslinking was carried out overnight at 85°C. Polymerized films were unmolded and punched to form 8 mm diameter discs. Elastic moduli (G') and viscous moduli (G'') were recorded for each condition using a Kinexus Pro rotational rheometer with the rSpace software (Malvern Instruments, UK; n=1). Frequency sweeps with angular frequencies from 100 rad/s to 0.1 rad/s were recorded using a 8 mm diameter parallel plate with a constant strain of 3%. Gaps were set at 3 mm to allow the plate to come into contact with the sample without deforming it. Measurements were obtained at 37°C to mimic body temperature. Prior to each measurement, a time sweep was performed for 5 min at 1 rad/s and 3% strain to ensure the steady state of the material. After each measurement, an amplitude sweep was recorded with strains from 0.1 to 100% at a constant 5 rad/s frequency to ensure that the sample did not irreversibly deform during the measurement. For the sake of clarity, G' and G'' were isolated from frequency sweeps for each condition. As cell pulling movements occur at low speeds and to be physiologically relevant, G'

and G'' values were taken for the lowest angular frequency tested (0.1 rad/s). As references, cells pull against substrate at 20-120 nm/s[33] and the upper limit of relevant frequency is considered as 1 Hz (2π rad/s), which corresponds to heart beat frequency[21]. Complete frequency sweeps are available in Supporting information (section 6 of this chapter).

2.2 3D model and printing

Gyroid scaffolds were printed in PLA as previously described.[9] Since the previous study, the printer was modified with an added fan and a fanduct. The fanduct was attached on the head and oriented towards extruded polymer. This allows a quick cooling of the extruded PLA and exempts from the need of supporting polymer. The nozzle temperature was set to 210°C though the effective obtained temperature was 200°C owing to the cooling ensured by the added fan. Nine gyroid samples were printed in parallel and around 2 h were needed to complete the printing process. After printing, scaffolds were easily detached from the raft and remaining polymer fibers due to oozing were removed with tweezers.

2.3 PDMS coating on the PLA gyroid scaffold

The protocol used for the coating of PDMS onto 3D-printed PLA scaffolds was adapted from Nguyen and coworkers.[27] The two components of the Sylgard 184 PDMS kit were mixed in two different proportions of base and curing agent (w:w): 10:1 and 10:0.2. The PDMS obtained from those two proportions were called PDMS(10:1) and PDMS(10:0.2), respectively. For each condition, PDMS was mixed with n-hexane and 1,4-dioxane at the ratio 12.5:75:12.5 (PDMS: n-hexane : 1,4-dioxane) (v:v:v). The mixture between a non-solvent (n-hexane) and a solvent (1,4-dioxane) of PLA allows the surface of PLA to swell and to interpenetrate with uncured PDMS chains.[27] The scaffolds were immersed in the PDMS:n-hexane:1,4-dioxane mixture in a hermetically-closed vial. The vial was plunged in a 65°C water bath for one hour. The vial cooled for half an hour at room temperature. Scaffolds were hanged, oriented with printed layer parallel to the ground and the solvent was evaporated from the scaffolds for an hour. Scaffolds were then heated at 85°C overnight to crosslink the PDMS and form the SIPN. To increase coating thickness and interpenetrate uncured PDMS with PDMS deposited in the previous cycle, scaffolds went through several cycles of this procedure with a slight modification: the coating mixture did not contain 1,4-dioxane and the intermediate curing step was reduced to 30 min. Indeed, as the PDMS was crosslinked, the use of a non-solvent of PDMS was useless as no

complete dissolution could occur. To reach a similar coating thickness between PDMS(10:1) and PDMS(10:0.2), the number of cycles differed. For PDMS(10:1) a total of 2 cycles was required while for PDMS(10:0.2), four cycles were necessary. For each condition and each cycle, scaffolds were always hanged in the same orientation.

3 Evaluation of coating morphology and thickness

PDMS coating thickness on the scaffold was first evaluated by weighing the scaffold before and after coating. PDMS coating thickness of three batches of 24, 24 and 36 scaffolds was evaluated using the following equation:

$$Coating\ thickness\ [m] = \frac{m_f[kg] - m_i[kg]}{\rho_{PDMS}[kg/m^3] x\ S\ [m^2]} \quad (1)$$

Where:
m_i and m_f are masses of the scaffold before and after all coating cycles, respectively;
ρ_{PDMS} is the density of crosslinked Sylgard 184 PDMS, equal to 1030 kg/m³ according to the technical data sheet provided by Dow;
S is the theoretical surface area of the gyroid scaffold model used, evaluated using netfabb Basic V5.1 (netfabb GmbH, Germany) and equal to 1.076×10^{-3} m².

Coating morphology and homogeneity were evaluated using a scanning electron microscope (SEM). Three scaffolds of each condition (PDMS(10:1) and PDMS(10:0.2)) from three different coating batches as well as an uncoated scaffold were cut perpendicular to the printed layer using a razor blade. A slice from the inner part of the scaffold was exposed and sputter-coated with 20 nm of gold. Images were acquired using a JSM-7600F (JEOL, Belgium) SEM at 15 keV and using a probe current of 2×10^{-10} A. Twenty-five images in low magnification per sample were acquired and reconstructed using Image Composite Editor 2.0.3.0 (Microsoft Corporation, USA).

Coating thicknesses observed on SEM images were measured using ImageJ 1.52a software (Wayne Rasband, National Institutes of Health, USA).[34] The borders of the coating were determined manually and the software converted the number of pixels between these borders into a distance in micrometer. The length in pixel of the scale bar present on the picture as well as its value in micrometer were used to define the conversion factor.

Between 750 and 1000 measurements were obtained for each reconstituted picture of PDMS(10:1)- and PDMS(10:0.2)-coated samples.

3.1 Preparation of scaffolds for SCAP culture and seeding in 3D scaffolds

PDMS(10:1)-coated, PDMS(10:0.2)-coated and uncoated gyroid PLA scaffolds were disinfected in ethanol 70% and dried. To improve cell adhesion, scaffolds were coated with fibronectin (10 µg/ml; 1 ml/scaffold) overnight at room temperature and under agitation. Scaffolds were rinsed three times using ultrapure water and dried. SCAP previously isolated from immature permanent teeth of a 17-year-old girl and characterized (RP89 cells) were used at passage 8 or 9.[31] RP89 were grown at 37°C and with 5% CO_2 in Minimum Essential Medium (Sigma-Aldrich, Belgium) supplemented with 10% bovine serum (Sigma-Aldrich, Belgium), 1% of L-glutamine (Life Technologies, Belgium) and 1% of Penicillin-Streptomycin mixture (Life Technologies, Belgium). Passages were achieved using Accutase (Life Technologies, Belgium) when cells were reaching around 90% confluence. For seeding, SCAP were suspended in $1.7x10^6$ cells/ml. Sixty µl of medium containing 10^5 cells were seeded at the top of each scaffold. Scaffolds were incubated for 5 hours at 37°C before the addition of 2 ml of medium per scaffold. Medium was replaced three times a week.

3.2 Evaluation of SCAP seeding and proliferation

SCAP metabolic activity was evaluated at days 1, 3, 7 and 14 for uncoated (n=4), PDMS(10:1)-coated (n=4) and PDMS(10:0.2)-coated (n=4) PLA scaffolds using a resazurin-based *in vitro* toxicology assay kit (VWR). Medium was removed and the scaffolds were washed with phosphate-buffered saline (PBS) and 2 ml of fresh medium containing 5% of the reagent were added on the scaffolds. Scaffolds were incubated for 4 h at 37°C. Supernatants were collected and their fluorescence was measured (excitation wavelength: 560 nm; emission wavelength: 590 nm) using Spectramax M3 plate reader (Molecular devices, USA). As the test is not destructive, scaffolds were washed twice with PBS and were processed for DNA quantification.

After metabolic activity evaluation, scaffolds were transferred in tubes (15 ml, 76 mm height and 20 mm diameter). Cells were detached from the scaffolds using 2 ml/scaffold of Accutase. Scaffold were centrifuged, removed and rinsed with 4 ml of PBS to recover all the cells. SCAP were recovered and the cell pellets were frozen at -80°C before DNA quantification

(CyQUANT Cell Proliferation Assay Kit, Thermo Fisher Scientific, Belgium). The whole process (cell culture, resazurin-based *in vitro* toxicology assay kit and CyQUANT) was performed in duplicate.

When media were collected at day 1, 3, 7 and 14, the potential cytotoxicity of the coating was evaluated using a LDH assay kit (Roche, Germany) to dose extracellular LDH activity. Cell media were diluted five times in PBS to limit medium absorbance and were processed according to manufacturer protocol. Absorbance was measured at 492 nm using a Spectramax M3 plate reader.

SCAP on uncoated (n=1), PDMS(10:1)-coated (n=1) and PDMS(10:0.2)-coated (n=1) PLA scaffolds were stained for visualization by fluorescence microscopy. $5x10^4$ cells in 30 µl medium were seeded on gyroids scaffolds, which were cut in half. After 7 days, samples were fixed and permeabilized. SCAP were stained with Hoechst staining dye (Sigma-Aldrich, Belgium) and Rhodamin-phalloidin dye (Thermo Fisher Scientific, Belgium) to color cell nucleus and cell actin filament (cytoskeleton), respectively. Images were acquired using a Olympus IX71 epifluorescence microscope (Olympus, Germany).

3.3 Evaluation of SCAP *in vitro* osteogenic differentiation

SCAP were seeded on uncoated, PDMS(10:1)-coated and PDMS(10:0.2)-coated scaffold and cultured for two weeks. Then, for half of the samples, basal medium was replaced by osteogenic differentiation medium (StemPro Osteogenesis Differentiation Kit, Life Technologies). For the other half, fresh basal medium was added. From that point, basal medium or osteogenic differentiation medium were changed twice a week for 7 days and 21 days. Samples were then processed for quantitative reverse-transcriptase polymerase chain reaction (qRT-PCR) analysis. For each time point and each condition, four replicates were used. The whole experiment was performed in duplicate.

At the end of the experiment, scaffolds were washed with PBS and 600 µl of Trizol (Life Technologies) were added. Samples were then kept at -80°C until further processing. Total messenger RNA (mRNA) was extracted using the phenol/chloroform extraction method and stored at -80°C. One µg of mRNA was reverse transcribed using the Reverse Transcription System kit (Promega, Madison, WI) and the resulted cDNA was stored at -20°C. Gene expression of runt-related transcription factor 2 (RUNX2), alkaline

phosphatase (ALP), osteocalcin (OCN) (osteogenic differentiation markers), survivin (SURVIVIN) (stemness marker) and 60S ribosomal protein L13 (RPL13) (housekeeping gene) (Table 1) was evaluated. The GoTaq qPCR MasterMix Kit (Promega) was used to perform a SYBR green real-time qRT-PCR analysis on a StepOne Plus Real-Time PCR System (Applied Biosystems, Life Technologies). Samples were analyzed in duplicate. Results were exported using the Step One software (Version 2.3) and relative expression were computed using the delta-delta Ct method ($2^{-\Delta\Delta Ct}$). Each gene expression at day 7 and 21 was compared to gene expression at day 7 for uncoated samples in basal medium. Then, comparison was separated for basal medium and osteogenic differentiation medium to emphasize the effect of the coating.

Table 1: Forward and reverse primers used for qRT-PCR evaluation.

	Forward (5'-3')	Reverse (5'-3')
Human RPL13	CATAGGAAGCTGGGAGCAAG	GCCCTCCAATCAGTCTTCTG
Human RUNX2	CCCTCGGAGAGGTACCAGA	TTGGGGAGGATTTGTGAAGA
Human SURVIVIN	CATGCAAAGGAAACCAACAA	GGTGGCACCAGGGAATAAAC
Human ALP	GACAAGAAGCCCTTCACTGC	AGACTGCGCCTGGTAGTTGT
Human OCN	GGCAGCGAGGTAGTGAAGAG	CCTGAAAGCCGATGTGGT

3.4 Statistical analysis

Student's t-test and Tukey's HSD were performed using JMP® Pro 14.1.0 (SAS Institute Inc., USA) (α=0.05).

4 Results and discussion

4.1 PDMS viscoelastic properties

The aim here was to confirm that PDMS coating mechanical properties depended on the ratio between base and curing agent. G' and G'' increased with the curing agent proportion (Figure 1). G' increased from 5 kPa to 228 kPa, while G'' increased from 0.4 kPa to 17.5 kPa for PDMS(10:0.2) and

PDMS(10:3.5), respectively. G' and G'' for PDMS(10:1) were 30 times and 20 times higher than PDMS(10:0.2), respectively.

PDMS(10:1) and PDMS(10:0.2) conditions were selected for the gyroid scaffold coating as PDMS(10:1) is the ratio recommended by the supplier and PDMS(10:0.2) corresponds to the lowest concentration in curing agent that still allows polymer handling. Young's elactic moduli for Sylgard 184 PDMS obtained by stretching PDMS strips were measured by Degand and coworkers.[35] For base-to-curing agent proportions ranging from (10:0.015) to (10:3.5), resulting Young's modulus varied from 1 kPa to a plateau value of 1200 kPa. This plateau appeared between PDMS(10:1) and PDMS(10:3.5). Those values were confirmed by other studies. Similar results were obtained either by tensile testing[36, 37] or by AFM nanoindentation measurements at the surface of PDMS[38]. PDMS(10:1) and PDMS(10:0.2) were thus selected and further described as "stiff" and "soft", respectively, to produce gyroids presenting surfaces with 2 different stiffnesses.

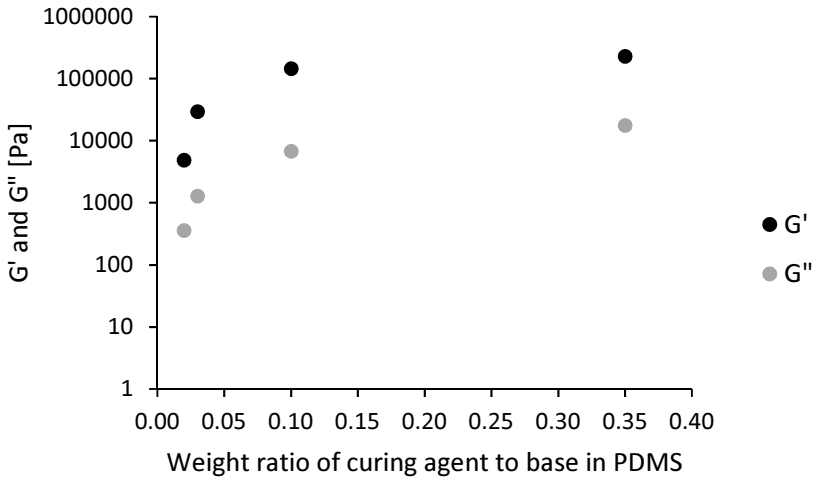


Figure 1: Impact of the ratio of curing agent compared to base on PDMS mechanical properties. Elastic modulus (G') and viscous modulus (G") for increased ratios of curing agent compared to base. For the sake of clarity, values for the lowest frequency (0.1 rad/sec) were isolated from each frequency sweep. Complete frequency sweeps are available in suplementary data.

4.2 Validation of PDMS coating and measurement of coating thickness on PLA gyroid scaffolds

The objective was to first assess the success of the coating on 3D PLA gyroids and second to measure its thickness. Low magnification pictures showed PLA

in dark grey while PDMS was light grey (Figure 2). Pores interconnectivity after coating was reasonably preserved, even if a few pores were clogged at the bottom of the structure due to coating mixture drainage at the bottom of the scaffold during the solvent evaporation step of the coating. Grooves and ridges present at the surface of uncoated scaffolds resulted from the layer-by-layer process of fused deposition modelling. Stiff and soft PDMS coatings fully covered the PLA surface, filled the grooves and smoothed the surface. Higher magnification pictures showed the PDMS layer surrounding the PLA scaffold. PDMS was torn from the PLA at some places due to the harsh cutting step. Even though PDMS was completely covering the PLA scaffold, thickness was not uniformly distributed.

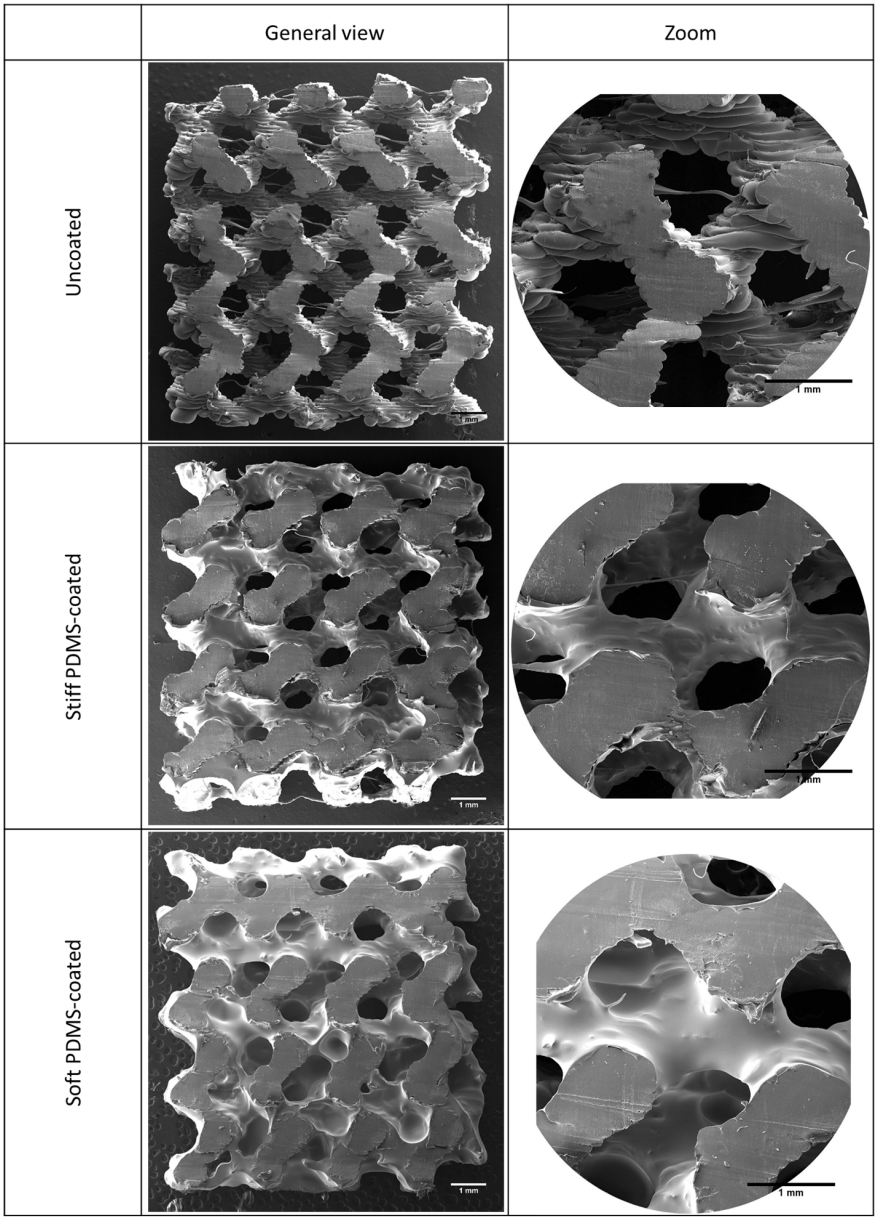


Figure 2: Evaluation of the PDMS coating on PLA scaffolds. SEM images of uncoated (top), stiff PDMS-coated (middle) and soft PDMS-coated (bottom) scaffolds. Samples were cut to see inside the scaffolds. General views (middle vertical column) are reconstitutions of 25 images covering the entire section of the same sample. Zooms (right column) are one isolated image of each sample.

Two methods were used to measure the average coating thickness on the scaffolds. An average coating thickness was evaluated by subtracting the

weight of the scaffolds after coating to their weight before coating. The mean coating thickness of stiff PDMS and soft PDMS were 97 (16) µm and 106 (12) µm, respectively. These values were compared to measurements performed on SEM pictures. PDMS coating ranged from 1 µm to 400 µm, reflecting the heterogeneity observed on the macroscopic pictures (Figure 3). This was mitigated by the fact that 50% of the values were between 15 µm and 70 µm for both coatings. The mean thicknesses measured by SEM were 49 µm and 54 µm for stiff PDMS and soft PDMS, respectively.

The coating thickness impacts the stiffness sensing that cells can have regarding their support.[26, 39-51] The limit beyond which the cells can no longer sense the material below the coating is called the "critical thickness" (also known as "mechanosensing length"). The value of this parameter has been subjected to discussion in the literature. Many studies focused on this topic but results are difficult to compare and the unifying theory remains unclear. Mainly two points of view were explored: one physical and one biological.

The physical point of view is based on material elasticity theory and evaluates how traction forces are influenced by material thickness. At first, the minimum thickness at which the rigid underlying substrate is undetectable was proposed to be around 1 µm.[39-41] It was evaluated based on material displacement provoked by the cells at the surface of the coating material. Later, it was shown that other parameters such as cell size or focal adhesion size had to be taken into account.[42-44] According to those models, minimum thickness to hide hard material to the cells should be at least 10 µm thick or even much thicker than cell size.

The biological point of view evaluates the behavior of cells cultured on substrates presenting given thicknesses. Smooth muscles cells cultured on 5 µm and 70 µm PAA gels did not show significant differences in spreading.[45] On the contrary, adhesion of bone marrow stem cells and fibroblasts decreased as the thickness of a polyelectrolyte multilayer increased from 40 nm to 270 nm.[46] Some models were developed to explain the observed disparity among models and experiments.[26, 47] The wide range of what is claimed as critical thicknesses can be explained by the different parameters used, either relative to the cell (*e.g.* size, adhesion site radius) or to the material (*e.g.* Young's elastic modulus).

Regarding our study, 75% of the coating thickness measurements were above 15 µm. Buxboim and coworkers plated MSCs on PAA films presenting a Young's elastic modulus around 1 kPa and observed a critical thickness of

10-20 µm.[49] Young's elastic modulus was previously measured for our softest condition (PDMS(10:0.2)) and was around 8 kPa.[35] As coating Young's moduli for both PDMS(10:1) and PDMS(10:0.2) were higher than the one of Buxboim and coworkers and as measured thicknesses are higher than their critical thicknesses for 75% of the measurements, in most regions of the scaffolds, cells should not be able to sense the hard PLA material present under PDMS coating.

The protocol used to coat the 3D gyroids was adapted from Nguyen and coworkers who showed that coating thickness depends on coating solution composition, incubation time and structure size.[27] Considering the results we obtained, we suspect that three major additional phenomena govern coating success. In the case of millimeter-sized pore samples, capillarity, gravity and viscosity of the coating solution seem to play a major role. Pores with millimeter sizes tend to retain PDMS:n-hexane (: 1,4-dioxane) mixture during the solvent evaporation step. As pore size was relatively large, PDMS was drained by gravity. To slow down PDMS drainage and to ensure that the whole surface is coated, one solution would be to increase the PDMS solution viscosity. However, this could result in clogging of some of the pores. Rinsing the scaffold or draining coating mixture before evaporation resulted in a decrease of coating thickness on our gyroid scaffolds even after multiple cycles. Our protocol was then the best compromise, ensuring a uniform coating of the surface with a thickness masking the stiffness of the PLA structures sensed by the cells.

The thicknesses obtained by the two methods were in the same range of values. The higher average thicknesses obtained for measurement from differences in scaffold weight before and after coating compared to the ones measured on SEM picture was expected and can be easily explained. First, to compute a thickness from a mass of coating polymer, the surface of the scaffold was evaluated from the model. As the surface of the scaffold had grooves and ridges, the surface was underestimated. Hence, according to the equation 1, this resulted in an overestimation of the thickness using scaffold weight. Then, some pores were clogged with PDMS, which was part of the scaffold weight and contributed to the thickness measurement while it was not considered for the SEM thickness measurement. This also overestimated the coating thickness measured by weight. Considering this, thickness measurements from scaffold weight were in agreement with measurements from SEM images.

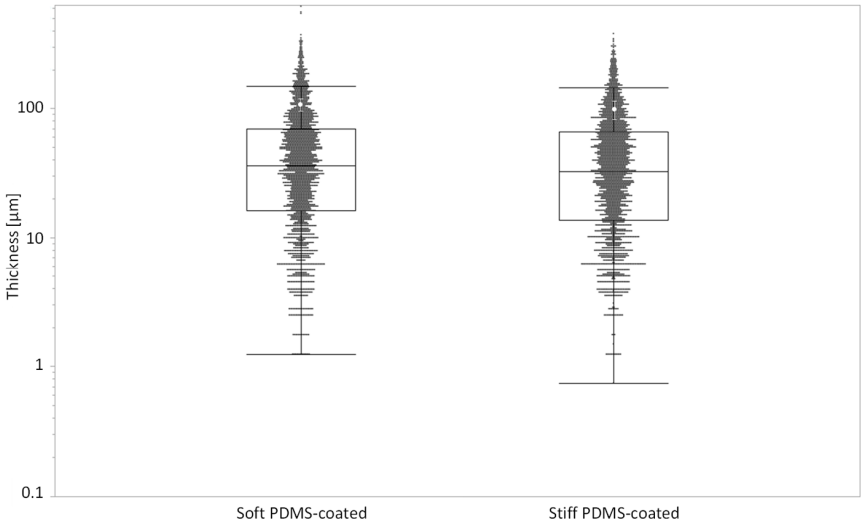


Figure 3: Evaluation of PDMS coating thickness on PLA gyroid scaffolds. Measurements of coating thickness obtained from SEM images (grey dots) and box plot (black) (n=3, 750 to 1000 measurements per sample). White dots represent coating thickness evaluation obtained from differences in scaffold weight before and after coating (n=24, 24 and 36; white error bars show the standard deviation).

4.3 SCAP seeding and proliferation on coated gyroid scaffolds

SCAP were seeded on uncoated, stiff PDMS-coated and soft PDMS-coated scaffolds. Metabolic activity and cell number were measured to evaluate *in vitro* adhesion and proliferation of cells at day 1, 3, 7 and 14 after seeding.

Pictures showed that SCAP attached, spread and laid flat at the surface of the scaffolds (Figure 4 A). Cell metabolic activity and number on the scaffolds increased similarly with culture time whatever the conditions (Figure 4 B and C). Trends observed among conditions were also similar for both metabolic activity and cell number. Metabolic activity for uncoated samples at day 1 was significantly higher than the ones for PDMS-coated samples. At Day 7, uncoated samples showed both higher metabolic activity and higher cell number compared to PDMS-coated samples, while no significant differences were observed between stiff PDMS-coated and soft PDMS-coated scaffolds. At day 14, all conditions were significantly different for both experiments with the lowest values for soft PDMS-coated scaffolds and the highest values for uncoated scaffolds. Additionally, no cytotoxicity effect of the PDMS coating was observed as no LDH was detected in any condition (data not shown).

Once seeded, SCAP were able to attach, spread and proliferate at the surface of the scaffolds as they would do on a 2D substrate. Seeding efficiency seemed better on uncoated sample compared to PDMS-coated samples as metabolic activity and number of cells at day 1 tended to be higher. As the number of cells was similar at day 1 for both PDMS-coated samples and as a lower number of cells was observed at day 7 and 14 for soft PDMS-coated scaffolds, cell proliferation rate was lower for the soft compared to the stiff PDMS-coated scaffolds. This result is consistent with literature as in 2D conventional culture, cell proliferation rate is lower on soft PDMS compared to stiff PDMS.[25] No conclusion could be drawn regarding cell proliferation rate on uncoated scaffolds compared to PDMS-coated scaffolds as the number of cells at day 1 was different.

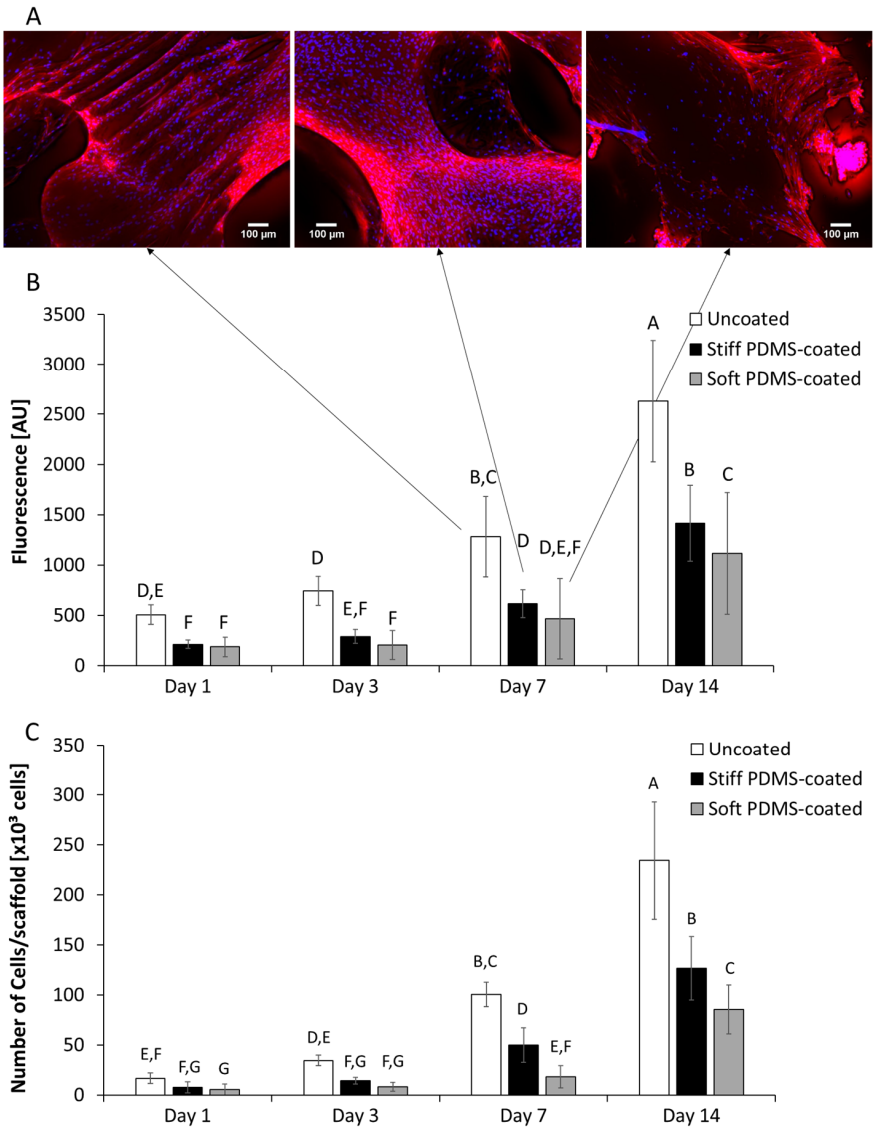


Figure 4: Monitoring of SCAP seeding and SCAP proliferation on uncoated and PDMS-coated gyroid scaffolds. (A) Fluorescence microscopy, (B) metabolic activity evaluation and (C) number of SCAP cultured on uncoated, PDMS(10:1)-coated and PDMS(10:0.2)-coated scaffolds. Fluorescence microscopy was realised 7 days after seeding (n=1). Cell nuclei are stained in blue and actin filaments in red. Metabolic activity (n=2x4; error bars show the standard deviation) and cell number (n=2x4; error bars show the standard deviation) were measured at day 1, 3 ,7 and 14 after seeding. Values not sharing the same letter are significantly different ($p<0.05$).

4.4 SCAP *in vitro* differentiation on PDMS-coated gyroid scaffolds

Here, the goal was to evaluate the effect of the basal medium and the osteogenic differentiation medium on osteogenic differentiation of SCAP cultured on uncoated and PDMS-coated samples. Furthermore, the effect of the coating as well as its mechanical properties were assessed in each medium.

Gene expression values were normalized to the expression of cells for uncoated samples at day 7 in basal medium (Figure 5). When comparing uncoated and PDMS-coated samples in basal medium to their counterparts in osteogenic differentiation medium, no significant differences in gene expression were observed for RUNX2 and for most of ALP. Indeed, ALP expression was drastically decreased at day 21 in osteogenic differentiation medium. No significant differences or tendencies could be highlighted for OCN. SURVIVIN expression was significantly upregulated for all but one tested condition in osteogenic differentiation medium compared to basal medium.

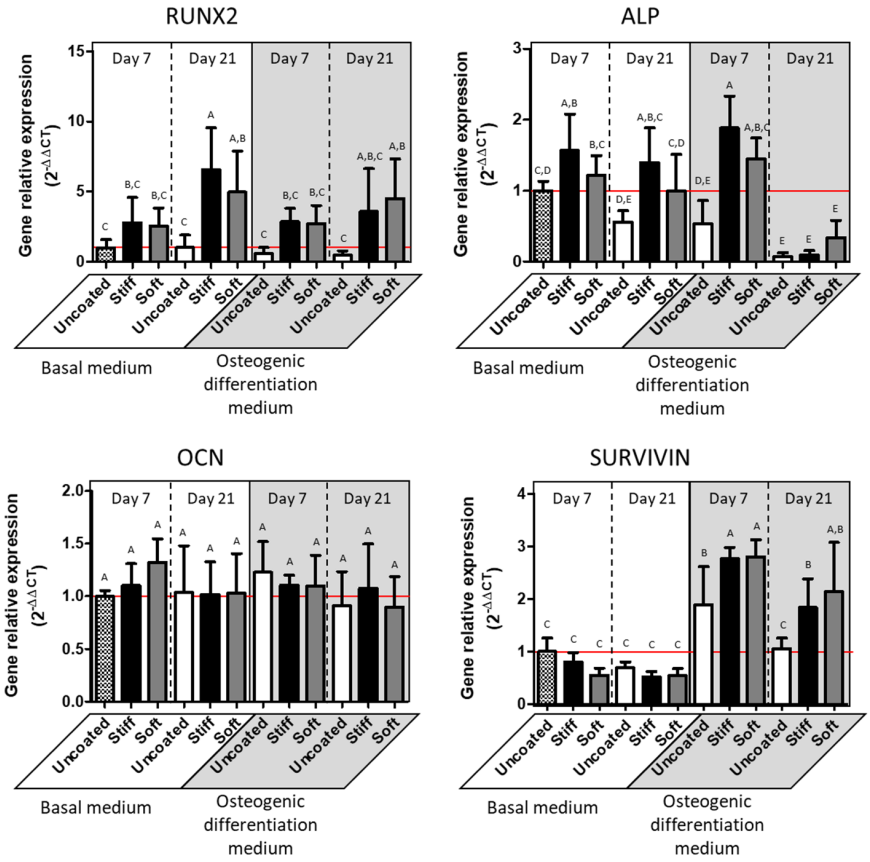


Figure 5: Evaluation of SCAP osteogenic differentiation on uncoated and PDMS-coated gyroid scaffolds. SCAP osteogenic markers (RUNX2, ALP and OCN) and stemness marker expression (SURVIVIN) in basal and osteogenic differentiation media. Expression was evaluated 7 and 21 days after induction. RPL13 was used as housekeeping gene. For each medium used, gene expression in all the tested samples was normalized by gene expression of the cells in uncoated samples at day 7 in basal medium. Values not sharing the same letter are significantly different ($p<0.05$, n=2x4, error bars show the standard deviation).

Focusing on the coating, no significant difference was observed between stiff and soft PDMS whatever the gene analyzed.

RUNX2 expression was upregulated at day 21 for all PDMS-coated samples compared to uncoated samples in both media. The same tendency was already observed at day 7.

In basal medium, ALP expression was maintained whatever the sample and the culture time even though a tendency of increased expression was observed for PDMS-coated samples compared to uncoated samples. In

osteogenic differentiation medium, ALP expression was three to four times upregulated at day 7 for PDMS-coated samples compared to uncoated samples. This expression was drastically decreased for all samples at day 21.

Regarding OCN expression, no significant differences or tendencies could be highlighted in both media.

SURVIVIN expression in basal medium was two times lower at day 7 for soft PDMS-coated samples than in uncoated samples, while it was decreased at day 21 in uncoated and stiff PDMS-coated samples. In osteogenic differentiation medium, SURVIVIN expression was 50% higher at day 7 for PDMS-coated samples compared to uncoated samples. Its expression decreased at day 21 for both uncoated and PDMS-coated samples.

No significant differences were highlighted between osteogenic marker expressions in both media, while higher osteogenic marker expressions was expected in cells growing in osteogenic differentiation medium. Even osteogenic marker expressions on uncoated samples in basal medium (considered as our negative control) and in osteogenic differentiation medium (considered as our positive control) were not significantly different. This is in contradiction with our previous work, where the osteodifferentiation of RP89 cells was observed, on TCPS, using the same osteogenic differentiation medium.[32] Our current results would indicate that osteogenic differentiation was induced in all tested conditions and even in basal medium potentially due to the seeding on the gyroid scaffolds. To validate this hypothesis, gene expression of non-seeded cells, cells grown on TCPS in basal medium or cells grown on another type of scaffold could be analyzed.

RUNX2 is the earliest molecular marker of osteoblastic lineage and is considered as the "master switch" of osteogenic differentiation.[52] Expression of this transcription factor is necessary and sufficient to induce differentiation in osteoblast. RUNX2 is also necessary at later stages of osteogenic differentiation as it induces alkaline phosphatase activity, expression of bone matrix genes and mineralization of this matrix. Deletion of this gene in mice prevented mineralization of their skeleton, which remained cartillaginous.[53]

ALP is an enzyme involved in biomineralization of the extracellular matrix.[52, 53] ALP gene expression is considered as an early marker of osteogenic differentiation. This is consistent with the decrease observed at day 21 for all

samples in osteogenic differentiation medium. The maintained expression of ALP in basal medium was unexpected. This result could be related to a delayed differentiation of some cells. Not all the cells would differentiate at the same time as in osteogenic differentiation medium and the differentiation would not occur homogeneously throughout the scaffold but more gradually.

Significant differences and tendencies observed for RUNX2 were consistent with the ones observed for ALP. Cells on PDMS-coated samples showed a better osteogenic differentiation in each condition. Silicon atom (Si) and especially silicate are osteoinductive.[54] Si, along with calcium (Ca), are primary dissolution products of bioglass.[55] Osteostimulation was observed for concentration in Si and Ca ranging from 15-30 ppm and 60-90 ppm, respectively. PDMS chains are long and chemically stable. However, Sylgard 184 contains filler such as dimethylvinylated and trimethylated silica fillers.[56, 57] As fillers have a higher mobility, they could have reached cells and could have triggered an osteogenic response. Nevertheless, it has to be noted that the difference in surface topography between uncoated and PDMS-coated scaffolds could also have influenced cell differentiation. Cells are indeed sensitive to topography and to cell-scale curvature.[58]

OCN is a matrix protein that plays a role in the regulation of mineralization and remodeling.[52, 53] The gene is expressed in late stage of osteogenic differentiation when osteogenic maturation and bone mineralization are well engaged. No change of expression was observed with culture time. OCN could already be fully expressed at day 7 or OCN expression could be upregulated later than 21 days post induction.

SURVIVIN is a protein belonging to the family of apoptosis inhibitors.[59] Besides its role in blocking apoptosis, SURVIVIN is involved in cell division regulation.[60, 61] SURVIVIN can be considered as a stemness marker as its expression is present in stem cells but is rarely detectable in fully differentiated cells.[60, 62] In both basal and osteogenic differentiation media conditions, the decrease in SURVIVIN expression with culture time suggests that cells are differentiating. Its upregulation in osteogenic differentiation medium was unexpected. SURVIVIN was upregulated in human osteoblasts by higher calcium concentration in the medium.[63]

Even though PDMS coating increased osteogenic gene expression in most of the cases, no significant differences were observed between soft and stiff coatings. According to classical 2D culture, a better osteogenic

differentiation was expected on the stiff PDMS as the material is closer to mechanical properties of the native tissue compared to the soft PDMS. While the study of mechanotransduction inside macroporous samples is rather unexplored, some hypothesis explaining the results can be formulated.

The three first hypotheses are based on conventional 2D culture literature. First, the difference in mechanical properties of soft and stiff PDMS may be too weak to be distinguished by cells. However, Evans and coworkers obtained surface elastic moduli of 0.26 MPa and 1.9 MPa using the same material in similar proportions of base and curing agent (3% and 9% of curing agent, respectively).[25] They observed a significant upregulated RUNX2 expression in embryonic stem cells for the stiffer PDMS. On the contrary, Trappmann and coworkers observed that differences in PDMS presenting Young's moduli between 0.1 kPa (PDMS(10:0.1)) and 800 kPa (PDMS(10:1)) did not influence human mesenchymal stem cell osteogenic differentiation.[64] Wen and coworkers claimed that mechanical properties are different at the cellular mechanosensing scale compared to macroscopic scale.[33] Hence, both conditions tested by Trappmann and coworkers would be felt as "stiff" by cells. Therefore, cells would sense both coatings as stiff in our study.

The second hypothesis is based on coating thickness. Cells might sense the PLA structure below the coating. Indeed, it was earlier described that cells are able to sense mechanical properties present under a soft coating.[26, 39-51] An insufficient thickness or inhomogeneities in coating thickness could have resulted in different cell sensing depending on their location on the structure. Then, similar average values of osteogenic gene expression could be observed whatever the coating stiffness. Besides, cell colonies are able to sense the material deeper than isolated cells.[29] As cells were cultured until confluence, depth sensed by cells could have been deeper than originally thought.

A third hypothesis would be linked to the deposition of the adhesion proteins at the surface of the 3D macroporous system. Indeed, the density of ligands influences cell behavior[65] as well as the expression of many different genes[66]. In our study, a fibronectin coating was applied by simple physisorption of the proteins to improve cell adhesion on our materials. These coatings were not studied due to the complexity raised by the use of 3D structures. Proteins could be insufficiently attached to the material when a cell is pulling, which would prevent the transfer of the mechanical feedback from the material to the cell. The cell would not sense the material but only the adhesion of the

proteins to the material. In the study from Evans and coworkers, type I collagen was covalently bound to PDMS, which could explain the divergence between our study and theirs.[25]

The 3D macroporous configuration could influence cell behavior. In macroporous hydrogel made of recombinant elastin-like protein, both adipogenic and osteogenic differentiations of mesenchymal stem cells were increased with increasing stiffness of the scaffold.[23] This indicates that within porous substrates, mesenchymal stem cell differentiation behavior diverges from classical observation on 2D substrates. Furthermore, the curves present in the gyroid scaffold could influence cell behavior, as concavities with radii larger than cell size were more favorable for mineral deposition than planar substrates made in the same material (calcium phosphate).[67]

In addition to 2D and 3D considerations, effects of mechanical properties on cell differentiation could be cell-type dependent. Results obtained here may be specific to SCAP or even to RP89 cells.

Cell behavior depending on the surface mechanical properties in such 3D macroporous scaffolds are rather unexpected in the light of conventional 2D culture. Further mechanotransduction studies in macroporous structures are needed for a better comprehension of these results. Future works could be centered on the use of other coatings such as PAA gels. Like PDMS, they were also largely used to study the effect of mechanical properties on cell behavior on 2D substrates and could present more adapted mechanical properties on a cellular level.[33] Different coating thicknesses could be tested and the effect of the crosslinking of adhesion proteins on cell mechanical sensing could also be investigated.

5 Conclusions

PDMS was successfully coated on the surface of complex macroporous gyroid scaffolds. PDMS crosslinking density influenced SCAP proliferation rate but not osteogenic differentiation.

The increase in PDMS mechanical properties for increased amount of curing agent was confirmed using rotational rheometry. Coating thicknesses for both stiff PDMS-coated and soft PDMS-coated samples were measured to be about 50 µm. The high pore interconnectivity of the gyroid scaffold was maintained in spite of the coating steps. SCAP were seeded in stiff PDMS-coated and soft PDMS-coated gyroid scaffolds as well as on uncoated gyroid

scaffolds. Cell metabolic activity and proliferation in scaffolds increased over two weeks. Proliferation rates were lower on soft PDMS-coated scaffolds compared to stiff PDMS-coated scaffolds. Gene expression reflecting osteogenic differentiation was investigated without induction and after induction using a commercial osteogenic differentiation medium. Surprisingly, the differentiation medium did not induce a higher expression of osteogenic genes compared to the basal medium. This would suggest that osteogenic differentiation occurred in all tested conditions. A tendency in upregulation of osteogenic marker expression was observed on PDMS-coated samples but no differences were observed between stiff PDMS-coated and soft PDMS-coated scaffolds, though they presented different macroscopic mechanical properties. Osteogenic differentiation results thus diverge from the ones obtained for common 2D substrates, thereby highlight the interest and importance to study mechanotransduction in macroporous samples.

6 Supporting information

PDMS viscoelastic properties

Base and curing agent of the Sylgard 184 PDMS kit were mixed, cured and viscoelastic properties were studied using frequency sweeps. G' and G'' were measured for frequency sweeps between 0.1 and 100 rad/s (Figure SI1). Both G' and G'' increased with an increased concentration in curing agent in the mixture. This result is observed whatever the frequency tested except for the G'' at 100 rad/s for PDMS(10:1) and PDMS(10:3.5).

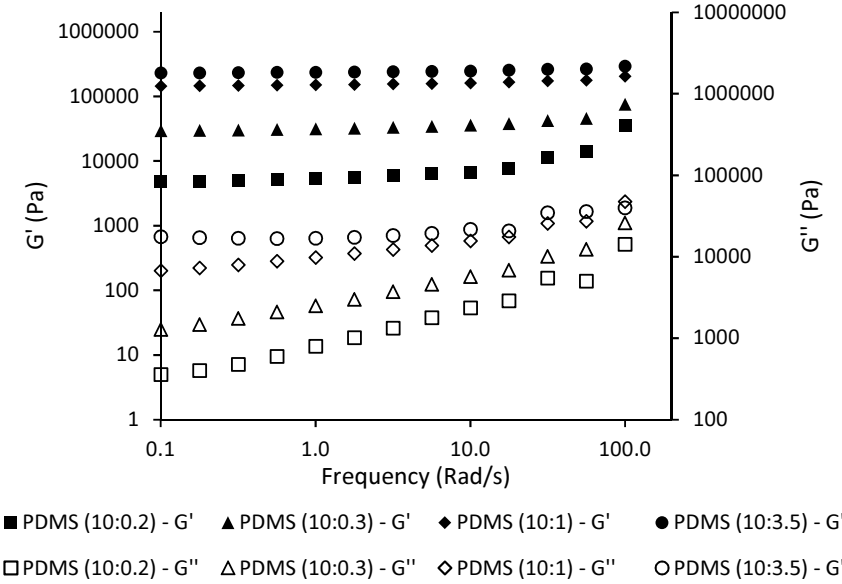


Figure SI1: Elastic modulus (G') and viscous modulus (G") for increased ratios of curing agent compared to base. Values were recorded in frequency sweeps for frequencies between 0.1 rad/sec and 100 rad/s.

7 References

1. Langer, R.; Vacanti, J. P., Tissue engineering. *Science* **1993,** *260* (5110), 920-926.

2. Verhulsel, M.; Vignes, M.; Descroix, S.; Malaquin, L.; Vignjevic, D. M.; Viovy, J. L., A review of microfabrication and hydrogel engineering for micro-organs on chips. *Biomaterials* **2014,** *35* (6), 1816-1832.

3. Cox, S. C.; Thornby, J. A.; Gibbons, G. J.; Williams, M. A.; Mallick, K. K., 3D printing of porous hydroxyapatite scaffolds intended for use in bone tissue engineering applications. *Mater. Sci. Eng. C Mater. Biol. Appl.* **2015,** *47*, 237-247.
4. Khang, G., Biomaterials and manufacturing methods for scaffold in regenerative medicine. In *Handbook of Intelligent Scaffolds for Tissue Engineering and Regenerative Medicine*, Pan Stanford Publishing Pte. Ltd.: 2012; pp 3-47.
5. Thavornyutikarn, B.; Chantarapanich, N.; Sitthiseripratip, K.; Thouas, G. A.; Chen, Q., Bone tissue engineering scaffolding: computer-aided scaffolding techniques. *Prog. Biomater.* **2014,** *3* (2), 61-102.
6. Levengood, S. K. L.; Zhang, M., Chitosan-based scaffolds for bone tissue engineering. *J. Mater. Chem. B* **2014,** *2* (21), 3161-3184.
7. Shi, C.; Yuan, Z.; Han, F.; Zhu, C.; Li, B., Polymeric biomaterials for bone regeneration. *Ann. Joint* **2016,** *1* (9), 27.
8. Trachtenberg, J. E.; Mountziaris, P. M.; Miller, J. S.; Wettergreen, M.; Kasper, F. K.; Mikos, A. G., Open-source three-dimensional printing of biodegradable polymer scaffolds for tissue engineering. *J. Biomed. Mater. Res. A* **2014,** *102* (12), 4326-4335.
9. Germain, L.; Fuentes, C. A.; van Vuure, A. W.; des Rieux, A.; Dupont-Gillain, C., 3D-printed biodegradable gyroid scaffolds for tissue engineering applications. *Mater. Des.* **2018,** *151*, 113-122.
10. Challis, V. J.; Xu, X.; Zhang, L. C.; Roberts, A. P.; Grotowski, J. F.; Sercombe, T. B., High specific strength and stiffness structures produced using selective laser melting. *Mater. Des.* **2014,** *63*, 783-788.
11. Yánez, A.; Herrera, A.; Martel, O.; Monopoli, D.; Afonso, H., Compressive behaviour of gyroid lattice structures for human cancellous bone implant applications. *Mater. Sci. Eng. C Mater. Biol. Appl.* **2016,** *68*, 445-448.
12. Speirs, M.; Van Hooreweder, B.; Van Humbeeck, J.; Kruth, J. P., Fatigue behaviour of NiTi shape memory alloy scaffolds produced by SLM, a unit cell design comparison. *J. Mech. Behav. Biomed. Mater.* **2017,** *70*, 53-59.
13. Melchels, F. P. W.; Bertoldi, K.; Gabbrielli, R.; Velders, A. H.; Feijen, J.; Grijpma, D. W., Mathematically defined tissue engineering scaffold architectures prepared by stereolithography. *Biomaterials* **2010,** *31* (27), 6909-6916.
14. Zadpoor, A. A., Bone tissue regeneration: The role of scaffold geometry. *Biomater. Sci.* **2015,** *3* (2), 231-245.
15. Geiger, B.; Spatz, J. P.; Bershadsky, A. D., Environmental sensing through focal adhesions. *Nat. Rev. Mol. Cell Biol.* **2009,** *10* (1), 21-33.

16. Holle, A. W.; Engler, A. J., More than a feeling: Discovering, understanding, and influencing mechanosensing pathways. *Curr. Opin. Biotechnol.* **2011,** *22* (5), 648-654.
17. von der Mark, K.; Park, J., Engineering biocompatible implant surfaces: Part II: Cellular recognition of biomaterial surfaces: Lessons from cell–matrix interactions. *Prog. Mater. Sci.* **2013,** *58* (3), 327-381.
18. Giliberti, D. C.; White, K. K.; Dee, K. C., Control of Cell-Biomaterial Interactions. In *Polymeric Biomaterials, Revised and Expanded*, Dumitriu, S., Ed. Marcel Dekker, Inc.: New York, Basel, 2002; pp 361-375.
19. Chen, G.; Lv, Y.; Guo, P.; Lin, C.; Zhang, X.; Yang, L.; Xu, Z., Matrix mechanics and fluid shear stress control stem cells fate in three dimensional microenvironment. *Curr. Stem Cell Res. Ther.* **2013,** *8* (4), 313-323.
20. Janson, I. A.; Putnam, A. J., Extracellular matrix elasticity and topography: Material-based cues that affect cell function via conserved mechanisms. *J. Biomed. Mater. Res. A* **2015,** *103* (3), 1246-1258.
21. Dingal, P. C. D. P.; Discher, D. E., Material control of stem cell differentiation: Challenges in nano-characterization. *Curr. Opin. Biotechnol.* **2014,** *28*, 46-50.
22. Cameron, A. R.; Frith, J. E.; Cooper-White, J. J., The influence of substrate creep on mesenchymal stem cell behaviour and phenotype. *Biomaterials* **2011,** *32* (26), 5979-5993.
23. Haugh, M. G.; Vaughan, T. J.; Madl, C. M.; Raftery, R. M.; McNamara, L. M.; O'Brien, F. J.; Heilshorn, S. C., Investigating the interplay between substrate stiffness and ligand chemistry in directing mesenchymal stem cell differentiation within 3D macro-porous substrates. *Biomaterials* **2018,** *171*, 23-33.
24. Davies, J. E.; Matta, R.; Mendes, V. C.; Perri de Carvalho, P. S., Development, characterization and clinical use of a biodegradable composite scaffold for bone engineering in oro-maxillo-facial surgery. *Organogenesis* **2010,** *6* (3), 161-166.
25. Evans, N. D.; Minelli, C.; Gentleman, E.; LaPointe, V.; Patankar, S. N.; Kallivretaki, M.; Chen, X.; Roberts, C. J.; Stevens, M. M., Substrate stiffness affects early differentiation events in embryonic stem cells. *Eur. Cells Mater.* **2009,** *18*, 1-13.
26. Maloney, J. M.; Walton, E. B.; Bruce, C. M.; Van Vliet, K. J., Influence of finite thickness and stiffness on cellular adhesion-induced deformation of compliant substrata. *Phys. Rev. E Stat. Nonlin. Soft. Matter. Phys.* **2008,** *78* (4), 041923.
27. Nguyen du, T.; Kleiman, M.; Ryu, K. A.; Hiew, S.; Brubaker, K.; Mughnetsyan, R.; Truong, R.; Dolan, B.; Tackett, E.; Esser-Kahn, A. P., Three-dimensional conformal coatings through the entrapment of polymer membrane precursors. *ACS Appl. Mater. Inter.* **2014,** *6* (4), 2830-2835.

28. Chapter 1 - Deposition Technologies: An Overview. In *Handbook of Deposition Technologies for Films and Coatings (Third Edition)*, Martin, P. M., Ed. William Andrew Publishing: Boston, 2010; pp 1-31.
29. Tusan, C. G.; Man, Y. H.; Zarkoob, H.; Johnston, D. A.; Andriotis, O. G.; Thurner, P. J.; Yang, S.; Sander, E. A.; Gentleman, E.; Sengers, B. G.; Evans, N. D., Collective Cell Behavior in Mechanosensing of Substrate Thickness. *Biophys. J.* **2018,** *114* (11), 2743-2755.
30. Volponi, A. A.; Pang, Y.; Sharpe, P. T., Stem cell-based biological tooth repair and regeneration. *Trends Cell Biol.* **2010,** *20* (12), 715-722.
31. Ruparel, N. B.; de Almeida, J. F.; Henry, M. A.; Diogenes, A., Characterization of a stem cell of apical papilla cell line: effect of passage on cellular phenotype. *J. Endod.* **2013,** *39* (3), 357-363.
32. Vanacker, J.; Viswanath, A.; De Berdt, P.; Everard, A.; Cani, P. D.; Bouzin, C.; Feron, O.; Diogenes, A.; Leprince, J. G.; des Rieux, A., Hypoxia modulates the differentiation potential of stem cells of the apical papilla. *J. Endod.* **2014,** *40* (9), 1410-1418.
33. Wen, J. H.; Vincent, L. G.; Fuhrmann, A.; Choi, Y. S.; Hribar, K. C.; Taylor-Weiner, H.; Chen, S.; Engler, A. J., Interplay of matrix stiffness and protein tethering in stem cell differentiation. *Nat. Mater.* **2014,** *13* (10), 979-987.
34. Schneider, C. A.; Rasband, W. S.; Eliceiri, K. W., NIH Image to ImageJ: 25 years of image analysis. *Nat. Methods* **2012,** *9* (7), 671-675.
35. Degand, S.; Knoops, B.; Dupont-Gillain, C. C., Design and characterization of surfaces presenting mechanical nanoheterogeneities for a better control of cell-material interactions. *Colloids Surf. A Physicochem. Eng. Asp.* **2013,** *442*, 164-172.
36. Fuard, D.; Tzvetkova-Chevolleau, T.; Decossas, S.; Tracqui, P.; Schiavone, P., Optimization of poly-di-methyl-siloxane (PDMS) substrates for studying cellular adhesion and motility. *Microelectron. Eng.* **2008,** *85* (5-6), 1289-1293.
37. Brown, X. Q.; Ookawa, K.; Wong, J. Y., Evaluation of polydimethylsiloxane scaffolds with physiologically-relevant elastic moduli: Interplay of substrate mechanics and surface chemistry effects on vascular smooth muscle cell response. *Biomaterials* **2005,** *26* (16), 3123-3129.
38. Teixeira, A. I.; Ilkhanizadeh, S.; Wigenius, J. A.; Duckworth, J. K.; Inganäs, O.; Hermanson, O., The promotion of neuronal maturation on soft substrates. *Biomaterials* **2009,** *30* (27), 4567-4572.
39. Balaban, N. Q.; Schwarz, U. S.; Riveline, D.; Goichberg, P.; Tzur, G.; Sabanay, I.; Mahalu, D.; Safran, S.; Bershadsky, A.; Addadi, L.; Geiger, B., Force and focal adhesion assembly: A close relationship studied using elastic micropatterned substrates. *Nature Cell Biol.* **2001,** *3* (5), 466-472.

40. Dembo, M.; Wang, Y. L., Stresses at the cell-to-substrate interface during locomotion of fibroblasts. *Biophys. J.* **1999,** *76* (4), 2307-2316.
41. Schwarz, U. S.; Balaban, N. Q.; Riveline, D.; Bershadsky, A.; Geiger, B.; Safran, S. A., Calculation of forces at focal adhesions from elastic substrate data: The effect of localized force and the need for regularization. *Biophys. J.* **2002,** *83* (3), 1380-1394.
42. Butler, J. P.; Toli-Nørrelykke, I. M.; Fabry, B.; Fredberg, J. J., Traction fields, moments, and strain energy that cells exert on their surroundings. *Am. J. Physiol. Cell Physiol.* **2002,** *282* (3), C595-C605.
43. Del Álamo, J. C.; Meili, R.; Alonso-Latorre, B.; Rodríguez-Rodríguez, J.; Aliseda, A.; Firtel, R. A.; Lasheras, J. C., Spatio-temporal analysis of eukaryotic cell motility by improved force cytometry. *P. Natl. Acad. Sci. USA* **2007,** *104* (33), 13343-13348.
44. Yang, Z.; Lin, J. S.; Chen, J.; Wang, J. H. C., Determining substrate displacement and cell traction fields-a new approach. *J. Theor. Biol.* **2006,** *242* (3), 607-616.
45. Engler, A. J.; Richert, L.; Wong, J. Y.; Picart, C.; Discher, D. E., Surface probe measurements of the elasticity of sectioned tissue, thin gels and polyelectrolyte multilayer films: Correlations between substrate stiffness and cell adhesion. *Surf. Sci.* **2004,** *570* (1-2), 142-154.
46. Mehrotra, S.; Hunley, S. C.; Pawelec, K. M.; Zhang, L.; Lee, I.; Baek, S.; Chan, C., Cell adhesive behavior on thin polyelectrolyte multilayers: Cells attempt to achieve homeostasis of its adhesion energy. *Langmuir* **2010,** *26* (15), 12794-12802.
47. Sen, S.; Engler, A. J.; Discher, D. E., Matrix strains induced by cells: Computing how far cells can feel. *Cell. Mol. Bioeng.* **2009,** *2* (1), 39-48.
48. Banerjee, S.; Marchetti, M. C., Contractile stresses in cohesive cell layers on finite-thickness substrates. *Phys. Rev. Lett.* **2012,** *109* (10), 108101.
49. Buxboim, A.; Rajagopal, K.; Brown, A. E. X.; Discher, D. E., How deeply cells feel: Methods for thin gels. *J. Phys. Condens. Matter.* **2010,** *22* (19), 194116.
50. Lin, Y. C.; Tambe, D. T.; Park, C. Y.; Wasserman, M. R.; Trepat, X.; Krishnan, R.; Lenormand, G.; Fredberg, J. J.; Butler, J. P., Mechanosensing of substrate thickness. *Phys. Rev. E Stat. Nonlin. Soft. Matter. Phys.* **2010,** *82* (4), 041918.
51. Merkel, R.; Kirchgeßner, N.; Cesa, C. M.; Hoffmann, B., Cell force microscopy on elastic layers of finite thickness. *Biophys. J.* **2007,** *93* (9), 3314-3323.
52. Santiago-Cardona, P., The Retinoblastoma Protein in Osteogenesis and Osteosarcoma Formation. In *Osteogenesis*, Lin, Y., Ed. IntechOpen: Rijeka, 2012; pp 253-286.

53. Safadi, F. F.; Barbe, M. F.; Abdelmagid, S. M.; Rico, M. C.; Aswad, R. A.; Litvin, J.; Popoff, S. N., Bone structure, development and bone biology. In *Bone Pathology*, Humana Press: 2009; pp 1-50.
54. Anitha, A.; Menon, D.; Sivanarayanan, T. B.; Koyakutty, M.; Mohan, C. C.; Nair, S. V.; Nair, M. B., Bioinspired Composite Matrix Containing Hydroxyapatite-Silica Core-Shell Nanorods for Bone Tissue Engineering. *ACS Appl. Mater. Inter.* **2017,** *9* (32), 26707-26718.
55. Kaur, G.; Kumar, V.; Pickrell, G. R.; Mauro, J. C.; Lin, Y.; Arya, S. K., Chapter 6 - Bioactive Glasses in Gene Regulation and Proliferation. In *Biomedical, Therapeutic and Clinical Applications of Bioactive Glasses*, Kaur, G., Ed. Woodhead Publishing: 2019; pp 175-200.
56. Efimenko, K.; Wallace, W. E.; Genzer, J., Surface modification of Sylgard-184 poly(dimethyl siloxane) networks by ultraviolet and ultraviolet/ozone treatment. *J. Colloid Interf. Sci.* **2002,** *254* (2), 306-315.
57. Lee, J. N.; Jiang, X.; Ryan, D.; Whitesides, G. M., Compatibility of mammalian cells on surfaces of poly(dimethylsiloxane). *Langmuir* **2004,** *20* (26), 11684-11691.
58. Pieuchot, L.; Marteau, J.; Guignandon, A.; Dos Santos, T.; Brigaud, I.; Chauvy, P. F.; Cloatre, T.; Ponche, A.; Petithory, T.; Rougerie, P.; Vassaux, M.; Milan, J. L.; Tusamda Wakhloo, N.; Spangenberg, A.; Bigerelle, M.; Anselme, K., Curvotaxis directs cell migration through cell-scale curvature landscapes. *Nat. Commun.* **2018,** *9* (1), 3995.
59. Ambrosini, G.; Adida, C.; Altieri, D. C., A novel anti-apoptosis gene, survivin, expressed in cancer and lymphoma. *Nat. Med.* **1997,** *3* (8), 917-921.
60. Bai, H.; Ge, S.; Lu, J.; Qian, G.; Xu, R., Hypoxia inducible factor-1α-mediated activation of survivin in cervical cancer cells. *J. Obstet. Gynaecol. Res.* **2013,** *39* (2), 555-563.
61. Coumoul, X.; Li, W.; Wang, R.-H.; Deng, C., Inducible suppression of Fgfr2 and Survivin in ES cells using a combination of the RNA interference (RNAi) and the Cre–LoxP system. *Nucleic Acids Res.* **2004,** *32* (10), e85.
62. Filion, T. M.; Qiao, M.; Ghule, P. N.; Mandeville, M.; van Wijnen, A. J.; Stein, J. L.; Lian, J. B.; Altieri, D. C.; Stein, G. S., Survival responses of human embryonic stem cells to DNA damage. *J. Cell. Physiol.* **2009,** *220* (3), 586-592.
63. Ortiz, J.; Chou, L. L., Calcium upregulated survivin expression and associated osteogenesis of normal human osteoblasts. *J. Biomed. Mater. Res. A* **2012,** *100A* (7), 1770-1776.
64. Trappmann, B.; Gautrot, J. E.; Connelly, J. T.; Strange, D. G.; Li, Y.; Oyen, M. L.; Cohen Stuart, M. A.; Boehm, H.; Li, B.; Vogel, V.; Spatz, J. P.; Watt, F. M.; Huck, W. T., Extracellular-matrix tethering regulates stem-cell fate. *Nat. Mater.* **2012,** *11* (7), 642-649.

65. Engler, A.; Bacakova, L.; Newman, C.; Hategan, A.; Griffin, M.; Discher, D., Substrate Compliance versus Ligand Density in Cell on Gel Responses. *Biophys. J.* **2004,** *86* (1), 617-628.
66. Darnell, M.; O'Neil, A.; Mao, A.; Gu, L.; Rubin, L. L.; Mooney, D. J., Material microenvironmental properties couple to induce distinct transcriptional programs in mammalian stem cells. *P. Natl. Acad. Sci. USA* **2018,** *115* (36), E8368-E8377.
67. Bianchi, M.; Urquia Edreira, E. R.; Wolke, J. G. C.; Birgani, Z. T.; Habibovic, P.; Jansen, J. A.; Tampieri, A.; Marcacci, M.; Leeuwenburgh, S. C. G.; Van Den Beucken, J. J. J. P., Substrate geometry directs the *in vitro* mineralization of calcium phosphate ceramics. *Acta Biomater.* **2014,** *10* (2), 661-669.

Part VI : Conclusions and future prospects

1 Main achievements

This multidisciplinary thesis aimed at producing a degradable scaffold displaying a defined geometry with added value for tissue engineering. This was achieved through the development of a fused deposition modeling-based process leading to the successful printing of macroporous scaffolds with a gyroid shape. Moreover, the focus was set on the development of a coating methodology to impart tunable surface mechanical properties to this scaffold, with a view to better control cell behavior. In this section, the main results and achievements of the work will be summarized.

1.1 PLA gyroid scaffold production

PLA scaffolds were printed according to a gyroid geometry using fused deposition modeling, a low-cost and easy-to-use additive manufacturing technique. The printed PLA gyroid scaffold was compared to a classical strut-based scaffold commonly found in the literature, and the effect of mesh geometry, layer resolution and crystallinity of the polymer was evaluated on resistance against compression and on scaffold degradation. Results and conclusions from this study are:

(i) µCT scan evidenced that PLA-printed gyroid structures matched the computerized model, with well-defined nodes and gyrating junctions.
(ii) Porous fraction was about 70-75%, as expected, demonstrating again the accuracy of printing.
(iii) Stress-strain curves were isotropic for gyroid scaffolds but orientation-dependent for strut-based scaffolds. Furthermore, thicker printed layers and higher crystallinity exacerbated orientation effects on yield strength for strut-based scaffolds.
(iv) Hydrolytic degradation rate was not significantly affected neither by mesh geometry nor by crystallinity. Only thicker layers made scaffold degradation slower. However, gyroid scaffolds retained their integrity longer, while common scaffolds lose struts one after another.

The obtained results highlight the interest to study scaffolds presenting a complex geometry. Different behaviors regarding mechanical properties and degradation can be obtained compared to strut-based scaffolds. Brought together, the results show the superior properties of the gyroid scaffolds compared to struts-based scaffolds. The gyroid design could be used as a mesh for personal implantable scaffolds for tissue engineering.

1.2 PCL gyroid scaffold production

Similar gyroid scaffolds were printed in PCL, which is a more flexible polymer than PLA. Observed results are:

(i) µCT scan and pictures showed that PCL-printed gyroid scaffolds matched the computerized model.
(ii) Porous fraction, evaluated based on mass and dimensions of the samples, was around 70%, which is close to the theoretical porous fraction and demonstrated printing accuracy.
(iii) In contrast with PLA, the isotropic behavior regarding stress-strain curves was not observed for the PCL gyroid scaffolds.

PCL gyroid scaffolds were successfully printed and may constitute alternative scaffolds for tissue engineering. Their compressive moduli is much lower than the one of PLA-based scaffolds, which could make them suitable for cartilage repair.

1.3 Optimization of PDMS coating protocol

A PDMS coating was applied to modulate the surface mechanical properties of the macroporous scaffolds. The coating protocol through the formation of a semi-interpenetrating polymer network (SIPN) was inspired from Nguyen and coworkers.[1] A solvent and a non-solvent of the polymer composing the structure swell its surface, allowing the interpenetration of PDMS chains with the swollen surface. The coating is then crosslinked. Major results and conclusions are the following:

(i) Both water contact angle measurements and XPS highlighted the presence of PDMS at the surface of coated PLA and PCL samples.
(ii) PDMS coating thickness on PLA and PCL cylinders varied from 14 to 43 µm depending on the composition of the coating mixture. No trend was however observed regarding the influence of the composition of the mixture on the coating thickness.
(iii) Thick and homogeneous coatings were obtained on the macroporous PLA scaffolds for both PDMS(10:1) and PDMS(10:0.2) owing to the repeated deposition and the formation of a SIPN.

Results from this chapter highlighted the critical parameters leading to thick and homogeneous PDMS coatings on macroporous scaffolds. This represents a major improvement when compared to the protocol that served as a starting point to develop the coating method.[1]

1.4 Preliminary cell culture studies

Before the studies in complex 3D macroporous scaffolds, the experimental conditions were set up for cell culture, first on both PLA and PDMS flat 2D substrates and then on PLA gyroid scaffolds.

(i) Fibronectin significantly improved AMSC adhesion on both PLA and PDMS.
(ii) The use of a high number of cells in a low volume of medium, *i.e.* of highly concentrated cell supensions, significantly improved the efficiency of cell seeding.
(iii) SCAP proliferated on both gyroid scaffolds and 2D substrates and their proliferation rate was higher on 2D substrates than on 3D scaffolds.

Conditions were identified to successfully seed SCAP on macroporous scaffolds and to obtain cell attachment on both PLA and PDMS.

1.5 Effect of macroporous scaffold surface mechanical properties on SCAP behavior and osteogenic differentiation

Effect of surface mechanical properties on SCAP was studied on gyroid macroporous scaffolds coated with two different PDMS coatings. SCAP were seeded and proliferation as well as osteogenic differentiation were studied. This last chapter's results and conclusions are:

(i) Gyroid scaffolds were successfully coated with stiff and soft PDMS by varying the amount of curing agent. Similar coating thicknesses of about 50 µm were obtained.
(ii) SCAP attached and proliferated in all conditions but proliferation rate was lower on soft than on stiff PDMS-coated samples.
(iii) Both PDMS coating upregulated osteogenic markers compared to uncoated PLA but no significant differences were observed between stiff and soft PDMS-coated scaffolds.

PLA macroporous scaffolds were coated with PDMS presenting different degree of crosslinking density but sharing a similar thickness. The difference in crosslinking density had an effect on proliferation but did not influence osteogenic marker expression. Some results are not fully understood in the light of literature about 2D conventional culture and highlight the interest and the importance to study mechanostransduction in macroporous scaffolds. This domain is still poorly studied but yet clinically relevant.

2 Future prospects

2.1 Production of scaffolds presenting complex geometry using fused deposition modelling

The gyroid was proposed as an interesting mesh for scaffold geometry. The gyroid design presents isotropic behavior regarding mechanical compression and multiple curvatures that are interesting to trigger cellular responses. Other porous fractions and pore sizes could now be tested to evaluate their effect on mechanical properties and degradation behavior.

Another interesting property of the gyroid, which could be exploited, is its chirality. Indeed, the gyroid and its mirror image cannot be superposed (Figure 1). On the contrary, they can perfectly interlace without touching each other. This structure, called double gyroid, could be printed and compared to the simple gyroid structure. An increase in resistance against compression as well as a reduced porous fraction will certainly result from this modification. However, the double gyroid could be compared to a thickened simple gyroid presenting the same porous fraction. It could be determined whether the porous fraction alone or the additional branches affect the scaffold mechanical properties.

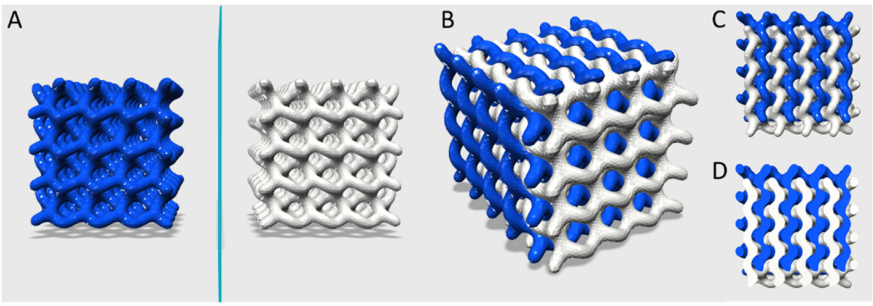


Figure 1: (A) Gyroid structure (white) and mirror image (blue). (B) Gyroid structure interlacing its mirror image. (C) Top view and (D) inside view of the interlacing structure. Gyroids do not touch one another.

Besides the gyroid, many other triply periodic minimal surfaces (TPMS) presenting, among other advantages, an ability to absorb compressive energy effectively could be printed using FDM. Some of them, printed in nylon using selective laser sintering[2] or in a resin of poly(trimethylene carbonate) and propylene carbonate using stereolithography[3] (Figure 2), were studied recently regarding their mechanical properties. Printing other TPMS-based structures in PLA and evaluating the effect of geometry, layer

thickness and porous fraction on mechanical properties and degradation could be interesting.

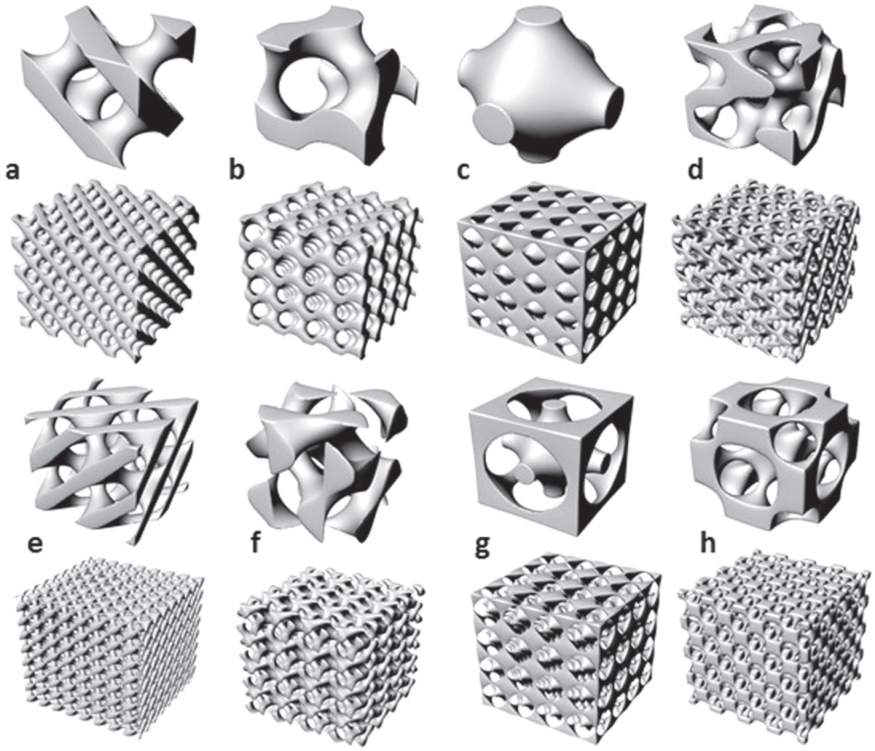


Figure 2: Examples of triply periodic minimal surfaces (TPMS): (a) Diamond; (b) Gyroid; (c) Schwarz P; (d) Fischer-Koch S; (e) Double Diamond; (f) Double Gyroid; (g) Double Schwarz P; (h) F-RD. For each structure, the top image represents a single unit cell and the bottom image represents a combination of 4x4x4 unit cells.[3]

In addition to studying the effect of layer thickness and PLA crystallinity on mechanical properties and on degradation, the impact of the size of the deposited polymer strut could also be evaluated. Nozzle diameter defines the dimension of the deposited struts during printing and, hence, defines X and Y resolution. A smaller nozzle diameter could result in a higher X and Y resolution to produce more defined structures. However, as layer thickness was shown to significantly impact mechanical properties and degradation, a smaller strut could also impact these parameters.

Much of the effort in this work was placed in PLA printing due to time constrains. It would be then interesting to further optimize and develop printing of PCL scaffolds. Furthermore, circular pore projections could be obtained to confirm the influence of elliptical pore shape on mechanical

properties. Improvement could be achieved using an enhanced cooling system (cool and low relative humidity), when using PVA as supporting material, or through a precise nozzle positioning.

PLA scaffold degradation in PBS was proposed to study the influence of differences between geometry, layer resolution and crystallinity but incubation in PBS might not reflect properly the complexity of implantation in a living organism. Even though PLA mainly degrades by a non-enzymatic reactions[4], enzymes seem to participate to PLA degradation[5]. To get closer to the degradation of implanted scaffolds, solutions mimicking body fluids could be prepared using proper salt composition and enzymes such as esterases. Results that are even more reliable would be obtained owing to the implantation of those scaffolds in animals even if scaffold degradation over time is difficult to assess *in vivo*.

Finally, one major downside of PLA is the decrease in pH linked to the release of lactic acid, its degradation product.[6] If implant size is large and if the flux of body fluid in implanted region is not sufficient, the decrease in pH can be detrimental to surrounding tissues. To overcome this issue, a buffer component such as calcium carbonate salt[6, 7] or hydroxyapatite[8] can be added to PLA before printing. This buffer will limit pH decrease and, consequently, will lower the toxic effect of lactic acid. However, as the degradation of PLA is catalyzed by the pH, lower degradation rates of PLA-buffer composites are expected.

2.2 PDMS polymer coating

It would be nice to demonstrate the formation of the semi-interpenetrating polymer network between PDMS and PLA chains, but it is quite difficult as the interpenetration occurs on a molecular scale. If PLA and PDMS polymers interpenetrate, cohesion between them should be better than if the PDMS is simply deposited on PLA by spin coating or dip coating. This is especially true for PLA and PDMS as they do not share the same hydrophilicity and do not have affinity for each other. Therefore, if we peel the PDMS coating layer from the PLA using a peel test machine (or equivalent), a higher force should be recorded to detach the PDMS layer interpenetrating with PLA compared to the PDMS layer simply deposited. Another way to prove PDMS and PLA interpenetration could be via Time Of Flight – Secondary Ion Mass Spectrometry (TOF-SIMS) in depth profiling mode. Cluster ions are used to bombard a surface and to create and eject secondary ions characteristic of the surface chemistry. Those secondary ions are collected and analyzed to

determine surface chemical composition. The analysis can be performed in depth profiling mode, in which the beam continuously digs the surface to evaluate the chemistry deeper and deeper under the surface. If PDMS is deposited on PLA without interpenetration, a sudden switch between PDMS secondary ions (present at the surface) and PLA secondary ions (present under the coating) should be observed. If PDMS interpenetrates with PLA, a transition zone should be present showing a decreasing number in PDMS secondary ions and an increasing number in PLA secondary ions.

While some parameters of the coating protocol were tested, the impact of bath temperature and residence time were not studied owing to a lack of time. Their effect on coating thickness could be further studied. The gravity has a big effect on coating solution drainage and, hence, on pore clogging at the bottom of the structure. Systems rotating the structures during solvent evaporation or evaporating the solvent quicker could be developed to uniformly distribute the coating on the structure. We did not have the time either to evaluate pore interconnectivity, but this could be done via the perfusion of a colored solution inside the scaffold.

The templating method proposed to coat the structure is worth to be further developed as it could be used to have a thick and perfectly distributed PDMS coating without the use of solvents. Besides, it would allow to coat the structure with any bio- or synthetic polymer for which the crosslinking relies on chemical compounds (polyacrylamide), on heat (decellularised ECM, chitosan) or on diffusion of ions (alginate) without many other development. The use of hydrogel-ceramic composites, drug-loaded hydrogels or even cell-loaded hydrogels could be considered.

The solvogel method is also worth to be developed as it allows to get, in a simple way, a thick and homogeneous coating throughout the structure that is not influenced by gravity. However, the coating was not applicable for the PDMS presenting softer mechanical properties. Indeed, the polymer never crosslinked in the solvent. This could be related to a low concentration in curing agent in the mixture. As the concentration in curing agent was low, curing reaction happened very slowly due to the low encountering probability of the reagents. Another hypothesis would be that the network was so soft and fragile that macroscopic observation led to think that the crosslinking did not occur. If the reason is the limited concentration in reagent, theoretically the issue could be solved by varying the density of reactive functions instead of crosslinker concentration (Figure 3). Different

PDMS chains presenting different densities of reactive function could be used. Mechanical properties would be modified using the density of reactive functions present on the chains. Consequently, a high concentration of curing agent could be used to ensure the chemical reaction as mechanical properties depend on reactive function density and no more on curing agent concentration. Additionally, it would be interesting to test the solvogel methods to evaluate if the process is applicable to other polymers.

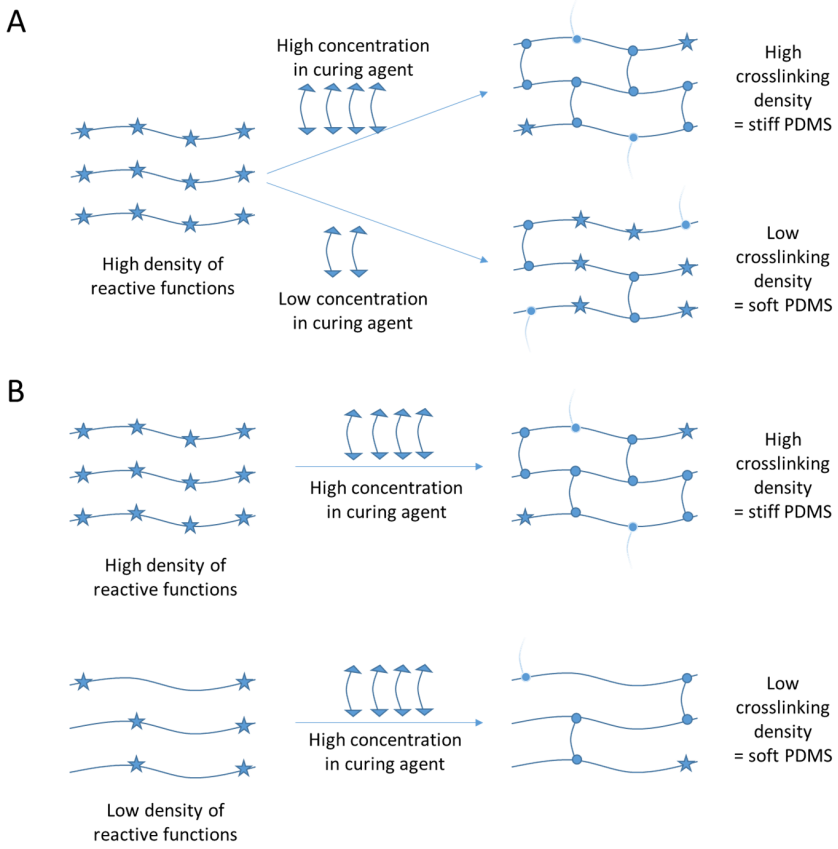


Figure 3: Modification of crosslinked PDMS mechanical properties through (A) the variation in curing agent concentration and through (B) the density of reactive functions on PDMS chains.

The mechanical properties of PDMS presenting different crosslinking densities were not measured directly on the scaffold but separately using rotational rheometry. Some attempts were performed using Atomic Force Microscopy (AFM) to record force-distance curves and directly measure them on the gyroid scaffold. However, the AFM tip could not approach the surface due to the high surface curvature. Alternatively, the coating could be

deposited on a strut-based scaffold, which present less curvature, or PDMS could be simply casted on a flat PLA substrate. The AFM tip should moreover be chemically modified to prevent its adhesion on PDMS. Micro- or nanoindentation testing devices could also be tried.

Even though PDMS possess many advantages, its chemistry presents some limitations. Owing to its high hydrophobicity, PDMS does not attach sufficiently on PLA. This was especially observed in Part V, Chapter 3 when using dip coating. Furthermore, PDMS hydrophobicity prevents cell adhesion. Silicone chemistry, as carbon chemistry, is highly tunable and many PDMS derivatives do exist. Amine-functionalized PDMS could be used to increase hydrophilicity and improve both adhesion to PLA and cell attachment. Another disadvantage of the crosslinked PDMS used in this work is its non-degradability which limit its translation to clinical applications. We could imagine adding ester functions in the PDMS chains to allow its degradation in sufficiently small chains to be evacuated by the body.

2.3 Cell mechanotransduction in macroporous scaffolds presenting tuned pore surface stiffness.

As far as we know, this is the first time that the impact of a PDMS-coated gyroid scaffold on SCAP osteodifferentiation has been studied, especially comparing two PDMS with different moduli. We observed that the different moduli did not influence osteogenic differentiation at the gene expression level, but these results could be completed by looking at osteodifferentiation at the protein level, measuring for instance alkaline phosphatase activity. Additionally, accumulation of calcium (Alizarin red S staining), a classical test used to confirm osteodifferentation[9], could also be evaluated. Calcium deposition could be then solubilized to perform a colorimetric quantification.

Osteogenic gene expression was shown to be similar in basal medium and in osteogenic differentiation medium. Osteogenic differentiation medium was previously shown in our laboratory to be efficient at inducing osteogenic differentiation on flat substrates.[10] In addition, SURVIVIN stemness marker expression decreased with culture time. Therefore, it was hypothesized that osteogenic differentiation is induced in both media. This hypothesis could be further confirmed using a complementary negative control such as cells before seeding.

No significant differences were observed between soft and stiff PDMS coatings regarding osteogenic differentiation. It could be checked whether

fibronectin adsorption and layer morphology are similar on these two PDMS presenting different crosslinked densities. A short UV/ozone exposure of the PDMS surface (increase of surface hydrophilicity) directly followed by fibronectin adsorption could be tested to homogenize fibronectin deposition whatever the conditions. Another reason might be the lack of covalent bonds between PDMS and fibronectin, the protein used for cell anchorage. Fibronectin could be insufficiently attached to the surface to properly transfer the mechanical properties of PDMS to the cells. And hence, cells would only sense the detachment of the protein from the surface. To test this hypothesis, fibronectin could be covalently attached to PDMS. To graft fibronectin on PDMS, two steps are required. First, PDMS is functionalized with amines using a UV/ozone treatment followed by an incubation in presence of (3-aminopropyl)triethoxysilane.[11] Alternatively, PDMS can be treated using ammonia plasma.[12] Then, a N-Sulfosuccinimidyl-6-(4'-azido-2'-nitrophenylamino)hexanoate (Sulfo-SANPAH) linker can be used to covalently attach proteins.[11]

Alternatively, the thickness of PDMS coating could be insufficient or not homogeneous enough to hide the stiff PLA present under the coating. To test this hypothesis, coating with increasing coating thickness could be used to evaluate cell response to coating thickness.[13] If cell response continues to evolve for coating thickness higher than coating thickness obtained on coated 3D scaffolds (around 50 µm), it is likely that cells were influenced by the PLA present under the PDMS coating. An alternative strategy would be to produce PDMS gyroid scaffolds using molding. A mold presenting the imprint of the gyroid would be 3D-printed in PVA. PDMS would be poured in the mold and crosslinked. After PVA dissolution in water, cell behavior in PDMS gyroid scaffolds could be compared to cell behavior in PDMS-coated gyroid scaffolds.

We focused on SCAP osteogenic differentiation as bone repair seemed the most adapted application for our scaffold but it could be interesting to study the impact of the PDMS coating mechanical properties on adipogenic, chondrogenic and neurogenic differentiation. Furthermore, stem cells of different origins as adipose-derived mesenchymal stem cells, bone marrow stem cells and embryonic stem cells could be used to evaluate if cell response to stiffness inside macroporous scaffolds is cell-dependent.

We showed that SCAP proliferation rate on 2D substrates was higher than on macroporous scaffolds, but additional experiments that would provide more

information on the effect of cell culture and differentiation on both configurations could be performed. For example, PLA discs could be printed in PLA as it was achieved for coating development. Uncoated and PDMS-coated (stiff and soft) PLA disks could be compared to their 3D counterparts regarding proliferation and differentiation to evaluate if culture in a macroporous environment affects cell behavior. Besides, cell culture in gyroid scaffolds could be compared to cell culture on strut-based scaffolds to evaluate the beneficial effect of curvatures in the scaffold.

Finally, the Sylgard 184 PDMS (Dow) is one of the materials that is often used to study mechanotransduction. The conventional way to modify its mechanical properties is through the decrease in curing agent to base proportion as it was achieved in this thesis. However, this method is suspected to lead to the leaching of uncured oligomers into culture medium and to their accumulation within the cell membrane.[14] Another method of controlling PDMS mechanical properties consists in the mixing of two different Sylgard kits in different proportions.[15] Sylgard 527 and 184 were mixed to their respective curing agent in the recommended proportions. Then the two kits were mixed in ratios from 5:1 to 1:10 (Sylgard 184:527) to get elastic moduli from 1.72 MPa to 5 kPa. Even though the surface roughness and water contact angle measurements were similar for the different formulations, further tests should be performed to evaluate the differences in chemistry between the two kits. If the components of the two kits are chemically too different, this could lead to differences in surface chemistry and could affect cell behavior. Other materials used for mechanotransduction studies such as polyacrylamide gels[16-18], alginate gels[19] or recombinant elastin-like proteins[20] could be used and compared to PDMS.

2.4 General long-term future prospects

To go even further, drugs, antibiotics[21] and growth factors such as recombinant human bone morphogenetic protein-2 (rhBMP-2)[22] could be loaded in PLA to improve tissue reconstruction or prevent infections. As most of those compounds are sensitive to heat, they could be loaded inside PLA after printing using supercritical CO_2.[23] Supercritical CO_2 allows PLA swelling and allows the impregnation of the proteins/molecules inside the PLA.[24]

As stated earlier, fused deposition modeling can be used to create molds.[25] Those molds can be used to produce natural hydrogels scaffold presenting complex shapes. The mold can be printed in PVA. The natural polymer is then introduced in the mold, crosslinked and the PVA mold is dissolved (Figure 4).

The complexity of the geometries that can be obtained by this technique will depend on the mechanical properties of the selected hydrogel. Complex geometries using a too soft hydrogel could collapse. However, natural polymers reinforced with ceramics present higher mechanical properties and can withstand higher loads.[26]

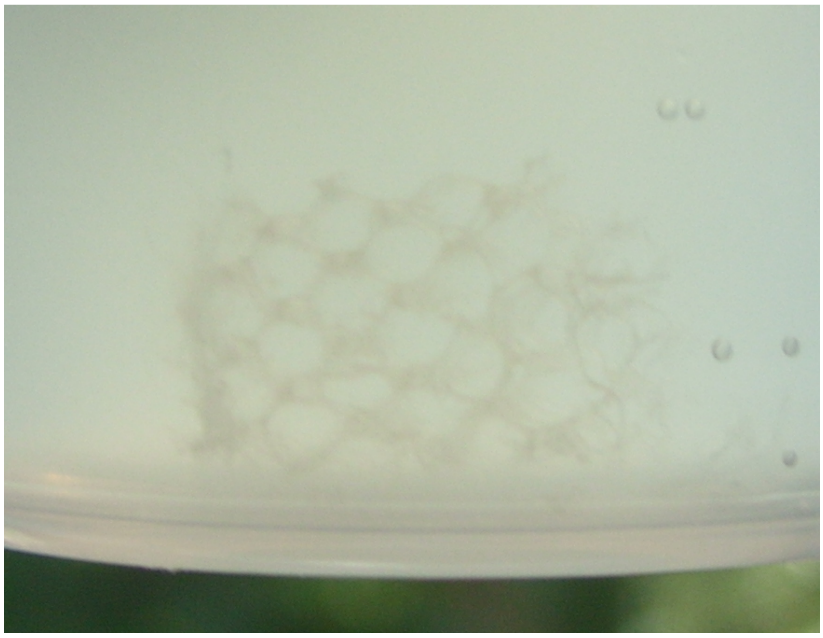


Figure 4: Alginate gyroid produced by molding. A PVA mold with the gyroid imprint was 3D-printed. The mold was filled with alginate. PVA mold was dissolved in a solution containing Ca^{2+} for alginate gelling.

Synthetic polymers are advantageous regarding mechanical properties but show relatively low bioactivity. Inversely, natural polymers possess low mechanical properties but favor cell-material interactions. More and more scientists propose hybrid scaffolds containing a part of synthetic polymer for their mechanical properties with natural polymers for their bioactivity.[27-32] In this thesis, the scaffold is built mainly using synthetic polymers. To create a composite and combine the advantages of both types of polymers, cell-loaded natural hydrogels such as decellularized extracellular matrix, chitosan, alginate or fibrin could be injected in the pores of the scaffold. Attention would have to be payed though to diffusion of oxygen, nutrient as well as in protein and signaling molecules.[33, 34] A limited diffusion can affect cell development, function and differentiation or even lead to cell death. An elegant way to produce hybrid scaffolds would be to take advantage of the

chiral property of the gyroid and to combine it to the use of molding. A PLA gyroid scaffold could be printed at the same time as a PVA mold presenting the imprint of the interlacing mirror image of the gyroid (Figure 5). A cell-loaded natural hydrogel could be then poured into the mold and jellified *in situ*. Finally, the PVA would be dissolved. This would give a hybrid scaffold presenting several advantages:

- Strength of the synthetic polymer;
- High porous fraction and large pore size between the gyroid hydrogel and the PLA gyroid structure;
- Improved bioactivity allowed by the presence of natural polymer;
- Encapsulation of the cells in a 3D environment closer to the *in vivo* configuration.

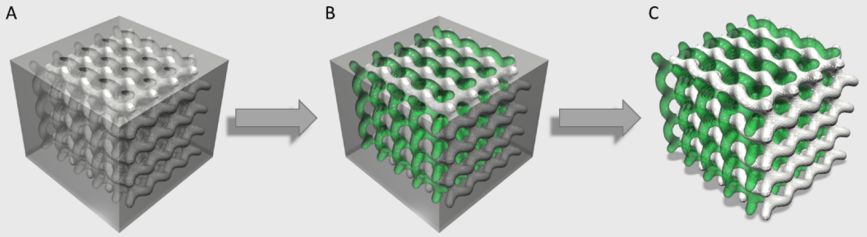


Figure 5: (A) Printing of a PLA gyroid (white) with a PVA mold (translucent grey) presenting the imprint of the gyroid mirror image. (B) Hydrogel (translucent green) poured in the mold and crosslinking. (C) PVA dissolution in water or cell medium.

3 References

1. Nguyen du, T.; Kleiman, M.; Ryu, K. A.; Hiew, S.; Brubaker, K.; Mughnetsyan, R.; Truong, R.; Dolan, B.; Tackett, E.; Esser-Kahn, A. P., Three-dimensional conformal coatings through the entrapment of polymer membrane precursors. *ACS Appl. Mater. Inter.* **2014,** *6* (4), 2830-2835.

2. Maskery, I.; Sturm, L.; Aremu, A. O.; Panesar, A.; Williams, C. B.; Tuck, C. J.; Wildman, R. D.; Ashcroft, I. A.; Hague, R. J. M., Insights into the mechanical properties of several triply periodic minimal surface lattice structures made by polymer additive manufacturing. *Polymer* **2018,** *152*, 62-71.

3. Blanquer, S. B. G.; Werner, M.; Hannula, M.; Sharifi, S.; Lajoinie, G. P. R.; Eglin, D.; Hyttinen, J.; Poot, A. A.; Grijpma, D. W., Surface curvature in triply-periodic minimal surface architectures as a distinct design parameter in preparing advanced tissue engineering scaffolds. *Biofabrication* **2017,** *9* (2), 025001.

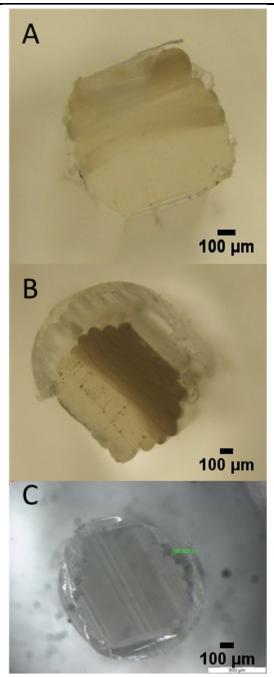
4. Domingues, R. C. C.; Pereira, C. C.; Borges, C. P., Effect of stereoisomerism of poly(lactic acid) during neural guide conduit membrane synthesis. *J. Appl. Polym. Sci.* **2018,** *135* (18), 46190.
5. Chappard, D.; Baslé, M. F.; Legrand, E.; Audran, M., Trabecular bone microarchitecture: A review. *Morphologie* **2008,** *92* (299), 162-170.
6. Agrawal, C. M.; Athanasiou, K. A., Technique to control pH in vicinity of biodegrading PLA-PGA implants. *J. Biomed. Mater. Res.* **1997,** *38* (2), 105-114.
7. Gayer, C.; Ritter, J.; Bullemer, M.; Grom, S.; Jauer, L.; Meiners, W.; Pfister, A.; Reinauer, F.; Vučak, M.; Wissenbach, K.; Fischer, H.; Poprawe, R.; Schleifenbaum, J. H., Development of a solvent-free polylactide/calcium carbonate composite for selective laser sintering of bone tissue engineering scaffolds. *Mater. Sci. Eng. C Mater. Biol. Appl.* **2019,** *101*, 660-673.
8. Akindoyo, J. O.; Beg, M. D. H.; Ghazali, S.; Alam, A. K. M. M.; Heim, H. P.; Feldmann, M., Synergized poly(lactic acid)–hydroxyapatite composites: Biocompatibility study. *J. Appl. Polym. Sci.* **2019,** *136* (15), 47400.
9. Gregory, C. A.; Grady Gunn, W.; Peister, A.; Prockop, D. J., An Alizarin red-based assay of mineralization by adherent cells in culture: comparison with cetylpyridinium chloride extraction. *Anal. Biochem.* **2004,** *329* (1), 77-84.
10. Vanacker, J.; Viswanath, A.; De Berdt, P.; Everard, A.; Cani, P. D.; Bouzin, C.; Feron, O.; Diogenes, A.; Leprince, J. G.; des Rieux, A., Hypoxia modulates the differentiation potential of stem cells of the apical papilla. *J. Endod.* **2014,** *40* (9), 1410-1418.
11. Wen, J. H.; Vincent, L. G.; Fuhrmann, A.; Choi, Y. S.; Hribar, K. C.; Taylor-Weiner, H.; Chen, S.; Engler, A. J., Interplay of matrix stiffness and protein tethering in stem cell differentiation. *Nat. Mater.* **2014,** *13* (10), 979-987.
12. Evans, N. D.; Minelli, C.; Gentleman, E.; LaPointe, V.; Patankar, S. N.; Kallivretaki, M.; Chen, X.; Roberts, C. J.; Stevens, M. M., Substrate stiffness affects early differentiation events in embryonic stem cells. *Eur. Cells Mater.* **2009,** *18*, 1-13.
13. Tusan, C. G.; Man, Y. H.; Zarkoob, H.; Johnston, D. A.; Andriotis, O. G.; Thurner, P. J.; Yang, S.; Sander, E. A.; Gentleman, E.; Sengers, B. G.; Evans, N. D., Collective Cell Behavior in Mechanosensing of Substrate Thickness. *Biophys. J.* **2018,** *114* (11), 2743-2755.
14. Regehr, K. J.; Domenech, M.; Koepsel, J. T.; Carver, K. C.; Ellison-Zelski, S. J.; Murphy, W. L.; Schuler, L. A.; Alarid, E. T.; Beebe, D. J., Biological implications of polydimethylsiloxane-based microfluidic cell culture. *Lab Chip* **2009,** *9* (15), 2132-2139.

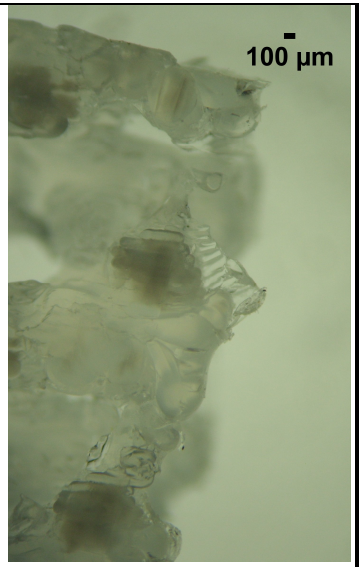
15. Palchesko, R. N.; Zhang, L.; Sun, Y.; Feinberg, A. W., Development of Polydimethylsiloxane Substrates with Tunable Elastic Modulus to Study Cell Mechanobiology in Muscle and Nerve. *PLOS ONE* **2012,** *7* (12), e51499.
16. Trappmann, B.; Gautrot, J. E.; Connelly, J. T.; Strange, D. G.; Li, Y.; Oyen, M. L.; Cohen Stuart, M. A.; Boehm, H.; Li, B.; Vogel, V.; Spatz, J. P.; Watt, F. M.; Huck, W. T., Extracellular-matrix tethering regulates stem-cell fate. *Nat. Mater.* **2012,** *11* (7), 642-649.
17. Engler, A. J.; Sen, S.; Sweeney, H. L.; Discher, D. E., Matrix Elasticity Directs Stem Cell Lineage Specification. *Cell* **2006,** *126* (4), 677-689.
18. Cameron, A. R.; Frith, J. E.; Cooper-White, J. J., The influence of substrate creep on mesenchymal stem cell behaviour and phenotype. *Biomaterials* **2011,** *32* (26), 5979-5993.
19. Darnell, M.; O'Neil, A.; Mao, A.; Gu, L.; Rubin, L. L.; Mooney, D. J., Material microenvironmental properties couple to induce distinct transcriptional programs in mammalian stem cells. *P. Natl. Acad. Sci. USA* **2018,** *115* (36), E8368-E8377.
20. Haugh, M. G.; Vaughan, T. J.; Madl, C. M.; Raftery, R. M.; McNamara, L. M.; O'Brien, F. J.; Heilshorn, S. C., Investigating the interplay between substrate stiffness and ligand chemistry in directing mesenchymal stem cell differentiation within 3D macro-porous substrates. *Biomaterials* **2018,** *171*, 23-33.
21. Weisman, J. A.; Nicholson, J. C.; Tappa, K.; Jammalamadaka, U.; Wilson, C. G.; Mills, D. K., Antibiotic and chemotherapeutic enhanced three-dimensional printer filaments and constructs for biomedical applications. *Int. J. Nanomed.* **2015,** *10*, 357-70.
22. Anderson, J. M.; Shive, M. S., Biodegradation and biocompatibility of PLA and PLGA microspheres. *Adv. Drug Deliv. Rev.* **2012,** *64* (Supplement), 72-82.
23. Ginty, P. J.; Whitaker, M. J.; Shakesheff, K. M.; Howdle, S. M., Drug delivery goes supercritical. *Mater. Today* **2005,** *8* (8, Supplement), 42-48.
24. Champeau, M.; Thomassin, J. M.; Tassaing, T.; Jérôme, C., Drug loading of polymer implants by supercritical CO2 assisted impregnation: A review. *J. Control. Release* **2015,** *209*, 248-259.
25. Mohanty, S.; Larsen, L. B.; Trifol, J.; Szabo, P.; Burri, H. V. R.; Canali, C.; Dufva, M.; Emnéus, J.; Wolff, A., Fabrication of scalable and structured tissue engineering scaffolds using water dissolvable sacrificial 3D printed moulds. *Mater. Sci. Eng. C Mater. Biol. Appl.* **2015,** *55*, 569-578.
26. Kane, R. J.; Weiss-Bilka, H. E.; Meagher, M. J.; Liu, Y.; Gargac, J. A.; Niebur, G. L.; Wagner, D. R.; Roeder, R. K., Hydroxyapatite reinforced collagen scaffolds with improved architecture and mechanical properties. *Acta Biomater.* **2015,** *17*, 16-25.

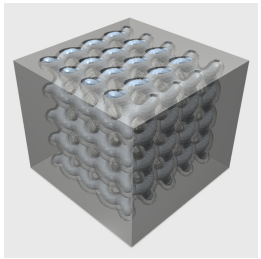
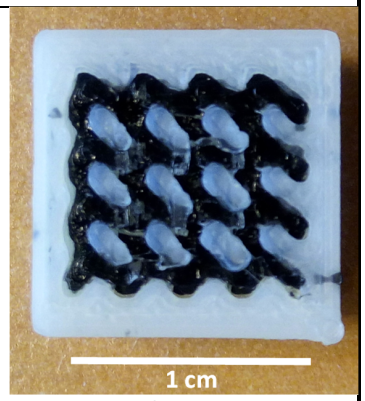
27. Zhao, X.; Liu, L.; Wang, J.; Xu, Y.; Zhang, W.; Khang, G.; Wang, X., *In vitro* vascularization of a combined system based on a 3D printing technique. *J. Tissue Eng. Regen. Med.* **2014,** *10* (10), 833-842.
28. Shim, J. H.; Kim, J. Y.; Park, M.; Park, J.; Cho, D. W., Development of a hybrid scaffold with synthetic biomaterials and hydrogel using solid freeform fabrication technology. *Biofabrication* **2011,** *3* (3), 034102.
29. Dong, L.; Wang, S.-J.; Zhao, X.-R.; Zhu, Y.-F.; Yu, J.-K., 3D-Printed Poly(ε-caprolactone) Scaffold Integrated with Cell-laden Chitosan Hydrogels for Bone Tissue Engineering. *Sci. Rep.* **2017,** *7* (1), 13412.
30. De Giglio, E.; Bonifacio, M. A.; Ferreira, A. M.; Cometa, S.; Ti, Z. Y.; Stanzione, A.; Dalgarno, K.; Gentile, P., Multi-compartment scaffold fabricated via 3D-printing as *in vitro* co-culture osteogenic model. *Sci. Rep.* **2018,** *8* (1), 15130.
31. Pati, F.; Ha, D.-H.; Jang, J.; Han, H. H.; Rhie, J.-W.; Cho, D.-W., Biomimetic 3D tissue printing for soft tissue regeneration. *Biomaterials* **2015,** *62*, 164-175.
32. Lee, H.; Ahn, S.; Bonassar, L. J.; Kim, G., Cell(MC3T3-E1)-printed poly(ε-caprolactone)/alginate hybrid scaffolds for tissue regeneration. *Macromol. Rapid. Comm.* **2013,** *34* (2), 142-149.
33. Amsden, B., Solute diffusion within hydrogels. Mechanisms and models. *Macromolecules* **1998,** *31* (23), 8382-8395.
34. McMurtrey, R. J., Analytic models of oxygen and nutrient diffusion, metabolism dynamics, and architecture optimization in three-dimensional tissue constructs with applications and insights in cerebral organoids. *Tissue Eng. Part. C Methods* **2016,** *22* (3), 221-249.

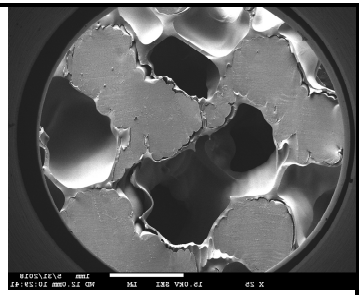
Annex : Detailed protocols of PDMS coating methods

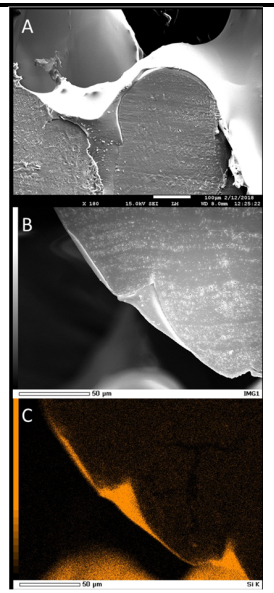
Coating method	Protocol	Result	Image
Coating by centrifugation (Figure 13)	Gyroid PLA structures were inserted in 15ml Falcon tubes. 1ml of uncured PDMS(10:1) (w:w) was poured over the structures. Falcon tubes were centrifuged 3x3 min at 9 g and then 1x3 min at 100 g to allow PDMS penetration and drainage of the excess, respectively. Structures were recovered and coating was cured overnight at 85°C.	No significant coating layer was observed.	Not Applicable (N/A)
	Gyroid PLA structures were inserted in 15ml Falcon tubes containing 3 ml of uncured PDMS(10:1) (w:w). Falcons were centrifuged 6 min at 100 g to allow PDMS penetration. Structures were removed and inserted in empty Falcons. Falcons containing structure full of PDMS were centrifuged 3 min at 100 g to allow PDMS penetration. Structures were recovered and coating was cured overnight at 85°C.	No significant coating layer was observed.	N/A
Dip coating (Figure 14)	Gyroid PLA structures were immersed in PDMS(10:1):hexane solutions (50:50) (v:v) for 5 min. Structures were dried at 60°C for 15 min or 3 min. 1, 2, 3, 4 or 5 cycles were performed to increase coating thickness. Structures were recovered and coating was cured overnight at 85°C.	For all tested samples, half of the pores were clogged.	N/A

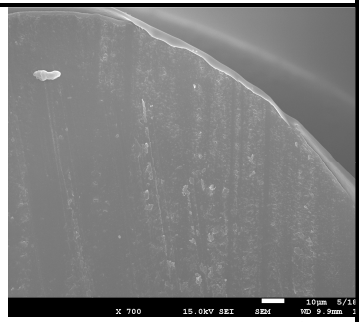
	• PLA cylinders (0.8 mm diameter) were hanged and dipped in hexane solutions containing different proportions of PDMS(10:1) (w:w) (25%, 20%, 15%, 10% or 5%, volume fractions) for 1 min. Structure were removed and dried for 30 min. Coating was cured overnight at 85°C. • Cycles of coating were tested on PLA cylinders (0.8 mm diameter) for 20% and 5% (volume fractions) of PDMS (2 and 5 cycles, respectively). Between cycles, samples were cured for 1h at 85°C. A final curing at 85°C was performed overnight. Samples were cut transversally before coating analysis. Pictures were taken using a low magnification microscope.	For all samples, PDMS solution was drained to the bottom of the structure. For PDMS 20% 1 dip coating step, PDMS 20% 2 dip coating steps and PDMS 5% 5 dip coating steps, a distinguishable coating layer was observed (Figure 1). However, PDMS did not attach to PLA.	 *Figure 1: PLA cylinders coated with PDMS using (A) 1 dip coating step in 20% PDMS in n-hexane, (B) 2 dip coating steps in 20% PDMS in n-hexane and (C) 5 dip coating steps in 5% PDMS in n-hexane.*

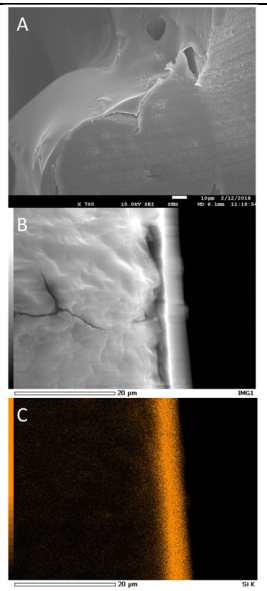
	Gyroid PLA structures were hanged and dipped in hexane solutions containing 5% (volume fraction) of PDMS(10:1) (w:w) for 1 min. Mixture retained by capillarity in the structure was **drained** using paper towels. Structures were deposited on a glass substrates for solvent evaporation. 5 cycles were performed. Between cycles, samples were cured for 1h at 85°C. A final curing at 85°C was carried out overnight. Samples were cut perpendicular to printed layers before coating analysis. Pictures were taken using a low magnification microscope.	A detaching layer of PDMS was observable at some places (Figure 2). No conclusion regarding coating homogeneity can be drawn.	 *Figure 2: PLA gyroid scaffold coated with PDMS using 5 dip coating steps in 5% PDMS in n-hexane.*
Coating using sacrificial templating (molding) (Figure 15)	PLA gyroid structure were printed with PVA support designed by the slicing program. PLA-PVA structures were inserted in 15ml Falcon tubes and immersed in uncured PDMS(10:1) (w:w). Falcon tubes were centrifuged 1 h at 728 g to allow PDMS penetration. Structures were removed and	In FDM as in other AM techniques, the support is printed with a view to be easily removed or dissolved. Hence, the support is printed with small interspaces between printed struts to make the structure weaker. PDMS filled all the gaps	N/A

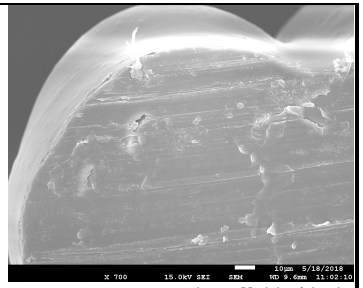
	PDMS was cured overnight at 85°C. PDMS was peeled off from the side of the sample and PVA was dissolved in water.	between PLA and PVA as wells as between PVA struts themselves. This led to a completely clogged structure.	
	A structure was designed to be the negative of the gyroid structure used. To that end, a filled cube vas drawn to surround the whole gyroid model. The gyroid model was then substracted to the filled cube to get gyroid-shaped channels. The channels were widened to have a gap between the gyroid structure and its negative with a view to form a template. Once the structure was printed (gyroid in PLA and template in PVA), the gap can be used as a mold for the coating and the template can be removed by selective dissolution. 	The gyroid structure and the template were overlapping at some places (Figure 3). As the model were aligned, this could be the consequence of a too high amount of deposited polymer, too large nozzles or wrong alignment of printed structures or nozzles during printing.	 *Figure 3: Templating structure (white) printed around the gyroid scaffold (black) with a small interspace for coating molding.*

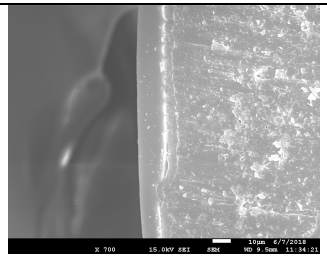
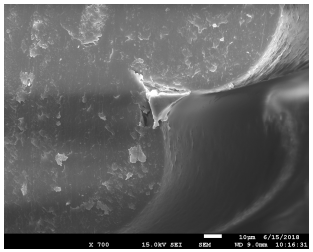
Coating through solvogel formation (Figure 16)	PLA gyroid scaffolds were immersed in a mixture of PDMS(10:1) : n-hexane : 1,4-dioxane (12.5:75:12.5, volume fractions). Vials were hermetically sealed and PDMS crosslinked during 7 days at room temperature. As vials are sealed, solvent cannot evaporate and PDMS in solvent crosslinks to form a gel. As the liquid phase is an organic solvent, the gel is called "solvogel" (in contrast with "hydrogel", for which water is the liquid phase). Once crosslinked, the gel around the structure is cut and solvent is evaporated at room temperature. When solvent is completely evaporated, PDMS is fully cured overnight at 85°C. The same process was carried out at 40°C to speed up PDMS crosslinking. The same protocol was tested for PDMS(10:0.2).	When solvent evaporated, PDMS shrinked on the PLA structure and formed a smooth and rather homogeneous coating (Figure 4). However, some bubbles remained and provoked some pore clogging. Theoretically, layer thickness could be controlled varying proportion of PDMS in the mixture. Similar results could not be obtained for PDMS(10:0.2) as crosslinking did occur neither at room temperature nor at 40°C.	 *Figure 4: SEM image of a PLA gyroid scaffold (dark grey) coated through solvogel formation with PDMS(10:1) (light grey). Curing was achieved at room temperature in the solvent.*
Coating through the formation of a semi-interpenetrating polymer network (SIPN) combined with dip coatings (Figure 17)	PLA gyroids were immersed in a mixture of PDMS(10:1) : n-hexane : 1,4-dioxane (12.5:75:12.5, volume fractions) and heated 1h at 65°C in a water bath. Structures were removed and their content was **drained** using paper towels. Structures were **rinsed** 5 second in hexane, exceeding content was **drained** and PDMS was cured overnight at 85°C. Gyroids structures were then dipped in a solution of 5% PDMS in hexane (volume	A coating was observed but thickness was relatively low (Figure 5). Drainage using paper towel and rinsing step in hexane were suspected to reduce coating thickness. Indeed, for those steps an amount of PDMS was removed. Besides, the deposition of a structure on a flat substrate sucked out the coating solution by	

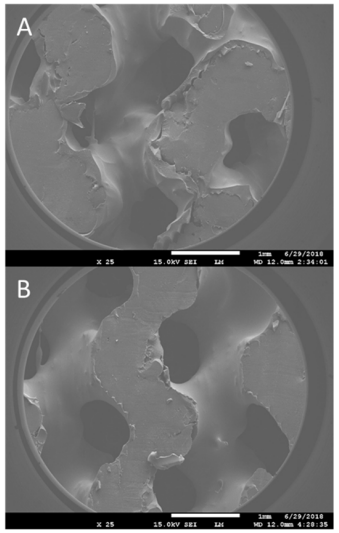
	fraction) for 1 min. Structures were deposited on a glass substrate. After solvent evaporation, PDMS coating was cured for 1h at 85°C. The same dipping protocol was performed 5 times to increase coating thickness. The last curing step was performed overnight.	capillarity. This further reduced the amount of deposited PDMS on the structure.	 *Figure 5: PLA gyroid scaffold (dark grey) coated with PDMS (light grey and yellow) through the formation of a SIPN combined with dip coating. (A) SEM image of a wide region of the sample, (B) SEM image of an enlarged region and (C) the corresponding Si signal (yellow) detected by EDX.*

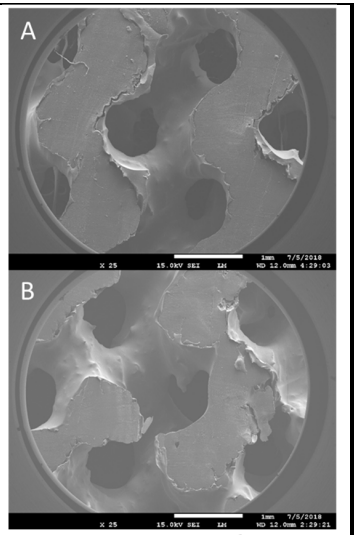
	PLA gyroid scaffolds were immersed in a mixture of PDMS(10:1) : n-hexane : 1,4-dioxane (12.5:75:12.5, volume fractions) and heated 1h at 65°C in a water bath. Structures were removed and **rinsed** 5 second in hexane (**no drainage** using paper towel). PDMS coating was cured at 85°C **for 30 min**. Gyroids structures were then dipped in a solution of 25%, 50% or 75% PDMS in hexane (volume fractions) for 1 min. Structure were hanged for drying (1h) and then cured for 2h.	Pores were completely clogged at the bottom of the structures whatever the concentration in PDMS.	N/A
Coating through the formation of a semi-interpenetrating polymer network (SIPN) with repeated cycles (Figure 18)	PLA gyroid scaffolds were immersed in a mixture of PDMS(10:1) : n-hexane : 1,4-dioxane (12.5:75:12.5, volume fractions) and heated 1h at 65°C in a water bath. Structures were removed and hanged (**no rinsing** and **no drainage**). Once solvent evaporated, PDMS coating was cured at 85°C for 2h.	Presence of PDMS coating but thickness was insufficient at some places (lower than 10 µm) (Figure 6).	 *Figure 6: PLA gyroid scaffolds (dark grey) coated with PDMS (light grey) through SIPN formation. One cycle was performed.*

	• PLA gyroid scaffolds were immersed in a mixture of PDMS(10:1) : n-hexane : 1,4-dioxane (12.5:75:12.5, volume fractions) and heated 1h at 65°C in a water bath. Structures were removed, **rinsed** 5 second in hexane (no drainage) and **hanged** for solvent evaporation. PDMS coating was cured at 85°C for 30 min. After curing, PLA gyroids were immersed in a mixture of PDMS(10:1) : n-hexane : isopropanol (9:36:55 proportions) and heated 1h at 65°C to swell the PDMS layer. Structures were removed, **rinsed** 5 second in isopropanol (no drainage) and **hanged** for solvent evaporation. PDMS coating was cured at 85°C for 30 min. The second coating was repeated once. Final curing was performed overnight at 85°C.	• PDMS layer were relatively small (<2µm). Thickness reached maximum 5 to 10 µm at some places (Figure 7). Presence of silicon atom in the layer was assessed (characteristic of PDMS).	
	• The same experiment was performed and two additional coating cycles in PDMS(10:1) : n-hexane : isopropanol were carried out.	• The added coating cycles did not significantly increase coating thickness.	*Figure 7: PLA gyroid scaffold (dark grey) coated with PDMS (light grey and yellow) through the formation of a SIPN with repeated cycles. (A) SEM image of a wide region of the sample, (B) SEM image of an enlarged region and (C) the corresponding Si signal (yellow) detected by EDX.*

	PLA gyroid scaffolds were immersed in a mixture of PDMS(10:1) : n-hexane : 1,4-dioxane (12.5:75:12.5, volume fractions) and heated 1h at 65°C in a water bath. Structures were removed, **rinsed** 5 s in hexane and their content was **drained** using paper towels. PDMS coating was not cured and PLA gyroids were directly immersed in a mixture of PDMS(10:1) : n-hexane : isopropanol (9:36:55, volume fractions). The mixture was heated for 1h at 65°C. Structures were removed, **rinsed** 5 s in isopropanol and their content was **drained** using paper towels. PDMS coating was not cured and PLA gyroids were directly engaged for next coating step. The second coating and rinsing steps were repeated 3 more times. Final curing was performed overnight at 85°C.	No significant PDMS coating layer was observed (Figure 8).	 *Figure 8: PLA gyroid scaffolds (dark grey) coated with PDMS (light grey) through SIPN formation with repeated cycles. Structures were rinsed and exceeding content was drained.*

	• PLA gyroid scaffolds were immersed in a mixture of PDMS(10:1) : n-hexane : 1,4-dioxane (12.5:75:12.5, volume fractions) and heated 1h at 65°C in a water bath. Structures were removed and hanged for solvent evaporation (no rinsing step). PDMS coating was cured overnight at 85°C. After curing, PLA gyroids were immersed in a mixture of 14% (volume fraction) of PDMS(10:1) in n-hexane and heated 1h at 65°C. Structures were removed, **rinsed** for 2 s in isopropanol (no drainage) and **hanged** for solvent evaporation. PDMS coating was cured at 85°C for 30 min. The second coating was repeated once. Final curing was performed overnight at 85°C.	• A PDMS coating thickness of around 10 µm was obtained (Figure 9).	 *Figure 9: SEM images of PLA gyroid scaffolds (dark grey) coated with PDMS (light grey) through SIPN formation with repeated cycles. Structures were rinsed and hanged.*
	• The same experiment was performed except that one **rinsing step** was added before the first solvent evaporation step. Besides, structures were **not hanged** but deposited on a glass substrate.	• No significant coating was obtained when the rinsing step was added and when structure were not hanged (Figure 10). These results tend to confirm what was previously mentioned. Rinsing step is suspected to remove an amount of PDMS, while the deposition on a flat substrate drain PDMS solution.	 *Figure 10: SEM images of PLA gyroid scaffolds (dark grey) coated with PDMS (light grey) through SIPN formation with repeated cycles. Structures were rinsed twice and not hanged*.

	• PLA gyroid scaffolds were coated using PDMS(10:1) and PDMS(10:0.2). Structures were immersed in a mixture of PDMS : n-hexane : 1,4-dioxane (12.5:75:12.5, volume fractions) (2ml/scaffold) and heated 1h at 65°C in a water bath. Structures were removed and **hanged** for solvent evaporation (**no rinsing step**). PDMS coating was cured overnight at 85°C. PLA gyroids were then immersed in a mixture of 14% (volume fractions) of PDMS(10:1) in n-hexane (2ml/scaffold) and heated 1h at 65°C. Structures were removed and **hanged** for solvent evaporation (**no rinsing step**). After solvent evaporation PDMS coating was cured at 85°C for 30 min. The second coating was repeated once. Final curing was performed overnight at 85°C.	• A significant coating layer thickness was obtained for PDMS(10:1) using a total of 3 coating cycles (1 in ternary mixture and 2 in PDMS 14%) (Figure 11). However, a thin coating was obtained for PDMS(10:0.2) in the same conditions.	 *Figure 11: SEM images of PLA gyroid scaffolds (dark grey) coated with PDMS (light grey) through SIPN formation with repeated cycles. (A) PDMS(10:1) and (B) PDMS(10:0.2) were coated using a total of 3 cycles.*

	• The same experiment was carried out except that - For PDMS(10:1): the last coating cycle was removed; - For PDMS(10:0.2): two coating cycles were added for a total of 4 coating cycles in 14% PDMS solution. Samples were weighed after each coating cycle.	• A significant coating layer thickness was obtained for PDMS(10:1) and the coating layer thickness increased for PDMS(10:0.2) for a total of 2 and 5 coating cycles, respectively (Figure 12). The weight of the samples increased after each coating.	 *Figure 12: SEM images of PLA gyroid scaffolds (dark grey) coated with PDMS (light grey) through SIPN formation with repeated cycles. (A) PDMS(10:1) and (B) PDMS(10:0.2) were coated using a total of 2 and 5 cycles, respectively.*

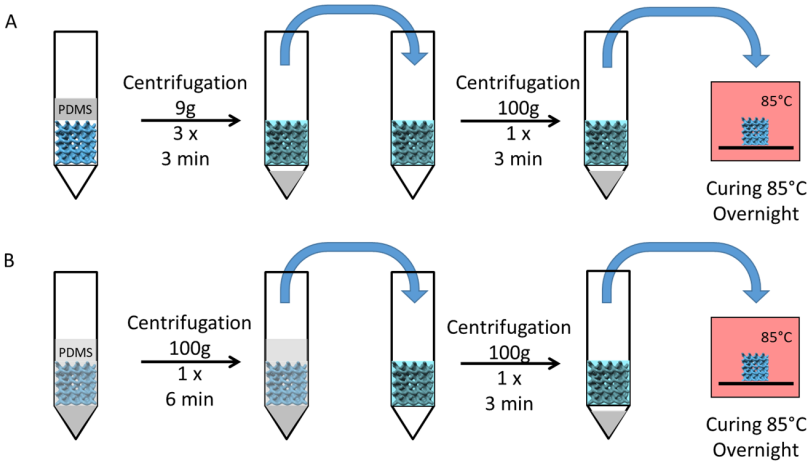


Figure 13: Coating by centrifugation. A and B are two different tested protocols.

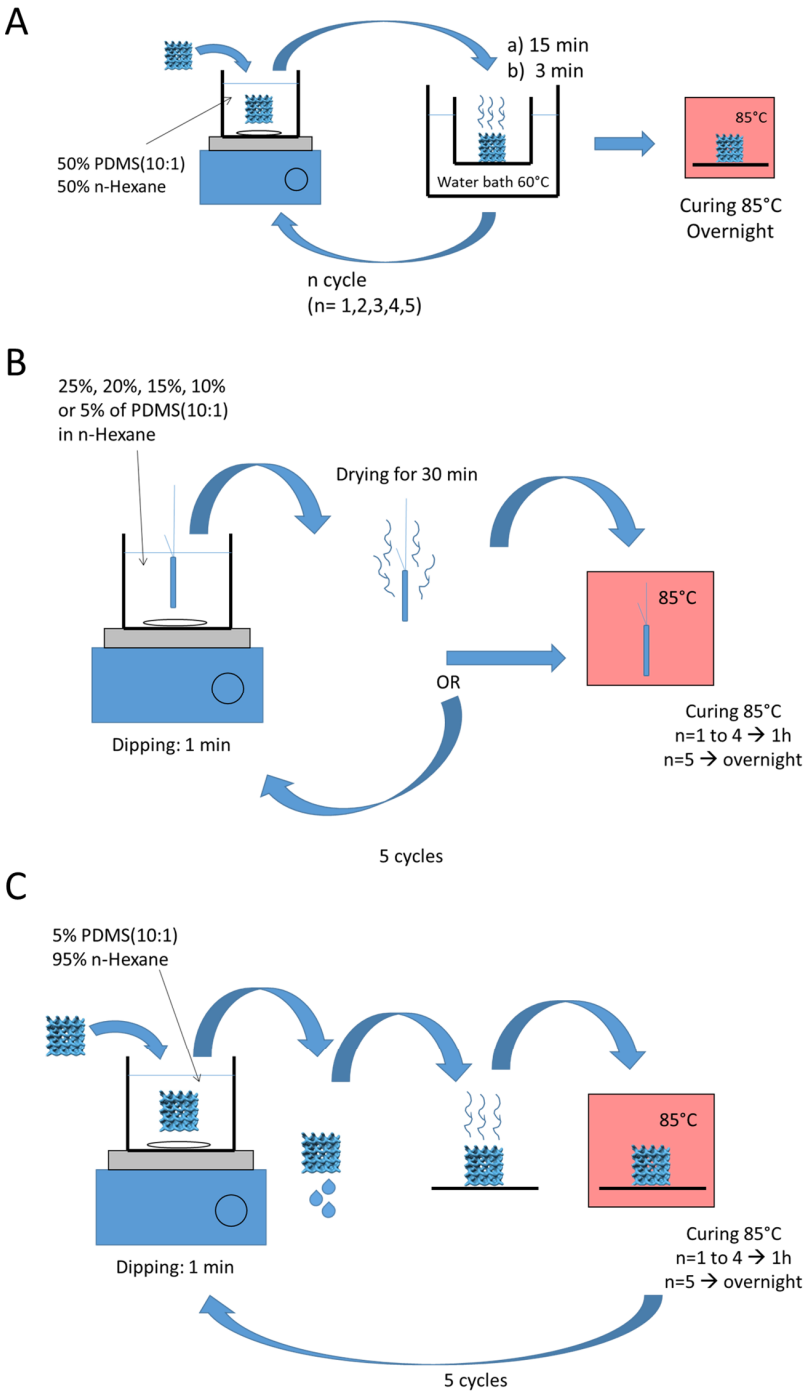


Figure 14: Dip coating. A, B and C are three different tested protocols.

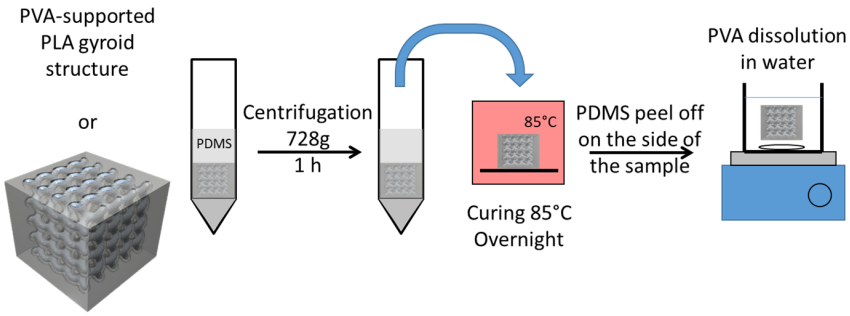


Figure 15: Coating using sacrificial templating (molding).

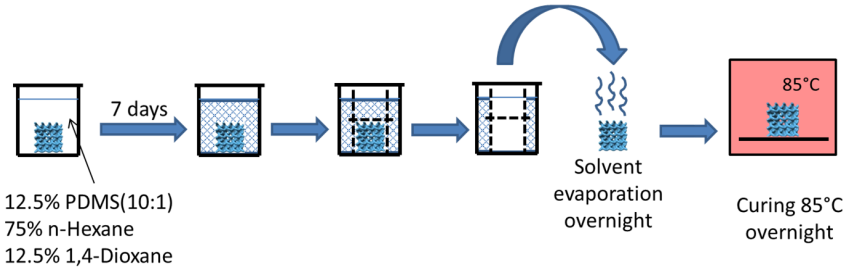


Figure 16: Coating through solvogel formation.

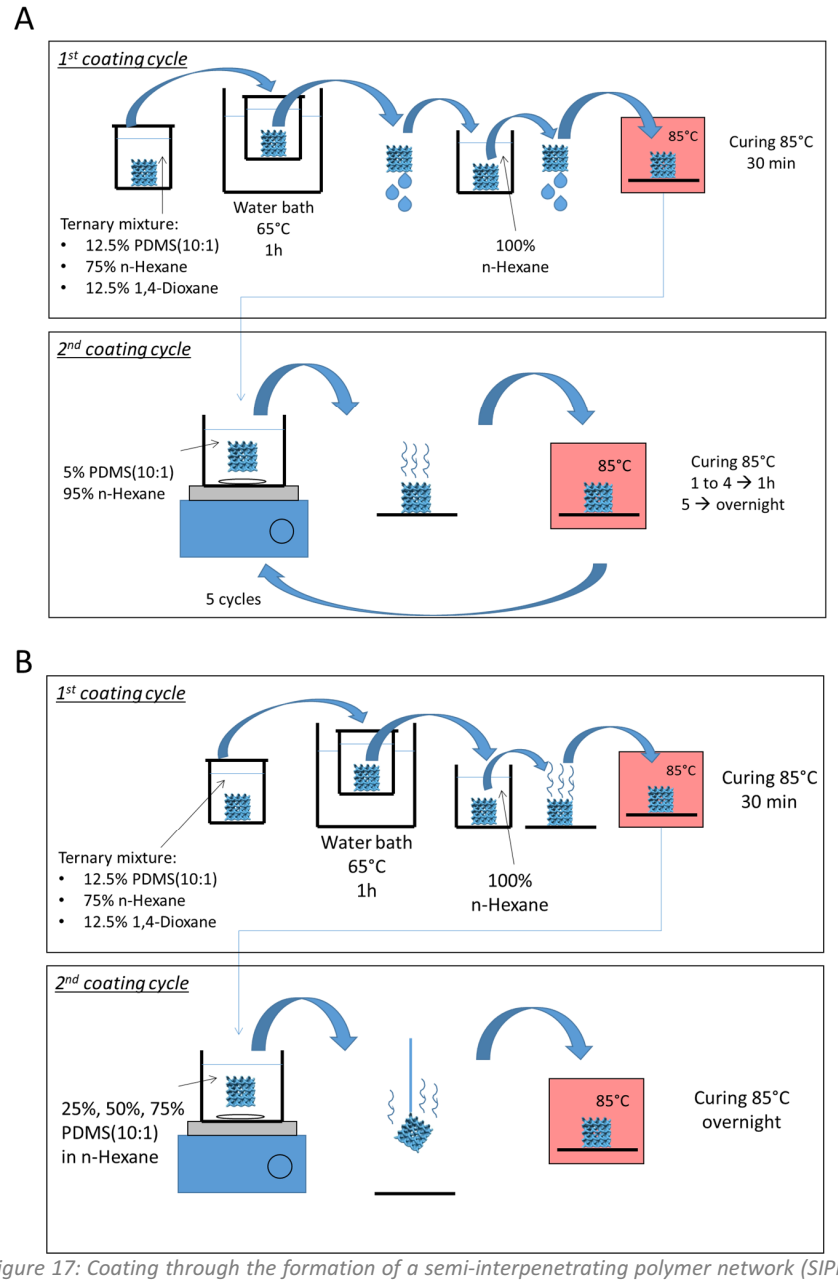


Figure 17: Coating through the formation of a semi-interpenetrating polymer network (SIPN) combined with dip coatings. A and B are two different tested protocols.

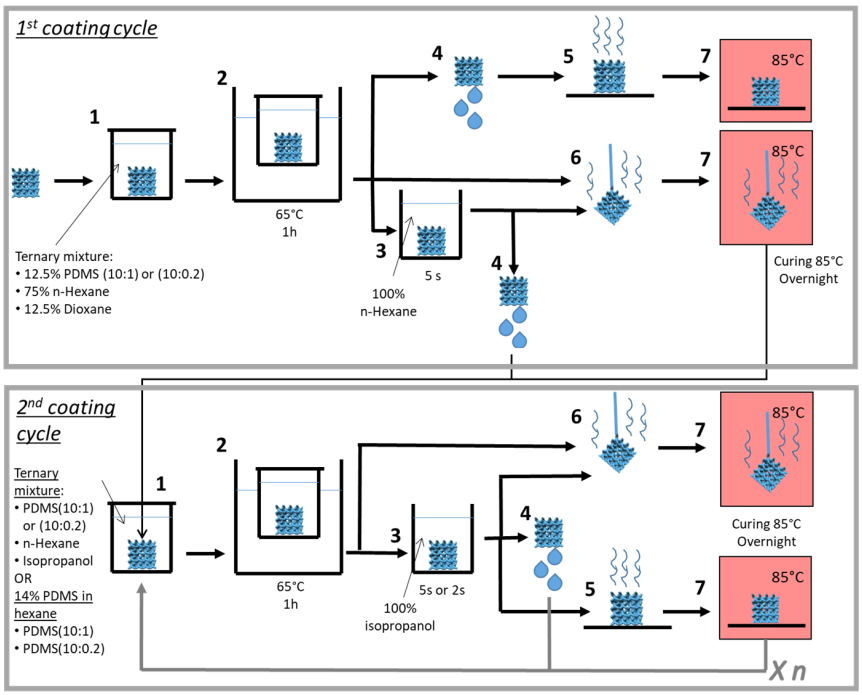


Figure 18: Schematic of the different steps and tested modifications in coating protocol through the formation of a SIPN. 1. Insertion of the scaffold in the ternary mixture or in n-hexane containing PDMS base and curing agent. 2. Scaffold remains in coating mixture for a defined period of time at a given temperature. This step allows surface swelling and uncured PDMS interpenetration with scaffold polymer chains. Besides, PDMS starts to crosslink. 3. Rinsing step in non-solvent of the scaffold shrinks back the swollen surface and traps PDMS. 4. Drainage of excess solvent retained by capillarity in the scaffold. 5. Deposition of the scaffolds on a glass substrate for solvent evaporation. 6. Hanging of scaffolds for solvent evaporation. 7. Curing of PDMS coating.